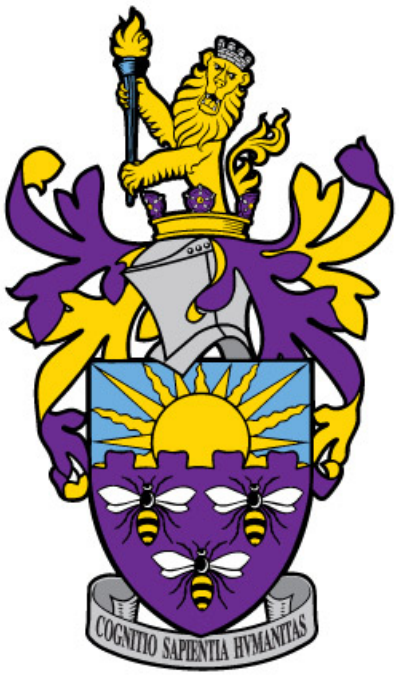

Computational Investigation into the Mechanism of Water Oxidation in Nature

Felix Rummel

A thesis submitted to The University of Manchester for the degree of Doctor of Philosophy in the Faculty of Science and Engineering

School of Natural Sciences
Department of Chemistry
2023

Contents

List of Abbreviations

Abbreviation	Definition
ACM	Adiabatic Connection Method
AF	Anti-Ferromagnetic
AO	Atomic Orbital
ATP	Adenosine Triphosphate
BO	Born-Oppenheimer
BS	Broken-Symmetry
BS-DFT	Broken-Symmetry Density Functional Theory
CPCM	Conductor-like Polarizable Continuum Model
CW	Continuous Wave
DFT	Density Functional Theory
EDNMR	Electron-electron Double resonance-detected Nuclear Magnetic Resonance
EPR	Electron Paramagnetic Resonance
EXAFS	Electron X-ray Absorption Fine Structure
FM	Ferromagnetic
GGA	Generalised Gradient Approximation
GTO	Gaussian Type Orbital
HDvV	Heisenberg-Dirac-van Vleck
HF	Hartree-Fock
HFC	Hyperfine Coupling
HS	High Spin
IBO	Intrinsic Bonding Orbital
IRC	Intrinsic Reaction Coordinate
LCAO	Linear Combination of Atomic Orbitals
LDA	Local Density Approximation
LS	Low Spin
MM	Molecular Mechanics
MW	Microwave

NADPH	Nicotinamide Adenine Dinucleotide Phosphate
NHE	Normal Hydrogen Electrode
NEB	Nudged Elastic Band
NIR	Near-Infrared Radiation
OEC	Oxygen Evolving Complex
PES	Potential Energy Surface
PDB	Protein Data Bank
PSII	Photosystem II
QM	Quantum Mechanics
SCF	Self-Consistent Field
STO	Slater Type Orbital
TS	Transition State
WOC	Water Oxidation Catalysis
XES	X-ray Emission Spectroscopy
XFEL	X-ray Free Electron Laser
ZFS	Zero Field Splitting
ZORA	Zeroth-Order Regular Approximation

List of Tables

List of Figures

List of Publications

Published

Bonding and Magnetic Exchange Pathways in Nature's Water-Oxidizing Complex

T. A. Corry, F. Rummel, P. J. O'Malley, *J. Phys. Chem. B*, **2021**, 125(26), 7147-7154

How Nature Makes O2: an Electronic Level Mechanism for Water Oxidation in Photosynthesis

F. Rummel, P. J. O'Malley, *J. Phys. Chem. B*, **2022**, 126(41), 8214-8221

Work Not Included in this Thesis

Magnetic and Electronic Structural Properties of the S3 State of Nature's Water Oxidizing Complex: A Combined Study in ELDOR-Detected Nuclear Magnetic Resonance Spectral Simulation and Broken-Symmetry Density Functional Theory

C. J. Rogers, O. Hardwick, T. A. Corry, F. Rummel, D. Collison, A. M. Bowen, P. J. O'Malley, *ACS Omega*, **2022**, 7(45),41783-41788

Abstract

Water oxidation into molecular oxygen is not only a key process for our aerobic atmosphere but also of high interest as potential source of green hydrogen. Improvements to this process could benefit plant growth and as such food yields. Though many advancements into the elucidation of its mechanism have been made both experimentally and computationally, there is still much uncertainty around the exact structures and electronic changes involved throughout the catalytic cycle performed by photosystem II. This thesis presents computational work, using broken-symmetry density functional theory primarily, on the nature of the bonding and magnetic exchange in the oxygen evolving complex, the nature of the S_3 state, the mechanism of deprotonation in the S_3 state and the identity of the $S_3Y_Z^{\bullet}$ state.
The exchange pathways between Mn centres are illustrated by the use of intrinsic bonding orbitals and corresponding orbitals, showing that protonation of linking oxygen bridges can interrupt superexchange couplings between the metal centres. It is established that Ca^{2+} is ionic in nature and acts to modulate the properties of the water oxidising complex as a whole. These illustrative methods are used subsequently to give insights into the S_3 state, in which a unique low energy barrier for O_2 formation via an $[O5O6]^{3-}$ intermediate was identified. This intermediate is shown to have a two-centre one-electron bond, with the shared oxygen spin strongly stabilised by anti-ferromagnetic interaction with the Mn centres. Inclusion of this intermediate in electron paramagnetic spectroscopy simulations better reproduces experimental observations. In order to form the formal O5-O6 bond a proton must be removed from O6, two possible pathways for O6 deprotonation are presented. While the Glu189 pathway is found unsuitable a promising pathway via W3 is identified and analysed at various O5-O6 distances. Finally the $S_3Y_Z^{\bullet}$ state is investigated and three intermediates on the path to O-O bond formation are analysed. It was found that as the O5-O6 bond is formed long range exchange interaction between the oxygen evolving complex and the nearby Y_Z increase in strength, encouraging subsequent reduction of Y_Z. As such a unique mechanism for the formation of molecular oxygen is presented and analysed.

Declaration

No portion of the work referred to in the thesis has been submitted in support of an application for another degree or qualification of this or any other university or other institute of learning.

Copyright Statement

i. The author of this thesis (including any appendices and/or schedules to this thesis) owns certain copyright or related rights in it (the "Copyright") and s/he has given The University of Manchester certain rights to use such Copyright, including for administrative purposes.

ii. Copies of this thesis, either in full or in extracts and whether in hard or electronic copy, may be made only in accordance with the Copyright, Designs and Patents Act 1988 (as amended) and regulations issued under it or, where appropriate, in accordance with licensing agreements which the University has from time to time. This page must form part of any such copies made.

iii. The ownership of certain Copyright, patents, designs, trade marks and other intellectual property (the "Intellectual Property") and any reproductions of copyright works in the thesis, for example graphs and tables ("Reproductions"), which may be described in this thesis, may not be owned by the author and may be owned by third parties. Such Intellectual Property and Reproductions cannot and must not be made available for use without the prior written permission of the owner(s) of the relevant Intellectual Property and/or Reproductions.

iv. Further information on the conditions under which disclosure, publication and commercialisation of this thesis, the Copyright and any Intellectual Property and/or Reproductions described in it may take place is available in the University IP Policy (see http://documents.manchester.ac.uk/DocuInfo.aspx?DocID=24420), in any relevant Thesis restriction declarations deposited in the University Library, The University Library's regulations (see http://www.library.manchester.ac.uk/about /regulations/) and in The University's Policy on Presentation of Theses.

Acknowledgement

I would like to thank the University of Manchester for providing me with the facilities to carry out my work, in particular the computational shared facility and its support team. I thank the UK BBSRC Doctoral Training Partnership program for their financial support and funding throughout my PhD.

Further thanks goes to my supervisor Patrick O'Malley who has supervised me for the last four years and who's knowledge of the ever-changing research area has been greatly beneficial to my development as a research scientist. Furthermore the group as a whole has aided me greatly throughout and allowed me to solve problems, discuss ideas and present my work.

Finally I would like to extend my gratitude to my friends and family for their continuing support throughout my time as a student. And further to both the University Boat Club and Grosvenor rowing club in their facilitation of my athletic career. In particular my coaches Jeff Hunt and Paul Turner who helped me to repeatedly achieve my sporting goals such as obtaining a medals at the British University Championship, and providing a great balance to my studying.

Journal Format Justification

The Journal format was chosen to present work in this thesis with each results chapter presenting published work, a submitted manuscript, or a manuscript prepared for submission. This format both encourages writing and publishing work throughout the PhD and avoids the superfluous need to reword results chapters. An introduction to the topics as a whole, with particular focus on areas of relevance for the published work is given prior to presentation of the results chapters. Furthermore each results chapter is introduced to give appropriate context of the work carried out within the chapter and to improve the overall flow of the thesis. Publications to which no major contributions were made are omitted in this thesis, but listed in the list of publications. Permission to reproduce published work has been obtained from the publishing body in each case.

Chapter 1

Photosystem II

Nature's development of Photosynthesis is key to the evolution of life on Earth as we know it, thought to have occurred roughly 3 billion years ago.[1] Photosynthesis has likely taken place with little change to the process since it first emerged in cyanobacteria, which allowed for our oxygen rich atmosphere to be formed, by the oxidation of water into oxygen using sunlight to drive the reaction.[2] The first step in natural photosynthesis takes place in Photosystem II (PSII), a 650 kD dimeric complex, containing $\approx$ 20 protein subunits as well as various cofactors such as chlorophyll and a unique manganese-calcium-oxygen cluster known as the oxygen-evolving-complex (OEC) which is the reaction centre for oxygen formation.[3] This chapter aims to give an outline of reactions involved in photosynthesis as well as a more in depths review of PSII and its workings.

1.1 Photosynthesis

Artificial Photosynthesis has become of interest as it could provide a route to the generation of oxygen and more importantly hydrogen from water, thus providing a green source of energy. As so often the case with technological advancement the initial inspiration is taken from nature, for example early wing designs were based on the study of bird wings. So the understanding of natural photosynthesis is important and highly relevant to the creation of artificial systems capable of photosynthesis.[4] Potential also lies in the engineering of more efficient photosynthesis in plants, resulting in faster growth and as such increased food yields.[5]

In order to create an efficient catalyst for water oxidation it would need to efficiently utilise the energy provided by sunlight, and to provide a reaction pathway for water oxidation with low energy requirements. In nature PSII uses P_{680}, a strong reducing agent, which is limited to a $\approx$ 1.2 V reducing power to carry out water oxidation. Figure 1.1 shows the energy requirements for water oxidation in aqueous solution, it is clear that the initial oxidation presents a high energy barrier, PSII effectively lowers this barrier, thus understanding its function would aid in the design of an artificial catalyst.[6]

PSII is located in the thylakoid membrane or cyanobacteria, green algae and higher plants, with the OEC located towards the lumenal side.[8, 9] There are two parts to photosynthesis, reactions depending on light *'Light Reactions'* and *'Dark Reactions'* that do not depend on light and typically take place in the stroma region. The *'Light Reactions'* produce oxygen, nicotinamide adenine dinucleotide

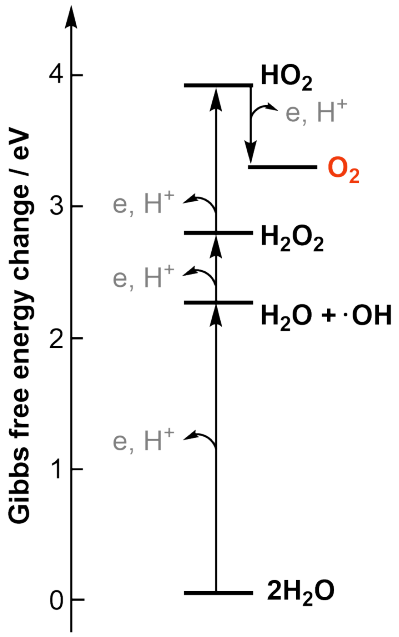

Figure 1.1: Gibbs free energy change for water oxidation in aqueous solution. The figure was adapted from reference[7].

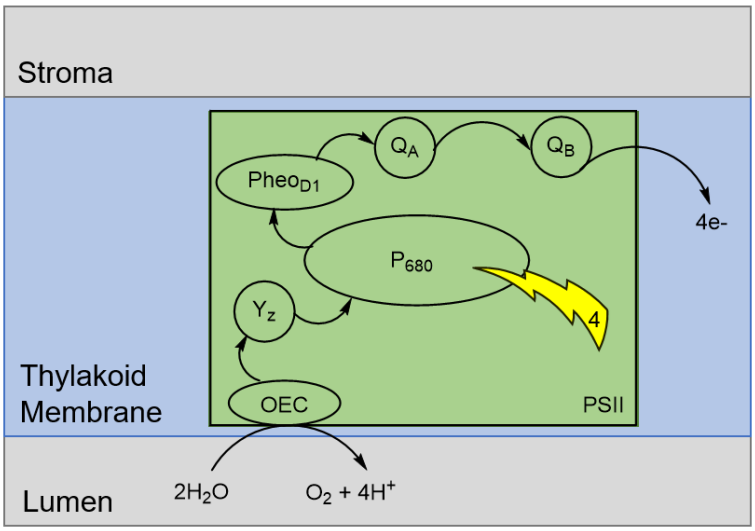

Figure 1.2: Summary of electron transport in PSII which takes place during photosynthesis, arrows indicate the direction of electron movements.

phosphate (NADPH) and adenosine triphosphate (ATP) while the *'Dark Reactions'* produce sugars using CO_2, ATP and NADPH.[10] Figure 1.2 shows PSII's role during photosynthesis specifically electron movement.[11, 12]

Initially a Chlorophyll residue absorbs a photon and becomes excited, one electron is donated to a nearby Pheophytin, $Pheo_{D1}$, this electron is transferred to the primary and secondary plastoquinone acceptors, Q_A and Q_B, respectively.[13] The transfer between Q_A and Q_B takes place via a non-heme Fe site, and plastoquinone Q_B after coupling with two protons is released as PQH_2 and replaced by a new plastoquinone.[11] The reducing equivalent PQH_2 is then transferred down the photosynthetic electron-transport chain, *via* cytochrome b_6f and photosystem I resulting finally in the production of NADPH.[12] As a result of the electron transfer a $P_{680}^{+\bullet}$ radical cation is formed within PSII which oxidises the nearby Tyrosine residue Tyr161 more commonly referred to as Y_Z. As the Y_Z radical is formed it simultaneously deprotonates with the proton going to the nearby hydrogen bonded His190 residue. This finally leads to the oxidation of the OEC Manganese cluster, which performs the water oxidation to protons and oxygen. Overall it is necessary for 4 photons to be absorbed to complete one catalytic cycle in PSII converting two equivalents of water into one equivalent of oxygen and 4 protons.[13, 14]

1.2 The Oxygen Evolving Complex

As outlined in section 1.1.1 one catalytic cycle to produce oxygen requires 4 photon absorptions, and so 4 oxidations of the Manganese cluster by Y_Z. Kok proposed in 1970 that the OEC cycles through 5 different "S-States" labelled S_n where n is the number of oxidative equivalents stored in the OEC, making S_0 the

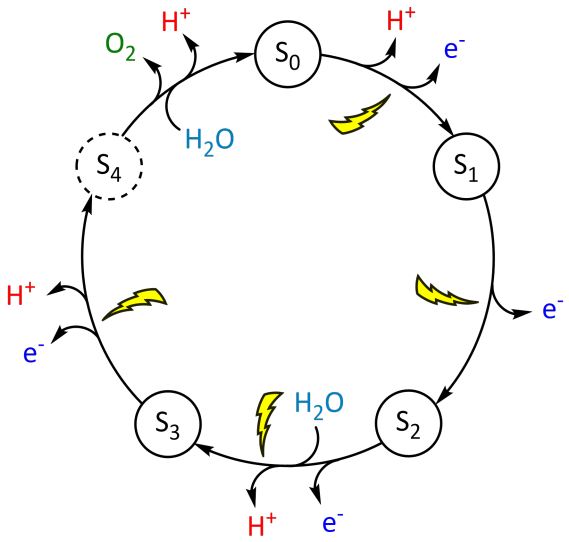

Figure 1.3: The Kok cycle, the OEC cycles through the 5 S-stated by successive one electron oxidations.

most reduced and S_4 the most oxidised state. Each one electron oxidation of the OEC leads to the "formation" of the next S-state, thus the OEC will proceed from the S_0 state through S_{1-3} to S_4, at this point oxygen is released and the OEC returns to the S_0 state, this is known as the Kok cycle and is summarised in figure 1.3.[15]

The structure of the OEC was determined initially by Umena et al. in 2011, publishing a crystallographic structure of the S_1 state with a resolution of 1.9 Å.[16] This structure confirmed that the OEC contained a Mn_4O_5Ca complex as well as the presence of four directly bonded water molecules W1-W4, with W1 and W2 bound to Mn_4 and W3 and W4 bound to the Ca ion. The structure and labelling of the OEC is shown in figure 1.4.

As can be seen in figure 1.4 the OEC adopts a cubic like structure with Mn_1-Mn_3, O1-3, O4 and Ca, to which Mn_4 is connected by two bridging oxygen ligands O4 and O5. However the precise protonation state of the various oxygens in W1-W4 and O1-O5 is still a source of discussion.[11, 18, 19] Similarly for the Manganese ions there is discussion as to their oxidation state throughout the Kok cycle. With either a high or low spin scheme being adopted.[20] The two approaches differ by two unpaired electrons in each state, for example in the S_2 the high spin scheme would assign the centres as $Mn^{III}Mn^{IV}_3$ whereas the low spin scheme assigns them as $Mn^{III}_3Mn^{IV}$. This thesis uses the high spin scheme throughout, as it has greater experimental and theoretical support compared to the low spin-scheme which while it supports many structural observations fails to support magnetic properties, this has been discussed at length in the references.[20–23] Calcium the final component of the OEC cluster is of critical importance to its function, removal causes oxygen production to fail, with the only ion which can successfully be substituted being Sr, although oxygen is then evolved at a much lower rate.[11, 24, 25] It is thought

that Calcium is involved in water delivery to the complex[26], recently a theoretical and experimental study on an isolated $CaMn_4O_5^+$ complex proposed that water would adsorb dissociatively to the isolated cluster at the Ca site due to a low water dissociation barrier. The cluster then reorganises with hydrogen migration between the various oxygen ligands. This rationalises the importance of Ca in the OEC as it would allow the two water molecules added to the complex throughout the Kok cycle to be efficiently integrated and deprotonated.[27]

The structure of PSII can be studied using crystallographic methods, early studies lacked the resolution to identify all OEC ligands but allowed for the general shape and size of the OEC cluster to be determined,[28, 29] it was only in 2011 that the first "complete" structure showing all oxygen bridges in the OEC was obtained by Umena et al..[16]

Using X-ray free electron laser (XFEL) crystallography Suga et al. was able to obtain a more refined structure of PSII in 2014, which was deemed radiation damage free and was found to be similar to the Umena structure.[30] This more refined structure shows the Mn cluster to be an open cubane, as shown in figure 1.4, in which O5 is closer to Mn_4 than it is to Mn_1. Conversely a closed cubane is differentiated by the position of O5 being closer to Mn_1. Over recent years these studies have been extended to cover the various S states of the Kok cycle, as well as giving insights into the changes that occur between the S-states allowing for example for the insertion of water molecules to be seen.[31–34] So far it has not been possible to isolate the final S_4 state in the Kok cycle as it is transient. Figure 1.5 shows the Mn cluster in the S_2 state as well as nearby residues.

Furthermore a recent theoretical study by Sirohiwal and Pantazis[35] has uncovered some issues with existing structures, namely that during preparation

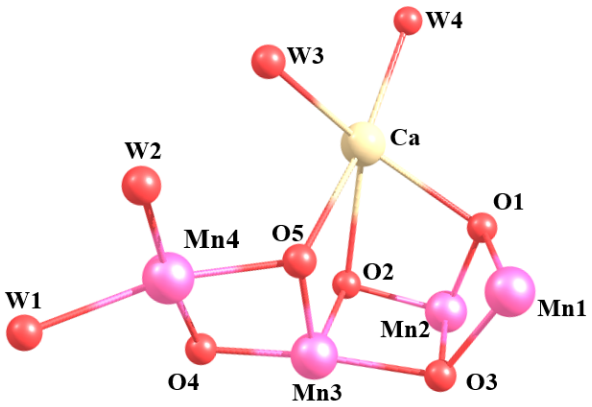

Figure 1.4: Structure of the OEC and labels for each atom. The model pictured was generated from the S_2 4UB6 structure published by Suga et al..[17] Colours are as follows, Mn(pink), O(red), Ca(beige), hydrogens are omitted for the sake of clarity.

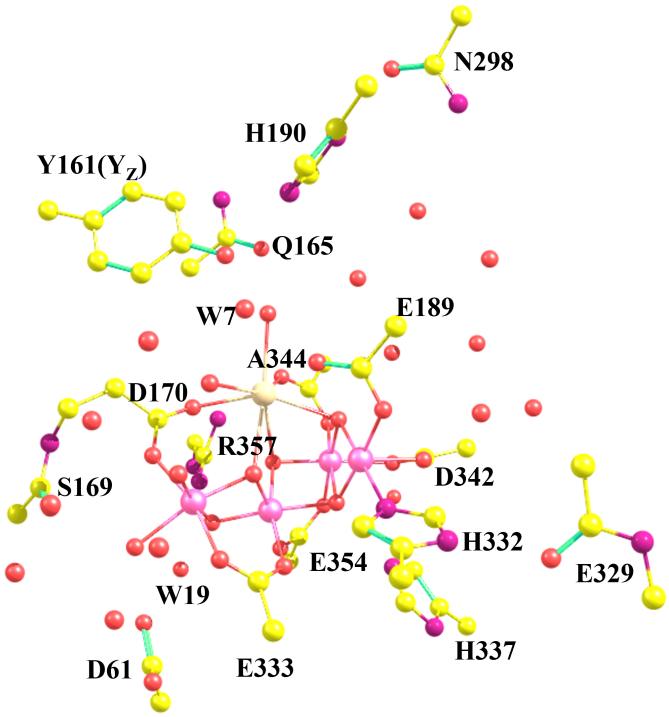

Figure 1.5: Structure of the OEC and nearby residues. The model pictured was generated from the S_2 4UB6 structure published by Suga et al..[17] Colours are as follows, Mn(pink), O(red), C(yellow), Ca(beige), N(purple), hydrogens are omitted for the sake of clarity.

of XFEL samples the PSII complex often becomes dehydrated, their results have shown that all of the data obtained by XFEL corresponds to dehydrated or severely dehydrated PSII. With the data often missing water molecules and channels even close to the OEC. Comparing their theoretical data to the various available structures they found the structure determined by Tanaka et al.[36] to match their fully hydrated model best.

There are further issues with the current and older crystal structures also, as they are not in complete agreement with the oxidation states assigned by EPR spectroscopy, showing various extends of over reduction of the Mn ions, impure S-states and incorrect electronic changes for S-state transitions. As such care should be taken when interpreting these structures and conclusions drawn solely on structural data are likely flawed.[37–41]

This Thesis discusses the S_2 and S_3 state as well as the S_3 to S_0 transition via S_4 and its intermediate. As such these will be discussed in the following sections. For discussion of the other S states S_0 and S_1 as well as their intermediates see references.[11, 20, 40, 42–50]

1.2.1 The S_2 State

The S_2 state is generated from the dark stable S_1 state by a single flash of light, during the transition no chemical changes occur, only an electron is removed from the OEC. Before the more recent high resolution structures were obtained the S_2 state was primarily studied by Electron Paramagnetic Resonance (EPR) spectroscopy. First reported in 1981 by Dismukes and Siderer[51] it has since been extensively studied by EPR spectroscopy.[42, 52–55] The S_2 continuous-wave (CW) EPR spectra for the S_2 state is shown in figure 1.6.

As can be seen from figure 1.6 there are two distinct signals. A more complex multi line signal at $g = 2$ which is often referred to as the low spin (LS) signal as it corresponds to a ground state spin of 1/2. The other signal is known as the high spin (HS) signal it is centred $\approx g = 4.1$ and corresponds to a ground state spin of 5/2.[42] It has been determined that these are not excited state signals but instead ground state signals, suggesting heterogeneity in the S_2 state.[56] Furthermore it has also been found that it is the HS form which progresses to the S_3 state.[57]

To rationalise this apparent heterogeneity a model of the OEC for the S_2 state was proposed wherein the complex would be an equilibrium between a closed and open cubane form, with the closed cubane responsible for the HS signal and the open cubane responsible for the LS signal. This was first suggested by Pantazis et al. in 2012.[58] Pantazis et al. proposed that there are two structural isomers present in the S_2 state which differ in the position and bonding of O5, form either the closed- or open-cubane, furthermore in the open cubane Mn1 was found to be Mn^{III} and Mn_4 to be Mn^{IV} whereas in the closed cubane Mn_1 was found to be Mn^{IV} and Mn_4 to be Mn^{III}. Theoretical calculations showed the barrier between these two forms to be low ≈ 9 kcal mol^{-1}.[58] This is shown in figure 1.7 by equilibrium "A". It was also found that the relative intensities of the low and high spin signals in the S_2 spectra could be changed by various chemical treatments, for example high pH conditions would favour the HS signal whereas methanol enriched samples

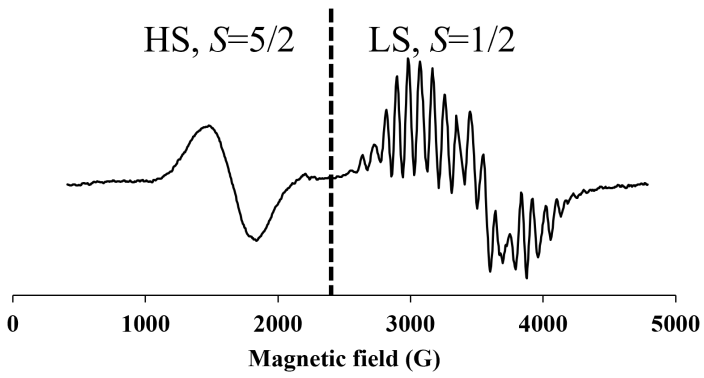

Figure 1.6: S2 cw-EPR spectra reproduced from Peloquin and Britt, the high spin (HS) and low spin (LS) signals are indicated.[42]

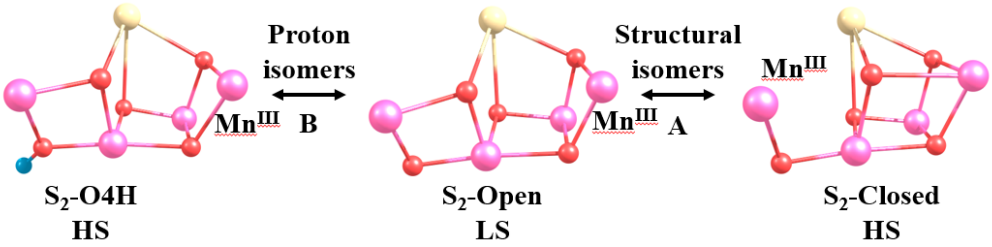

Figure 1.7: A: Proposed open/closed-cubane equilibrium, differing in the position of the Mn^{III} ion.[58] B: Proposed proton isomers for the LS/HS equilibrium.[63] Positions of the Mn^{III} ion are indicated for each form of the S_2 state.

favoured the LS signal, the open/closed-cubane equilibrium failed to rationalise these observations.[59] Furthermore while several crystallographic structures have been reported by different groups [31, 32] so far a closed-cubane has never been reported with the experimental Mn-Mn distances agreeing with an open-cubane form.[60–62] Alternatively to the open/closed-cubane isomerism in 2019 Corry and O'Malley proposed that the HS and LS form in the S_2 state are proton isomers differing in the protonation state of O4 and W1, with the LS form being an open cubane as before and the HS form being an O4 protonated form with W1 as OH ligand, this is shown as equilibrium "B" in figure 1.7.[63]

The proposed S_2 proton isomers can to some extent rationalise why chemical treatment may intensify one signal over the other, it also explains the observation that the hydrogen bonding network around O4 changes when the S_1 state progresses to the S_2 state. Namely the distance between O4 and W19 shortens and a nearby water (W20) which hydrogen bonds to W19 disappears suggesting it has increased in mobility due to changes in the hydrogen bonding network.[31, 32] It was found using broken symmetry density functional theory (BS-DFT) that O4 protonation changes the interaction between Mn_3 and Mn_4 from anti-ferromagnetic to ferromagnetic which causes the ground state spin to change from the LS $S = 1/2$ to the HS $S = 5/2$ and furthermore that the relative energy difference was ≈ 9 kcal mol^{-1}.[63] This agreed with observations that transition between the LS and HS states can take place at low energy.[57] The proton isomers do not rely on the formation of a closed cubane to explain the LS/HS heterogeneity but do not exclude their existence.

1.2.2 Water within PSII

The OEC sits within the larger structure of PSII, during the Kok cycle two water molecules are consumed to yield 4 protons and molecular oxygen which must be removed from the protein to enable continuing function, therefore studies into how water is inserted into the protein and how it binds to the OEC, as well as studies investigating H-bond networks are of importance in order to understand the

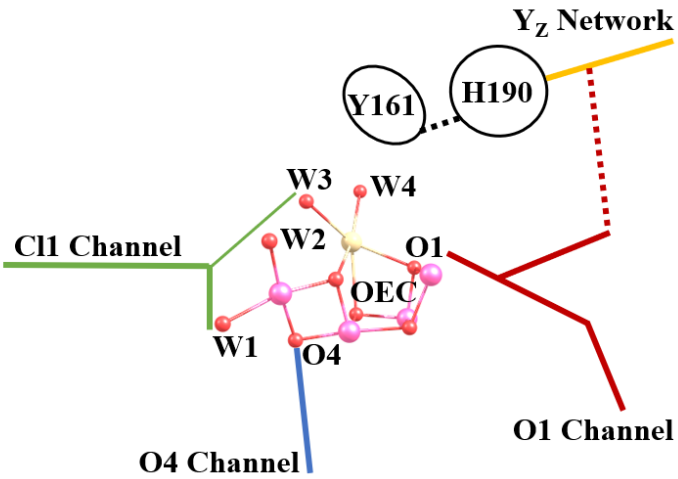

Figure 1.8: Water network and channels around the OEC based on recent experimental and theoretical findings.[35, 65] The Cl1 channel is shown in green, the O4 channel in blue, the O1 channel in red and the Y_Z network in yellow. The positions of the Y_Z residue and its hydrogen bonding partner H190 are indicated in black.

functioning of the OEC and PSII. Extensive theoretical, experimental and hybrid studies have been published on this topic.[35, 64–72] Section 1.2.2.1 will discuss the structures and roles of water chains, networks and channels around the OEC while section 1.2.2.2 will discuss theories on how water is inserted into the OEC during the Kok cycle.

1.2.2.1 Water Networks around the OEC

Water networks are readily revealed using crystallographic structures of PSII, showing cavities as well as sufficiently stationary water molecules and chains. Furthermore calculations and simulations can analyse the properties of the networks and channels. Figure 1.8 summarises the structure of water networks and channels around the OEC, based on theoretical [35, 64, 70] and experimental [31, 65, 72] studies.

By more recent convention the channels are named after the which atom in the OEC is closest to the end of the channel. There are three main channels which connect the OEC to the bulk, the O1, O4 and Cl1 channel, each of these consists of several water chains and branches of differing sizes which may connect to the bulk separately.[35, 65]

The Cl1 channel connects the bulk to Mn_4 and the OEC water ligands W1, W2 and W3, it is named after a chloride ion which sits near Mn_4 and W1. The

channel contains several different branches connected at various points from the bulk, notably the Cl1 channel contains narrow bottlenecks and is thought to regulate proton transfer from the OEC to the bulk during S state transitions.[65] It is thought that water is not taken in via this channel, as the mobility of water molecules in the channel throughout the Kok cycle is low, especially close to the OEC.[65, 72] There are few changes observed in the channel with the exception of the S_1 to S_2 and S_2 to S_3 transition. In the former the O4-W19 distance decreases, potentially explained as O4 may become protonated as suggested by Corry and O'Malley.[19] During the S_2 to S_3 transition it was possible to obtain several structural snapshot, these revealed a shortening between the S169 residue and W1, as well as rotation by a residue acting as a bottleneck which led to significant rearrangement in the hydrogen bonding network in that region. It was also found that this rotation reduced the size of the bottleneck thus not allowing for water transport. After 250 μs the residue returned to its original position. Furthermore some new water appeared and disappeared in the region between the bulk and bottleneck. It was concluded that the rotation causes the bottleneck to temporarily open thus enabling proton transport between the OEC and bulk allowing for deprotonation of the water inserted in the S_2 to S_3 transition while preventing unwanted interactions and reactions in the closed state. [65]

The O4 channel is a narrow channel connecting the bulk to the O4 oxygen in the OEC, it also contains a bottleneck. During the S_1 to S_2 transition the second water in the channel from the OEC (W20) disappears, which could be due to either W20 moving away or increased mobility. Both would result in disruption of the H-bond network to the OEC in the S_2 state. The connection is not restored till the OEC returns to the S_0 state.[31, 32, 73] This may imply that the O4 channel is used as a proton release channel only for the S_0 to S_1 transition, suggesting the proton release channel may depend on which transition is occurring.[65]

The O1 channel contains a 5 membered water wheel adjacent to the OEC and also connects to the bulk, notably Sirohiwal and Pantazis found in their theoretical hydration study of PSII[35] that there is a transient channel between the O1 channel and the Tyrosine Y_Z water network. The O1 network water mobility is higher compared to the O4 and Cl1 channel, as such it has been suggested that it is likely the O1 channel which is responsible for water intake.[65, 72] During the transition to the S_3 state the E189 residue, ligating Mn_1 and Ca, moves away from Ca and after the transition no longer ligates it.[72] Concurrently a drop in electron density of two waters which are hydrogen bonded to E189 and one of which is bonded to W3 and Y_Z also (W7) is detected. Other waters close to the OEC are also observed to have their electron density decrease, this coincides with the water

inserted in the S_3 state starting to be detected. Out of the four water molecules directly bound to the Mn atoms W1-W4, W4 becomes increasingly more mobile compared to W1-W3 during the S_2 to S_3 transition.[65]

The tyrosine water network connects to the OEC via the Y_Z residue and its hydrogen bonding partner H190, initially structures of PSII obtained at cryogenic temperatures showed that the network was linked by a proton pathway to the bulk via an Asparagine residue.[74, 75] However the more recently obtained structure at room temperature shows that a key water molecule is missing or too mobile thus no stable proton pathway is present, potentially isolation the Tyrosine network. The residues lining this pocket are observed to stay static in the S_2 to S_3, and so it likely is not a proton release pathway.[65] It has instead been suggested that the network may act as a proton store, as the pocket is lined by asparagine residues which together with the water network may stabilise protons. Furthermore the theoretical study found a transient pathway to the O1 channel which may permit the stored protons to be released to the bulk when the pathway is open.[35]

1.2.2.2 Water insertion

Throughout the Kok cycle two water molecules are inserted, one in the S_2 to S_3 transition and one in the S_4 to S_0 transition. The first water is fully inserted by the S_3 state, proton release is also observed and a new oxygen (O6) is detected in the OEC.[31, 65, 72] The light flash responsible for the S_2 to S_3 transition initially leads to the formation of a $P_{680}^{+\bullet}$ radical, this oxidises the Y_Z residue forming $Y_Z^{+\bullet}$ often referred to as the $S_2Y_Z^{\bullet}$ state, which leads to motion of the Y_Z residue as well as the nearby H190 and E189 residue.[72] The oxidation of the Y_Z residue causes it to deprotonate with the proton moving to its hydrogen bonding partner H190.[74] The E189 shifts away from the calcium ion in the OEC this is likely caused by the change of charge in the vicinity or the need to accommodate an additional water ligand in the OEC. These changes were observed within 50 µs of the second flash. Following this the Mn_1-Mn_4 distance is observed to increase, however the $Mn_4Mn_3O_4O_5$ unit remains unchanged, proposed to be due to Mn_4 and Mn_1 moving apart by 150 µs. Full appearance of the newly inserted oxygen's electron density is then observed, initially detected by 150 µs it reaches its maximum by 400 µs. As the new water appears Mn_1 is oxidised.[65, 72] The origin of the new water and its protonation state upon insertion is less clear. Few changes in structure are detected around Mn_3-Mn_4 nor is a closed cubane formed, so it is unlike for either W1 or W2 to be the newly inserted water. Instead it has been suggested that the O6 oxygen originates from W3 or is inserted via W3, which is bound to Ca.[25, 65, 72, 76, 77] In either case since W3 is observed in the S_3 state, the empty W3 or the empty origin site of O6 (W_x) would have to be filled again, as discussed in the previous

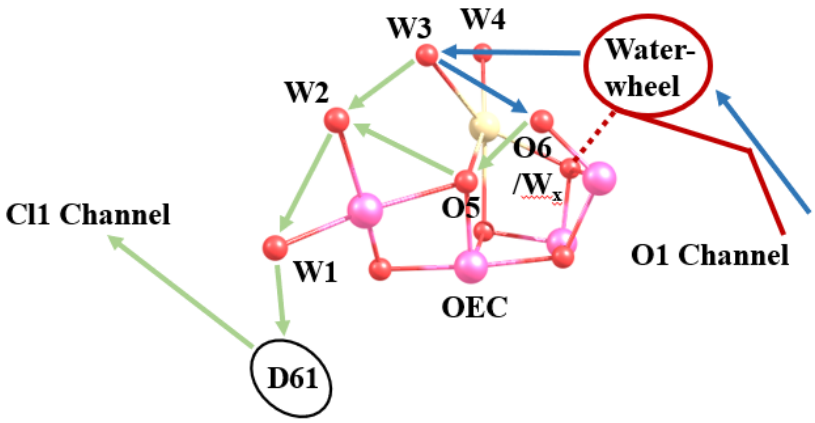

Figure 1.9: Proposed path of water insertion during the S_2 to S_3 transition.[65] Green arrows indicate potential proton transfers, while blue arrows indicate movement of water or hydroxide. The structure was generated from the PDB:7RF8 crystal structure.[65]

section 1.2.2.1 it is likely the O1 channel from which this water originates.[65, 72]

Hussein et al.[65] observed that during the S_2 to S_3 transition the S169 residue rotates towards W1, likely forming a hydrogen bond, this could be rationalised by W1 releasing a proton to the bulk via the D61 residue and becoming an OH^- which would interact with the S169 residue. W1 has been suggested to deprotonate during the transition by various studies.[50, 57, 65, 78] And a theoretical study by Siegbahn [79] has shown that for this S state transition there exists only a low barrier for proton release via the D61 residue.

It is likely that the newly inserted water W_x binds to Mn_1 as a hydroxide ion rather than water, this would agree with EPR data of the S_3 state[20, 80, 81] and a theoretical study on water adsorption on $CaMn_4O_5$[27]. The theoretical study by Zhou et al.[27] found that water initially binds to the calcium while forming a hydrogen bond to one of the oxygen bridges and then inserts itself into the cluster as hydroxide ion, with the other proton going to the hydrogen bond acceptor, it should be noted that a study on an isolated metal cluster is unlikely to accurately model the protein environment and also that in this study both the Ca and Mn_4 equivalent do not have two water ligands each. This would suggest however that in PSII if W3 becomes O6, it will insert concurrently as it deprotonates, and the empty W3 site is filled by a mobile water from the O1 channel. Alternatively a mobile water from the O1 channel may simply fill the pocket directly and deprotonate while or before binding. It is thought that the proton which is lost from W_x during its insertion reprotonates W1 to water. The path the proton takes is not clear, as it could feasibly go from W3 to W1 via W2 or to W1 via O5 and W2, or by the use of another hydrogen bonding pathway.[65] The path described above for Oxygen insertion is shown in figure 1.9.

1.2.3 The S_3 State

The S_3 state is the last S state of the Kok cycle which is long-lived enough to be isolated. The S_3 state also precedes oxygen formation which is thought to occur after the formation of the transient S_4 state. The mechanism of O-O bond formation is likely key in understanding PSII's functioning. In the S_2 to S_3 transition a new water is inserted into the OEC, forming a new ligand often referred to as O6. The first crystallographic structure of the S_3 state which resolved the newly inserted oxygen ligand (O6) was found by Suga et al..[33] In this initial structure the O5-O6 distance reported was $\approx$ 1.5 Å which would indicate a peroxo bond between O5 and O6. However, subsequent structures found this distance to be greater, in 2018 2.1 Å (Kern et al.)[31], in 2019 1.9 Å (Suga et al.)[32] and in 2021 2.0 Å (Husseinet al.)[65], these are summarised also in table 1.1 but all suggest a lack of O5-O6 bond. The later structures would suggest the presence of an oxo-oxyl like structure for O5 and O6. They also preclude the presence of oxo-hydroxo or peroxo as major component in the S_3 state as these would require much longer or shorter O5-O6 separation. However as clearly shown by Boussac et al.[82] there is heterogeneity in the S_3 state, Boussac et al. employed EPR studies and chemical and structural treatments to show this.

Alongside crystallographic structures Extended X-ray absorption fine structure (EXAFS) and EPR spectroscopy have been used to provide experimental information. EXAFS have revealed Mn-Mn bond lengths which are overall in agreement with the more recent crystallographic structures. These are summarised in Table 1.1 also. It can be seen that XFEL and EXAFS data generally agrees with each other with 3 of the 4 Mn-Mn distances being shorter $\approx$ 2.7 Å, and one being longer $\approx$ 3.3 Å. It should be noted that as before a closed cubane has never been detected experimentally. EPR spectroscopy has shown a signal attributed to a ground state spin $S = 3$ species. The D[85] and W[86] band EPR spectra are shown in figures 1.10 and 1.11 respectively.

Table 1.1: Crystallographic (XFEL) and EXAFS Mn-Mn distances in the S_3 state, all values are in Å.

	Mn_3-Mn_4	Mn_3-Mn_2	Mn_3-Mn_1	Mn_2-Mn_1	Mn_4-Mn_1	O5-O6
XFEL 2017[33]	2.74	2.80	3.26	2.63	5.03	1.45
XFEL 2018[31]	2.77	2.86	3.33	2.75	5.06	2.09
XFEL 2019[32]	2.96	2.69	3.35	2.55	5.34	1.90
XFEL 2021[65]	2.70	2.87	3.37	2.80	5.01	2.04
EXAFS 2005[83]	2.73 2.77 3.18 (2:1:1)					
EXAFS 2008[84]	2.75 2.88 >3.00 (2:1:1)					
EXAFS 2013[61]	2.75 2.79 3.26 (2:1:1) or 2.72 2.82 (2:2)					

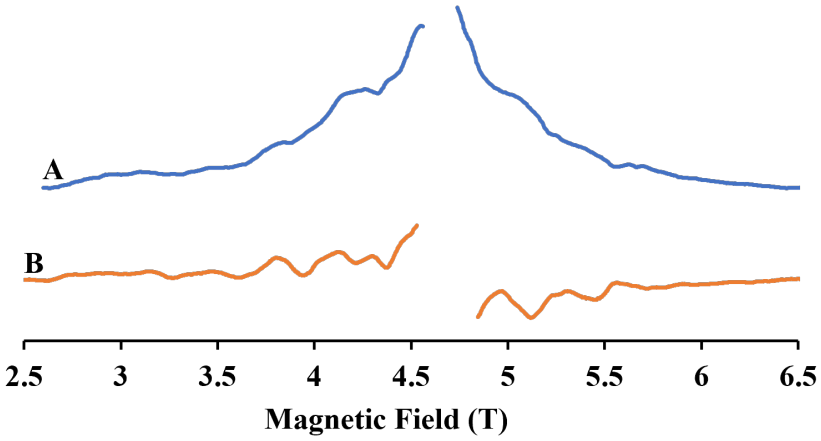

Figure 1.10: A: The D band EPR spectrum for the S_3 state isolated from cyanobacteria. B: Derivative-like D band EPR spectrum for the S_3 state isolated from cyanobacteria. Spectra adopted from[85].

The use of electron-electron double resonance-detected nuclear magnetic resonance (EDNMR) was successfully employed by Cox et al. in 2014[81] to determine the ^{55}Mn hyperfine coupling (HFC) constants, this presents another experimental set of data which can be compared to theoretically obtained values to ascertain the validity of models. A pair of high and low magnitude couplings are observed, with the lack of anisotropic character suggesting the presence of Mn^{IV} ions. Cox et al. showed through theoretical models that an open-cubane oxo(O5)-hydroxo(O6) model with all Mn ions as Mn^{IV} could rationalise this data.[81] However an

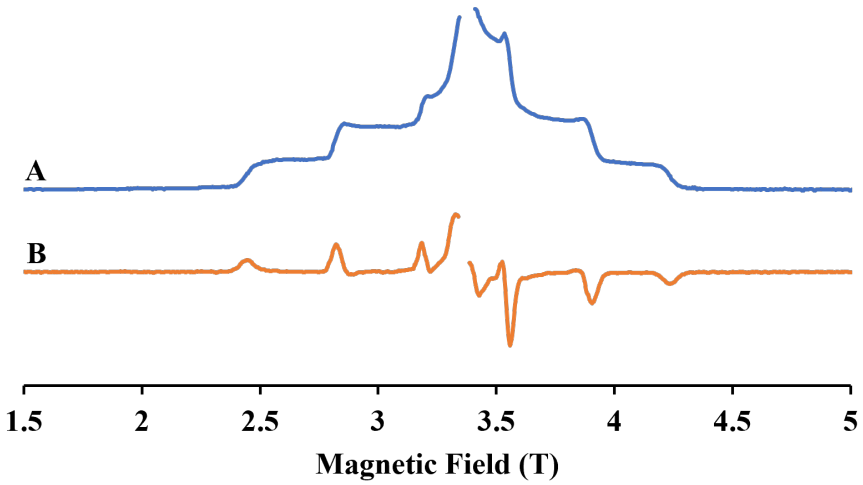

Figure 1.11: A: The W band EPR spectrum for the S_3 state isolated from cyanobacteria. B: Derivative-like W band EPR spectrum for the S_3 state isolated from cyanobacteria. Spectra adopted from[86].

oxo-hydroxo model typically has a larger O5-O6 separation of 2.4 Å which has so far been ruled out by the various crystallographic models, see table 1.1. It became clear that the S_3 state did not only contain a $S = 3$ species, a second EPR active species was identified in 2001 by Sanakis et al., this was identified as an $S = 7/2$ ground state spin species, it was found to only be EPR active upon near infrared illumination at cryogenic temperatures.[87] Boussac et al. confirmed this signal, and showed it to be distinct from the $S = 3$ species in the S_3 state.[82] Retegan et al. on the other hand suggested around the same time that this signal was due to a species formed during the formation of the S_3 state [88]. Corry and O'Malley later identified a $S = 7/2$ species in a theoretical study, formed in the S_2 to S_3 transition, this species was formed by deprotonation of W1 for an open-cubane S_2 state model with O4 as hydroxo.[89] It is entirely feasible that while there is a $S = 7/2$ species formed in the S_2 to S_3 transition, there is also a distinct $S = 7/2$ species in the S_3 state as shown by Boussac et al. and Sanakis et al.[82, 87] Recently a $S = 6$ species was identified for spinach samples in the S_3 state by Q-band EPR.[90] Zahariou et al. went on to show that the $S = 6$ coexists with a $S = 3$ species in the S_3 state of spinach, likely with 80% of the sample being the $S = 6$ species. This $S = 6$ species would likely have been identified before as an EPR inactive form of the S_3 state[82] as it was predicted to yield no EPR signals for X-band experiments.[90] It is clear that there is heterogeneity in the S_3 state as well as uncertainty about the precise nature of the species involved.

1.2.4 Oxygen Bond Formation

The S_3 state is the final stable state of the Kok cycle, upon oxidation it proceeds via the transient S_4 state back to the S_0 state, this is accompanied by the release of a proton, release of molecular oxygen, intake of a water molecule and a further deprotonation event. So far experimentally it has not been possible to isolate the S_4 state. There have been several proposals for how the oxygen-oxygen bond is formed. Figure 1.12 summarises proposed S_4 state structures each associated with a mechanism for oxygen bond formation.

One such proposal shown in figure 1.12;A is nucleophilic attack, wherein a water molecule attacks either an Mn_4 bound oxo or oxyl to form the O-O bond.[23, 91–95] Earlier proposals of the nucleophilic attack mechanism required a Mn_4^V=O to be attacked by a water molecule, usually suggested to be the Ca bound W3.[91–94] Oxygen bond formation has been studied experimentally, and while it has not been possible to obtain structures of the elusive S_4 state Haumann et al. in 2005 published time resolved data with a 10 µs resolution.[96] This study was able to monitor redox changes as well as structural changes in metal centres, helping to understand the

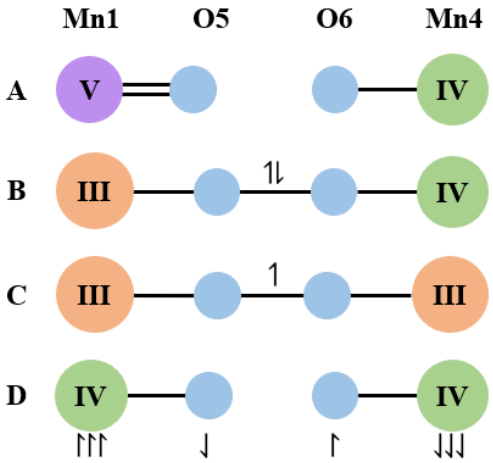

Figure 1.12: Proposed S_4 structures each associated with a proposed mechanism for oxygen bond formation. A: nucleophilic attack[91–94] B: Nonadiabatic one-electron transfer[101] C: Superoxo intermediate[102, 103] D: Oxo-oxyl radical mechanism[104–106]

sequence of events in the S_3 to S_0 transition. The transition was split into three parts, initially a fast phase assigned to the oxidation of Y_Z, then a slow phase in which no oxidation was observed, this was attributed to deprotonation taking place. Finally there is another slow phase, in which the $Y_Z^{\bullet}$ is reduced leading to the formation of the S_0 state.[96] This would suggest that there is no change in metal-oxidation states, and as such no Mn_4^V=O intermediate as proposed for nucleophilic attack would be possible since no Mn^V is observed in the S_3 state. Instead ligand oxidation would take place. It is of course possible for a very short lived Mn^V intermediate to be formed which would have not been detected experimentally.[96, 97] Alternatively to a Mn_4^V=O it has been proposed that instead nucleophilic attack occurs on a Mn^{IV}-oxyl moiety (Mn_4^{IV}-$O^{\bullet}$) by the Ca bound W3 .[95, 97, 98] The advantage here being that it is not necessary to form Mn^{IV}. Siegbahn performed theoretical studies for both of the above mechanisms to estimate their barrier, it was found that nucleophilic attack presents a large energy barrier, compared to other proposed mechanisms and as such are unlikely to be taking place, especially in light of the transient nature of the transition.[99] More recently Guo et al. proposed O-O formation to occur in the S4 state, for a case in which there is no additional O6 ligand in the OEC and instead Mn_4 initially takes on an additional water ligand and then the former W2 forms a bond with O5. This proceeds to form molecular oxygen via a superoxo species.[100]

Shoji et al. in 2018 proposed the non-adiabatic one-electron transfer mechanism for oxygen bond formation, in this mechanism the S_3 state is an open cubane with O6 as OH, O5 as oxo, and W2 as OH, this is shown in figure 1.12;B. Y_Z is

oxidised then an internal proton transfer from O6 to W2 via W3 takes place, with simultaneous reduction of Mn_4 to Mn^{III} by the forming oxo-oxyl. The oxo-oxyl forms a O_2^{3-} moiety which continues on to form a peroxide unit and then triplet dioxygen, throughout the reaction all Mn ions must remain ferromagnetically aligned requiring a high spin state of the OEC.[101] The spin requirements are independently supported by findings made by Jiao et al..[107]

Shown in figure 1.12;C is the superoxo intermediate mechanism proposed by Corry and O'Malley[102, 103] in this mechanism a superoxo species is formed between O5 and O6 in the S_4 state from a peroxo species. Superoxo is highly unstable and would spontaneously react to form oxygen with simultaneous reduction of a Mn ion. However these proposals relied on the formation of Peroxo in the S_3 state, with little crystallographic evidence, since O5 and O6 are not detected in a sufficiently close proximity, so it would rely on an equilibrium between oxo-hydroxo and peroxo in favour of oxo-hydroxo. The superoxo intermediate would explain the transient nature of the S_4 state as it readily forms oxygen.[102, 103] An early onset of oxygen bond formation in the S_3 has also been suggested by Isobe et al..[108] However experimental studies have suggested that no formal Oxygen-Oxygen bond is formed in the S_3 state or indeed any earlier S state. This is based on the observation that in all S states both substrate waters readily exchange with bulk solvent.[109–113]

Finally shown in figure 1.12;D is the oxo-oxyl radical mechanism originally proposed by Siegbahn[104–106]. It is proposed that in the S_4 state O5 and O6 are an oxo and oxyl respectively, with both Mn_1 and Mn_4 being Mn^{IV}, the O6 radical spin and the Mn_4 spin are β while other Mn centres are α. The O5 and O6 then couple to form the O-O bond. After the bond is formed the resulting peroxide forms molecular oxygen with simultaneous reduction of two Mn centres.[104] Notably whether O5 or O6 is the oxyl radical is trivial to the reaction and both are entirely possible.[97] Suga et al. suggested based on their XFEL structure [32] that the oxo/oxyl species was already formed in the S_3 state since they detected an O5-O6 separation of only 1.9 Å which is consistent with and oxo/oxyl rather than a hydroxo/oxo or peroxo structure.

Another area of uncertainty is which oxygens form the oxygen bond. The oxygen forming reaction can either take place within the cubane unit of the OEC or outside of it at Mn_4. Most of the theoretical studies described above suggest the oxygen-oxygen bond is formed between O5 and O6, or O5 and a water in the case of nucleophilic attack. Some suggestions have been made as to oxygen bond formation between O5 and W2,[113, 114] although more recently it has been concluded that this would require some structural rearrangements of the OEC structure to

facilitate this.[115] Substrate exchange studies have identified O5 to be a substrate for the reaction, however so far it has not been possible to identify the second substrate experimentally, furthermore these studies also show that oxygen release and water insertion likely occur simultaneously making it difficult to trap an intermediate for structural analysis in which the empty sites can be observed.[109–112]

The aim of this thesis is to:

- Improve understanding of the interactions within the OEC and the roles of its constituents.
- Investigate the nature of the S_3 state.
- Propose a mechanism for the formation of the oxygen-oxygen bond.

References

[1] J. Barber, *Philosophical Transactions of the Royal Society A: Mathematical Physical and Engineering Sciences* **2007**, *365*, 1007–1023.

[2] F. A. Armstrong, *Philosophical Transactions of the Royal Society B: Biological Sciences* **2008**, *363*, 1263–1270.

[3] T. M. Iverson, *Current Opinion in Chemical Biology* **2006**, *10*, Bioinorganic chemistry / Biocatalysis and biotransformation, 91–100.

[4] H. Dau, E. Fujita, L. Sun, *ChemSusChem* **2017**, *10*, 4228–4235.

[5] N. Ahmad, S. S.-e.-A. Zaidi, S. Mansoor, *Trends in Plant Science* **2020**, *25*, 958–960.

[6] J. Barber, *Quarterly Reviews of Biophysics* **2016**, *49*, e14.

[7] G. Renger, *Biochimica et Biophysica Acta (BBA) - Bioenergetics* **2012**, *1817*, Photosynthesis Research for Sustainability: From Natural to Artificial, 1164–1176.

[8] R. J. Debus, *Biochimica et Biophysica Acta (BBA) - Bioenergetics* **1992**, *1102*, 269–352.

[9] P. E. M. Siegbahn, *Journal of the American Chemical Society* **2009**, *131*, PMID: 19961231, 18238–18239.

[10] M. M. Najafpour, A. N. Moghaddam, S. I. Allakhverdiev, Govindjee, *Biochimica et Biophysica Acta (BBA) - Bioenergetics* **2012**, *1817*, Photosynthesis Research for Sustainability: From Natural to Artificial, 1110–1121.

[11] D. A. Pantazis, *ACS Catalysis* **2018**, *8*, 9477–9507.

[12] M. M. Najafpour, A. N. Moghaddam, S. I. Allakhverdiev, Govindjee, *Biochimica et Biophysica Acta (BBA) - Bioenergetics* **2012**, *1817*, Photosynthesis Research for Sustainability: From Natural to Artificial, 1110–1121.

[13] J.-R. Shen, *Annual Review of Plant Biology* **2015**, *66*, PMID: 25746448, 23–48.

[14] T. Cardona, A. Sedoud, N. Cox, A. W. Rutherford, *Biochimica et Biophysica Acta (BBA) - Bioenergetics* **2012**, *1817*, Photosystem II, 26–43.

[15] B. KOK, B. FORBUSH, M. McGLOIN, *Photochemistry and Photobiology* **1970**, *11*, 457–475.

[16] U. Yasufumi, K. Keisuke, S. Jian-Ren, K. Nobuo, *Nature* **2011**, *473*, 55–60.

[17] M. Suga, F. Akita, K. Hirata, G. Ueno, H. Murakami, Y. Nakajima, T. Shimizu, K. Yamashita, M. Yamamoto, H. Ago, J.-R. Shen, *Nature* **2015**, *517*, 99–103.

[18] W. Ames, D. A. Pantazis, V. Krewald, N. Cox, J. Messinger, W. Lubitz, F. Neese, *Journal of the American Chemical Society* **2011**, *133*, PMID: 22092013, 19743–19757.

[19] T. A. Corry, P. J. O'Malley, *The Journal of Physical Chemistry Letters* **2019**, *10*, PMID: 31429574, 5226–5230.

[20] V. Krewald, M. Retegan, N. Cox, J. Messinger, W. Lubitz, S. DeBeer, F. Neese, D. A. Pantazis, *Chem. Sci.* **2015**, *6*, 1676–1695.

[21] M. H. Cheah, M. Zhang, D. Shevela, F. Mamedov, A. Zouni, J. Messinger, *Proceedings of the National Academy of Sciences* **2020**, *117*, 141–145.

[22] M. H. Cheah, M. Zhang, D. Shevela, F. Mamedov, A. Zouni, J. Messinger, *Proceedings of the National Academy of Sciences* **2020**, *117*, 141–145.

[23] J. P. McEvoy, G. W. Brudvig, *Chemical Reviews* **2006**, *106*, PMID: 17091926, 4455–4483.

[24] N. Cox, L. Rapatskiy, J.-H. Su, D. A. Pantazis, M. Sugiura, L. Kulik, P. Dorlet, A. W. Rutherford, F. Neese, A. Boussac, W. Lubitz, J. Messinger, *Journal of the American Chemical Society* **2011**, *133*, 3635–3648.

[25] I. Ugur, A. W. Rutherford, V. R. Kaila, *Biochimica et Biophysica Acta (BBA) - Bioenergetics* **2016**, *1857*, 740–748.

[26] D. Bovi, D. Narzi, L. Guidoni, *Angewandte Chemie* **2013**, *52 45*, 11744–11749.

[27] T. Zhou, M. Abe, Y. Zhang, S. Kudoh, F. Mafuné, *The Journal of Physical Chemistry A* **2022**, *126*, 8218–8224.

[28] A. Guskov, J. Kern, A. Gabdulkhakov, M. Broser, A. Zouni, W. Saenger, *Nature Structural & Molecular Biology* **2009**, *16*, 334–342.

[29] A. Zouni, H.-T. Witt, J. Kern, P. Fromme, N. Krauss, W. Saenger, P. Orth, *Nature* **2001**, *409*, 739–743.

[30] M. Suga, F. Akita, K. Hirata, G. Ueno, H. Murakami, Y. Nakajima, T. Shimizu, K. Yamashita, M. Yamamoto, H. Ago, J.-R. Shen, *Nature* **2015**, *517*, 99–103.

[31] J. Kern, R. Chatterjee, I. D. Young, F. D. Fuller, L. Lassalle, M. Ibrahim, S. Gul, T. Fransson, A. S. Brewster, R. Alonso-Mori, R. Hussein, M. Zhang, L. Douthit, C. de Lichtenberg, M. H. Cheah, D. Shevela, J. Wersig, I. Seuffert, D. Sokaras, E. Pastor, C. Weninger, T. Kroll, R. G. Sierra, P. Aller, A. Butryn, A. M. Orville, M. Liang, A. Batyuk, J. E. Koglin, S. Carbajo, S. Boutet, N. W. Moriarty, J. M. Holton, H. Dobbek, P. D. Adams, U. Bergmann, N. K. Sauter, A. Zouni, J. Messinger, J. Yano, V. K. Yachandra, *Nature* **2018**, *563*, 421–425.

[32] M. Suga, F. Akita, K. Yamashita, Y. Nakajima, G. Ueno, H. Li, T. Yamane, K. Hirata, Y. Umena, S. Yonekura, L.-J. Yu, H. Murakami, T. Nomura, T. Kimura, M. Kubo, S. Baba, T. Kumasaka, K. Tono, M. Yabashi, H. Isobe, K. Yamaguchi, M. Yamamoto, H. Ago, J.-R. Shen, *Science* **2019**, *366*, 334–338.

[33] M. Suga, F. Akita, M. Sugahara, M. Kubo, Y. Nakajima, T. Nakane, K. Yamashita, Y. Umena, M. Nakabayashi, T. Yamane, T. Nakano, M. Suzuki, T. Masuda, S. Inoue, T. Kimura, T. Nomura, S. Yonekura, L.-J. Yu, T. Sakamoto, T. Motomura, J.-H. Chen, Y. Kato, T. Noguchi, K. Tono, Y. Joti, T. Kameshima, T. Hatsui, E. Nango, R. Tanaka, H. Naitow, Y. Matsuura, A. Yamashita, M. Yamamoto, O. Nureki, M. Yabashi, T. Ishikawa, S. Iwata, J.-R. Shen, *Nature* **2017**, *543*, 131–135.

[34] J. Wang, W. H. Armstrong, V. S. Batista, *Proceedings of the National Academy of Sciences* **2021**, *118*, e2023982118.

[35] A. Sirohiwal, D. A. Pantazis, *Journal of the American Chemical Society* **2022**, *144*, PMID: 36413491, 22035–22050.

[36] A. Tanaka, Y. Fukushima, N. Kamiya, *Journal of the American Chemical Society* **2017**, *139*, PMID: 28102667, 1718–1721.

[37] M. Drosou, G. Comas-Vilà, F. Neese, P. Salvador, D. A. Pantazis, *Journal of the American Chemical Society* **2023**, *145*, 10604–10621.

[38] M. Amin, *Photosynthesis Research* **2023**, *156*, 89–100.

[39] A. Galstyan, A. Robertazzi, E. W. Knapp, *Journal of the American Chemical Society* **2012**, *134*, 7442–7449.

[40] S. Luber, I. Rivalta, Y. Umena, K. Kawakami, J.-R. Shen, N. Kamiya, G. W. Brudvig, V. S. Batista, *Biochemistry* **2011**, *50*, PMID: 21678908, 6308–6311.

[41] M. Amin, M. Askerka, V. S. Batista, G. W. Brudvig, M. R. Gunner, *The Journal of Physical Chemistry B* **2017**, *121*, PMID: 28915048, 9382–9388.

[42] J. M. Peloquin, R. Britt, *Biochimica et Biophysica Acta (BBA) - Bioenergetics* **2001**, *1503*, Photosynthetic water oxidation, 96–111.

[43] R. Pal, C. F. A. Negre, L. Vogt, R. Pokhrel, M. Z. Ertem, G. W. Brudvig, V. S. Batista in **2013**.

[44] T. Lohmiller, V. Krewald, A. Sedoud, A. W. Rutherford, F. Neese, W. Lubitz, D. A. Pantazis, N. Cox, *Journal of the American Chemical Society* **2017**, *139 41*, 14412–14424.

[45] N. J. Beal, T. A. Corry, P. J. O'Malley, *The Journal of Physical Chemistry B* **2018**, *122*, PMID: 29300480, 1394–1407.

[46] M. Shoji, H. Isobe, J.-R. Shen, M. Suga, F. Akita, K. Miyagawa, Y. Shigeta, K. Yamaguchi, *Chemical Physics Letters* **2019**, *730*, 416–425.

[47] D. Koulougliotis, C. Teutloff, Y. Sanakis, W. Lubitz, V. Petrouleas, *Phys. Chem. Chem. Phys.* **2004**, *6*, 4859–4863.

[48] N. Cox, F. M. Ho, N. Pewnim, R. Steffen, P. J. Smith, K. G. Havelius, J. L. Hughes, L. Debono, S. Styring, E. Krausz, R. J. Pace, *Biochimica et Biophysica Acta (BBA) - Bioenergetics* **2009**, *1787*, 882–889.

[49] M. Chrysina, G. Zahariou, Y. Sanakis, N. Ioannidis, V. Petrouleas, *Journal of Photochemistry and Photobiology B: Biology* **2011**, *104*, Special Issue on Recent Progress in the Studies of Structure and Function of Photosystem II, 72–79.

[50] M. Retegan, N. Cox, W. Lubitz, F. Neese, D. A. Pantazis, *Physical chemistry chemical physics : PCCP* **2014**, *16 24*, 11901–10.

[51] G. C. Dismukes, Y. Siderer, *Proceedings of the National Academy of Sciences* **1981**, *78*, 274–278.

[52] J. M. Peloquin, K. A. Campbell, D. W. Randall, M. A. Evanchik, V. L. Pecoraro, W. H. Armstrong, R. D. Britt, *Journal of the American Chemical Society* **2000**, *122*, 10926–10942.

[53] L. V. Kulik, B. Epel, W. Lubitz, J. Messinger, *Journal of the American Chemical Society* **2007**, *129*, PMID: 17927172, 13421–13435.

[54] J. Zimmermann, A. Rutherford, *Biochimica et Biophysica Acta (BBA) - Bioenergetics* **1984**, *767*, 160–167.

[55] T. Lohmiller, V. Krewald, M. P. Navarro, M. Retegan, L. Rapatskiy, M. M. Nowaczyk, A. Boussac, F. Neese, W. Lubitz, D. A. Pantazis, N. Cox, *Phys. Chem. Chem. Phys.* **2014**, *16*, 11877–11892.

[56] A. Boussac, A. W. Rutherford, *Biochimica et biophysica acta* **2000**, *1457 3*, 145–56.

[57] A. Boussac, I. Ugur, A. Marion, M. Sugiura, V. R. Kaila, A. W. Rutherford, *Biochimica et Biophysica Acta (BBA) - Bioenergetics* **2018**, *1859*, 342–356.

[58] D. A. Pantazis, W. Ames, N. Cox, W. Lubitz, F. Neese, *Angewandte Chemie International Edition* **2012**, *51*, 9935–9940.

[59] R. Pokhrel, G. W. Brudvig, *Phys. Chem. Chem. Phys.* **2014**, *16*, 11812–11821.

[60] J. Yano, Y. Pushkar, P. Glatzel, A. Lewis, K. Sauer, J. Messinger, U. Bergmann, V. Yachandra, *Journal of the American Chemical Society* **2005**, *127*, PMID: 16248606, 14974–14975.

[61] C. Glöckner, J. Kern, M. Broser, A. Zouni, V. Yachandra, J. Yano, *Journal of Biological Chemistry* **2013**, *288*, 22607–22620.

[62] R. Chatterjee, G. Han, J. Kern, S. Gul, F. D. Fuller, A. Garachtchenko, I. D. Young, T.-C. Weng, D. Nordlund, R. Alonso-Mori, U. Bergmann, D. Sokaras, M. Hatakeyama, V. K. Yachandra, J. Yano, *Chem. Sci.* **2016**, *7*, 5236–5248.

[63] T. A. Corry, P. J. O'Malley, *The Journal of Physical Chemistry Letters* **2019**, *10*, PMID: 31429574, 5226–5230.

[64] M. Shoji, H. Isobe, S. Yamanaka, Y. Umena, K. Kawakami, N. Kamiya, J.-R. Shen, T. Nakajima, K. Yamaguchi in (Eds.: J. R. Sabin, E. J. Brändas), Advances in Quantum Chemistry, Academic Press, **2015**, pp. 325–413.

[65] R. Hussein, M. Ibrahim, A. Bhowmick, P. S. Simon, R. Chatterjee, L. Lassalle, M. Doyle, I. Bogacz, I.-S. Kim, M. H. Cheah, S. Gul, C. de Lichtenberg, P. Chernev, C. C. Pham, I. D. Young, S. Carbajo, F. D. Fuller, R. Alonso-Mori, A. Batyuk, K. D. Sutherlin, A. S. Brewster, R. Bolotovsky, D. Mendez, J. M. Holton, N. W. Moriarty, P. D. Adams, U. Bergmann, N. K. Sauter, H. Dobbek, J. Messinger, A. Zouni, J. Kern, V. K. Yachandra, J. Yano, *Nature Communications* **2021**, *12*, 6531.

[66] D. Kaur, X. Cai, U. Khaniya, Y. Zhang, J. Mao, M. Mandal, M. Gunner, *Inorganics* **2019**, *7*, 14.

[67] S. Nakamura, K. Ota, Y. Shibuya, T. Noguchi, *Biochemistry* **2016**, *55*, PMID: 26716470, 597–607.

[68] A.-N. Bondar, H. Dau, *Biochimica et Biophysica Acta (BBA) - Bioenergetics* **2012**, *1817*, Photosynthesis Research for Sustainability: From Natural to Artificial, 1177–1190.

[69] N. Sakashita, H. Ishikita, K. Saito, *Phys. Chem. Chem. Phys.* **2020**, *22*, 15831–15841.

[70] K. Ogata, M. Hatakeyama, Y. Sakamoto, S. Nakamura, *The Journal of Physical Chemistry B* **2019**, *123*, PMID: 31268711, 6444–6452.

[71] I. Ghosh, S. Khan, G. Banerjee, A. Dziarski, D. J. Vinyard, R. J. Debus, G. W. Brudvig, *The Journal of Physical Chemistry B* **2019**, *123*, PMID: 31496245, 8195–8202.

[72] M. Ibrahim, T. Fransson, R. Chatterjee, M. H. Cheah, R. Hussein, L. Lassalle, K. D. Sutherlin, I. D. Young, F. D. Fuller, S. Gul, I.-S. Kim, P. S. Simon, C. de Lichtenberg, P. Chernev, I. Bogacz, C. C. Pham, A. M. Orville, N. Saichek, T. Northen, A. Batyuk, S. Carbajo, R. Alonso-Mori, K. Tono, S. Owada, A. Bhowmick, R. Bolotovsky, D. Mendez, N. W. Moriarty, J. M. Holton, H. Dobbek, A. S. Brewster, P. D. Adams, N. K. Sauter, U. Bergmann, A. Zouni, J. Messinger, J. Kern, V. K. Yachandra, J. Yano, *Proceedings of the National Academy of Sciences* **2020**, *117*, 12624–12635.

[73] I. D. Young, M. Ibrahim, R. Chatterjee, S. Gul, F. D. Fuller, S. Koroidov, A. S. Brewster, R. Tran, R. Alonso-Mori, T. Kroll, T. Michels-Clark, H. Laksmono, R. G. Sierra, C. A. Stan, R. Hussein, M. Zhang, L. Douthit, M. Kubin, C. de Lichtenberg, L. Vo Pham, H. Nilsson, M. H. Cheah, D. Shevela, C. Saracini, M. A. Bean, I. Seuffert, D. Sokaras, T.-C. Weng, E. Pastor, C. Weninger, T. Fransson, L. Lassalle, P. Bräuer, P. Aller, P. T. Docker, B. Andi, A. M. Orville, J. M. Glownia, S. Nelson, M. Sikorski, D. Zhu, M. S. Hunter, T. J. Lane, A. Aquila, J. E. Koglin, J. Robinson, M. Liang, S. Boutet, A. Y. Lyubimov, M. Uervirojnangkoorn, N. W. Moriarty, D. Liebschner, P. V. Afonine, D. G. Waterman, G. Evans, P. Wernet, H. Dobbek, W. I. Weis, A. T. Brunger, P. H. Zwart, P. D. Adams, A. Zouni, J. Messinger, U. Bergmann, N. K. Sauter, J. Kern, V. K. Yachandra, J. Yano, *Nature* **2016**, *540*, 453–457.

[74] M. Chrysina, J. C. de Mendonça Silva, G. Zahariou, D. A. Pantazis, N. Ioannidis, *The Journal of Physical Chemistry B* **2019**, *123*, 3068–3078.

[75] R. Nagao, H. Ueoka-Nakanishi, T. Noguchi, *Journal of Biological Chemistry* **2017**, *292*, 20046–20057.

[76] C. J. Kim, R. J. Debus, *Biochemistry* **2019**, *58*, PMID: 31276397, 3185–3192.

[77] M. Askerka, G. W. Brudvig, V. S. Batista, *Accounts of Chemical Research* **2017**, *50*, PMID: 28001034, 41–48.

[78] P. E. M. Siegbahn, *Phys. Chem. Chem. Phys.* **2018**, *20*, 22926–22931.

[79] P. E. M. Siegbahn, *Phys. Chem. Chem. Phys.* **2012**, *14*, 4849–4856.

[80] T. A. Corry, P. J. O'Malley, *The Journal of Physical Chemistry B* **2021**, *125*, PMID: 34463499, 10097–10107.

[81] N. Cox, M. Retegan, F. Neese, D. A. Pantazis, A. Boussac, W. Lubitz, *Science* **2014**, *345*, 804–808.

[82] A. Boussac, A. W. Rutherford, M. Sugiura, *Biochimica et Biophysica Acta (BBA) - Bioenergetics* **2015**, *1847*, 576–586.

[83] M. Haumann, C. Müller, P. Liebisch, L. Iuzzolino, J. Dittmer, M. Grabolle, T. Neisius, W. Meyer-Klaucke, H. Dau, *Biochemistry* **2005**, *44*, PMID: 15697215, 1894–1908.

[84] Y. Pushkar, J. Yano, K. Sauer, A. Boussac, V. K. Yachandra, *Proceedings of the National Academy of Sciences* **2008**, *105*, 1879–1884.

[85] D. A. Marchiori, R. J. Debus, R. D. Britt, *Biochemistry* **2020**, *59*, PMID: 33319991, 4864–4872.

[86] M. Chrysina, E. Heyno, Y. Kutin, M. Reus, H. Nilsson, M. M. Nowaczyk, S. DeBeer, F. Neese, J. Messinger, W. Lubitz, N. Cox, *Proceedings of the National Academy of Sciences* **2019**, *116*, 16841–16846.

[87] Y. Sanakis, N. Ioannidis, G. Sioros, V. Petrouleas, *Journal of the American Chemical Society* **2001**, *123*, PMID:11674021, 10766–10767.

[88] M. Retegan, V. Krewald, F. Mamedov, F. Neese, W. Lubitz, N. Cox, D. A. Pantazis, *Chem. Sci.* **2016**, *7*, 72–84.

[89] T. A. Corry, P. J. O'Malley, *Journal of the American Chemical Society* **2020**, *142*, PMID: 32431144, 10240–10243.

[90] G. Zahariou, N. Ioannidis, Y. Sanakis, D. A. Pantazis, *Angewandte Chemie International Edition* **2021**, *60*, 3156–3162.

[91] T. A. Betley, Y. Surendranath, M. V. Childress, G. E. Alliger, R. Fu, C. C. Cummins, D. G. Nocera, *Philosophical Transactions of the Royal Society B: Biological Sciences* **2008**, *363*, 1293–1303.

[92] D. J. Vinyard, S. Khan, G. W. Brudvig, *Faraday Discuss.* **2015**, *185*, 37–50.

[93] T. Saito, S. Yamanaka, K. Kanda, H. Isobe, Y. Takano, Y. Shigeta, Y. Umena, K. Kawakami, J.-R. Shen, N. Kamiya, M. Okumura, M. Shoji, Y. Yoshioka, K. Yamaguchi, *International Journal of Quantum Chemistry* **2012**, *112*, 253–276.

[94] V. Krewald, F. Neese, D. A. Pantazis, *Journal of Inorganic Biochemistry* **2019**, *199*, 110797.

[95] E. M. Sproviero, J. A. Gascón, J. P. McEvoy, G. W. Brudvig, V. S. Batista, *Journal of the American Chemical Society* **2008**, *130*, 3428–3442.

[96] M. Haumann, P. Liebisch, C. Müller, M. Barra, M. Grabolle, H. Dau, *Science* **2005**, *310*, 1019–1021.

[97] N. Cox, D. A. Pantazis, W. Lubitz, *Annual Review of Biochemistry* **2020**, *89*, PMID: 32208765, 795–820.

[98] Y. Pushkar, K. M. Davis, M. C. Palenik, *The Journal of Physical Chemistry Letters* **2018**, *9*, PMID: 29863871, 3525–3531.

[99] P. E. M. Siegbahn, *Proceedings of the National Academy of Sciences* **2017**, *114*, 4966–4968.

[100] Y. Guo, J. Messinger, L. Kloo, L. Sun, *Journal of the American Chemical Society* **2023**, *145*, PMID: 36763485, 4129–4141.

[101] M. Shoji, H. Isobe, Y. Shigeta, T. Nakajima, K. Yamaguchi, *Chemical Physics Letters* **2018**, *698*, 138–146.

[102] T. A. Corry, P. J. O'Malley, *The Journal of Physical Chemistry Letters* **2020**, *11*, PMID: 32374174, 4221–4225.

[103] T. A. Corry, P. J. O'Malley, *The Journal of Physical Chemistry Letters* **2018**, *9*, PMID: 30336040, 6269–6274.

[104] P. E. Siegbahn, *Biochimica et Biophysica Acta (BBA) - Bioenergetics* **2013**, *1827*, Metals in Bioenergetics and Biomimetics Systems, 1003–1019.

[105] P. E. M. Siegbahn, *Accounts of Chemical Research* **2009**, *42*, PMID: 19856959, 1871–1880.

[106] P. E. M. Siegbahn, *Chemistry – A European Journal* **2006**, *12*, 9217–9227.

[107] Y. Jiao, R. Sharpe, T. Lim, J. W. H. Niemantsverdriet, J. Gracia, *Journal of the American Chemical Society* **2017**, *139*, PMID: 29064697, 16604–16608.

[108] H. Isobe, M. Shoji, J.-R. Shen, K. Yamaguchi, *Inorganic Chemistry* **2016**, *55*, PMID: 26717045, 502–511.

[109] J. Messinger, M. Badger, T. Wydrzynski, *Proceedings of the National Academy of Sciences* **1995**, *92*, 3209–3213.

[110] W. Hillier, J. Messinger, T. Wydrzynski, *Biochemistry* **1998**, *37*, PMID: 9836583, 16908–16914.

[111] W. Hillier, T. Wydrzynski, *Biochemistry* **2000**, *39*, PMID: 10757989, 4399–4405.

[112] W. Hillier, T. Wydrzynski, *Phys. Chem. Chem. Phys.* **2004**, *6*, 4882–4889.

[113] N. Cox, J. Messinger, *Biochimica et Biophysica Acta (BBA) - Bioenergetics* **2013**, *1827*, Metals in Bioenergetics and Biomimetics Systems, 1020–1030.

[114] B. Zhang, L. Sun, *Dalton Trans.* **2018**, *47*, 14381–14387.

[115] Y. Guo, B. Zhang, L. Kloo, L. Sun, *Journal of Energy Chemistry* **2021**, *57*, 436–442.

Chapter 2

Computational Theory

Computational Chemistry has become an invaluable theoretical tool for the study of systems which are experimentally too difficult to investigate. Computational tools are continually becoming more powerful as our computational capabilities increase, already computational methods are capable of producing data comparable in accuracy to experiment comparable by experimental error. These tools can be applied in many areas of chemistry, and are capable of yielding results that are repeatable, reliable and quantitative. The use of computer models allow for the study of short lived intermediates and transition states which are experimentally inaccessible making them particularly useful for the study of reactions.[1–3]

Computational methods are diverse with a lot of different tools available. Depending on the area some are more appropriate than others as computational power is limited, and some methods suffer from poor scalability. Broadly speaking a system may be modelled using quantum mechanics (QM) based methods, able to accurately model electronic aspects and changes within a system, this is often limited to systems up to 500 atoms. Alternatively molecular mechanics (MM) based methods can be used, these can handle much bigger systems, able to treat entire proteins.[4] One type of QM method is Density Functional Theory (DFT) an alternative to expensive post Hartree-Fock (HF) methods such as coupled cluster techniques. DFT is a commonly employed model, with thousands of references to its original papers[5, 6] as well as the award of the Nobel Prize in chemistry in 1998 to Water Kohn for his development of DFT.[7] This chapter aims to give an overview of DFT, BS-DFT and other computational tools employed in this thesis for the study of PSII. For more detailed accounts of DFT and other key theoretical principles see references.[8–14]

2.1 The Schrödinger Equation

The Schrödinger Equation is one of the corner stones of quantum mechanics. In its simplest time independent form the Schrödinger Equation is:

$$\hat{\mathcal{H}}\Psi = E\Psi \tag{2.1}$$

The Hamiltonian operator $\hat{\mathcal{H}}$ operates on the wavefunction Ψ to yield the energy E of the system and returning the wavefunction, E is said to be an eigenvalue of the wavefunction. There are various ways to express the wavefunction of a system. The Max Born interpretation first proposed in 1926[15] stated that the probability of a finding a particle at a point r in space dr is the square of the wavefunction, $|\Psi(r)|^2 dr$, this is the probability density of the particle. Alternatively it is thought that the wavefunction is an eigenfunction of a system, such that it can return information on any property when the correct operator acts on it. As in the case of the Schrödinger equation where $\hat{\mathcal{H}}$, the Hamiltonian operator, returns the energy of the system.

The Hamiltonian operator can be expressed as:

$$\hat{\mathcal{H}} = -\frac{1}{2}\sum_{i=1}^{N}\nabla_i^2 - \frac{1}{2}\sum_{A=1}^{M}\frac{1}{m_A}\nabla_A^2 - \sum_{i=1}^{N}\sum_{A=1}^{M}\frac{Z_A}{r_{iA}} + \sum_{i=1}^{N}\sum_{j>i}^{N}\frac{1}{r_{ij}} + \sum_{A=1}^{M}\sum_{B>A}^{M}\frac{Z_A Z_B}{R_{AB}} \tag{2.2}$$

The electronic terms are denoted by i and nuclei terms by A. The equation can be simplified and split into five terms each describing one aspect of a system:

$$\hat{\mathcal{H}} = \hat{T}_e + \hat{T}_N + \hat{V}_{Ne} + \hat{V}_{ee} + \hat{V}_{NN} \tag{2.3}$$

There are two kinetic terms, $\hat{T}_e$ and $\hat{T}_N$, for electrons and nuclei respectively. Three Potential terms, $\hat{V}_{Ne}$, the electrostatic attraction between nuclei and electrons, while $\hat{V}_{ee}$ and $\hat{V}_{NN}$ represent electron-electron and nuclei-nuclei repulsion respectively. While it is possible to solve this equation for an isolated hydrogen atom, for larger systems it is infeasible due to computational cost and theoretical complexity. Therefore it is necessary to make various approximations in order to apply this theory to more complex systems.

One such approximation is the Born-Oppenheimer (BO) approximation, which assumes that nuclei remain stationary with respect to electron movement. This is due to the relative weights of electrons and nuclei, with electrons being far lighter they should move far quicker. So one can either treat the electrons as moving through the fixed structure formed by the nuclei. Or for any change in positions of the nuclei to lead to an instantaneous change in electronic structure. This allows the Hamiltonian equation to be separated into a nuclear and an electronic problem which can then be solved separately. For the electronic Hamiltonian, $\hat{\mathcal{H}}_{el}$, the nuclear kinetic energy term, $\hat{T}_N$, in equation 2.3 is zero when the BO approximation

is applied and the nuclei-nuclei potential $\hat{V}_{NN}$ becomes a constant (V_{NN}). Thus the electronic Hamiltonian $\hat{\mathcal{H}}_{el}$ can be reduced to:

$$\hat{\mathcal{H}}_{el} = -\frac{1}{2}\sum_{i=1}^{N}\nabla_i^2 - \sum_{i=1}^{N}\sum_{A=1}^{M}\frac{Z_A}{r_{iA}} + \sum_{i=1}^{N}\sum_{j>i}^{N}\frac{1}{r_{ij}} = T_e + V_{eN} + V_{ee} \tag{2.4}$$

Notably the system dependent nuclear repulsion term can be ignored as it is a constant, and so only acts to scale the eigenvalue obtained from the Schrödinger equation. We can therefore obtain the energy of a system by solving the Schrödinger equation using the electronic Hamiltonian and adjust this value by a constant afterwards.

2.1.1 Solving the Schrödinger equation

In order to solve the Schrödinger equation some description of the wavefunction is needed, having applied the BO approximation the problem can be reduced to determining only the electronic wavefunction for any given structure. In order to further simplify the treatment of a multi-electron system the electron-electron repulsion term in equation 2.4 can be assumed to be a constant, equivalent to the average repulsion across the system.

Mathematically any many-body function may be expressed as a product of many single-body functions, this allows for a many-body problem to be broken down into several single body problems. As such the molecular wavefunction for any complex molecule can be expressed as the product of many one electron wavefunctions. Since any function can be expressed as a product of other functions it is necessary to select chemically relevant functions to express the electronic wavefunction, spin orbitals are appropriate for this since they are easily conceptualised and interpreted. Each orbital can be described by coordinates in space as well as the spin distribution across it. At the most basic level for a single electron the Schrödinger equation thus becomes:

$$\hat{h}\chi_i = \epsilon_i\chi_i \tag{2.5}$$

With ϵ_i being the energy eigenvalues of a spin orbital, χ_i the spin orbital wavefunction and $\hat{h}$ being the single-electron Hamiltonian having applied the BO approximation and assuming the electron-electron repulsion to be a constant. For a multi-electron system the overall wavefunction, known as the Hartree product wavefunction (Ψ^{HP}), can thus be defined as the product of the single-electron wavefunctions for all n electrons:

$$\Psi^{HP} = \prod_{i=1}^{n}\chi_i \tag{2.6}$$

The Schrödinger equation then becomes:

$$\hat{\mathcal{H}}\Psi^{HP} = E\Psi^{HP} \tag{2.7}$$

The so called Hartree product described above however fails to account for the fact that electrons are indistinguishable and poses spin.

2.1.1.1 The Slater Determinant

The method proposed by Hartree in 1927[16] was further refined in 1930 by Fock and Slater.[17, 18] Fock noted in his work that while his approach was no more complicated it should yield far more accurate results compared to the Hartree method. The method proposed by Fock and Slater allowed for a multi-body wavefunction to be approximated using a Slater determinant (Φ_{SD}). Electrons poses a non-integer spin of $\frac{1}{2}$, this makes them a type of sub-atomic particle known as a fermion, the Pauli exclusion principle states that fermions cannot have the same quantum state in the same quantum system, in order to satisfy this the wavefunction of an electron must be anti-symmetric with respect to the interchange of two electrons. This is also sometimes referred to as the antisymmetric principle. An orbital can be described by its spacial coordinates, as well as spin, for electrons this can be either up (α) or down (β). The spin of the electron can be described by two functions describing this, the $\alpha(\omega)$ and $\beta(\omega)$ functions. By definition the pair of functions is complete and orthogonal satisfying the conditions:

$$< \alpha|\alpha > = < \beta|\beta > = 1 \tag{2.8}$$

$$< \beta|\alpha > = < \alpha|\beta > = 0 \tag{2.9}$$

Mathematically a complete and orthogonal set is one that describes the entire system with none of the parts of the sets overlapping. Therefore an n electron system wavefunction can be expressed as $\Psi(\mathbf{x}_1, \mathbf{x}_2, \ldots, \mathbf{x}_N)$ where $\mathbf{x}$ is described by four dimensions, the spatial coordinates and spin, $\mathbf{x} = \{\mathbf{r},\omega\}$. As required by the Pauli exclusion principle this wavefunction must be antisymmetric such that:

$$\Psi(\mathbf{x}_1, \mathbf{x}_2) = -\Psi(\mathbf{x}_2, \mathbf{x}_1) \tag{2.10}$$

The Slater determinant for two electrons is:

$$\Psi(\mathbf{x}_1, \mathbf{x}_2) = \frac{1}{\sqrt{2}} \begin{vmatrix} \chi_i(\mathbf{x}_1) & \chi_j(\mathbf{x}_1) \\ \chi_i(\mathbf{x}_2) & \chi_j(\mathbf{x}_2) \end{vmatrix} \tag{2.11}$$

Where the $\frac{1}{\sqrt{2}}$ term is a normalisation factor. An N electron wavefunction can then be written as:

$$\Psi(\mathbf{x}_1, \mathbf{x}_2, \ldots, \mathbf{x}_N) = \frac{1}{\sqrt{N!}} \begin{vmatrix} \chi_i(\mathbf{x}_1) & \chi_j(\mathbf{x}_1) & \cdots & \chi_k(\mathbf{x}_1) \\ \chi_i(\mathbf{x}_2) & \chi_j(\mathbf{x}_2) & \cdots & \chi_k(\mathbf{x}_2) \\ \vdots & \vdots & & \vdots \\ \chi_i(\mathbf{x}_N) & \chi_j(\mathbf{x}_N) & \cdots & \chi_k(\mathbf{x}_N) \end{vmatrix} \tag{2.12}$$

In this case $\frac{1}{\sqrt{N!}}$ is the normalisation factor. This new expression of the wavefunction can be used to determine the solution for a multi electron system using the Hartree-Fock approximation. This is based on the fact that the ground state of a system may be expressed by the Slater determinant in equation 2.12 and the variational principle.

The variational principle states that the energy determined for the system using any set of wavefunctions is always greater than the true ground state energy of the system. Therefore the minimisation of the calculated energy will yield the best result. It also means that an energy lower than the true ground state energy can never be obtained. This allows for the quality of a basis set to be assessed as the lower the energy the better.

The Schrödinger equation can now be modified to allow for the minimisation of energy, this is done through the inclusion of the one-electron Fock operator ($f(i)$) which acts on the spin orbitals (χ) to return the eigenvalue energy and the spin orbital function. However the Fock operator assumes the electron-electron repulsion to be a constant, which must be included in $f(i)$, thus it is expressed as:

$$f(i) = T_e(i) + V_{eN}(i) + \upsilon^{HF}(i) \tag{2.13}$$

Here the Fock operator is a sum of the ith kinetic single electron energy, the attraction between nuclei and the ith electron and the $\upsilon^{HF}(i)$ term which represents the average electron-electron repulsion between the ith and non-ith electron. In order to calculate the $\upsilon^{HF}(i)$ term an initial guess as to the spin orbitals must be made, the $\upsilon^{HF}(i)$ field is then determined and can be used to calculate a more accurate guess of the spin-orbitals, this can be done iteratively until the difference between each iteration is less than a pre-determined threshold, at which point the minimisation is said to be converged. This method yields a set of orbitals with their corresponding energies, this is known as the self-consistent field (SCF) method. The choice and size of basis set will affect how close the calculated energy is to the true ground state energy of the system, only an infintely large basis set would yield the true value although this is practically impossible due to computational cost and theoretical difficulty. However it can be said that a basis set yielding a lower energy is better

compared to a basis set yielding a higher energy due to the variational principle.

One of the limitations of the Hartree-Fock approximation is that it assumes electrons to move independently of each other thereby neglecting electron correlation effects, E_C, the correlation energy can be defined as:

$$E_C = E_0 - E_{HF} \tag{2.14}$$

E_0 is the true non-relativistic ground state energy and E_{HF} is the theoretical exact solution for the Hartree-Fock energy. Correlation can be further divided into dynamic or static correlation. Static correlation implies a few determinants are needed to describe the system at large with each determinant having a significant contribution. Whereas dynamic correlation is a large number of determinants each holding little weight to describe the system.

2.2 Density Functional Theory

While Slater determinants for many single-electron wavefunctions can adequately describe a more complex system, the computational cost increases quickly and exponentially, limiting its application to small systems. Density Functional Theory (DFT) offers an alternative method to this, rather than dealing with the wavefunction of a system, it deals with the far more easily interpreted electron density. Another advantage of DFT over HF based methods is that HF methods use 3 spatial variables for each one of the N electrons as well as a spin variable to describe a system, whereas DFT relies only on the density, ρ across the system to describe it thus scaling much better as the system size is increased. The theory behind DFT was published by Kohn and Hohenberg in 1964[6] their work established a link between electron density, energy and an external potential. The relationship between the number of electrons in a system and electron density is simply described by:

$$N = \int \rho(\mathbf{r})\, d\mathbf{r} \tag{2.15}$$

DFT is also capable of determining the position of nuclei from the electron density function. Nuclei can be treated as point charges meaning that they should be located at local maxima for electron density and it can be shown that the density relates to atomic number,Z_A. The relationship between N and ρ and ρ and Z_A means that given a known density it is possible to determine the Hamiltonian, and thus to determine energies and wavefunctions, i.e. all necessary information is contained in the density function to recover the electronic wavefunction. Since it is possible to determine all properties from the wavefunction by the use of an appropriate operator, and to determine the wavefunction from the density, it should be possible to determine all properties from density without dealing with the computationally

and theoretically difficult wavefunction by the use of some other operators.

Work by Thomas[19] and Fermi[20] in 1927 allowed for the first definition of DFT equations, through modelling the electronic distribution as a uniform electron gas. However this early approach to DFT was too inaccurate to find any application in a majority of cases in chemistry.

2.2.1 Hohenberg-Kohn Theorem

Within DFT electrons interact with other electrons as well as the external potential, in a molecule this is the electron-nuclei attraction. The first Hohenberg-Kohn theorem, proposed in 1964[6], states that the Hamiltonian operator for a system can be determined by only the ground state density. The external potential must be defined for this, it can be proven that this potential is determined by the ground state density also and that the Hamiltonian can also generate all excited state functions. Each unique ground state density is consistent with only a single external potential which can be used to determine the Hamiltonian operator. Therefore it was shown that both the Hamiltonian and external potential could be found from density alone. The first theorem did not provide a practical way of obtaining the density for a system. The second theorem proposed was the variational theorem, here it was shown that the density also obeys the variational principle which provides the ability to optimise a system, since densities giving a lower overall energy for a system can now be said to be closer to the true density. However overall this still required for the Hamiltonian and wavefunction to be used to solve the Schrödinger equation to obtain the enregy thus offering no advantages. It would be far more preferable to obtain the energy directly from the density without needing to deal with the electronic wavefunction.

2.2.2 Kohn-Sham Methodology

In 1965 Kohn and Sham proposed that a system of non-interacting electrons would be easier to deal with and a correctional value could be used to address the interacting aspects.[5] The Hamiltonian operator for a non-interacting multi-electron system is simply the sum of all one-electron operators. Similarly the eigenfunction are Slater determinants of one-electron eigenfunctions and eigenvalues are a sum of single-electron eigenvalues.

From here a theoretical system of non-interacting electrons is created, this system is such that the overall ground state density is equivalent to that of a real system wherein electrons interact. As the density determines the nuclear positions and the densities are equivalent these systems must be identical. The energy of this system can be written as a function of its density such that:

$$E(p) = T_{ke}(\rho) + V_{ee}(\rho) + V_{Ne}(\rho) + \Delta T(\rho) + \Delta V_{ee}(\rho) \tag{2.16}$$

Where the density ρ is a function of position $\mathbf{r}$, $\rho(\mathbf{r})$. $T_{ke}(\rho)$ is the kinetic energy of the non-interacting electrons, $V_{ee}(\rho)$ classical electron-electron repulsion, $V_{Ne}(\rho)$ nuclear-electron attraction, and $\Delta T(\rho) + \Delta V_{ee}(\rho)$ represent the correction to the kinetic and electron-electron energetic terms due to the interaction between electrons. Electron density can be expressed by the Slater determinant for a N non-interacting electron system:

$$\rho = \sum_{i=1}^{N} \langle \chi_i | \chi_i \rangle \tag{2.17}$$

Therefore the full expression for energy in terms of density becomes:

$$E[\rho(\mathbf{r})] = \sum_{i}^{N} (\langle \chi_i | - \frac{1}{2}\nabla_i^2 | \chi_i \rangle - \langle \chi_i | \sum_{k}^{nuclei} \frac{Z_k}{|\mathbf{r}_i - \mathbf{r}_k|} | \chi_i \rangle + \sum_{i}^{N} \langle \chi_i | \frac{1}{2} \int \frac{\rho(\mathbf{r}')}{|\mathbf{r}_i - \mathbf{r}'|} d\mathbf{r}' | \chi_i \rangle) + E_{XC}[\rho(\mathbf{r})] \tag{2.18}$$

Here the correctional terms from equation 2.16 are combined and expressed as E_{XC}, the exchange-correlation energy. It is possible to minimise the energy as described previously (section 2.1.1) by satisfying:

$$h_i^{KS} \chi_i = \varepsilon_i \chi_i \tag{2.19}$$

Where h_i^{KS} is the Kohn-Sham single-electron operator:

$$h_i^{KS} = -\frac{1}{2}\nabla_i^2 - \sum_{k}^{nuclei} \frac{Z_k}{|\mathbf{r}_i - \mathbf{r}_k|} + \int \frac{\rho(\mathbf{r}')}{|\mathbf{r}_i - \mathbf{r}'|} d\mathbf{r}' + V_{XC} \tag{2.20}$$

With V_{XC}, the functional derivative, being the first derivative of E_{XC} ($V_{XC} = \delta E_{XC}/\delta\rho$). Since the energy calculated in equation 2.16 is exact, the orbitals χ must also be exact, therefore the system described must correspond to reality, and the calculated minima must correspond to reality at the minima, yielding the exact density. The Kohn-Sham orbitals may be expressed as a basis set of functions ϕ with the individual orbital coefficients $K_{\mu\nu}$ given by:

$$K_{\mu\nu} = \left\langle \phi_\mu | - \frac{1}{2}\nabla^2 - \sum_{k}^{nuclei} \frac{Z_k}{|\mathbf{r}_i - \mathbf{r}_k|} + \int \frac{\rho(\mathbf{r}')}{|\mathbf{r}_i - \mathbf{r}'|} d\mathbf{r}' + V_{XC} | \phi_\nu \right\rangle \tag{2.21}$$

DFT contains no approximations so far beyond the BO approximation and is said to be exact, if $E_{XC}(\rho)$ is known the exact energy can be found. However while this was proven the exact nature of E_{XC} remains unknown and much work has been done to approximate it. It should be noted that once approximations of the exchange-correlations energies are made DFT is no longer variational and as such

lower energies cannot be said to necessarily be better.[13]

2.2.3 Approximating the Exchange-Correlation Functional

As outlined in section 2.2.2 DFT allows for the exact determination of the energy of a system from the electron density, however this relies on the use of the exact exchange-correlation functional, E_{XC}, which must so far be approximated. E_{XC} is a correctional term, describing the QM aspect of electron-electron interaction as well as classical self-interaction and the kinetic energy correction to the hypothetical system. There have been various different approaches as to the approximation of E_{XC}. In discussing these approaches it is convenient to first define a new term, the energy density, of a system, ε_{XC}, which in itself is dependent on the electron density. E_{XC} is dependent on both the electron and energy density such that:

$$E_{XC}[\rho(\mathbf{r})] = \int \rho(\mathbf{r})\varepsilon_{XC}[\rho(\mathbf{r})]d\mathbf{r} \tag{2.22}$$

Local Density Approximation (LDA) is a simple way of treating E_{XC}, it is based on the analysis of a uniform electron gas, in which the energy density, ε_{XC}, depends only on the density, ρ, at that position, $\mathbf{r}$. Of course in a real system electron density is not uniform, electron density for example is greater around the position of nuclei so LDA is not the best representation. While being relatively simple the exact derivation of the exchange functional even for an uniform electron gas has not been possible. However it has been possible to calculate the total energy of various uniform electron gases to very high accuracy. This can then be used to determine the exchange energies in these systems. [21, 22] While functionals using LDA have been developed[23, 24] for use, they often fall short of accurately describing a system due to their obvious shortcomings.[11]

One improvement which can be made to LDA is to account for the deviation of electron density from uniformity, by taking into account both the local density as well as the change in density at that point. This can be done by inclusion of the density gradient. The resulting method is the Generalised Gradient Approximation (GGA). The easiest way to apply this gradient correction is by adding it to LDA functional:

$$\varepsilon_{x/c}^{GGA}[\rho(\mathbf{r})] = \varepsilon_{x/c}^{LDA}[\rho(\mathbf{r})] + \Delta\varepsilon_{x/c}\left[\frac{|\nabla\rho(\mathbf{r})|}{\rho^{\frac{4}{3}}(\mathbf{r})}\right] \tag{2.23}$$

The correction term is dimensionless reduced gradient. The first of these GGA functionals were developed in 1986 by Becke[25] or Perdew and Wang[26] Some popular GGA functionals are BP86, based on work by Becke[27] and Perdew[28] as well as BLYP based on work by Becke and Lee, Yang and Parr.[29] GGA

functionals are a popular choice for geometry optimisation due to their relatively cheap computational cost and reasonable results, however GGA methods often underestimate reaction barriers, this is due to the self-interaction errors of electrons interacting with themsevles.[13, 30]

A further improvement which can be made then is to include the second order derivative of density, the Laplacian (∇^2), this is known as meta-GGA, the first of which (BR) was proposed by Becke and Roussel.[31] Due to technical challenges involved in the use of this Laplacian more commonly a dependence of the exchange-correlation potential on the kinetic energy density (τ) is used:

$$\tau(\mathbf{r}) = \sum_{i}^{occupied} \frac{1}{2}|\nabla\psi_i(\mathbf{r})|^2 \tag{2.24}$$

with ψ_i being the Kohn Sham orbitals.

A further consideration is the inclusion of HF exchange in the exchange-correlation functional, this is a fixed percentage, which may vary between functionals but is consistent within them. This allows for the amount of electron-electron interaction within a system to be taken into account and modelled. The HF exchange is included by use of the Adiabatic Connection Method (ACM), named for its ability to allow non-interacting and interacting states to be connected. The Hellmann-Feynmann theorem states that the exchange-correlation energy is given by:

$$E_{XC} = \int_0^1 \langle\Psi(\lambda)|\, \mathbf{V}_{XC}(\lambda)\, |\Psi(\lambda)\rangle\, d\lambda \tag{2.25}$$

with λ corresponding to the degree of electron-electron interaction, $\lambda = 0$ signifying no interaction and $\lambda = 1$ representing exact interaction. More commonly the exchange correlation energy is expressed as:

$$E_{XC} = (1-\alpha)E_{XC}^{DFT} + \alpha E_X^{HF} \tag{2.26}$$

here α represents the amount of HF included in the model, such that $0 \leq \alpha \leq 1$.

The choice of functional in DFT is essential, different functionals and even differing amounts of HF exchange within a functional can have large effects on the energies of chemical species.[32, 33] For the study of PSII popular functionals are TPSSh[34, 35] including 10 % HF exchange and B3LYP[29, 36, 37] which includes 20 % HF exchange. The B3LYP model can be expressed as:

$$E_{XC}^{\mathrm{B3LYP}} = (1-a)E_X^{\mathrm{LSDA}} + E_X^{\mathrm{HF}} + b\Delta E_X^{\mathrm{B}} + (1-c)E_C^{\mathrm{LSDA}} + cE_C^{\mathrm{LYP}} \tag{2.27}$$

where $a = 0.20$, $b = 0.72$ and $c = 0.81$, the LSDA terms are the local spin density approximation terms based on LDA and Slater exchange, E_X^{B} is the Becke gradient

corrected exchange term [27] and E_C^{LYP} the gradient corrected correlation proposed by Lee, Yang and Parr [29].

2.2.4 Empirical Dispersion Corrections

One short coming of DFT which became clear as its development progressed was its failure to accurately describe long-range dispersion interactions.[38–40] These are known as London-dispersion effects, identified first in 1930[41], they are weak intermolecular forces due to spontaneously formed dipole-dipole interactions caused by momentary changes in electron density and are a type of Van der Waals force.[42, 43] They are a long range interaction described by:

$$E_{disp} = -\sum_{n=6}^{\infty} \frac{C_n}{R^n} \tag{2.28}$$

wherein R is the distance between two fragments and C_n the dispersion coefficient. For interatomic interactions n must be even, $n = 6$ corresponds to dipole-dipole interactions and higher n values to other dipole interactions such as dipole-quadrupole or dipole-octopole. A popular correction, and one which is used throughout the work presented in this thesis is the D3BJ correction developed by Grimme et al.[44, 45], which utilises Becke-Johnson[46–49] damping. The D3 correction, based on the earlier D2 correction by Grimme[50], takes into account both $n = 6$ and $n = 8$ interactions, which overall allows it to describe interactions in the short, mid and long range region. Higher n values are not included as it was either concluded to have little or a negative effect on the outcome. The D3BJ energy correction is given by:

$$E_{disp}^{D3BJ} = -\frac{1}{2} \sum_{A \neq B} \sum_{n=6,8} s_n \frac{C_n^{AB}}{R_{AB}^n + \left[f_{damp}^{D3BJ}(R_{BJ}^{AB})\right]^n} \tag{2.29}$$

here C_n^{AB} is a dispersion coefficient for atoms A and B these coefficients are atom specific. R_{AB}^n is the separation between AB and s_n a scaling factor. The damping function is given by:

$$f_{damp}^{D3BJ}(R_{BJ}^{AB}) = a_1 R_{BJ}^{AB} + a_2 \tag{2.30}$$

where both a_n terms are constants which can be varied to control the dispersion correction for short and mid range distances. The R_{BJ}^{AB} term is given by:

$$R_{BJ}^{AB} = \sqrt{\frac{3}{2}} \sqrt{\sqrt{Z_A} \frac{\langle r^4 \rangle_A}{\langle r^2 \rangle_A} \sqrt{Z_B} \frac{\langle r^4 \rangle_B}{\langle r^2 \rangle_B}} \tag{2.31}$$

with $Z_{A/B}$ being the nuclear charge, and $\langle r^4 \rangle_A$ and $\langle r^2 \rangle_A$ being the quadrupole and dipole moments for the atoms.

2.2.5 Basis Sets

A basis set is a set of mathematical functions which together describe the wavefunction of a system. There are three considerations to be made when constructing a basis set, the number of basis functions, the ease with which it can be solved, and chemical accuracy. A basis set is constructed from basis functions, the more basis functions are included the better the results, however computational cost increases exponentially. Using the linear combination of atomic orbitals (LCAO) the molecular wavefunction ϕ can be expressed as the sum of N atomic orbitals φ with some coefficient a:

$$\phi = \sum_{i=1}^{N} a_i \varphi_i \tag{2.32}$$

The only truly accurate description would require $N = \infty$ this is practically impossible. However the more atomic orbitals are used to describe a system the more accurate a description will be obtained. The set of N function is known as a basis set, and φ the basis function. Chemically it is convenient to use an atomic orbital (AO) for this, they are centred on the atoms of the molecule, and are more easily conceptualised.

2.2.5.1 Modelling Atomic Orbitals

Two main ways of describing the atomic orbital have emerged, the Slater type orbital (STO) and the Gaussian type orbital (GTO). STOs have the advantage of more accurately describing the electronic wavefunction, however they are severely limited by system size and not applicable in most systems due to computational cost. For example the normalised $1s$ orbital STO for an orbital centered on nuclei A at position $\mathbf{R_A}$ is given by:

$$\phi_{1s}^{SF}(\zeta, \mathbf{r} - \mathbf{R}_A) = \left(\frac{\zeta^3}{\pi}\right)^{\frac{1}{2}} e^{-\zeta|\mathbf{r}-\mathbf{R}_A|} \tag{2.33}$$

where ζ is the Slater orbital exponent. GTOs however do not suffer from this problem, an equivalent $1s$ orbital is given by:

$$\phi_{1s}^{GF}(\alpha, \mathbf{r} - \mathbf{R}_A) = \left(\frac{2\alpha}{\pi}\right)^{\frac{3}{4}} e^{-\alpha|\mathbf{r}-\mathbf{R}_A|^2} \tag{2.34}$$

here α is the Gaussian orbital exponent. Considering the 1s atomic orbital best illustrates their difference. The decay of the function away from the atom's centre for an STO is proportional to e^{-r}, presenting a very diffuse decay. For a GTO on the other hand the decay is described by e^{-r^2}, this leads it to decay much faster as r is increased. Similarly the behaviour at $r = 0$ differs between STOs and GTOs, at $r = 0$ an STO still has a non-zero gradient, whereas a GTO has a gradient of zero. The STO orbital is preferable in theory as it more accurately represents the features of a molecular orbital, in fact the $1s$ orbital for a hydrogen atom can be expressed as $\pi^{-\frac{1}{2}}e^{-r}$ which is an STO type function. However practically the GTO is computationally far more convenient, as the product of two Gaussian functions is a single third Gaussian function and a constant. During SCF convergence many two-electron integrals must be evaluated, since the product of two Gaussian functions is a third Gaussian this problem can be simplified for GTOs but not STOs. So while STOs better describe the properties of an orbital and would be preferential to use, the more convenient practical aspects of the GTO make them quickly necessary as the system scale increases.

2.2.5.2 The Minimal Basis Set

Through the linear combination of GTO functions it is possible to improve the description of an atomic orbital, more accurately describing its decay and essentially mimicking STOs. This is called a contracted Gaussian basis function, where each basis function (primitive) has a contraction coefficient and exponent associated with it. The number of primitives known as the degree of contraction determines how accurate the description becomes. A further issue with GTOs is their failure to model nodes, for example they fail to describe the 2s orbital, however this can be solved fairly easily by changing the sign of the contraction coefficient. Hehre, Stewart and Pople were the first to develop a basis set like this in 1969.[51] This basis set is the STO-MG basis set, where M represents the number of primitives used to approximate the STO. In particular the STO-3G basis set strikes a good compromise between computational cost and accuracy.

2.2.5.3 Multi-Valence Basis Sets

STO-3G is a minimal basis set (single-ζ) this implies that each atomic orbital is described by only one function. For example Ne would be described by one function each for the 1s, 2s, $2p_x$, $2p_y$ and $2p_z$ orbitals. To more accurately describe the system each AO may rather be described by two functions, known as double-ζ, three functions, triple-ζ and so on. These are often abbreviated as SZ, DZ and TZ respectively. Where the inclusion of more functions always increase accuracy and

comes increasingly closer to the true form but computational cost increases.

However by the introduction of split-valence also known as valence-multiple-ζ computational cost can be decreased while maintaining accuracy. This is based on the idea that core orbitals are not affected as much by chemical bonding whereas valence orbitals are and as such it is sufficient to represent core orbitals by single-ζ functions and only employ multi-ζ methods for valence orbitals. An example of this are the basis sets developed by Binkley, Pople and Hehre[52] such as 6-311G, which uses 6 Gaussians for each core orbitals, and 3 separate functions for the valence orbitals, one which in itself is defined by three Gaussians and two which are defined by a single Gaussian.

2.2.5.4 Polarization

So far the effect of polarization has not been considered. To account for this the orbitals would have to be allowed to change their shape, to illustrate the 1s orbital is spherical, however only in an electrostatically uniform environment. In for example NH_3 this is not the case and additional functions need to be included to allow the 1s orbital in the hydrogen to not be perfectly spherical. Practically this is done by including basis functions for higher angular momentum orbitals than the valence orbitals, for example including d-type orbitals for p-type functions, and p-type orbitals to better describe hydrogen. This polarisation is often abbreviated by "P" or "*" as in the case of 6-311G** which uses d-functions to polarise p-functions and p-functions for hydrogen and helium. For the study of PSII the polarised def2 all-electron Gaussian basis sets developed by Weigend and Ahlrichs[53], such as QZVPP, have found popularity.

2.2.5.5 Diffuse Basis Sets

Another electronic property which can be accounted for in the basis set is how diffuse the orbitals are, this becomes important for weakly bound electrons and their proper modelling. Most basis sets can be "augmented" to account for this, for example the 6-311G+ set where the "+" indicates that diffuse s and p functions are included for heavy atoms. sometimes the prefix "aug" is used to indicate this. A basis function can be made more diffuse by decreasing the exponent that dictates electron decay. One downside of more diffuse basis sets is that as more diffuse character is introduced convergence can become more difficult.

2.2.5.6 Computational approximations

Computational efficiency is important especially when dealing with larger systems and so efforts into finding better approximations are continuously being undertaken. One example of this is the "resolution of identity Coulomb approximation" often referred to simply as RI-J, developed by Eichkorn, Ahlrichs, Weigend et al..[54–56] This approximation speeds up the calculation of the Coulomb interaction term, increasing computational efficiency ≈ 10-100 fold, without compromising the accuracy. The increased speed is achieved by reducing the amount of data stored and assembled. Charge distributions in DFT are obtained from products of basis functions, this requires for repulsion integrals to be defined and the RI-J approximation uses a two rather than four index lists of repulsion integrals. The error incurred through this is usually outweighed by the error in the numerical integration of the exchange energy or indeed the error due to basis set incompleteness. However absolute energies obtained with methods using RI-J and without should not be compared. The RI-J approximation is only appropriate for functionals not including HF exchange, for this Neese et al. developed the "chain-of-spheres" approximation this in combination with the work established for the RI-J approximation yields RI-JCOSX allowing for an increase in efficiency even when using hybrid functionals.[57] Both of these approximations are employed throughout work presented in this thesis.

2.2.6 Solvation

Not all systems exist in a vacuum, and especially biological systems, such as PSII, exist in the presence of a solvent. Accounting for this is important when dealing with these systems, practically there are multiple approaches which may be taken to model the solvent environment. While the inclusion of physical solvent molecules is possible, it is not clear how many of these molecules would have to be added to accurately model the solvent environment, it may well be necessary to include several solvation spheres at which point there is significant computational cost which quickly becomes infeasible for larger models. Furthermore, there would be countless arrangements possible at virtually identical energies.

However including some explicit solvent molecules is important to accurately model many protein reactions. Computationally cheapest is neglecting solvent molecules completely, this is followed by using continuum solvent models or a mix of explicit and implicit solvent, with some selected solvent molecules included in the cluster model, this comes with some increased computational cost depending on how many molecules are included.[58]

Continuum solvation models solve this problem by removing solvent molecules and instead modelling the solvent as a continuum with electrostatic properties

equivalent to the solvent. The first step is the creation of a cavity in the solvent continuum, wherein the molecule lies, there are various approaches and methods for this.[59–62] They generally all rely on the manipulation of the Van der Waals radii of the atoms within the solute to obtain a molecular surface which can then be used to define the cavity. Two common models for creating a cavity containing the solute atoms exist, both of these model the solvent molecule as a sphere which is rolled around the surface created by the Van der Waals radii of the solute atoms. The solvent-excluding surface traces the contact between the surfaces of the solute Van der Walls radii and the solvent molecule as it is rolled around. Whereas the solvent-accessible surface traces the centre of the solvent sphere as it is rolled around.

Next the interaction between the solvent and the solute is defined. Again various models can be used to describe this, throughout the work presented in this thesis the Conductor-like Polarizable Continuum Model (CPCM) is used[63] which is based on the polarised continuum model developed in 1981.[64]

2.2.7 Localisation

Once a converged chemical structure has been obtained it is often of interest to analyse the electronic structure, one of the ways in which this can be done is by visualising occupied molecular orbitals. Multiple approaches for this are available such as Weinhold's bond orbital analysis, while this is perfectly suitable for a single structure it does not allow for the tracking of electron movement throughout a reaction. [65–67] As such throughout work presented in this thesis Intrinsic Bonding Orbital (IBO) analysis is used. In essence IBOs are obtained from occupied molecular orbitals obtained from the molecular wavefunction, these are localised and then represent bonds or lone pairs. A mathematical derivation for these can be found in the references.[68–70] One advantage of IBO analysis is that it is possible to follow orbital transitions along a reaction coordinate, allowing for mechanistic insights since electron movement can be tracked.

2.3 Broken-Symmetry Density Functional Theory

DFT also allows for the description of spin systems and their magnetic properties by the use of broken-symmetry density functional theory (BS-DFT), this compared to post-HF methods is computationally feasible for complex systems such as the OEC. For systems such as PSII containing several unpaired spin centres it is important to be able to accurately model their properties, especially the interaction between the spin centres. BS-DFT has been applied extensively for the study of

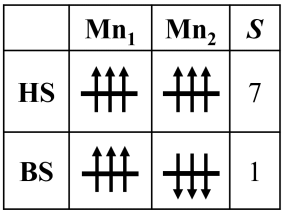

Figure 2.1: The HS and LS broken symmetry states for a Mn_2^{IV} dimer, arrows indicate either alpha or beta spin for each electron. Note that in BS-DFT the whole spin centre is flipped while spins on the same spin centre remain parallel.

the OEC as well as other multi-metal-centre complexes.[71–77] For a two spin centre system, for example a manganese dimer, the two spin centres may be parallel, resulting in a high spin (HS) system where the spin centres interact ferromagnetically (FM) here $S_{\mathrm{HS}} = S_A + S_B$. Or they may be antiparralel, resulting in a low spin (LS) system in which the spin centres interact anti-ferromagnetically (AF) here $S_{\mathrm{LS}} = |S_A - S_B|$. This is illustrated in figure 2.1 for a Mn_2^{IV} dimer.

As the number of unpaired spin centres increase so do the number of possible spin states. Broken-symmetry Density Functional Theory (BS-DFT) aims to calculate the electronic structure of systems with at least two open-shell magnetic ions, such as manganese in the OEC. DFT can handle HS systems well enough as just a single Kohn-Sham determinant is needed to describe the system. However as soon as two spin centres are linked anti-ferromagnetically several determinants are necessary for each electronic configuration, as each spin can occupy a number of orbitals, and a picture with just one of these configurations is insufficient to describe the complex at large.

2.3.1 The Principles of Broken Symmetry Density Functional Theory

BS-DFT aims to circumnavigate this configurational problem without resorting to the use of expensive configuration interaction methods. BS-DFT does this by constructing a single determinant broken-symmetry (BS) wavefunction which accounts for the anti-ferromagnetic characteristics but has the wrong spin symmetry:

$$\Psi_{\mathrm{BS}}^{\mathrm{guess}} = |(\mathrm{core})\eta_a\bar{\eta}_b| \tag{2.35}$$

here the "core" denotes all doubly occupied orbitals and $\eta_{a,b}$ are localised molecular orbitals formed from symmetric and anti-symmetric molecular orbitals, with the overbar indicating a spin down (beta) electron. Equation 2.35 has three key properties:

(1) $E(\Psi_{BS}) > E(\Psi_{FM})$

(2) Ψ_{BS} is a 1:1 mix of Ψ_{AF} and Ψ_{FM}

(3) Ψ_{BS} and Ψ_{AF} or indeed Ψ_{FM} have the same charge density but the wrong spin density. A true singlet wavefunction would have a spin density of zero at every point, whereas Ψ_{BS} has regions of positive and negative spin at points in space around a and b.

To properly describe the anti-ferromagnetic wavefunction it is necessary to apply the variational principle to the initial guess BS wavefunction and re-optimise the orbitals, thus yields the true BS wavefunction:

$$\Psi_{\mathrm{BS}} = |(\mathrm{core})'\eta'_a\bar{\eta}'_b| \tag{2.36}$$

The BS approach is however not perfect, it should yield the correct charge density, but the spin density is not always correctly modelled and can appear in regions as an artefact of the method. As such properties dependent only on the former charge density should be reliably determinant by BS-DFT.

It is possible to determine the Heisenberg exchange coupling constant, J_{AB}, for a system (containing spin centres A and B), from the energies obtained through the use of BS-DFT. Positive values of J indicate ferromagnetic coupling between A and B while a negative value indicates AF coupling. The magnitude of J is proportional to the strength of the coupling. This will be discussed further in section 3.2.8. The background to as well as the interpretation of BS-DFT has been thoroughly reviewed in literature, see references for further details.[8, 78]

2.4 The Potential Energy Surface

The Potential Energy Surface (PES) is a key concept in computational chemistry, and is discussed in many available physical chemistry texts.[79–81] In the simplest terms it links the energy of a system to its structure. During a reaction the structure changes from a starting structure to a final structure via some transition state (TS). This corresponds to movement across the potential energy surface. Similarly when a computational model is constructed it is generally not in its energetically most favourable state, and optimisation aims to minimise the energy of a system, here the movement across the models potential energy surface is downhill terminating in a minimum on the PES.

The PES is multidimensional, for a simple diatomic system in isolation it would be two-dimensional, an energy which relates to interatomic separation. A triatomic system is more complex here there are two interatomic distances and a bond angle

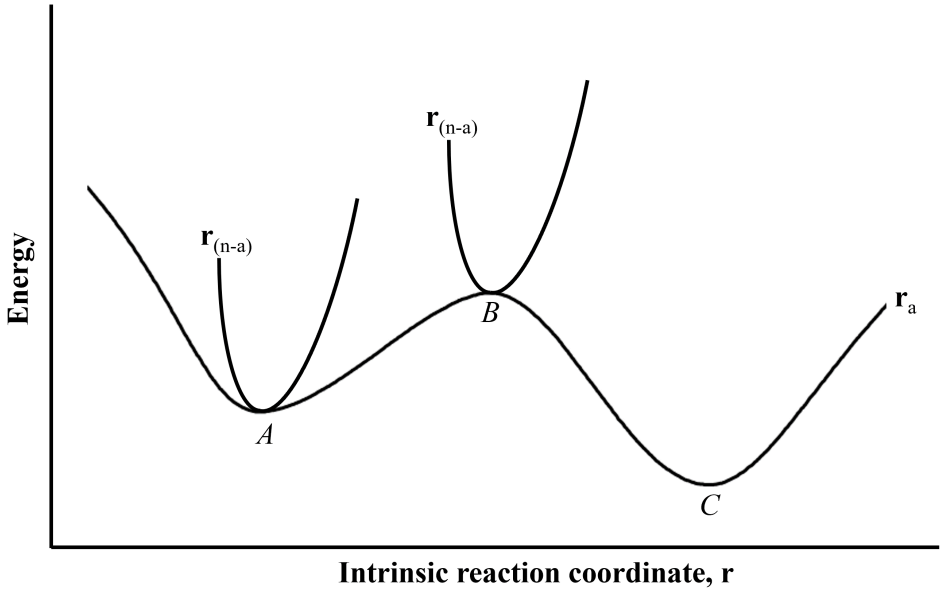

Figure 2.2: The PES for a reaction, here reactant A forms product C via a transition state B. Structures A and C represent minima in all n IRCs. The TS B corresponds to a maxima in IRC $\mathbf{r}_a$ but a minima for all other IRCs.

and can be represented as a three-dimensional plot. For a system of N atoms there are then N atomic coordinates forming a N dimensional energy "landscape". It is important to properly define the features of this landscape. Of most interest are turning points where the gradient at that point on the surface $\mathbf{r}$ is zero, $dE/d\mathbf{r} = 0$. Furthermore by examining the second derivative $d^2E/d^2\mathbf{r}$ for all N dimensions of $\mathbf{r}$ for these turning points it is possible to identify transitions states as well as true minima. The former TS is a turning point on the PES where $dE/d\mathbf{r} = 0$, such that it is a maxima for one of the N dimensions, $d^2E/d^2\mathbf{r} < 0$, and a minima, $d^2E/d^2\mathbf{r} > 0$ in all other dimensions. While a structure located at a minima will have all $d^2E/d^2\mathbf{r} > 0$.

It is common to construct a PES for a reaction, where the PES is expressed in terms of intrinsic reaction coordinate (IRC) and Energy. The IRC represents the minimum energy path between two different minima, for a simple diatomic reaction this would simply be the interatomic distance, but for a more complex system would involve more complex changes in structure involving potentially changes in many atomic coordinates. This PES is illustrated in figure 2.2 with the difference between the TS and a minima highlighted.

The PES of a more complex structure will contain many minima, the lowest energy minima is known as the global minima. The PES has several implications for computational models, for one it is important to construct a good starting structure for geometry optimisation, typically since energy is minimised a model between A

and B in figure 2.2 will optimise to A while if the initial guess falls between B and C in figure 2.2 it will optimise to C. This highlights the importance of comparing results to experimental findings to determine the validity of the model, as while there are many computationally accessible minima they may not all be of relevance.

It is also possible to confirm that a structure corresponds to a minima, by calculation of vibrational frequencies. If the structure corresponds to a minima only positive vibrational modes will be found. On the other hand at the TS a single negative, imaginary frequency, will be found which corresponds to movement along the IRC.

2.4.1 Reaction Pathways and the Potential Energy Surface

In order to study a reaction one may scan along the IRC which should locate the reactant, the TS as well as the product. A complete PES scan for a larger system is computationally prohibitively expensive. However several alternatives exist, this thesis uses relaxed surface scans, here only one structural parameter such as the bond length between two atoms of interest is varied in fixed steps from a starting structure, at each point of the scan this structural parameter is fixed while the rest of the structure is optimised. This allows for the tracking of electrons using IBO analysis, see section 2.2.7 as well as monitoring structural and electronic changes along the PES. Another method gaining popularity for the study of PSII is the nudged elastic band (NEB) method.[82–84] For NEB several intermediary structures (beads) between the reactant and product are placed. These beads are connected by springs and the energy of the beads is minimised along all perpendicular directions to the springs. The connecting springs ensure that the spacing between beads remains constant. The highest energy bead has its spring forces inverted so as to maximise the energy along the paths and minimise it in all other directions, thus yielding the exact TS.[85–87] However, this method is highly dependent on the path chosen onto which the beads are placed, some chemical intuition or knowledge of the correct paths would be needed to make an informed choice. Both ends of the NEB paths are fixed and as such must be known, whereas the relaxed surface scan method does not rely on this. Furthermore due to spring strain "kinks" can occur in the elastic band and as such the minimum energy paths isn't always found.[85]

2.5 Computational Model Creation

This thesis presents a range of computational models. Models of the OEC, are created from crystallographic data published in the protein data bank, initially the desired constituents are selected, for example the relevant amino acid residues, crys-

tallographic water molecules and the OEC complex. Since often the amino acids are truncated or differing protonation states of oxygen ligands are of interest, hydrogens were added manually as appropriate to ensure the correct protonation states and covalencies. For smaller dimer models, literature metal-metal distances were used to construct the model, with ligands being places manually around the metals. The choice of what to include and what not to is more difficult, the fewer atoms are included in a model the faster results can be obtained, however the accuracy of the results may suffer by neglecting effects of important residues or atoms. Small systems have the benefit that it is easier to investigate the effect of changing an aspect of a system, to compare systems to each other, and allow for a higher level of theory to be used to calculate results. Conversely a larger system can include more residues and so more accurately model the protein environment. As such a balance must be struck, to minimise computational cost while still producing reliable and relevant results. In all cases presented here ligands immediately bonded to the OEC were included to ensure correct ligation. Further some key residues identified in previous work within the group as well as various computational studies by other groups were included, see references for discussion.[88–90]

After the initial model had been created geometry optimisation was performed to minimise the system's energy. In the case of the OEC models the amino acids on the periphery of the model had one or more atoms in their backbone fixed, since in nature the protein framework would hold these in space, restricting their freedom of movement. Additionally if a specific bond length or atomic separation was investigated this could be fixed to the desired value also. Having obtained an optimised structure, properties could be obtained, such as ground state spins, broken symmetry energies or spin distributions.

The choice of basis set and functional is another important consideration and can have major effects on the results. As such in general it is of importance to compare calculated properties to experimentally observed equivalents, such as interatomic distances, hyperfine couplings, relative stabilities and ground state spins. Proper validation of the methodology is not only important to determine the accuracy of the results obtained, but also to identify the most time and cost effective methodology which still provides reliable results.[91] Specific computational details for all models presented in this thesis are given in each of the corresponding chapters.

References

[1] H. Hu, W. Yang, *Annual Review of Physical Chemistry* **2008**, *59*, PMID: 18393679, 573–601.

[2] M. W. van der Kamp, A. J. Mulholland, *Biochemistry* **2013**, *52*, PMID: 23557014, 2708–2728.

[3] R. Lonsdale, J. N. Harvey, A. J. Mulholland, *Chem. Soc. Rev.* **2012**, *41*, 3025–3038.

[4] H. M. Senn, W. Thiel, *Angewandte Chemie International Edition* **2009**, *48*, 1198–1229.

[5] W. Kohn, L. J. Sham, *Phys. Rev.* **1965**, *140*, A1133–A1138.

[6] P. Hohenberg, W. Kohn, *Phys. Rev.* **1964**, *136*, B864–B871.

[7] A. Zangwill, *Physics Today* **2015**, *68*, 34–39.

[8] F. Neese, *Coordination Chemistry Reviews* **2009**, *253*, Theory and Computing in Contemporary Coordination Chemistry, 526–563.

[9] H. Grant, G., W. Richards, G., *Computational Chemistry*, Oxford Science Publications, Oxford, **1995**.

[10] A. Szabó, N. S. Ostlund in **1982**.

[11] F. Jensen, *Introduction to Computational Chemistry*, Wiley, **2013**.

[12] W. Koch, C. Holthausen, M., *A Chemist's Guide to Density Functional Theory*, John Wiley & Sons, Ltd, **2001**.

[13] C. Cramer, *Essentials of Computational Chemistry: Theories and Models*, Wiley, **2013**.

[14] R. Parr, Y. Weitao, *Density-Functional Theory of Atoms and Molecules*, Oxford University Press, **1994**.

[15] M. Born, W. Heisenberg, P. Jordan, *Zeitschrift für Physik* **1926**, *35*, 557–615.

[16] D. R. Hartree, *Mathematical Proceedings of the Cambridge Philosophical Society* **1928**, *24*, 89–110.

[17] J. C. Slater, *Phys. Rev.* **1930**, *35*, 210–211.

[18] V. Fock, *Zeitschrift für Physik* **1930**, *61*, 126–148.

[19] L. H. Thomas, *Mathematical Proceedings of the Cambridge Philosophical Society* **1927**, *23*, 542–548.

[20] E. Fermi, *Rend. Accad. Naz. Lincei* **1927**, *6*, 32.

[21] J. C. Slater, *Phys. Rev.* **1951**, *81*, 385–390.

[22] D. M. Ceperley, B. J. Alder, *Phys. Rev. Lett.* **1980**, *45*, 566–569.

[23] J. P. Perdew, Y. Wang, *Phys. Rev. B* **1992**, *45*, 13244–13249.

[24] S. H. Vosko, L. Wilk, M. Nusair, *Canadian Journal of Physics* **1980**, *58*, 1200–1211.

[25] A. D. Becke, *The Journal of Chemical Physics* **1986**, *84*, 4524–4529.

[26] J. P. Perdew, W. Yue, *Phys. Rev. B* **1986**, *33*, 8800–8802.

[27] A. D. Becke, *Phys. Rev. A* **1988**, *38*, 3098–3100.

[28] J. P. Perdew, *Phys. Rev. B* **1986**, *33*, 8822–8824.

[29] C. Lee, W. Yang, R. G. Parr, *Phys. Rev. B* **1988**, *37*, 785–789.

[30] A. Ghosh in *Comprehensive Semiconductor Science and Technology*, (Eds.: P. Bhattacharya, R. Fornari, H. Kamimura), Elsevier, Amsterdam, **2011**, pp. 383–479.

[31] A. D. Becke, M. R. Roussel, *Phys. Rev. A* **1989**, *39*, 3761–3767.

[32] H. Isobe, M. Shoji, J.-R. Shen, K. Yamaguchi, *Inorganic Chemistry* **2016**, *55*, PMID: 26717045, 502–511.

[33] H. Isobe, M. Shoji, T. Suzuki, J.-R. Shen, K. Yamaguchi, *Journal of Chemical Theory and Computation* **2019**, *15*, 2375–2391.

[34] V. N. Staroverov, G. E. Scuseria, J. Tao, J. P. Perdew, *The Journal of Chemical Physics* **2003**, *119*, 12129–12137.

[35] J. Tao, J. P. Perdew, V. N. Staroverov, G. E. Scuseria, *Phys. Rev. Lett.* **2003**, *91*, 146401.

[36] A. D. Becke, *Journal of Chemical Physics* **1993**, *98*, 1372–1377.

[37] P. J. Stephens, F. J. Devlin, C. S. Ashvar, C. F. Chabalowski, M. J. Frisch, *Faraday Discuss.* **1994**, *99*, 103–119.

[38] P. Hobza, J. Šponer, T. Reschel, *Journal of Computational Chemistry* **1995**, *16*, 1315–1325.

[39] J. Pérez-Jordá, A. Becke, *Chemical Physics Letters* **1995**, *233*, 134–137.

[40] S. Kristyán, P. Pulay, *Chemical Physics Letters* **1994**, *229*, 175–180.

[41] F. London, *Zeitschrift für Physik* **1930**, *63*, 245–279.

[42] I. Kaplan, *Intermolecular Interactions: Physical Picture, Computational Methods and Model Potentials*, Wiley, **2006**.

[43] In *Encyclopedic Dictionary of Polymers*, (Ed.: J. W. Gooch), Springer New York, New York, NY, **2007**, pp. 582–582.

[44] S. Grimme, S. Ehrlich, L. Goerigk, *Journal of Computational Chemistry* **2011**, *32*, 1456–1465.

[45] S. Grimme, J. Antony, S. Ehrlich, H. Krieg, *The Journal of chemical physics* **2010**, *132 15*, 154104.

[46] A. D. Becke, E. R. Johnson, *The Journal of Chemical Physics* **2005**, *123*, 154101.

[47] E. R. Johnson, A. D. Becke, *The Journal of Chemical Physics* **2006**, *124*, 174104.

[48] A. D. Becke, E. R. Johnson, *The Journal of Chemical Physics* **2005**, *122*, 154104.

[49] A. D. Becke, E. R. Johnson, *The Journal of Chemical Physics* **2007**, *127*, 124108.

[50] S. Grimme, *Journal of Computational Chemistry* **2006**, *27*, 1787–1799.

[51] W. J. Hehre, R. F. Stewart, J. A. Pople, *Journal of Chemical Physics* **1969**, *51*, 2657–2664.

[52] J. S. Binkley, J. A. Pople, W. J. Hehre, *ChemInform* **2002**, *11*.

[53] F. Weigend, R. Ahlrichs, *Phys. Chem. Chem. Phys.* **2005**, *7*, 3297–3305.

[54] K. Eichkorn, O. Treutler, H. Öhm, M. Häser, R. Ahlrichs, *Chemical Physics Letters* **1995**, *240*, 283–290.

[55] K. Eichkorn, F. Weigend, O. Treutler, R. Ahlrichs, *Theoretical Chemistry Accounts* **1997**, *97*, 119–124.

[56] F. Weigend, *Phys. Chem. Chem. Phys.* **2006**, *8*, 1057–1065.

[57] F. Neese, F. Wennmohs, A. Hansen, U. Becker, *Chemical Physics* **2009**, *356*, 98–109.

[58] G. Norjmaa, G. Ujaque, A. Lledós, *Topics in Catalysis* **2022**, *65*, 118–140.

[59] M. L. Connolly, *Science* **1983**, *221*, 709–713.

[60] B. Lee, F. Richards, *Journal of Molecular Biology* **1971**, *55*, 379–IN4.

[61] M. L. Connolly, *Journal of Molecular Graphics* **1993**, *11*, 139–141.

[62] M. F. Sanner, A. J. Olson, J.-C. Spehner, *Biopolymers* **1996**, *38*, 305–320.

[63] V. Barone, M. Cossi, *The Journal of Physical Chemistry A* **1998**, *102*, 1995–2001.

[64] S. Miertuš, E. Scrocco, J. Tomasi, *Chemical Physics* **1981**, *55*, 117–129.

[65] F. Weinhold, *Journal of Computational Chemistry* **2012**, *33*, 2363–2379.

[66] A. E. Reed, F. Weinhold, *The Journal of Chemical Physics* **1985**, *83*, 1736–1740.

[67] J. P. Foster, F. Weinhold, *Journal of the American Chemical Society* **1980**, *102*, 7211–7218.

[68] G. Knizia, J. E. M. N. Klein, *Angewandte Chemie International Edition* **2015**, *54*, 5518–5522.

[69] G. Knizia, *Journal of Chemical Theory and Computation* **2013**, *9*, PMID: 26583402, 4834–4843.

[70] J. Pipek, P. G. Mezey, *The Journal of Chemical Physics* **1989**, *90*, 4916–4926.

[71] E. Ruiz, J. Cano, S. Alvarez, P. Alemany, *Journal of Computational Chemistry* **1999**, *20*, 1391–1400.

[72] V. Krewald, F. Neese, D. A. Pantazis, *Journal of the American Chemical Society* **2013**, *135*, 5726–5739.

[73] M. Orio, D. A. Pantazis, T. Petrenko, F. Neese, *Inorganic Chemistry* **2009**, *48*, 7251–7260.

[74] L. Rapatskiy, W. M. Ames, M. Pérez-Navarro, A. Savitsky, J. J. Griese, T. Weyhermüller, H. S. Shafaat, M. Högbom, F. Neese, D. A. Pantazis, N. Cox, *The Journal of Physical Chemistry B* **2015**, *119*, 13904–13921.

[75] D. A. Pantazis, M. Orio, T. Petrenko, S. Zein, W. Lubitz, J. Messinger, F. Neese, *Phys. Chem. Chem. Phys.* **2009**, *11*, 6788–6798.

[76] W. Ames, D. A. Pantazis, V. Krewald, N. Cox, J. Messinger, W. Lubitz, F. Neese, *Journal of the American Chemical Society* **2011**, *133*, PMID: 22092013, 19743–19757.

[77] N. Cox, L. Rapatskiy, J.-H. Su, D. A. Pantazis, M. Sugiura, L. Kulik, P. Dorlet, A. W. Rutherford, F. Neese, A. Boussac, W. Lubitz, J. Messinger, *Journal of the American Chemical Society* **2011**, *133*, 3635–3648.

[78] F. Neese, *Journal of Physics and Chemistry of Solids* **2004**, *65*, Design, Characterization and Modelling of Molecule-Based Magnetic Materials Proceedings of Symposium K, EMRS Spring Meeting, June 2003, Strasbourg, France, 781–785.

[79] E. G. Lewars in *Computational Chemistry: Introduction to the Theory and Applications of Molecular and Quantum Mechanics*, Springer International Publishing, Cham, **2016**, pp. 9–49.

[80] H.-Y. Kwon, Z. Morrow, C. T. Kelley, E. Jakubikova, *The Journal of Physical Chemistry A* **2021**, *125*, 9725–9735.

[81] P. Atkins, de Paulia, *Physical Chemistry*, W H Freeman & Co., **2009**.

[82] M. Shoji, H. Isobe, K. Yamaguchi, *Chemical Physics Letters* **2019**, *714*, 219–226.

[83] M. Capone, D. Bovi, D. Narzi, L. Guidoni, *Biochemistry* **2015**, *54*, PMID: 26466193, 6439–6442.

[84] M. Schilling, S. Luber in *Water Oxidation Catalysts*, (Eds.: R. van Eldik, C. D. Hubbard), Advances in Inorganic Chemistry, Academic Press, **2019**, pp. 61–114.

[85] G. Henkelman, H. Jónsson, *The Journal of Chemical Physics* **2000**, *113*, 9978–9985.

[86] G. Henkelman, B. P. Uberuaga, H. Jónsson, *The Journal of Chemical Physics* **2000**, *113*, 9901–9904.

[87] C. Bergonzo, C. Simmerling in *Annual Reports in Computational Chemistry*, (Ed.: R. A. Wheeler), Annual Reports in Computational Chemistry, Elsevier, **2011**, pp. 89–97.

[88] P. E. M. Siegbahn, *Journal of the American Chemical Society* **2009**, *131*, PMID: 19961231, 18238–18239.

[89] M. M. Najafpour, A. N. Moghaddam, S. I. Allakhverdiev, Govindjee, *Biochimica et Biophysica Acta (BBA) - Bioenergetics* **2012**, *1817*, Photosynthesis Research for Sustainability: From Natural to Artificial, 1110–1121.

[90] D. A. Pantazis, *ACS Catalysis* **2018**, *8*, 9477–9507.

[91] M. Bursch, J.-M. Mewes, A. Hansen, S. Grimme, *Angewandte Chemie International Edition* **2022**, *61*, e202205735.

Chapter 3

Electron Paramagnetic Resonance

Electron Paramagnetic Resonance (EPR) spectroscopy is used to study systems containing unpaired electrons, this is particularly useful since it is insensitive to paired electrons and so even in large systems containing many electrons it can selectively study only the unpaired spins, making it particularly useful for the study of PSII, or indeed any other metalloproteins, radical intermediates, and transition metal complexes. The EPR phenomenon was discovered in 1945 by Zavoisky,[1] shortly before the discovery of nuclear magnetic resonance, both of which rely on quantum mechanical angular momentum or spin in order to study a system. In the study of PSII EPR has provided insights into the bonding and oxidation states of the OEC's Mn ions as well as its surroundings throughout the Kok cycle, see section 1.1.2. While EPR has proven very useful in the ongoing effort to understand the mechanism of water oxidation the data obtained is often highly complex, and theoretical models are often needed to fully rationalise spectra. This chapter discusses the basic background theory of EPR, as well as experimental and theoretical aspects. EPR theory and application has been reviewed extensively in various textbooks and reviews see references for more details.[2–7]

3.1 Principles of Electron Paramagnetic Resonance

EPR concerns itself with unpaired electrons, each electron has a spin represented by the angular momentum quantum number, m_s, where for an electron $m_s = \pm 1/2$ depending on if the electronic spin is alpha or beta. Since an electron is charged and has angular momentum it can be thought of as a magnet possessing a magnetic moment, μ, where:

$$\mu = m_s g \mu_B \tag{3.1}$$

here μ_B is the Bohr magneton. The g value of a system describes the unpaired electron's interaction with the magnetic field, it is independent of the magnetic field strength and depends only on the chemical environment of the electron, for a free electron $g = g_e$ and ($g_e \approx 2.00$).[8]

In practise the state of the sample (liquid or solid) must be considered. In a solid sample the g value depends on the orientation of the sample and has components in all dimensions, it is then often expressed by the $\boldsymbol{g}$ tensor. The $\boldsymbol{g}$ tensor is a 3×3 matrix, and diagonalising it yields the dimensional g_x, g_y and g_z components. The extent of anisotropy can be used as a measure of the symmetry of the electronic distribution of the unpaired spin. If $g_x = g_y = g_z = g_{iso}$ it is said to be isotropic with cubic symmetry. Axial symmetry satisfies $g_x = g_y \neq g_z$, here $g_x = g_y = g_\perp$ and $g_z = g_\parallel$. Finally if $g_x \neq g_y \neq g_z$ the symmetry is rhombic.[2]

However in a liquid sample all sample molecules are in motion and so only an average g value is observed, this is often referred to as g_{iso} and is the average of all g_x, g_y and g_z contributions.

During EPR microwave (MW) radiation is applied in order to probe the system, in practise transitions can either be measured by MW irradiation in a fixed magnetic field, or by applying a fixed MW frequency and changing the magnetic field. Depending on the frequency of MWs used EPR spectra can be said to be in a different "band", for example X-band EPR will use MWs between $\approx$ 8.8-9.6 GHz.[9] Generally EPR spectra are presented as first derivatives of absorption. Furthermore the MW radiation used can be either parallel or perpendicular to the magnetic field. Most EPR experiments use perpendicular, sometimes referred to as "normal" mode. However some systems are EPR silent, *i.e.* yield no signals using normal mode EPR. Here parallel mode EPR can be used to resolve these as formerly forbidden spin transitions are now allowed, see section 3.2.3.

Higher frequency MWs yield more highly resolved spectra as sensitivity is proportional to the square of the frequency. However higher frequencies also require greater magnetic field strength which becomes more difficult to produce. Compared to nuclear magnetic resonance EPR benefits from a higher overall sensitivity and even small amounts of sample are usually sufficient when compared to techniques such as nuclear magnetic resonance spectroscopy.

3.2 The Spin Hamiltonian

Mathematically it is possible to describe all the interactions in a system with an unpaired electron using the spin Hamiltonian:

$$\hat{H} = \hat{H}_{EZ} + \hat{H}_{HF} + \hat{H}_{ZF} + \hat{H}_{NQ} - \hat{H}_{NZ} + \hat{H}_{NN} + \hat{H}_{JT} \tag{3.2}$$

here the various $\hat{H}$ terms represent Electron Zeeman ($\hat{H}_{EZ}$), Hyperfine ($\hat{H}_{HF}$), Zero-Field ($\hat{H}_{ZF}$), Nuclear Quadrupole ($\hat{H}_{NQ}$), Nuclear Zeeman ($\hat{H}_{NZ}$), Nuclear-Nuclear ($\hat{H}_{NN}$) and Jahn-Teller ($\hat{H}_{JT}$) interaction. Not all of these interactions are necessarily present in every system. In a system with multiple unpaired electrons each of these electrons is described by its own spin Hamiltonian if they are non-interacting. If there are multiple interacting unpaired electrons additional coupling terms must be included to account for electron-electron interaction. The following sections will describe the individual interactions in more detail. For a more thorough discussion on the Spin Hamiltonian see references.[3, 10]

3.2.1 Electron Zeeman Interaction

While in the absence of a magnetic field the alpha and beta spins are of equivalent energy as soon as a magnetic field is applied this degeneracy is lost. Having obtained the magnetic moment, the electron energy, E, can be obtained using:

$$E = \mu B_0 \tag{3.3}$$

where B_0 is the magnetic field strength. By combining equations 3.1 and 3.3 the difference between the energy levels for a given magnetic field can be found:

$$\Delta E = g\mu_B B_0 \tag{3.4}$$

Figure 3.1 gives a visual representation of the Electron Zeeman interaction for a given applied magnetic field of strength B_0. The degeneracy of the spin is lost, Parallel alignment of the electronic spin and the magnetic field is favourable, while antiparallel alignment is disfavoured.

During EPR spectroscopy microwave radiation is used at various frequencies to promote the transition between these spin levels, transitions occur when:

$$\Delta E = g\mu_B B_0 = h\nu \tag{3.5}$$

where ν is the frequency.

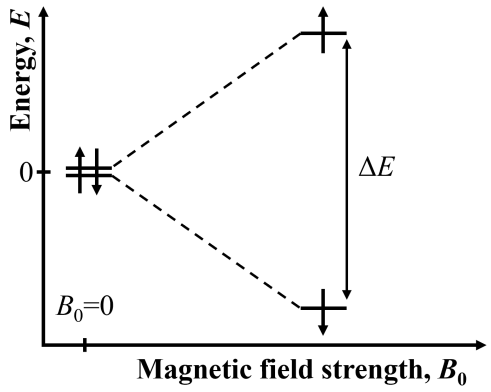

Figure 3.1: The Electron Zeeman interaction, an unpaired spin is degenerate in terms of its spin in the absence of a magnetic field, but when a magnetic field is applied the alpha and beta levels are split.

3.2.1.1 Spin-Orbit Interaction

An electron in a system occupies an orbital and possess orbital angular momentum. The magnetic moment caused by the orbital angular momentum can couple with the spin magnetic moment inherent to the electron. Spin-Orbit interaction depends largely on the nuclei around the electron, with greater atomic numbers causing a greater spin-orbit interaction, this is due to the exited electronic states becoming closer in energy to the ground state. The electron is overall then affected by the artificially applied magnetic field, the magnetic field generated by its orbital angular momentum, as well as any magnetic field generated by its surroundings. The combination of all this shifts its g value away from that of a free electron and allows information about its properties to be determined, since each unique structure should provide a unique magnetic environment.

3.2.2 Electron-Nuclear Hyperfine Interaction

Hyperfine coupling arises through the interaction of electronic and nuclear spin. The Hyperfine coupling (HFC) constant, A, represents the strength of this interaction. In practise this interaction is responsible for the observed fine structure in a spectrum. The Hyperfine interaction can be split into an isotropic, a_{iso}, and an anisotropic, a_{aniso}, part. The Isotropic hyperfine interaction, sometimes referred to as Fermi contact interaction, is independent of B_0 and dependent on the magnetic moments of nuclear and electronic spins as well as the spin density of its environment. It splits the spin levels into further sub-levels as shown in figure 3.2, and the extend of the splitting depends on the spin of the nucleus, where the number of sub-levels it splits into is $2nI + 1$, with n being the number of nuclei the spin is coupled to and I the nuclear spin. Transitions between various levels must follow the selection rules $\Delta m_s = \pm 1$ and $\Delta m_l = 0$.

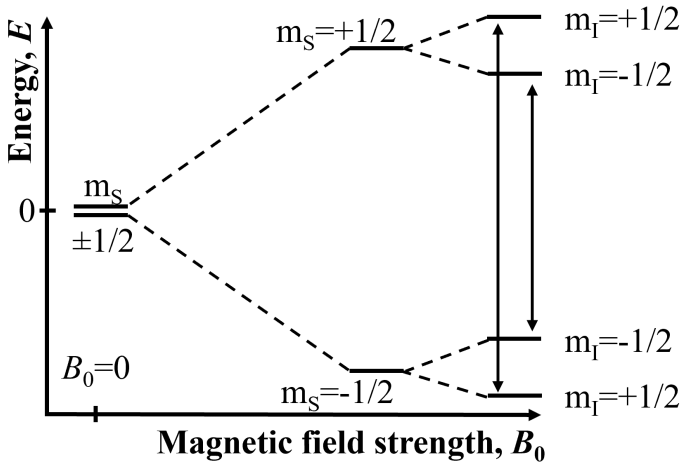

Figure 3.2: The Electron-Nuclear Hyperfine Interaction for an unpaired electron interaction with one nuclei of $I = 1/2$, the Zeeman levels are further split into hyperfine levels by coupling of the electronic and nuclear spins. Allowed transitions are indicated by the arrows, here there are two allowed transitions, and so the resultant spectra would contain two peaks with a 1:1 ratio.

For example a methyl radical would result in 4 hyperfine levels and a spectra with 4 peaks in a 1:3:3:1 ratio, while a nitrogen based radical would have 3 hyperfine levels and a spectra with 3 peaks in a 1:1:1 ratio. Here the distance between the peaks would correspond to A.

The anisotropic hyperfine interaction is the result of dipole-dipole interaction between the electron and nuclei, it is orientation dependent, and so only detected in solid samples. The contributions in each Cartesian axis can be measured and depends on orientation of the sample in respect to the external field as well as the relative dipole-dipole orientation. The magnitude depends on separation and the strength of the dipoles. As it is orientation depend it is only observed in solid samples where the **A** tensor is a sum of the isotropic and anisotropic parts:

$$\mathbf{A} = a_{iso} + \begin{vmatrix} -T & 0 & 0 \\ 0 & -T & 0 \\ 0 & 0 & 2T \end{vmatrix} \tag{3.6}$$

where T is the dipolar coupling constant and a function of g_n, the nuclear g value and the electron-nuclear distance. In a liquid sample this becomes zero and can be ignored.

The hyperfine Hamiltonian is a product of the two types of interaction such that:

$$\hat{H}_{HF} = \hat{H}_F + \hat{H}_{DD} \tag{3.7}$$

with $\hat{H}_F$ corresponding to the Fermi contact interaction and $\hat{H}_{DD}$ the dipole-dipole interaction. The dipole-dipole interaction can be written as:

$$\hat{H}_{DD} = -g_e g_n \mu_e \mu_n \left(\frac{\mathbf{IS}}{\mathbf{r}^3} - \frac{3(\mathbf{Ir})(\mathbf{Sr})}{\mathbf{r}^5} \right) \tag{3.8}$$

Here $\mathbf{I}$ and $\mathbf{S}$ are the nuclear and electronic spin matrices and $\mathbf{r}$ the vector between the electron and nuclear spins. The Fermi contact interaction is given by:

$$\hat{H}_F = \frac{2\mu_o}{3\hbar} g_e g_n \beta_e \beta_n |\Psi_o(0)|^2 \tag{3.9}$$

where $|\Psi_o(0)|^2$ is the electron spin density at the nucleus and β_e, n are the electronic and nuclear Bohr magnetons. Clearly the Fermi contact is only relevant for electrons in s-orbitals or indeed s-hybridized orbitals since only then can electron density be found at the nucleus. However the interaction can be seen even for other orbitals such as p-orbitals by spin polarization from the orbitals to the nucleus through an s-orbital.[3, 10]

3.2.3 Zero Field Splitting

If more than one unpaired electron is present in a system the spin levels may be split even without the application of an external field, this is known as zero field splitting (ZFS) and is denoted by two parameters, D and E. With D being the energy difference between the lowest energy level and the average of the higher degenerate levels or the reverse if the lower energy states are degenerate and the higher state is not, while E is half the energy difference between the degenerate states. This is due to dipolar interaction as well as spin-orbit coupling.

There are two cases to consider, either the system has an odd number of electrons or an even number. For a system with an even number of unpaired electrons (S=1,2,3,...) m_s can take values from $-m_s$ to m_s in steps of one. For the sake of simplicity the following considers an S=1 system where $m_s = -1, 0, 1$ The magnitude of D has a significant effect on the observed EPR spectrum, these are illustrated in figure 3.3. If there is no ZFS, $D = 0$, any transition obeying the selection rule $\Delta m_s = \pm 1$ is allowed and so there are two possible transitions which are degenerate. If $h\nu > D$ ZFS removes the degeneracy and then further splitting is introduced by the applied magnetic field, now the two transitions are no longer degenerate and two signals are observed. Finally if $D >> h\nu$, strong ZFS causes no EPR transitions to be observed since any allowed transitions with $\Delta m_s = \pm 1$ are too high in energy.

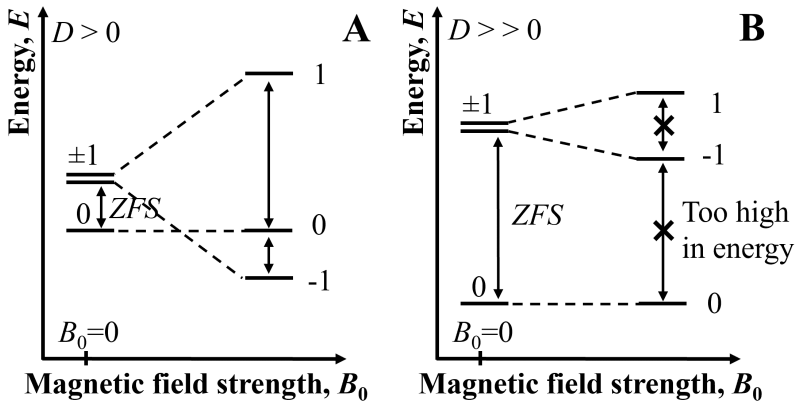

Figure 3.3: ZFS in a system with two unpaired electrons, numbers indicate m_s values of the spin levels. **A:** $D > 0$ The degeneracy of the two spin allowed transitions is removed resulting in two signals being observed in the EPR spectra. **A:** $D >> 0$ The degeneracy of the two spin allowed transitions is lost however no signals are observed as the only spin allowed transitions is too high in energy to by stimulated by the applied MW energy.

However in parallel mode EPR the selection rule $\Delta m_s = \pm 1$ may be broken. Considering a $S = 1$ system in absence of a magnetic field the magnetic sub levels are split by ZFS. If the magnetic field is applied parallel to one of these sublevels its energy is not affected by the magnetic field whereas the other two sublevels are. In which case the $\Delta m_s = \pm 2$ transitions may be observed when the unaffected and affected sublevels are equivalent to each other in energy. See references for more detail.[2, 11]

In a system with an odd number of electrons (S=3/2,5/2,...) the spin degeneracy remains doubly degenerate referred to as Kramers' degeneracy. ZFS split the various m_s levels which are then split into a pair of singlets each by the applied magnetic field according to the Zeeman interaction. As a result each $-m_s$ to m_s levels is observed resulting in a more extensive fine structure. This becomes particularly complex for transition metals like manganese as each m_s spin level is further split through hyperfine coupling by the $I = 5/2$ nuclei in which case each m_s spin level is split into 6 hyperfine levels.

ZFS can be described by tensors **E** and **D** both of which depend on the symmetry of the system as outlined above. The 3×3 **D** tensor is symmetric and traceless, $D_x^2 + D_y^2 + D_z^2 = 0$, with the diagonal elements corresponding to the directional D_x, y, z contributions, as a result the following holds true:

$$D = 3D_z/2 \tag{3.10}$$

$$E = (D_x - D_y)/2 \tag{3.11}$$

In a cubic system $D = E = 0$, for axial symmetry $D > 0$ and $E = 0$ finally for rhombic symmetry $D \neq E \neq 0$.

3.2.3.1 Calculation of Zero Field Splitting

Throughout this thesis methods outlined by Chrysina et al.[12] is used for the calculation of D values in systems with more than one spin centre. Here the overall D value is:

$$D = \sum_i \kappa_i d_i \tag{3.12}$$

where d_i is the site fine structure value and κ_i the a spin projection factor. The spin projection factor is given by:

$$\kappa_i = 3\frac{\langle S_{i,z}^2 - \frac{1}{3}S_i(S_i+1)\rangle}{S(2S-1)} \tag{3.13}$$

where $\langle S_{i,z}\rangle$ is the spin expectation value of site i, S_i the spin on that site and S the overall spin of the system.

The D and E value in a model system can be calculated easily in a system in which there are no more than two spin centres. In a system with more than 2 spin centres the process becomes more difficult, the use of BS-DFT is required. BS-DFT can be used to obtain the on-site spin expectation values as well as the ground state spin of the system. To obtain the individual d_i values it is necessary to create several model systems with only one spin centre each. In the case of PSII three of the Mn centres may be substituted for Ge or Ga depending on their oxidation states, these metals while possessing no unpaired spin have the same charge thus allowing for the individual Mn d_i values to be obtained.

3.2.4 Nuclear Quadrupole Interaction

Nuclei with spins such that, $I > 1/2$, possess an electric quadrupole moment which interacts with the electric field gradient generated by the electrons. While it can be difficult to detect in EPR it manifests itself as a shift in the peaks without causing further splitting of the spin levels. The Nuclear Quadrupole is given by:

$$\hat{H}_{NQ} = \hat{\mathbf{I}}^{\intercal}\mathbf{Q}\hat{\mathbf{I}} \tag{3.14}$$

where $\mathbf{Q}$ is the traceless quadrupole tensor and $\hat{\mathbf{I}}$ the nuclear spin vector.

3.2.5 Nuclear Zeeman Interaction

Much like the electron Zeeman interaction the nuclear zeeman interaction describes the coupling of the nuclear spins to the applied magnetic field. Similarly it is given by:

$$\hat{H}_{NZ} = -\mu_n g_n B_0 \mathbf{I} \tag{3.15}$$

where μ_n and g_n are the nuclear magnetic moment and g factor, B_0 the applied field and I the nuclear spin quantum number. Generally this interaction is isotropic and does not influence the observed EPR spectra but becomes relevant in some types of EPR experiments.

3.2.6 Nuclear Nuclear Interaction

Nuclear-nuclear interaction is generally negligible in EPR as their relative magnitudes compared to electron-electron and electron-nuclear interactions are small. However the Nuclear-nuclear interaction is highly relevant in nuclear magnetic resonance spectroscopy.

3.2.7 Jahn-Teller Distortion

Jahn-Teller splitting occurs in a non-linear system in which degenerate orbitals are unevenly occupied, this leads to a distortion, usually a lengthening along a bonding axis, in order to remove this degeneracy leading to overall stabilisation through the decrease in symmetry. This has an effect on the EPR spectra of systems in which Jahn-Teller distortion occurs as the relative energies of the spin levels will be different.

3.2.8 Spin Exchange coupling

In a system with multiple spin centres, the spin exchange or Heisenberg exchange coupling constant, J, can be used to describe the interaction between the two. Indeed in any multi-spin centre system a J value for each unique pair of spin centres exists. The J value describes the nature of the interaction between the centres and is obtained in part from the energy difference between states of different spin. As eluded to in section 2.2.3 spin centres may interact ferro- or anti-ferromagnetically, with anti-ferromagnetic interaction corresponding to negative values of J and ferromagnetic interaction to positive values. The magnitude of J indicates the strength of this interaction. The Heisenberg-Dirak-van Vleck (HDvV) Hamiltonian models this interaction as:

$$\hat{H}_{\mathrm{HDvV}} = -2J\hat{S}_A\hat{S}_B \tag{3.16}$$

where $\hat{S}_{A/B}$ are the spin operators for the spin centres A and B. The solution to this yields the spin eigenstates and their energies including the lowest energy ground state spin and all excited spin states.

In order to calculate the various J values it is necessary to calculate the energies of the various spin states. While for small system this is possible using various approaches such as multi-configurational methods, for larger and more complex systems such as PSII BS-DFT based methods are widely used and will be employed throughout this thesis to obtain the energies of the various spin states since BS-DFT methods are computationally cheaper. Alternatives to BS-DFT do exist and can be used but show no significant advantage.[13, 14]

3.2.8.1 Calculation of the Spin Exchange Coupling

In a multi spin centre system various approaches have been outlined for the calculation of the J value[15–18] with some consideration specifically for the BS-DFT approach.[19–22] Using the equation:

$$J_{AB} = \frac{E^{\mathrm{BS}} - E^{\mathrm{HS}}}{\hat{S}^2_{\mathrm{HS}} - \hat{S}^2_{\mathrm{BS}}} \tag{3.17}$$

where E represents the energy of that spin state and $\hat{S}$ is the spin operator, the J coupling for a dinuclear system can be obtained. This equation has been shown to work well in systems with both weak and strong coupling. The Pantazis group has successfully applied this for studies of manganese dimers also[23].

In order then to study a more complex system a different approach is needed as equation 3.17 is no longer applicable. Throughout work presented in this thesis the approach developed and used for the study of PSII by the Pantazis group[24–26] is used to determine the J values for all systems.

Using this approach the system containing N spin centres has M J values such that:

$$M = \frac{N(N-1)}{2} \tag{3.18}$$

here each J value is a unique pair interaction between two spin centres. Furthermore a system with N spin centres contains $i = 2^{N-1}$ spin states including all unique broken symmetry states and the "high spin" state in which all centres are parallel. Each of these i states can be described by a $M_{S,i}$ determinant such that:

$$|M_{S,i}\rangle = |m_{s_1}, m_{s_2}, ..., m_{s_N}\rangle \tag{3.19}$$

where m_{s_N} is the spin on each site. The total M_S value for each $M_{S,i}$ is then simply the sum of all m_{s_N}, and must be a positive value, if it is negative all spin centres are inverted, this represents the same unique spin alignment of the spin centres.

The energy of each spin state is then obtained and the J values can be obtained by solving all possible equations defined by the Ising Hamiltonian such that:

$$E = -2\sum J_{ij} M_{S,i} M_{S,j} \tag{3.20}$$

However there are only $\frac{N(N-1)}{2}$ exchange couplings in the system and as such it is said to be overdetermined by the set of equations 3.20 and therefore the solution for each J value must be approximated. This can be done using singular value decomposition as outlined by Ames et al.[26], while this is an approximation in practise for PSII the solution can be considered exact.

3.2.9 Spin Projection

As outlined in section 2.3.1 while the BS wavefunction gives the correct charge density it yields a suboptimal spin density at each point in space. For a low spin singlet the correct wavefunction would have no spin density at every point in space, whereas in the BS solution this is not necessarily the case due to the loss of spin symmetry. An accurate description of the spin density is however still necessary for the calculation of any property of the system which depends on it. This issue can be addressed by the use of spin projection, which will be used throughout work presented in this thesis. Spin projection has been applied to PSII by the Pantazis group and the details of the methodology are outlined in their study.[24]

The spin projection coefficient is defined for each spin centre i as:

$$c_i = \frac{\langle S_i \rangle}{S_{total}} \tag{3.21}$$

where S_{total} is the total spin of the system and $\langle S_i \rangle$ is the spin expectation value for the spin operator for centre i. To obtain $\langle S_i \rangle$ first a basis function describing the vector $|S_1 M_{S_1}, ..., S_N M_{S_N}\rangle$ is constructed, the spin Hamiltonian elements identified and their matrix diagonalised which allows for the eigenstates of the system to be obtained. The lowest energy eigenstate can then be used after re-diagonalising to obtain the spin expectation value of the site. The spin projection coefficient can then be used to correct BS-DFT calculated values such as the hyperfine couplings which can then be compared to experimental values.

3.3 Electron Paramagnetic Spectroscopy in Practise

3.3.1 Electron Paramagnetic Spectroscopy Apparatus

A typical EPR spectrometer consists of a monochromatic microwave source, generally EPR spectrometers operate between 1 and 260 GHz, different frequencies are referred to as "bands". X-band EPR for example uses MW radiation of $\approx$ 9.8 GHz,[9] Q-band $\approx$ 34 GHz,[27] W-band $\approx$ 94 GHz [28] and D-band $\approx$ 130 GHz.[29] The EPR spectrometer contains an electromagnet which applies the magnetic field to the sample. Higher EPR frequencies require stronger magnetic fields but are generally more sensitive. Typically magnetic fields will vary between 0.03 T to 9 T. The sample is contained in the EPR spectrometer cavity, allowing for the application of the uniform magnetic field and irradiation by MW radiation. The spectra is then recorded by a detector. Both fluid and solid samples can be used. MW radiation can be applied either perpendicular or parallel to the magnetic field, these are known as normal and parallel mode EPR respectively. Parallel mode allows for the observation of forbidden spin transitions and can better resolve integer spin systems (S=1,2,...,etc). Furthermore the cavity temperature can be controlled and changing this can have a significant effect.[3, 10, 30]

3.3.2 Electron Paramagnetic Spectroscopy Experiments

Not just the affects outlined by the spin Hamiltonian have to be taken into account when performing EPR another factor are the relaxation times (T_1 and T_2). T_1 is the spin-lattice relaxation time and corresponds to the spin transitioning from the upper excited spin state to the lower level, with the energy being released as thermal vibration through the lattice. T_2 is the spin-spin relaxation time and corresponds to the redistribution of energy within an ensemble of spins with no net energy change. Relaxation is required to observe a signal, the MW radiation disturbs the equilibrium spin distribution and relaxation returns it to equilibrium. Fast relaxation times are often observed in experiments at ambient temperatures and can lead to broadening of the spectrum. Both T_1 and T_2 become longer at lower temperatures and so often cryogenic temperatures are necessary for systems with fast relaxation times.[2]

Continuos Wave (CW) EPR refers to experiments in which the MW radiation is applied constantly at a set frequency, typically using low-intensity MW radiation. The magnetic field then scans through a pre-determined range, this brings the different spin transitions into resonance with the MW radiation which are then observed. While it is a simple experiment it suffers from poor signal to noise ratio.

Alternatively pulse EPR can be used, here the applied magnetic field is constant

while the sample is irradiated with short bursts of high-intensity MW radiation of a specific frequency. The frequency of each MW burst can be varied allowing for individual transitions to be isolated. This experiment generally gives a more resolved result compared to CW EPR. Pulse EPR usually requires the experiment to be performed at cryogenic temperatures, usually meaning the samples are solids, this allows for anisotropic contributions to also be observed.

There are a variety of pulse EPR techniques available. Electron-nuclear double resonance (ENDOR) uses radiofrequency to stimulate nuclear spin flips which are not normally observed in EPR experiments. This is useful when investigating strongly coupled nuclei, and can provide information on the first coordination sphere of the unpaired spin centre in question.

Electron spin echo envelope modulation (ESEEM) can be used to investigate more weakly coupled nuclei, typically in the second coordination sphere of the unpaired spin. Double electron-electron resonance (DEER) can be used to determine the distance between two weakly coupled electron spins. These techniques as well as related techniques are discussed in more detail in the references.[31–33]

References

[1] K. Zavoisky, Evgenii, *Zhur. Eksperiment. i Theoret. Fiz.* **1945**, *15*, 344–350.

[2] M. Roessler, E. Salvadori, *Chem. Soc. Rev.* **2018**, *47*, 2534–2553.

[3] C. Karunakaran, M. Balamurugan in *Spin Resonance Spectroscopy*, (Ed.: C. Karunakaran), Elsevier, **2018**, pp. 169–228.

[4] C. Karunakaran, M. Balamurugan, M. Karthikeyan in *Spin Resonance Spectroscopy*, (Ed.: C. Karunakaran), Elsevier, **2018**, pp. 281–347.

[5] J. Weil, J. Bolton, *Electron Paramagnetic Resonance: Elementary Theory and Practical Applications*, Wiley, New Jersey, **2007**.

[6] M. Brustolon, E. Giamello, *Electron Paramagnetic Resonance: A Practitioner's Toolkit*, Wiley, New Jersey, **2009**.

[7] W. Hagen, *Biomolecular EPR Spectroscopy*, CRC Press, Boca Raton, **2008**.

[8] B. Odom, D. Hanneke, B. D'Urso, G. Gabrielse, *Phys. Rev. Lett.* **2006**, *97*, 030801.

[9] J. Klare in *Encyclopedia of Spectroscopy and Spectrometry (Third Edition)*, (Eds.: J. C. Lindon, G. E. Tranter, D. W. Koppenaal), Academic Press, Oxford, **2017**, pp. 442–446.

[10] M. Mostafanejad, *International Journal of Quantum Chemistry* **2014**, *114*, 1495–1512.

[11] P. Pietrzyk, T. Mazur, Z. Sojka in *Local Structural Characterisation*, John Wiley & Sons, Ltd, **2013**, Chapter 4, pp. 225–300.

[12] M. Chrysina, E. Heyno, Y. Kutin, M. Reus, H. Nilsson, M. M. Nowaczyk, S. DeBeer, F. Neese, J. Messinger, W. Lubitz, N. Cox, *Proceedings of the National Academy of Sciences* **2019**, *116*, 16841–16846.

[13] H. R. Zhekova, M. Seth, T. Ziegler, *The Journal of chemical physics* **2011**, *135 18*, 184105.

[14] J. J. Phillips, J. E. Peralta, *The Journal of chemical physics* **2011**, *135 18*, 184108.

[15] E. Ruiz, S. Alvarez, J. Cano, V. Polo, *The Journal of Chemical Physics* **2005**, *123*, 164110.

[16] L. Noodleman, *The Journal of Chemical Physics* **1981**, *74*, 5737–5743.

[17] L. Noodleman, E. R. Davidson, *Chemical Physics* **1986**, *109*, 131–143.

[18] K. Yamaguchi, Y. Takahara, T. Fueno in Applied Quantum Chemistry, (Eds.: V. H. Smith, H. F. Schaefer, K. Morokuma), Springer Netherlands, Dordrecht, **1986**, pp. 155–184.

[19] I. Ciofini, C. A. Daul, *Coordination Chemistry Reviews* **2003**, *238-239*, Theoretical and Computational Chemistry, 187–209.

[20] T. Soda, Y. Kitagawa, T. Onishi, Y. Takano, Y. Shigeta, H. Nagao, Y. Yoshioka, K. Yamaguchi, *Chemical Physics Letters* **2000**, *319*, 223–230.

[21] L. Noodleman, J. Li, X. Zhao, W. Richardson, *Density Functional Methods in Chemistry and Materials Science* **1997**, 149–188.

[22] E. Ruiz, J. Cano, S. Alvarez, P. Alemany, *Journal of Computational Chemistry* **1999**, *20*, 1391–1400.

[23] D. A. Pantazis, V. Krewald, M. Orio, F. Neese, *Dalton Trans.* **2010**, *39*, 4959–4967.

[24] D. A. Pantazis, M. Orio, T. Petrenko, S. Zein, E. Bill, W. Lubitz, J. Messinger, F. Neese, *Chemistry* **2009**, *15 20*, 5108–23.

[25] D. A. Pantazis, W. Ames, N. Cox, W. Lubitz, F. Neese, *Angewandte Chemie International Edition* **2012**, *51*, 9935–9940.

[26] W. Ames, D. A. Pantazis, V. Krewald, N. Cox, J. Messinger, W. Lubitz, F. Neese, *Journal of the American Chemical Society* **2011**, *133*, PMID: 22092013, 19743–19757.

[27] A. Haddy, K. Lakshmi, G. W. Brudvig, H. A. Frank, *Biophysical Journal* **2004**, *87*, 2885–2896.

[28] N. Cox, M. Retegan, F. Neese, D. A. Pantazis, A. Boussac, W. Lubitz, *Science* **2014**, *345*, 804–808.

[29] T. M. Casey, Z. Liu, J. M. Esquiaqui, N. L. Pirman, E. Milshteyn, G. E. Fanucci, *Biochemical and Biophysical Research Communications* **2014**, *450*, 723–728.

[30] L. Kevan, *Foundations of Physics* **1997**, *27*, 959–960.

[31] D. M. Murphy, R. D. Farley, *Chem. Soc. Rev.* **2006**, *35*, 249–268.

[32] G. Hanson, L. Berliner, *High resolution EPR: applications to metalloenzymes and metals in medicine*, *Vol. 28*, Springer Science & Business Media, **2009**.

[33] J. Harmer, G. Mitrikas, A. Schweiger in *High Resolution EPR: Applications to Metalloenzymes and Metals in Medicine*, (Eds.: L. Berliner, G. Hanson), Springer New York, New York, NY, **2009**, pp. 13–61.

Chapter 4

Bonding and Magnetic Exchange Pathways in Nature's Water-Oxidizing Complex

Authors: Felix Rummel, Thomas A. Corry and Patrick J. O'Malley

Address: School of Chemistry, The University of Manchester, Manchester, M139PL, U.K.

Published at: *J. Phys. Chem. B*, **2021**, 125, 7147-7154

DOI: https://doi.org/10.1021/acs.jpcb.1c03864

4.1 Preface

Structural data for the OEC located at the heart of PSII has shown a Mn_4CaO_5 cluster to be present.[1–6] However structural data alone is not sufficient to understand the mechanism by PSII produces molecular oxygen, EPR studies[7–9] as well as theoretical studies[10, 11] have provided information on the oxidation states and electronics of the OEC. Understanding the electronic structure is of particular importance, in particular the Mn ions which undergo sequential oxidation throughout the Kok cycle.[8] The Mn ions in PSII or indeed any two centres possessing unpaired spin interact through magnetic interactions as discussed in section 3.2.8. Understanding these interactions is of interest in order to better understand the electronic structure of PSII and the mechanism for water oxidation.

Presented in this publication is work on the nature of the interactions between the Mn ions and their bonding nature in the OEC using BS-DFT which has been used extensively for the analysis of both the OEC and smaller Mn systems.[12–18] Both small oxygen bridged Mn-Mn dimers are presented as well as models of the OEC.

4.2 Abstract

The nature of the bonding and magnetic exchange pathways of the water-oxidizing complex of photosystem 2 is explored using broken symmetry density functional theory. The electronic structure and superexchange pathways are illustrated and analysed using corresponding orbitals and intrinsic bond orbitals. These demonstrate a dominating influence on the bonding and magnetic interactions by both the geometrical structure of the Mn_4CaO_5 core complex and the ionic interactions of the oxo bridges with the neighbouring Ca^{2+} ion. The demonstrated ionic nature of the Ca^{2+} bonds is proposed to contribute to the stabilization of the oxygen atoms participating in O-O bond formation.

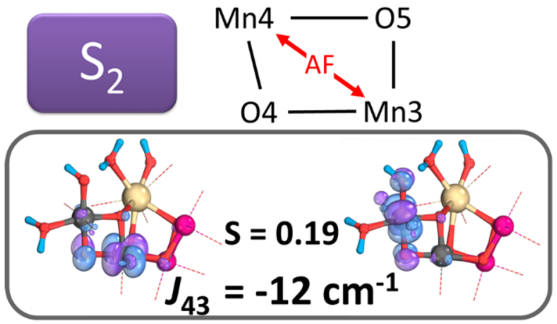

Figure 4.1: Table of Content graphic adapted from *J. Phys. Chem. B*, **2021**, 125, 7147-7154.[19]

4.3 Manuscript *J. Phys. Chem. B*, 2021, 125, 7147-7154.

4.3.1 Introduction

Photosystem 2 (PS2) is a multi-unit pigment protein complex found in the thylakoid membrane of organisms that perform oxygenic photosynthesis.[20, 21] Its key function is the accumulation of visible-light-driven oxidizing equivalents on its donor side, leading to the oxidation of water to molecular oxygen in its water-oxidizing complex (WOC). The catalytic cycle is achieved using five distinct redox intermediates termed S_n states, Figure 4.2, where n labels the number of stored oxidizing equivalents, 0-4, required to oxidize two molecules of water to molecular oxygen. In recent years, the detailed atomic-level molecular structure of this important biological complex has been revealed first by synchrotron X-ray crystallography[22] and then subsequently using X-ray free electron laser (XFEL) crystallography.[23] This has provided the primary landmark for any realistic proposals regarding the molecular mechanism of water oxidation. The core structure, Figure 4.3, shows that the WOC is a Mn_4CaO_5 cluster with four

directly coordinated terminal oxygen atoms, presumably water or hydroxide, and labelled W1-W4. While theoretical modelling has suggested modifications of this core topology during the S-state cycle,[21] recent structural studies from XFEL time-resolved analysis show that this overall core structure remains essentially unchanged throughout the cycle of S-states.[24–28] Structural details alone however are not sufficient to find the mechanism of action of this important catalyst. What is needed additionally is the electronic structure. Of particular importance are the electronic structure factors governing the magnetic interactions between the four Mn ions.[29] This can be experimentally probed from analysis of the EPR spectra of the complex in its different oxidized S-states.[8]

Due to the complex nature of the spectra observed, their interpretation is

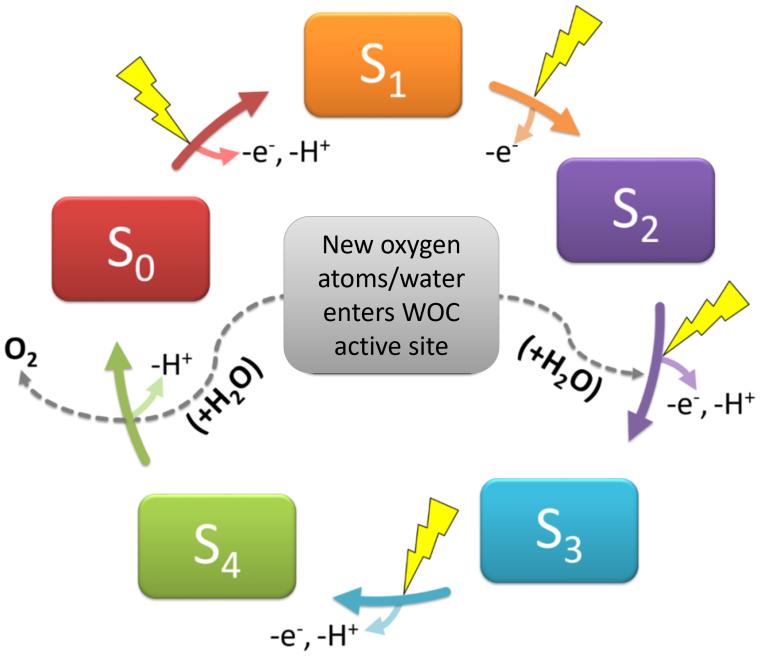

Figure 4.2: WOC S-state cycle. The four Mn ions of the complex are progressively oxidized with each photon flash. Substrate water molecules enter the cycle at the S_3- and S_0-states as indicated.

non-trivial and often requires combination with electronic structure calculations.[30] The oxo bridges of dimeric, trimeric, and tetramanganese clusters act as superexchange conduits between the Mn magnetic ions.[31–36] These can be altered by the bridge geometry and protonation state.[33, 37] The WOC core structure can be broadly described as the fusion of three $[Mn_2(\mu\text{-}O)_2(\text{carboxylato})]$ bridges, Mn_1/Mn_2, Mn_2/Mn_3, and Mn_3/Mn_4, Figure 4.3. The Ca^{2+} ion interacts closely with the bridging oxos, O1, O2, and O5, fixing the three bridged units in place. The major magnetic interaction pathways are between the neighbouring Mn ions linked via their $(\mu\text{-}O)_2(\mu\text{-carboxylato})$ bridges.

In this study, we use broken symmetry (BS) density functional methods to examine the electronic structure and superexchange pathways of the WOC focusing

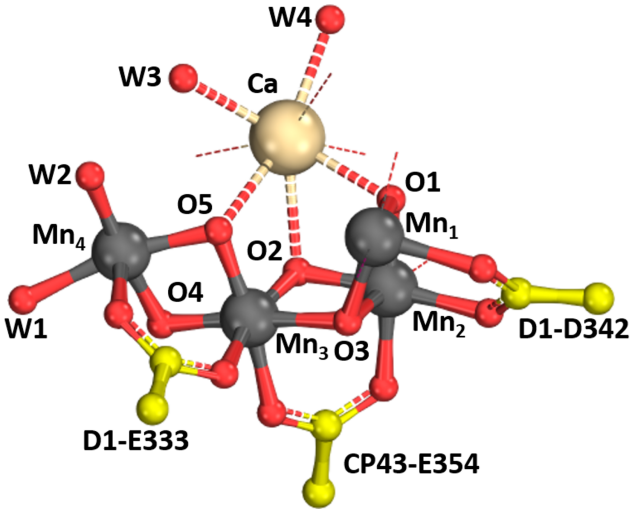

Figure 4.3: Illustration of the WOC core structure highlighting the fusion of three [Mn_2(μ-O)$_2$(μ-carboxylato)] units stabilized by a Ca^{2+} ion. All atoms within the model are not shown for illustrative purposes. Color code: Ca (cream), Mn (grey), O (red), and C (yellow). The full model used is shown in Figure S4.2, and coordinates are supplied in the Supporting Information.

on the S_2-state. We investigate the electronic superexchange pathways between the neighbouring Mn ions using both intrinsic bond orbitals (IBOs)[38] and corresponding orbitals (COs).[39–41] By comparison with simpler dimeric Mn_2(μ$_2$-O)$_2$(μ-carboxylato) models, we show how both the WOC geometry and the Ca^{2+} ion control and modulate its electronic structure and resultant magnetic interactions.

4.3.2 Methodology

For a system containing two or more interacting magnetic centres, the magnetic properties are typically interpreted in the context of the Heisenberg-Dirac-van Vleck (HDvV) spin Hamiltonian.[41] The effective exchange coupling constant serves as a measure of the strength of the interaction and is +ve for ferromagnetic and -ve for antiferromagnetic alignment. Multi-determinantal methods are required to properly construct the relevant proper configuration state functions. These are infeasible for the WOC model size covered in the present study. A way to circumvent this is offered by BS-density functional theory (BS-DFT) approaches. BS-DFT represents the antiferromagnetic state by a single unrestricted determinant where the singly occupied opposite-spin magnetic orbitals are variationally allowed to assume spatial parts that are localized on the magnetic centers. A number of different expressions have been proposed for computing the exchange coupling constant.[41] Here, we adopt the formulation proposed by Yamaguchi et al..[42]

Analysis and identification of superexchange orbital pathways can be carried

out by applying the CO transformation.[39] For BS solutions, this leads to an ordering of the orbitals into three chemically meaningful subsets.[40] These COs are (i) doubly occupied alpha and beta spin pairs with the overlap (S) value equal to 1.0, (ii) non-orthogonal magnetic pairs with S considerably less than 1.0, and (iii) non-overlapping spin orbitals. The non-orthogonal magnetic orbital pairs give rise to a quantitative and pictorial view of the interactions in the system with the spatial overlap value, S, associated with each magnetic pair directly corresponding to the strength of these interactions.

4.3.2.1 Models Used

The dimeric models $[Mn_2(\mu\text{-}O)_2(\mu\text{-}O_2CCH_3)(NH_3)_6]$, **dioxo** and $[Mn_2(\mu\text{-}O)(\mu\text{-}OCa)(\mu\text{-}O_2CCH_3)(NH_3)_6]$, **dioxo-Ca** are shown in Figure S4.1. Both Mn^{IV}/Mn^{IV} and Mn^{III}/Mn^{IV} forms are studied. The S_2-state WOC model used, Figure S4.2, is similar to that previously described[30, 43, 44] and uses the consensus Mn oxidation state assignment of Mn_1(III), Mn_2(IV), Mn_3(IV), and Mn_4(IV). XYZ coordinates of all models are supplied in the Supporting Information.

4.3.2.2 Computational Details

All calculations were carried out in ORCA 4[45] with models initially geometry-optimized in the HS oxidation state. The BP86[46, 47] functional was applied in the unrestricted form (UKS in ORCA) with the zeroth-order regular approximation (ZORA) Hamiltonian.[48–50] The ZORA versions of the def2-TZVP basis sets were used for all calculations on **dioxo/-Ca** models.[51] The resolution of identity approximation for Coulomb integrals, along with the deconstructed general Weigend auxiliary basis sets, was used.[52, 53] Grimme's treatment of dispersion corrections with Becke-Johnson damping (D3BJ) was used.[54–56] The conductor-like polarizable continuum model with a dielectric constant $\epsilon = 8.0$[57, 58] was applied in all calculations. Tight SCF convergence criteria and increased integration grids were incorporated using VeryTightSCF and Grid6/IntAcc 6, respectively, for WOC models and TightSCF and Grid4 for the **dioxo/Ca** models, in ORCA convention. The WOC model and coordinates[43] are given in the Supporting Information.

The hybrid meta-GGA TPSSh functional was used for all BS-DFT calculations. The chain of spheres (RIJCOSX) approximation to exact exchange was applied along with the same deconstructed auxiliary basis sets involved in geometry optimization calculations.[59, 60] For WOC calculations, the ZORA versions of the def2-TZVP basis set with f-functions removed were used for all atoms.[51] Initial BS guesses were constructed using the "flipspin" feature of ORCA.[61] Convergence to the correct BS and HS states in all calculations was confirmed by examination of the calculated Mulliken spin populations.

For the S_2-state of the WOC with Mn_1-4 oxidation states III-IV-IV-IV, a local S_z of 2 for the d_4-ion Mn(III) and 3/2 for the d_3-ion Mn(IV) is used. The high-spin determinant can be described as $|+2, +3/2, +3/2, +3/2\rangle$ (or "$\alpha\alpha\alpha\alpha$", $M_S = 13/2$), and six BS determinants were created by inverting local spins of Mn ions, for example, $|+2, +3/2, +3/2, -3/2\rangle$ ("$\alpha\alpha\alpha\beta$", $M_S = 7/2$) or $|+2, -3/2, -3/2, +3/2\rangle$ ("$\alpha\beta\beta\alpha$", $M_S = 1/2$). An M_S value and not S characterizes each BS determinant because it is not a spin eigenfunction. The energies of the BS determinants were used to deduce a set of J_{ij} values for the S_z-only (Ising) Hamiltonian. Subsequently, the same exchange coupling constants can be used to diagonalize the full HDvV Hamiltonian and obtain the spin ladder. The full details of the procedure have been described extensively in the literature and have been used successfully for many exchange-coupled Mn systems.[57, 62, 63]

IBOs were produced in IboView from the BS wave functions. To generate all plots, the following parameters in IboView were used unless otherwise stated in the text. These were an iboexp = 2, a high resolution of 1/20 Å, and a threshold of 85 for WOC models and 95 for **dioxo/-Ca** models to produce IBOs. The COs were produced using thresholds of 85 and 90 for WOC and **dioxo/-Ca** models, respectively.

To obtain the COs for the WOC S_2-state, enabling comparison with our dimer models, we use an atom substitution approach to "switch off" pathways except the bridge we are interested in and retaining the full model optimized geometry. For the Mn_3/Mn_4 bridge, we replace Mn_1 with Ga and Mn_2 with Ge. For the Mn_2/Mn_3 bridge, we replace Mn_1 with Ga and Mn_4 with Ge, and for the Mn_1/Mn_2 bridge, we replace Mn_3 and Mn_4 with Ge. The atom substitution method has only a minor influence on the values of the calculated exchange coupling constants of the bridges as shown in Table S4.1 where the relevant values are compared to the intact Mn cluster. This demonstrates that there is minimal perturbation of the magnetic structure of the Mn cluster and the pathways found are fully applicable to the full Mn cluster.

4.3.3 Results and Discussion

We first analyse the superexchange pathways present in the dimers, $[Mn_2(\mu\text{-}O)_2(\mu\text{-}O_2CCH_3)(NH_3)_6]$, **dioxo** and $[Mn_2(\mu\text{-}O)(\mu\text{-}OCa)(\mu\text{-}O_2CCH_3)(NH_3)_6]$, **dioxo-Ca**. The Mn^{IV}/Mn^{IV} and Mn^{III}/Mn^{IV} forms of each are first analysed in detail and then compared with the relevant WOC bridges in the S_2-state. Our analysis is based on the calculated exchange coupling constant, J, the IBOs,[38] and the COs.

4.3.3.1 Mn^{IV}/Mn^{IV}

Figure 4.4 illustrates the COs and J-couplings calculated for our model dimers **dioxo** and **dioxo-Ca** plus the Mn_3/Mn_4 and Mn_2/Mn_3 bridges in the S_2-state of the WOC. The magnitude of J is a measure of the ferromagnetism (+ve) or antiferromagnetism (-ve) between the two Mn magnetic centres. For two near-octahedral Mn^{IV} ions, the magnetic orbitals correspond to the d_{xz}, d_{xy}, and d_{yz} orbitals. In the absence of any bridge superexchange, the Mn magnetic orbitals would be aligned ferromagnetically, with positive J-values. The bridging oxos however give rise to superexchange which occurs via overlap of the oxo p and the above Mn magnetic orbitals which can, depending on the strength, stabilize antiferromagnetic coupling between the Mn centers. As discussed above, the CO S-value is a measure of the strength of this superexchange coupling between the Mn magnetic orbitals. For the small **dioxo** model containing two oxo bridges, the COs of Figure 4.4;a show that the d_π Mn magnetic orbitals, either d_{xz} or d_{yz}, interact via overlap with both oxo out-of-plane p_z orbitals displaying S-values near 0.20 and signifying strong magnetic overlap. The in-plane σ-bonding orbitals display much smaller overlap ($S = 0.06$) via the in-plane oxo p-orbitals due to the near orthogonal nature of their overlap at the bridging oxo. The two large values for S demonstrate that d_π-p_π overlap dominates the superexchange coupling for Mn^{IV}/Mn^{IV} bis μ-oxo dimers, in agreement with previous DFT studies[36, 37] and also supported by multi-configurational density matrix renormalisation group calculations.[64]

The calculated J value, -21 cm^{-1}, is a measure of this overlap, reflecting the stabilization of the BS state over the ferromagnetic state. The effect of a neighbouring Ca^{2+} ion is shown in Figure 4.4;b for the **dioxo-Ca** model. First of all, the lowered symmetry results in the Mn d_π-orbitals aligning along the Mn-oxo bonds leading to a more directed differential overlap with the oxo p_z-orbital for the two d_π-orbitals. The S-value overlap via the oxo bridge distal to Ca^{2+} is unaltered from **dioxo**. The S-value corresponding to overlap involving the out-of-plane oxo orbital proximal to the Ca^{2+} ion is lowered significantly to 0.14. The J-value magnitude is reduced by 12 cm^{-1}, indicating a reduced antiferromagnetic interaction. The Ca^{2+} interaction with the proximal oxo bridge reduces Mn d_π-p_π overlap, leading to reduced superexchange and reduced antiferromagnetic interactions.

With the main superexchange pathways delineated for the simple dimer models, we can now directly compare the COs and calculated J-values for the Mn^{IV}/Mn^{IV} bridges in the WOC, Figure 4.4;c,d, where they are oriented to allow direct comparison with the small dimer models. Their overall orientation and position within the WOC model are shown in Figure 4.5. From Figure 4.4;c, we can see the broad similarity of the WOC Mn_3/Mn_4 bridge to dimer model **dioxo-Ca**. The πpathway involving O4 gives the largest S-value. For the O5 pathway, the S-value is reduced due to the Ca^{2+} interaction similar to **dioxo-Ca** discussed above. Figure 4.4;d dis-

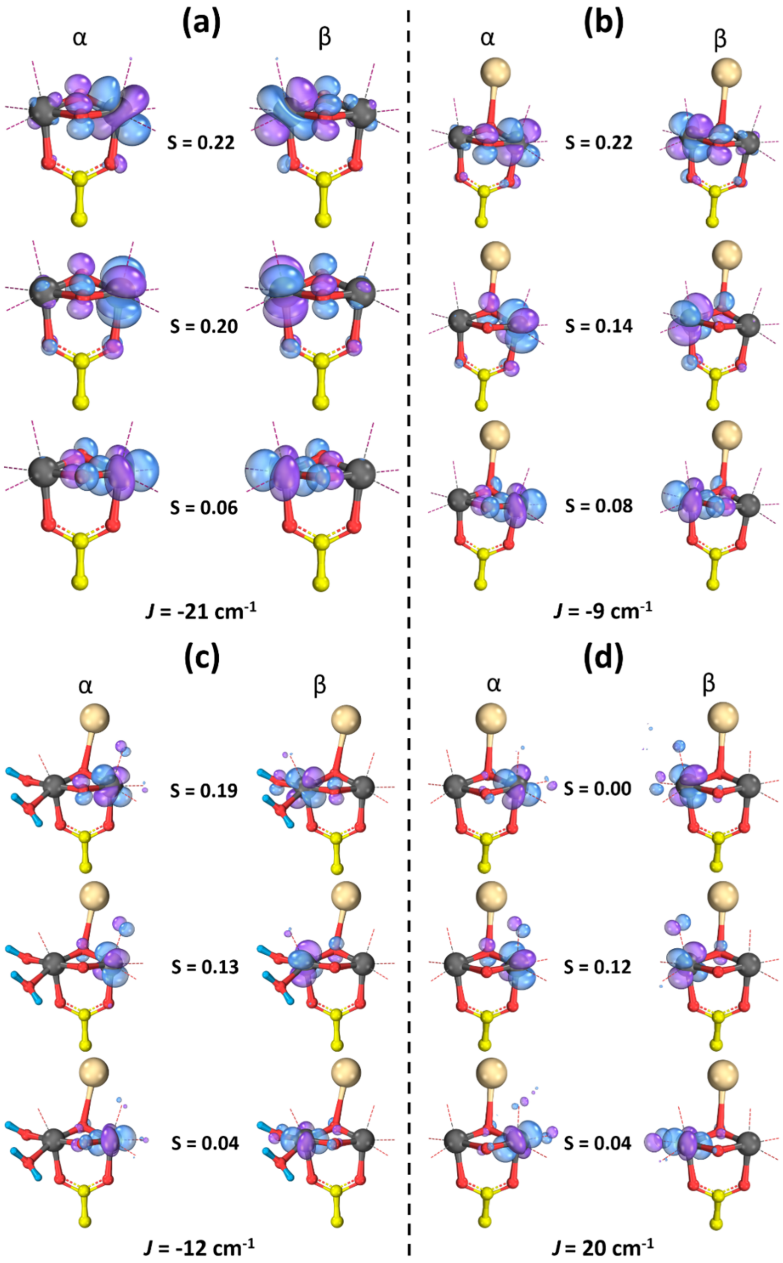

Figure 4.4: CO comparison: (a) **dioxo**; (b) **dioxo-Ca**; (c) S_2-WOC Mn_3/Mn_4, O4 at front, O5 at rear; and (d) S_2-WOC Mn_2/Mn_3, O3 at front, O2 at rear. S, overlap integral, values are given.

plays the COs and J-values for the Mn_2/Mn_3 WOC bridge. This differs from the Mn_3/Mn_4 WOC bridge and **dioxo-Ca** in having one S-value much lower in magnitude. This corresponds to the overlap pathway involving O3 of the WOC. O3 is a μ_3-O bridge covalently bonded to Mn_1, Mn_2, and Mn_3. This effectively, as seen in IBO analysis below, eliminates π-overlap pathways for the $Mn_{2/3}$ magnetic orbitals via this oxo. The O2 π-pathway is still available, but the complete blockage of the O3 route compared with **dioxo-Ca** and the Mn_3/Mn_4 bridge leads overall to a stabilization of the HS state for the link and a +ve J-value of +20 cm^{-1}.

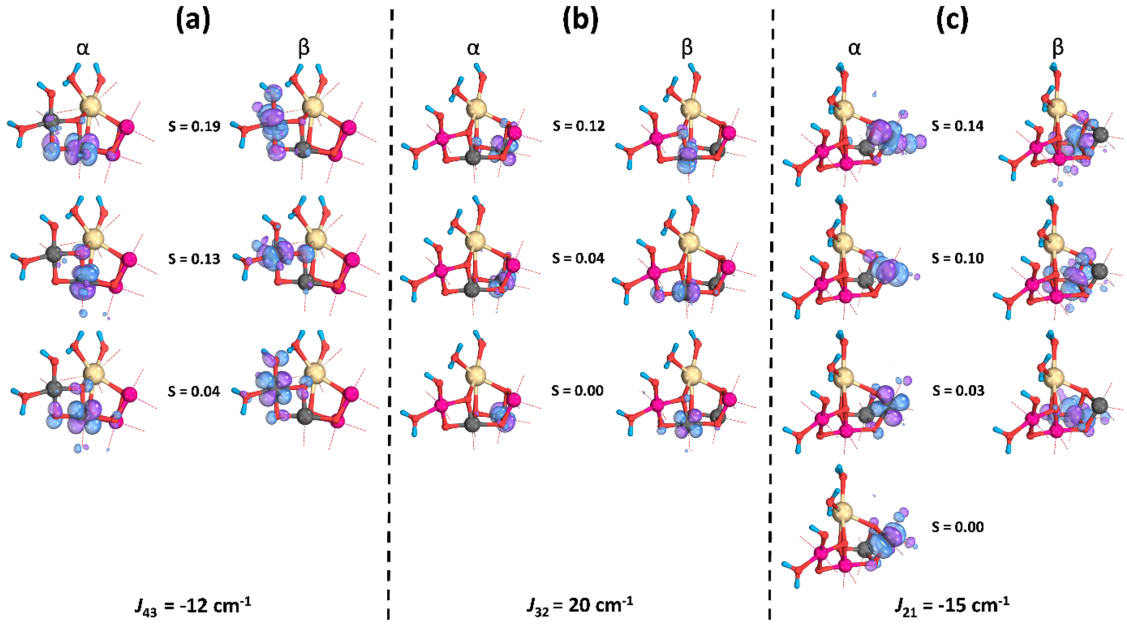

Figure 4.5: Location of COs within the S_2-WOC model for (a) Mn_3/Mn_4, (b) Mn_2/Mn_3, and (c) Mn_1/Mn_2 bridges. S, overlap integral, values are given. Model orientation is the same as Figure 4.3.

4.3.3.2 IBO Analysis

Our understanding of the exchange interactions in the WOC is also enlightened further by analysis of its IBOs. For the Mn_3/Mn_4 bridge of the WOC, the calculated IBOs are illustrated in Figure S4.3.

There are four sigma orbitals (α and β pairs) representing the $Mn_3O4/5$ and $Mn_4O4/5$ covalent bonds. There is also a lone pair ($\alpha\beta$) IBO on both O4 and O5. In addition, π-bond IBOs to Mn_3 and Mn_4 occur via O4, Figure 4.6;a, and O5, Figure 4.6;b, which are polarized toward Mn_3 (α) and Mn_4 (β). These give a pictorial illustration of the superexchange pathway, demonstrating spin polarization of the electron density on the bridging oxygen toward the opposite spin Mn ions, thereby stabilizing the antiferromagnetic spin alignment. We note the similar but somewhat smaller overlap for O5 which reflects weaker π-overlap compared with O4 due to the proximity of the Ca^{2+} ion. This is in accord with the lower S-overlap value for the COs discussed above.

For the Mn_2/Mn_3 bridge, the relevant IBOs are also given in Figure S4.4 and those involving O3 are highlighted in Figure 4.7. The O2 bridge is similar to O5 above, Figure 4.6;a, due to its similar immediate environment, that is, the interaction with Ca^{2+}. For O3 however, there are by contrast three sigma IBOs and a lone pair, Figure 4.7;a-d. As mentioned above, O3 represents a μ_3-O centre and has three sigma bonds to Mn_1, Mn_2, and Mn_3. The absence of π-bonding leads to an absence of a superexchange pathway via this oxo as demonstrated above in the CO analysis.

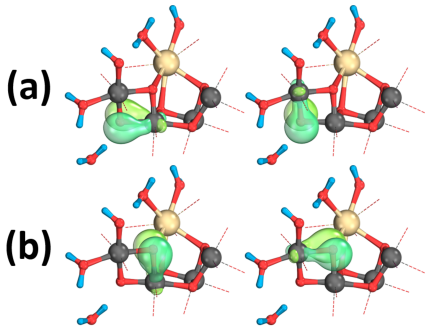

Figure 4.6: π-bond IBOs (α right and β left) for (a) $Mn_3O_4Mn_4$ and (b) $Mn_3O_5Mn_4$. The model is taken from the lowest-energy BS state where Mn_1-4 are αββα, $M_S = 1/2$.

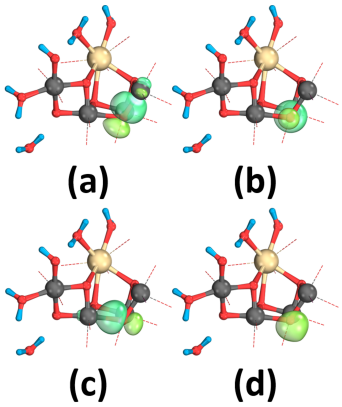

Figure 4.7: O3 α sigma and lone pair IBOs. (a) Mn_1-O3, (b) Mn_2-O3, and (c) Mn_3-O3. (d) Lone pair. The identical contour β-forms are given in the Supporting Information. The model is taken from the lowest-energy BS state where Mn_1-4 are αββα, $M_S = 1/2$.

4.3.3.3 Mn^{III}/Mn^{IV}

We now analyse and discuss the Mn^{III}/Mn^{IV} **dioxo** and **dioxo-Ca** models and the Mn_1/Mn_2 bridge of the S_2-WOC. The COs are compared in Figure 4.8.

For the Mn^{III}/Mn^{IV} units, there is an extra magnetic orbital present, that is, Mn^{III} d_{z^2}. Compared with Mn^{IV}/Mn^{IV}, Figure 4.8;a shows that this leads to an additional magnetic orbital overlap of the d_{z^2}-orbital with the d_{xy}-orbital of Mn^{IV} for the **dioxo** model. The large value of the S-overlap suggests that this is one of the dominant superexchange pathways for **dioxo** in addition to the two π-pathways identified for the Mn^{IV}/Mn^{IV} bridges. This extra pathway also presumably accounts for a considerable increase in the J-value magnitude of 96 cm^{-1} compared with Mn^{IV}/Mn^{IV}. The interaction of an oxo with Ca^{2+}, Figure 4.8;b, reduces the S-value for one of the π-pathways in a similar fashion to that found for the Mn^{IV}/Mn^{IV} model above with a corresponding decrease in the J-value magnitude. For the Mn_1/Mn_2 bridge of the WOC, Figure 4.8;c indicates a significant reduction in the overlap integral value, S, for all pathways, except the oxo near the Ca^{2+} which remains similar to **dioxo-Ca**. The other π-pathway is apparently eliminated. The

bridge oxo here is again O3 of the WOC which we have shown above does not undergo π-bonding with the neighbouring manganese ions, and its overlap with the Mn magnetic orbitals is eliminated. This also apparently leads to a strong reduction in the S-value for the in-plane interaction. From the **dioxo-Ca** model, we can see that this overlap is not affected by the nearby Ca^{2+}. The reduction in its value in the WOC Mn_1/Mn_2 bridge is thus attributed to the μ_3 nature of the O3 bridging oxo.

4.3.3.4 Oxo Bridge Protonation

Recent reports have suggested that an O4 protonated form of the WOC could be responsible for the high-spin ($S = 5/2$ or $7/2$) form of the S_2-state.[43, 44] This high-spin form has for many years been attributed to a closed cubane form of the WOC[57] as opposed to the open form used here and the only form detected using X-ray crystallography.[27] Other models for the high-spin S_2-state have been proposed.[65, 66] A number of recent reports[26, 43, 44, 67–69] have presented arguments for and against these different models of the S_2 high-spin state, and the reader is referred to these for details on the merits of each proposed model. In Figure 4.9, we illustrate the effect of protonation of O4 on the COs.

As already reported by us,[44] protonation of O4 changes the J_{34}-value from

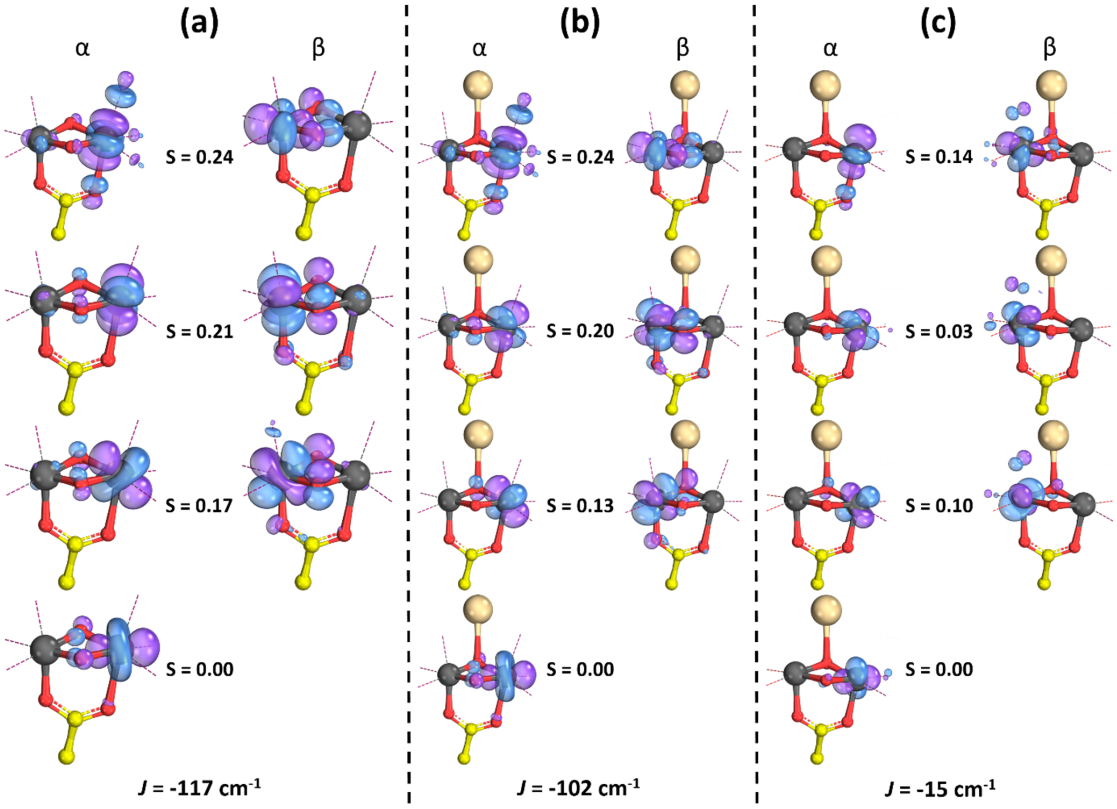

Figure 4.8: COs for (a) **dioxo**; (b) **dioxo-Ca**; and (c) S_2-WOC Mn_1/Mn_2 bridge, O3 at front, O1 at rear. S, overlap integral, values are given.

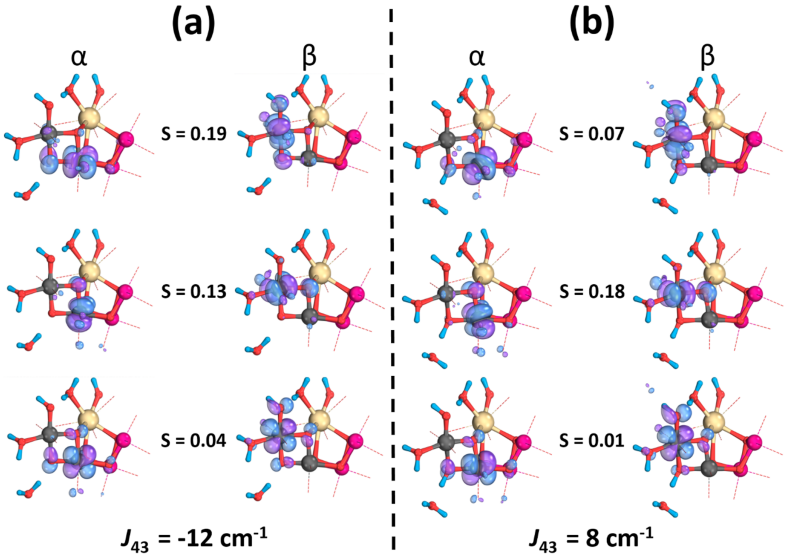

Figure 4.9: COs for (a) $Mn_3O4O5Mn_4$ and the (b) $Mn_3O4HO5Mn_4$ bridge. S, overlap integral, values are given.

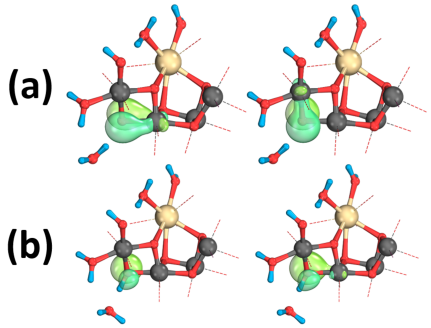

Figure 4.10: Effect of O4 protonation on π-bond IBOs for (a) O4 (the lowest-energy BS state where Mn_1-4 are αββα, $M_S = 1/2$) and (b) O4H (the lowest-energy BS state where Mn_1-4 are ααβα, $M_S = 5/2$). The α contour is shown on the left, and the β-contour is shown on the right.

antiferromagnetic -12 cm^{-1} to ferromagnetic +8 cm^{-1}. The CO analysis from Figure 4.9 shows that protonation of O4 reduces its S-value from 0.19 to 0.07, accounting for the change to ferromagnetic coupling between Mn_3 and Mn_4. This is also apparent from the IBOs shown in Figure 4.10 where the reduced π-overlap is apparent for the protonated form compared with deprotonated O4, Figure 4.10;a,b. The IBOs show that the protonation leads to three σ-bonds from O4 to the proton, Mn_3, and Mn_4 plus a pyramidal lone pair shown in Figure 4.10;b which effectively eliminates the π-superexchange pathway.

4.3.3.5 Nature of Ca^{2+} Bonds in the WOC

The analysis above provides insight into the nature of the Ca^{2+} bonds in the WOC. While the interaction of the bridging oxos, O5, O1, and O2 with Ca^{2+} does

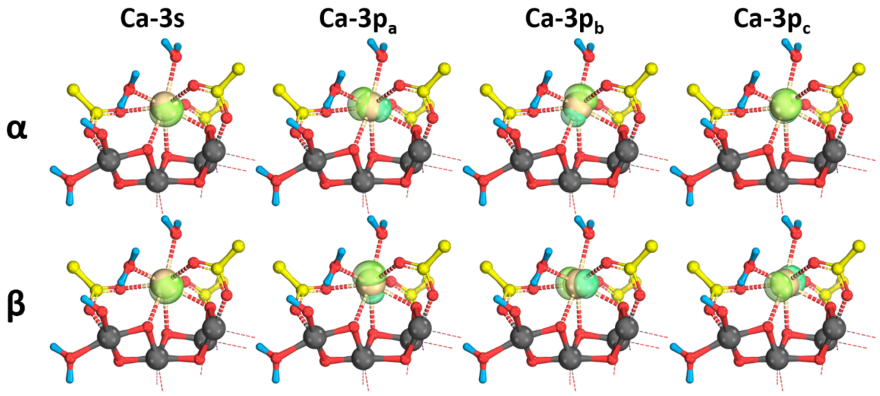

Figure 4.11: S_2-WOC Ca IBOs demonstrating the lack of covalent bond formation of its 3s and 3p valence orbitals.

reduce its S-value and the resulting superexchange, the effect is much smaller than that due to O3 perturbation by Mn-O bonding or indeed oxo protonation. This is due to the nature of the bonding involved. For Mn^{III}-O, Mn^{IV}-O, or O-H bonds, significant covalency is present as exemplified by the presence of σ- and π-bond IBOs. Ca^{2+} bonds in the WOC are by contrast all essentially ionic in nature. This is pictorially demonstrated by the lack of any bond IBOs to Ca^{2+} in the WOC where its valence 3s- and 3p-orbitals remain non-bonding, Figure 4.11.

This is also demonstrated by the partial charge and Mayer bond orders shown in Figure S4.6 and Table S4.2. Interactions with the O-atoms of its normally associated "ligands", W3, W4, O1, O2, O5, O6, D1-D170, D1-A344, and D1-E189, are purely ionic in nature. This leads to a non-directional nature of the Ca^{2+} oxygen interaction resulting in an ill-defined geometric shape and variable near neighbour interactions. While protonation of oxo bridges with covalent O-H bond formation effectively eliminates the π-pathway for superexchange, the ionic Ca^{2+} interaction has the less direct effect of decreasing the π-bond overlap. The ionic nature of the Ca^{2+} interactions is likely a key factor in the utility of the ion for the WOC function. XFEL structural studies of the S_3-state have shown that Ca^{2+} expands its coordination sphere by binding an additional oxygen O6[70] and positions it for O-O bond formation with O5. W3, a Ca^{2+} ligand, has additionally been proposed to be the source of O6 due to movement from its original position in the S_3-state.[71] In both scenarios, the ionicity and the resultant non-directional nature of the Ca-O bonding would be essential.

4.3.3.6 Conclusions

This study has provided a unique electronic-level view of the fundamental superexchange pathways used by Nature's WOC to electronically couple its four Mn ion magnetic centres. It reveals a dominating influence of both the WOC

geometrical structure and ionic interactions with the Ca^{2+} ion. While the study uses the S_2-state to exemplify these findings, similar scenarios can be demonstrated for the other S-states. Such an understanding is fundamental to understanding and interpreting the spectroscopic properties of the WOC. It is also fundamental to understanding the mechanism used by the WOC to facilitate low-barrier O-O bond formation.

References

[1] A. Guskov, J. Kern, A. Gabdulkhakov, M. Broser, A. Zouni, W. Saenger, *Nature Structural & Molecular Biology* **2009**, *16*, 334–342.

[2] A. Zouni, H.-T. Witt, J. Kern, P. Fromme, N. Krauss, W. Saenger, P. Orth, *Nature* **2001**, *409*, 739–743.

[3] M. Suga, F. Akita, K. Hirata, G. Ueno, H. Murakami, Y. Nakajima, T. Shimizu, K. Yamashita, M. Yamamoto, H. Ago, J.-R. Shen, *Nature* **2015**, *517*, 99–103.

[4] M. Ibrahim, T. Fransson, R. Chatterjee, M. H. Cheah, R. Hussein, L. Lassalle, K. D. Sutherlin, I. D. Young, F. D. Fuller, S. Gul, I.-S. Kim, P. S. Simon, C. de Lichtenberg, P. Chernev, I. Bogacz, C. C. Pham, A. M. Orville, N. Saichek, T. Northen, A. Batyuk, S. Carbajo, R. Alonso-Mori, K. Tono, S. Owada, A. Bhowmick, R. Bolotovsky, D. Mendez, N. W. Moriarty, J. M. Holton, H. Dobbek, A. S. Brewster, P. D. Adams, N. K. Sauter, U. Bergmann, A. Zouni, J. Messinger, J. Kern, V. K. Yachandra, J. Yano, *Proceedings of the National Academy of Sciences* **2020**, *117*, 12624–12635.

[5] J. Kern, R. Chatterjee, I. D. Young, F. D. Fuller, L. Lassalle, M. Ibrahim, S. Gul, T. Fransson, A. S. Brewster, R. Alonso-Mori, R. Hussein, M. Zhang, L. Douthit, C. de Lichtenberg, M. H. Cheah, D. Shevela, J. Wersig, I. Seuffert, D. Sokaras, E. Pastor, C. Weninger, T. Kroll, R. G. Sierra, P. Aller, A. Butryn, A. M. Orville, M. Liang, A. Batyuk, J. E. Koglin, S. Carbajo, S. Boutet, N. W. Moriarty, J. M. Holton, H. Dobbek, P. D. Adams, U. Bergmann, N. K. Sauter, A. Zouni, J. Messinger, J. Yano, V. K. Yachandra, *Nature* **2018**, *563*, 421–425.

[6] R. Hussein, M. Ibrahim, A. Bhowmick, P. S. Simon, R. Chatterjee, L. Lassalle, M. Doyle, I. Bogacz, I.-S. Kim, M. H. Cheah, S. Gul, C. de Lichtenberg, P. Chernev, C. C. Pham, I. D. Young, S. Carbajo, F. D. Fuller, R. Alonso-Mori, A. Batyuk, K. D. Sutherlin, A. S. Brewster, R. Bolotovsky, D. Mendez, J. M. Holton, N. W. Moriarty, P. D. Adams, U. Bergmann, N. K. Sauter, H. Dobbek, J. Messinger, A. Zouni, J. Kern, V. K. Yachandra, J. Yano, *Nature Communications* **2021**, *12*, 6531.

[7] A. Haddy, *Photosynthesis Research* **2007**, *92*, 357–368.

[8] *Biochimica et Biophysica Acta (BBA) - Bioenergetics* **2001**, *1503*, Photosynthetic water oxidation, 96–111.

[9] R. Britt, K. A. Campbell, J. M. Peloquin, M. Gilchrist, C. P. Aznar, M. M. Dicus, J. Robblee, J. Messinger, *Biochimica et Biophysica Acta (BBA) - Bioenergetics* **2004**, *1655*, 158–171.

[10] V. Krewald, M. Retegan, N. Cox, J. Messinger, W. Lubitz, S. DeBeer, F. Neese, D. A. Pantazis, *Chem. Sci.* **2015**, *6*, 1676–1695.

[11] V. Krewald, F. Neese, D. A. Pantazis, *Israel Journal of Chemistry* **2015**, *55*, 1219–1232.

[12] E. Ruiz, J. Cano, S. Alvarez, P. Alemany, *Journal of Computational Chemistry* **1999**, *20*, 1391–1400.

[13] V. Krewald, F. Neese, D. A. Pantazis, *Journal of the American Chemical Society* **2013**, *135*, 5726–5739.

[14] M. Orio, D. A. Pantazis, T. Petrenko, F. Neese, *Inorganic Chemistry* **2009**, *48*, 7251–7260.

[15] L. Rapatskiy, W. M. Ames, M. Pérez-Navarro, A. Savitsky, J. J. Griese, T. Weyhermüller, H. S. Shafaat, M. Högbom, F. Neese, D. A. Pantazis, N. Cox, *The Journal of Physical Chemistry B* **2015**, *119*, 13904–13921.

[16] D. A. Pantazis, M. Orio, T. Petrenko, S. Zein, W. Lubitz, J. Messinger, F. Neese, *Phys. Chem. Chem. Phys.* **2009**, *11*, 6788–6798.

[17] W. Ames, D. A. Pantazis, V. Krewald, N. Cox, J. Messinger, W. Lubitz, F. Neese, *Journal of the American Chemical Society* **2011**, *133*, PMID: 22092013, 19743–19757.

[18] N. Cox, L. Rapatskiy, J.-H. Su, D. A. Pantazis, M. Sugiura, L. Kulik, P. Dorlet, A. W. Rutherford, F. Neese, A. Boussac, W. Lubitz, J. Messinger, *Journal of the American Chemical Society* **2011**, *133*, 3635–3648.

[19] T. A. Corry, F. Rummel, P. J. O'Malley, *The Journal of Physical Chemistry B* **2021**, *125*, 7147–7154.

[20] G. Renger, *Biochimica et Biophysica Acta (BBA) - Bioenergetics* **2012**, *1817*, 1164–1176.

[21] D. A. Pantazis, *ACS Catalysis* **2018**, *8*, 9477–9507.

[22] K. Umena, Yasufumi and Kawakami, J.-R. Shen, N. Kamiya, *Nature* **2011**, *473*, 55–60.

[23] M. Suga, F. Akita, K. Hirata, G. Ueno, H. Murakami, Y. Nakajima, T. Shimizu, K. Yamashita, M. Yamamoto, H. Ago, J.-R. Shen, *Nature* **2015**, *517*, 99–103.

[24] J. Kern, R. Chatterjee, I. D. Young, F. D. Fuller, L. Lassalle, M. Ibrahim, S. Gul, T. Fransson, A. S. Brewster, R. Alonso-Mori, R. Hussein, M. Zhang, L. Douthit, C. de Lichtenberg, M. H. Cheah, D. Shevela, J. Wersig, I. Seuffert, D. Sokaras, E. Pastor, C. Weninger, T. Kroll, R. G. Sierra, P. Aller, A. Butryn, A. M. Orville, M. Liang, A. Batyuk, J. E. Koglin, S. Carbajo, S. Boutet, N. W. Moriarty, J. M. Holton, H. Dobbek, P. D. Adams, U. Bergmann, N. K. Sauter, A. Zouni, J. Messinger, J. Yano, V. K. Yachandra, *Nature* **2018**, *563*, 421–425.

[25] M. Suga, F. Akita, K. Yamashita, Y. Nakajima, G. Ueno, H. Li, T. Yamane, K. Hirata, Y. Umena, S. Yonekura, L.-J. Yu, H. Murakami, T. Nomura, T. Kimura, M. Kubo, S. Baba, T. Kumasaka, K. Tono, M. Yabashi, H. Isobe, K. Yamaguchi, M. Yamamoto, H. Ago, J.-R. Shen, *Science* **2019**, *366*, 334–338.

[26] R. Chatterjee, L. Lassalle, S. Gul, F. D. Fuller, I. D. Young, M. Ibrahim, C. de Lichtenberg, M. H. Cheah, A. Zouni, J. Messinger, V. K. Yachandra, J. Kern, J. Yano, *Physiologia Plantarum* **2019**, *166*, 60–72.

[27] M. Ibrahim, T. Fransson, R. Chatterjee, M. H. Cheah, R. Hussein, L. Lassalle, K. D. Sutherlin, I. D. Young, F. D. Fuller, S. Gul, I.-S. Kim, P. S. Simon, C. de Lichtenberg, P. Chernev, I. Bogacz, C. C. Pham, A. M. Orville, N. Saichek, T. Northen, A. Batyuk, S. Carbajo, R. Alonso-Mori, K. Tono, S. Owada, A. Bhowmick, R. Bolotovsky, D. Mendez, N. W. Moriarty, J. M. Holton, H. Dobbek, A. S. Brewster, P. D. Adams, N. K. Sauter, U. Bergmann, A. Zouni, J. Messinger, J. Kern, V. K. Yachandra, J. Yano, *Proceedings of the National Academy of Sciences* **2020**, *117*, 12624–12635.

[28] K. M. Davis, B. T. Sullivan, M. C. Palenik, L. Yan, V. Purohit, G. Robison, I. Kosheleva, R. W. Henning, G. T. Seidler, Y. Pushkar, *Phys. Rev. X* **2018**, *8*, 041014.

[29] K. Yamaguchi, S. Yamanaka, H. Isobe, T. Saito, K. Kanda, Y. Umena, K. Kawakami, J. Shen, N. Kamiya, M. Okumura, H. Nakamura, M. Shoji, Y. Yoshioka, *International Journal of Quantum Chemistry* **2013**, *113*, 453–473.

[30] N. J. Beal, T. A. Corry, P. J. O'Malley, *The Journal of Physical Chemistry B* **2017**, *121*, 11273–11283.

[31] S. Schinzel, M. Kaupp, *Canadian Journal of Chemistry* **2009**, *87*, 1521–1539.

[32] S. Sinnecker, F. Neese, L. Noodleman, W. Lubitz, *Journal of the American Chemical Society* **2004**, *126*, 2613–2622.

[33] V. Krewald, M. Retegan, F. Neese, W. Lubitz, D. A. Pantazis, N. Cox, *Inorganic Chemistry* **2016**, *55*, 488–501.

[34] S. Sinnecker, F. Neese, W. Lubitz, *JBIC Journal of Biological Inorganic Chemistry* **2005**, *10*, 231–238.

[35] J. E. McGrady, R. Stranger, *Journal of the American Chemical Society* **1997**, *119*, 8512–8522.

[36] C. D. Delfs, R. Stranger, *Inorganic Chemistry* **2001**, *40*, 3061–3076.

[37] D. A. Pantazis, V. Krewald, M. Orio, F. Neese, *Dalton Trans.* **2010**, *39*, 4959–4967.

[38] G. Knizia, *Journal of Chemical Theory and Computation* **2013**, *9*, 4834–4843.

[39] A. T. Amos, G. G. Hall, H. Jones, *Proceedings of the Royal Society of London. Series A. Mathematical and Physical Sciences* **1961**, *263*, 483–493.

[40] F. Neese, *Journal of Physics and Chemistry of Solids* **2004**, *65*, 781–785.

[41] F. Neese, *Coordination Chemistry Reviews* **2009**, *253*, 526–563.

[42] K. Yamaguchi, H. Isobe, M. Shoji, S. Yamanaka, M. Okumura, *Molecular Physics* **2016**, *114*, 519–546.

[43] T. A. Corry, P. J. O'Malley, *Journal of the American Chemical Society* **2020**, *142*, 10240–10243.

[44] T. A. Corry, P. J. O'Malley, *The Journal of Physical Chemistry Letters* **2019**, *10*, 5226–5230.

[45] F. Neese, *WIREs Computational Molecular Science* **2018**, *8*, e1327.

[46] A. D. Becke, *Phys. Rev. A* **1988**, *38*, 3098–3100.

[47] J. P. Perdew, *Phys. Rev. B* **1986**, *33*, 8822–8824.

[48] E. v. Lenthe, E. J. Baerends, J. G. Snijders, *The Journal of Chemical Physics* **1993**, *99*, 4597–4610.

[49] E. van Lenthe, E. J. Baerends, J. G. Snijders, *The Journal of Chemical Physics* **1994**, *101*, 9783–9792.

[50] C. van Wüllen, *The Journal of Chemical Physics* **1998**, *109*, 392–399.

[51] F. Weigend, R. Ahlrichs, *Phys. Chem. Chem. Phys.* **2005**, *7*, 3297–3305.

[52] K. Eichkorn, O. Treutler, H. Öhm, M. Häser, R. Ahlrichs, *Chemical Physics Letters* **1995**, *242*, 652–660.

[53] K. Eichkorn, F. Weigend, O. Treutler, R. Ahlrichs, *Theoretical Chemistry Accounts* **1997**, *97*, 119–124.

[54] S. Grimme, J. Antony, S. Ehrlich, H. Krieg, *The Journal of Chemical Physics* **2010**, *132*.

[55] S. Grimme, S. Ehrlich, L. Goerigk, *Journal of Computational Chemistry* **2011**, *32*, 1456–1465.

[56] F. Weigend, *Phys. Chem. Chem. Phys.* **2006**, *8*, 1057–1065.

[57] D. A. Pantazis, W. Ames, N. Cox, W. Lubitz, F. Neese, *Angewandte Chemie International Edition* **2012**, *51*, 9935–9940.

[58] N. Cox, M. Retegan, F. Neese, D. A. Pantazis, A. Boussac, W. Lubitz, *Science* **2014**, *345*, 804–808.

[59] V. N. Staroverov, G. E. Scuseria, J. Tao, J. P. Perdew, *The Journal of Chemical Physics* **2003**, *119*, 12129–12137.

[60] F. Neese, F. Wennmohs, A. Hansen, U. Becker, *Chemical Physics* **2009**, *356*, 98–109.

[61] F. Neese, *WIREs Computational Molecular Science* **2012**, *2*, 73–78.

[62] D. A. Pantazis, M. Orio, T. Petrenko, S. Zein, E. Bill, W. Lubitz, J. Messinger, F. Neese, *Chemistry - A European Journal* **2009**, *15*, 5108–5123.

[63] W. Ames, D. A. Pantazis, V. Krewald, N. Cox, J. Messinger, W. Lubitz, F. Neese, *Journal of the American Chemical Society* **2011**, *133*, 19743–19757.

[64] C. J. Stein, D. A. Pantazis, V. Krewald, *The Journal of Physical Chemistry Letters* **2019**, *10*, 6762–6770.

[65] Y. Pushkar, A. K. Ravari, S. C. Jensen, M. Palenik, *The Journal of Physical Chemistry Letters* **2019**, *10*, 5284–5291.

[66] P. E. M. Siegbahn, *Phys. Chem. Chem. Phys.* **2018**, *20*, 22926–22931.

[67] R. Chatterjee, G. Han, J. Kern, S. Gul, F. D. Fuller, A. Garachtchenko, I. D. Young, T.-C. Weng, D. Nordlund, R. Alonso-Mori, U. Bergmann, D. Sokaras, M. Hatakeyama, V. K. Yachandra, J. Yano, *Chem. Sci.* **2016**, *7*, 5236–5248.

[68] H. Mino, H. Nagashima, *The Journal of Physical Chemistry B* **2020**, *124*, 128–133.

[69] S. Taguchi, T. Noguchi, H. Mino, *The Journal of Physical Chemistry B* **2020**, *124*, 5531–5537.

[70] M. Suga, F. Akita, M. Sugahara, M. Kubo, Y. Nakajima, T. Nakane, K. Yamashita, Y. Umena, M. Nakabayashi, T. Yamane, T. Nakano, M. Suzuki, T. Masuda, S. Inoue, T. Kimura, T. Nomura, S. Yonekura, L.-J. Yu, T. Sakamoto, T. Motomura, J.-H. Chen, Y. Kato, T. Noguchi, K. Tono, Y. Joti, T. Kameshima, T. Hatsui, E. Nango, R. Tanaka, H. Naitow, Y. Matsuura, A. Yamashita, M. Yamamoto, O. Nureki, M. Yabashi, T. Ishikawa, S. Iwata, J.-R. Shen, *Nature* **2017**, *543*, 131–135.

[71] C. J. Kim, R. J. Debus, *Biochemistry* **2017**, *56*, 2558–2570.

4.3.4 Supporting Information

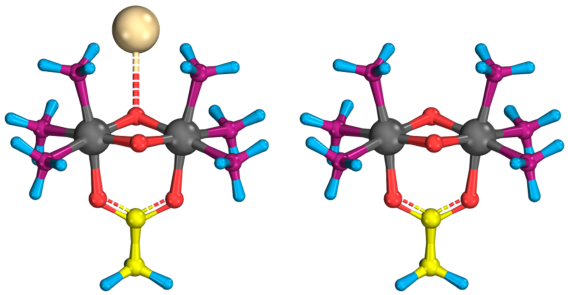

Figure S4.1: **Dioxo** (right) and **dioxo-Ca** (left) models used. H: blue, C: yellow, Ca: cream, Mn: grey, N: magenta, O: red. Z axis direction defined as along Mn-OAcetate bond.

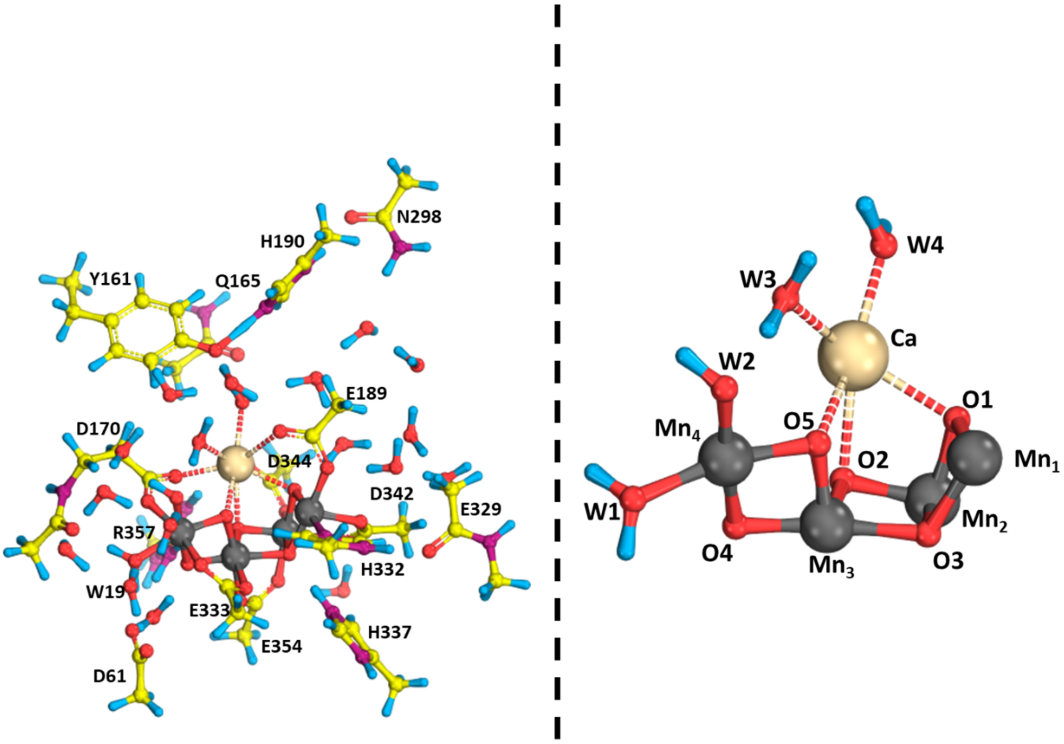

Figure S4.2: WOC model used on left with core structure of WOC on right. Protonation may vary depending on the model, some hydrogens are omitted for clarity. H: blue, C: yellow, Ca: cream, Mn: grey, N: magenta, O: red.

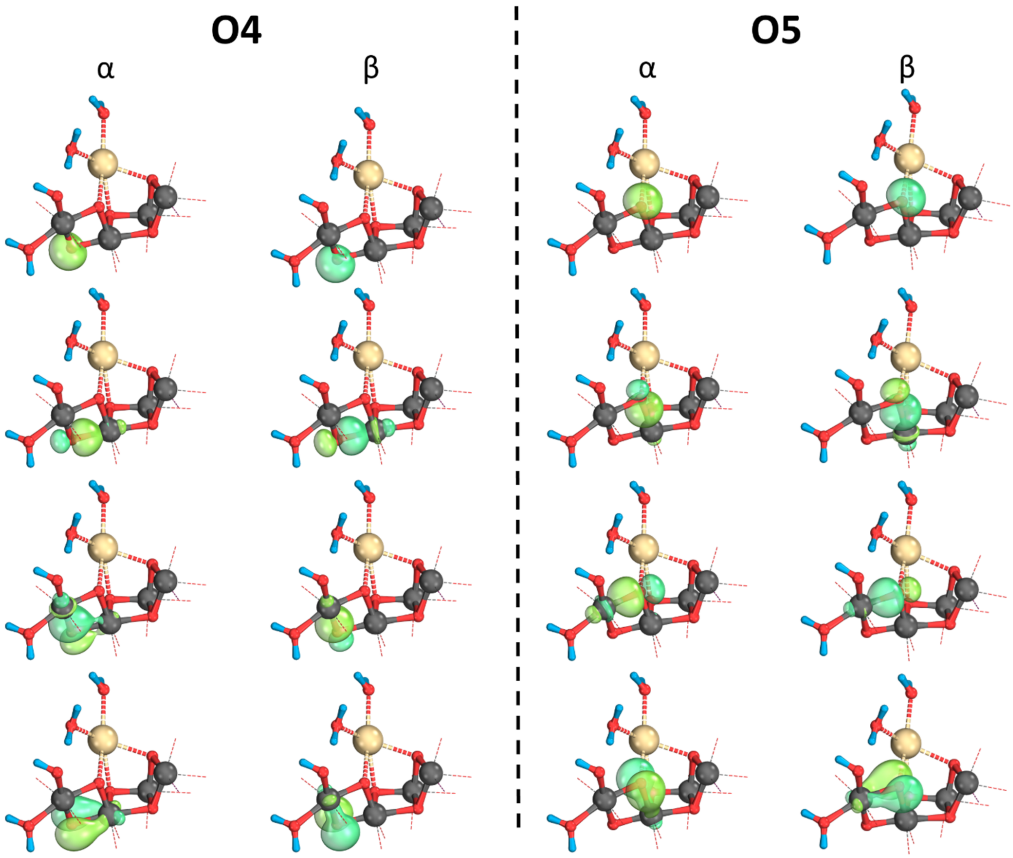

Figure S4.3: O4 and O5 based IBOs for WOC Mn_3/Mn_4 bridge. Both have two σ-bonds, one lone pair and one π-bond IBO.

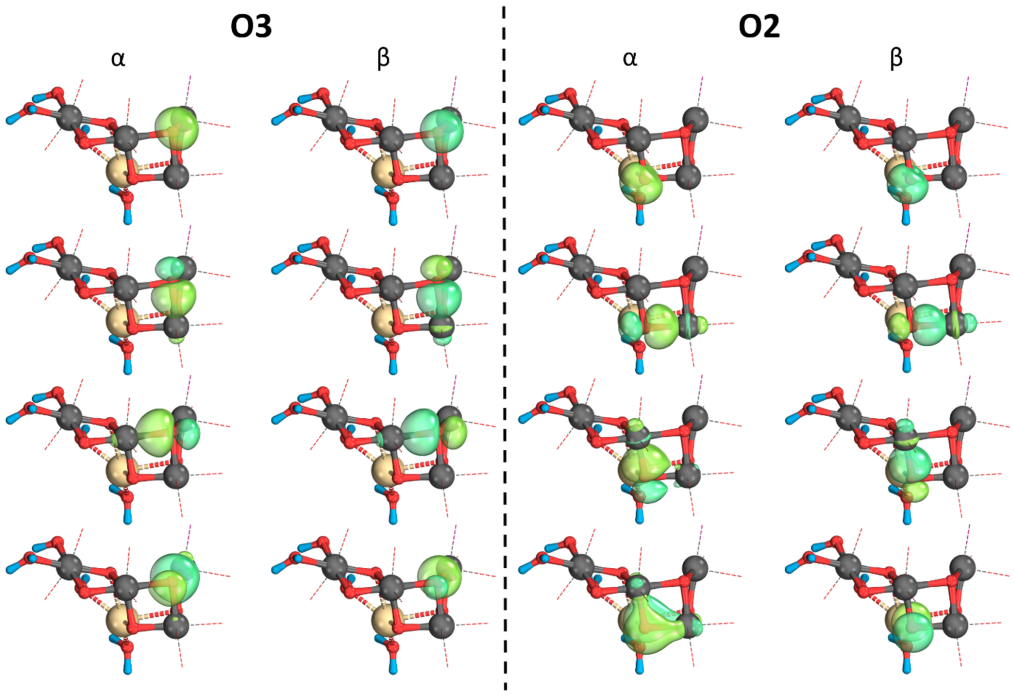

Figure S4.4: O3 and O2 IBOs for WOC Mn_2/Mn_3 bridge. O3 has three σ-bond and one lone pair IBO. O2 has two σ-bond, one lone pair and one π-bond IBO.

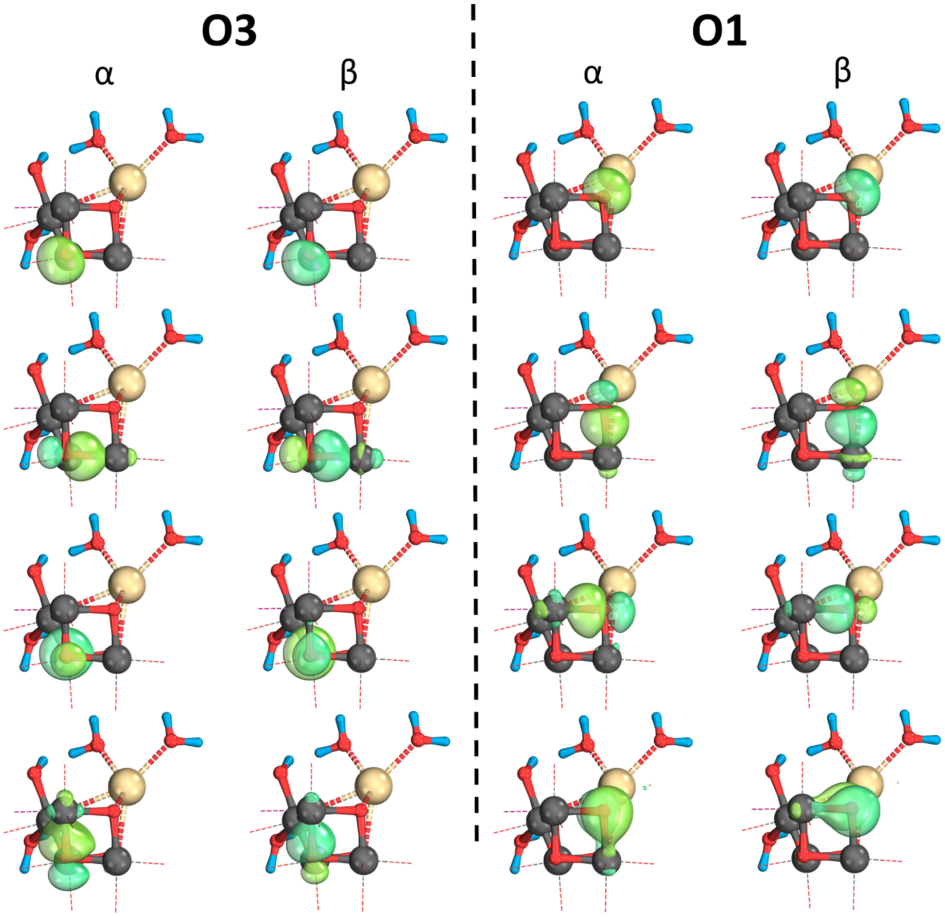

Figure S4.5: O3 and O1 IBOs for WOC Mn_1/Mn_2 bridge. O3 has three σ-bond and one lone pair IBO. O1 has two σ-bond, one lone pair and one π-bond IBO.

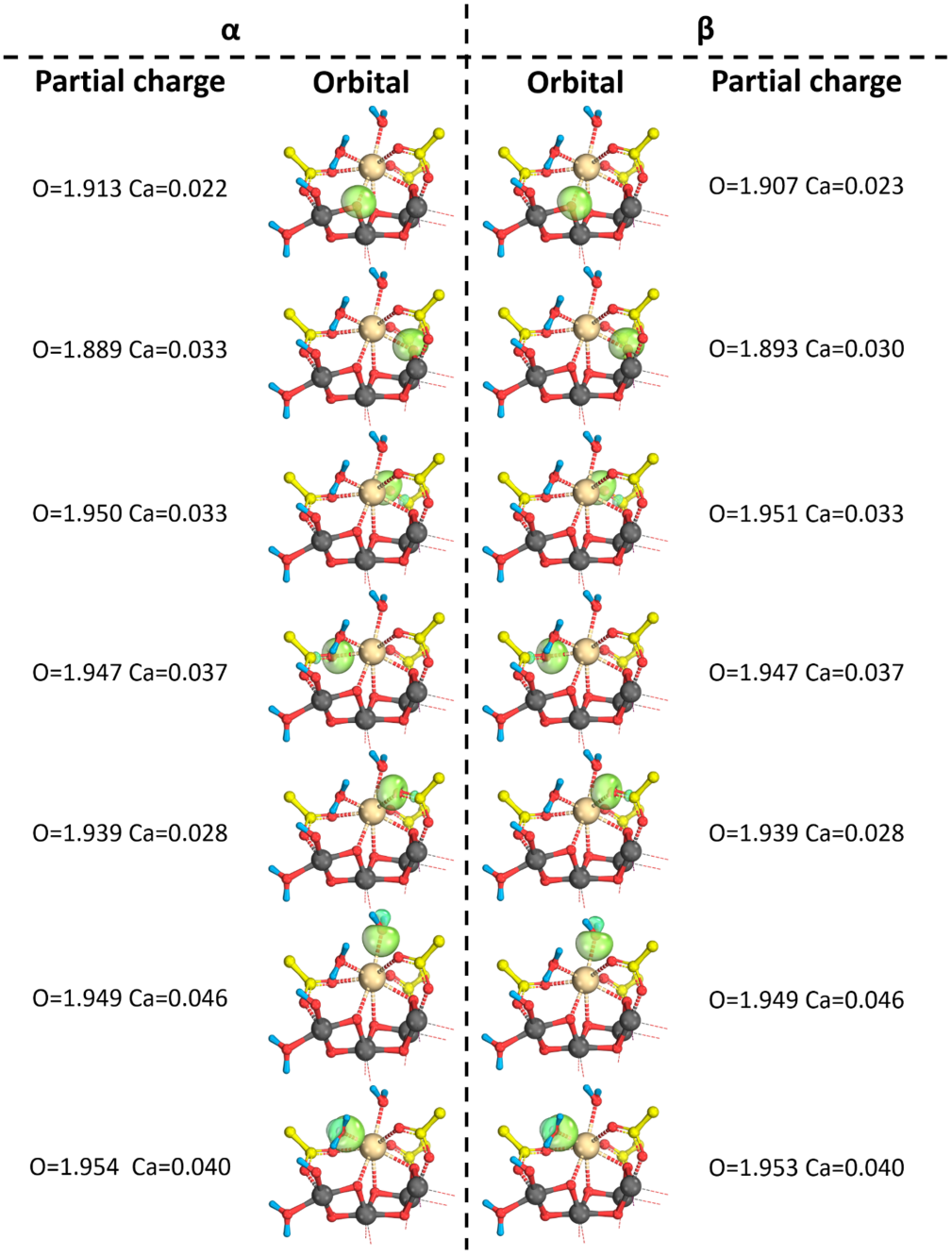

Figure S4.6: Ca^{2+} ion IBOs and partial charges.

Table S4.1: Comparison of J values, in cm^{-1}, for the intact Mn_4 WOC model cluster and its Ge, Ga substituted form. O4 protonated form, O4H, in brackets.

	Complete Mn_4 Cluster	GeGa substituted
J_{43}	-15(5)	-12(8)
J_{32}	18	20
J_{21}	-18	-15

Table S4.2: Ca^{2+} ion Mayer bond orders > 0.1.

Bond	Mayer Bond Order
Ca–D1-E189	0.12
Ca–D1-A344	0.12
Ca–W3	0.12

4.3.4.1 Coordinates

Mn(III)Mn(IV)$CaC_2N_6H_{21}O_4$

N -3.54216 1.46866 2.911479
Mn -2.68702 -0.05224 4.056522
N -4.59482 -0.15428 5.377808
O -0.9691 0.041336 2.471277
C 0.216454 0.052297 2.867111
O 0.587901 0.024432 4.116794
Mn -0.5659 -0.05321 5.66395
O -1.6712 -1.30312 5.001606
C 1.356888 0.069404 1.877852
O -1.72974 1.182299 5.081314
N -3.46419 -1.53424 2.807658
H 2.222363 0.607746 2.280774
H 1.661858 -0.97081 1.686355
H 1.029907 0.51422 0.931657
N 0.756852 -1.53295 6.361273
N 0.687283 1.438126 6.456581
N -1.51104 -0.13224 7.486741
H -4.43673 -1.42169 2.509207
H -2.88952 -1.58573 1.960709
H -3.39316 -2.44473 3.271152

H -3.49314 2.352368 3.426784
H -2.98926 1.591338 2.057384
H -4.51664 1.33713 2.627551
H -4.58206 -1.00439 5.947997
H -4.61947 0.636178 6.027861
H -5.49289 -0.15057 4.886204
H 1.155902 -1.42078 7.297097
H 0.275496 -2.43693 6.340223
H 1.539798 -1.59444 5.703247
H -0.90757 -0.18365 8.311867
H -2.10104 0.699011 7.582347
H -2.12097 -0.95448 7.493704
H 1.50973 1.525561 5.852096
H 0.186275 2.330653 6.413128
H 1.023723 1.322961 7.4162
Ca -2.94553 -2.68521 6.780301

Mn(IV)Mn(IV)CaC$_2$N$_6$H$_{21}$O$_4$

N -3.49044 1.435615 2.893256
Mn -2.56543 -0.0501 3.994565
N -4.21648 -0.13673 5.172347
O -1.14733 0.035959 2.680286
C 0.098726 0.051562 2.97061
O 0.546422 0.028451 4.16927
Mn -0.57632 -0.0559 5.742937
O -1.6798 -1.28659 4.988326
C 1.085558 0.070316 1.850529
O -1.74762 1.161936 5.073927
N -3.41041 -1.50584 2.793459
H 1.97844 0.634803 2.140978
H 1.385859 -0.97032 1.650947
H 0.63053 0.484676 0.945402
N 0.711225 -1.52317 6.42503
N 0.641079 1.424317 6.520859
N -1.53143 -0.13862 7.531093
H -4.4098 -1.40891 2.589228
H -2.92016 -1.52646 1.892841
H -3.27731 -2.42563 3.226862
H -3.41771 2.327593 3.393865

H -2.99628 1.552423 2.002274
H -4.48025 1.292333 2.671359
H -4.21119 -0.99909 5.726873
H -4.23122 0.656564 5.821604
H -5.10244 -0.11719 4.657108
H 1.160841 -1.35005 7.329277
H 0.21803 -2.41926 6.497662
H 1.461139 -1.65059 5.737029
H -0.90618 -0.258 8.334498
H -2.0692 0.719253 7.692105
H -2.18425 -0.92894 7.542573
H 1.50237 1.486099 5.967467
H 0.164491 2.328287 6.433261
H 0.919379 1.324434 7.501802
Ca -3.12169 -2.67905 6.625348

Mn(III)Mn(IV)$C_2N_6H_{21}O_4$

N -3.54216 1.46866 2.911479
Mn -2.68702 -0.05224 4.056522
N -4.59482 -0.15428 5.377808
O -0.9691 0.041336 2.471277
C 0.216454 0.052297 2.867111
O 0.587901 0.024432 4.116794
Mn -0.5659 -0.05321 5.66395
O -1.6712 -1.30312 5.001606
C 1.356888 0.069404 1.877852
O -1.72974 1.182299 5.081314
N -3.46419 -1.53424 2.807658
H 2.222363 0.607746 2.280774
H 1.661858 -0.97081 1.686355
H 1.029907 0.51422 0.931657
N 0.756852 -1.53295 6.361273
N 0.687283 1.438126 6.456581
N -1.51104 -0.13224 7.486741
H -4.43673 -1.42169 2.509207
H -2.88952 -1.58573 1.960709
H -3.39316 -2.44473 3.271152
H -3.49314 2.352368 3.426784
H -2.98926 1.591338 2.057384

H -4.51664 1.33713 2.627551
H -4.58206 -1.00439 5.947997
H -4.61947 0.636178 6.027861
H -5.49289 -0.15056 4.886204
H 1.155902 -1.42078 7.297097
H 0.275496 -2.43693 6.340223
H 1.539798 -1.59444 5.703247
H -0.90757 -0.18365 8.311867
H -2.10104 0.699011 7.582347
H -2.12097 -0.95448 7.493704
H 1.50973 1.525561 5.852096
H 0.186275 2.330653 6.413128
H 1.023723 1.322961 7.4162

Mn(IV)Mn(IV)$C_2N_6H_{21}O_4$

N -3.49044 1.435615 2.893256
Mn -2.56543 -0.0501 3.994565
N -4.21648 -0.13673 5.172347
O -1.14733 0.035959 2.680286
C 0.098726 0.051562 2.97061
O 0.546422 0.028451 4.16927
Mn -0.57632 -0.0559 5.742937
O -1.6798 -1.28659 4.988326
C 1.085558 0.070316 1.850529
O -1.74762 1.161936 5.073927
N -3.41041 -1.50584 2.793459
H 1.97844 0.634803 2.140978
H 1.385859 -0.97032 1.650947
H 0.63053 0.484676 0.945402
N 0.711225 -1.52317 6.42503
N 0.641079 1.424317 6.520859
N -1.53143 -0.13862 7.531093
H -4.4098 -1.40891 2.589228
H -2.92016 -1.52646 1.892841
H -3.27731 -2.42563 3.226862
H -3.41771 2.327593 3.393865
H -2.99627 1.552423 2.002274
H -4.48025 1.292333 2.671359
H -4.21119 -0.99909 5.726873

H -4.23122 0.656564 5.821604
H -5.10244 -0.11719 4.657108
H 1.160841 -1.35005 7.329277
H 0.21803 -2.41926 6.497662
H 1.461139 -1.65059 5.737029
H -0.90618 -0.258 8.334498
H -2.0692 0.719253 7.692105
H -2.18425 -0.92894 7.542573
H 1.50237 1.486099 5.967467
H 0.164491 2.328287 6.433261
H 0.919379 1.324434 7.501802

Chapter 5

How Nature makes O_2: an Electronic Level Mechanism for Water Oxidation in Photosynthesis

Authors: Felix Rummel and Patrick J. O'Malley

Address: School of Chemistry, The University of Manchester, Manchester, M139PL, U.K.

Published at: *J. Phys. Chem. B*, **2022**, 126, 8214-8221

DOI: https://pubs.acs.org/doi/full/10.1021/acs.jpcb.2c06374

5.1 Preface

The final stable intermediate in the Kok cycle is the S_3 state, directly preceding molecular oxygen bond formation and release. Just before the S_3 state is formed a new water molecule (O6) is inserted into the Mn cluster, this can be identified experimentally, and has been proposed to be one of the reactions substrate molecules (see section 1.2.4). The final flash forms a transient S_4 state, which rapidly returns to the most reduced S_0 state, simultaneously producing molecular oxygen (see section 1). While experimentally the S_4 state remains experimentally inaccessible the S_3 state has been studied more extensively using both crystallographic methods and EPR spectroscopy.[1–5] However the nature of the S_3 state and the sequence of events leading to oxygen bond formation is still subject to much discussion (see section 1.2.3 and 1.2.4)

EPR studies have concluded that the S_3 signal can be attributed to an $S = 3$ O5 oxo-O6 hydroxo species.[6] While other species have been proposed to also be present in the S_3 state, such as O5 oxo-O6 oxyl.[2, 7, 8] Furthermore while the EPR suggests an oxo-hydroxo species, the O5-O6 separation obtained from crystallographic experiments do not agree with this and suggest a shorter O5-O6 separation of ≈ 2 Å.[1, 2]

Here we report a PES for the S_3 state, following proposed early onset O-O bond formation[9], and identify a new species in the S_3 state, an $[O5O6]^{3-}$ species. The electronic structures of the PES species is presented and analysed. It is shown that heterogeneity in the S_3 state can better rationalise experimental (EPR and crystallographic) data.

5.2 Abstract

In this paper, we combine broken symmetry density functional calculations and electron paramagnetic resonance analysis to obtain the electronic structure of the penultimate S_3 state of nature's water-oxidizing complex and determine the electronic pathway of O-O bond formation. Analysis of the electronic structure changes along the reaction path shows that two spin crossovers, facilitated by the geometry and magnetism of the water-oxidizing complex, are used to provide a unique low-energy pathway. The pathway is facilitated via the formation and stabilization of the $[O_2]^{3-}$ ion. This ion is formed between ligated deprotonated substrate waters, O5 and O6, and is stabilized by antiferromagnetic interaction with the Mn ions of the complex. Combining the computational, crystallographic, and spectroscopic data, we show that an equilibrium exists between the O5 oxo and O6 hydroxo forms with an $S = 3$ spin state and a deprotonated O6 form containing a two-centre one-electron bond in $[O5O6]^{3-}$ which we identify as the form detected using crystallography. This form corresponds to an $S = 6$ spin state which we demonstrate gives rise to a low-intensity EPR spectrum compared with the accompanying $S = 3$ state, making its detection via EPR difficult and overshadowed by the $S = 3$ form. Simulations using 70 % of the $S = 6$ component give rise to a superior fit to the experimental W-band EPR spectral envelope compared with an $S = 3$ only form. Analyses of the most recent X-ray emission spectroscopy first moment changes for solution and time-resolved crystal data are also shown to support the model. The computational, crystallographic, and spectroscopic data are shown to coalesce to the same picture of a predominant $S = 6$ species containing the first one-electron oxidation product of two water molecules, that is, $[O5O6]^{3-}$. Progression of this form to the two-electron-oxidized peroxo and three-electron-oxidized superoxo forms, leading eventually to the evolution of triplet O_2, is proposed to be the pathway nature adopts to oxidize water. The study reveals the key electronic, magnetic, and structural design features of nature's catalyst which facilitates water oxidation to O_2 under ambient conditions.

5.3 Manuscript *J. Phys. Chem. B*, 2022, 126, 8214-8221.

5.3.1 Introduction

Every oxygen molecule we breathe is produced from two water molecules in the photosystem II protein complex of higher plants, algae, and cyanobacteria. This highly endothermic reaction is carried out during photosynthesis using visible light energy under ambient conditions. To perform this task, a unique water-oxidizing catalytic complex, $Mn_4CaO_{5/6}$, evolved some 3 billion years ago. This complex

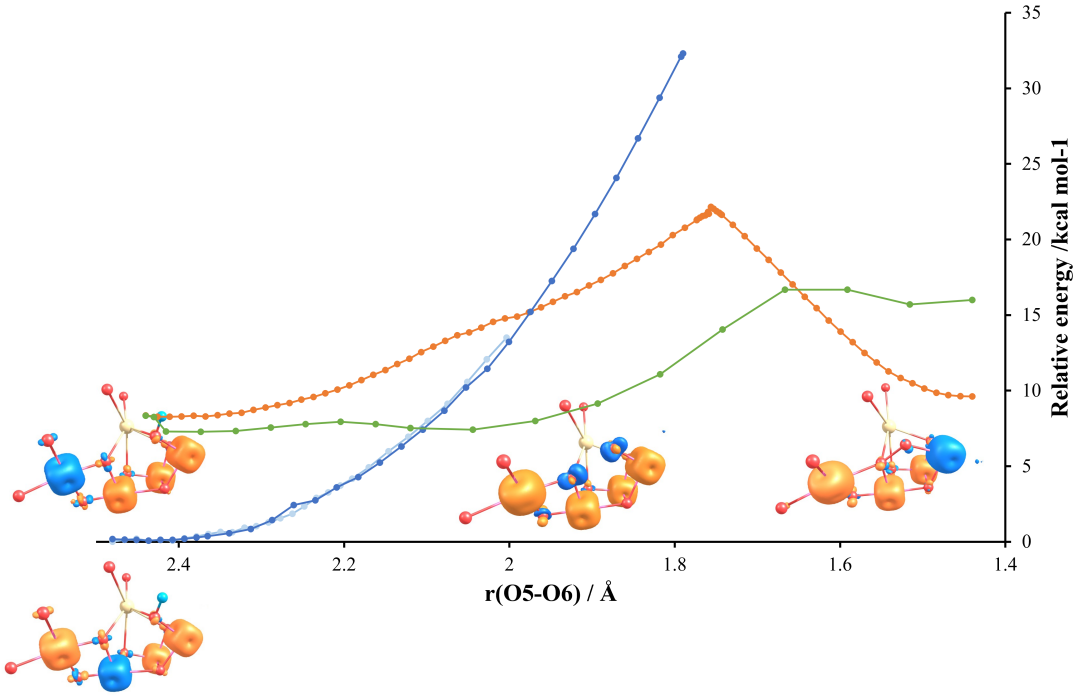

Figure 5.1: Table of Content graphic adapted from *J. Phys. Chem. B*, **2022**, 126, 8214-8221.[10]

oxidizes two water molecules to molecular oxygen at a rate approaching 1000 s^{-1} at ambient temperature and pressure.[9, 11] Besides being one of the most important reactions in biology, it is also of intense interest from a green energy perspective, where it is recognized to be the main barrier to the development of commercial solar devices for the generation of hydrogen from water.[12] Water oxidation to dioxygen is challenging due to the high endergonicity (E° = 0.82 V (vs NHE) at pH 7) of the reaction and the associated need to remove four protons and four electrons with the formation of an oxygen-oxygen, O-O, bond. Two broad mechanistic proposals, water nucleophilic attack of metal oxo and direct metal oxo radical coupling, have been proposed for artificial water oxidation catalysis (WOC).[13] Somewhat similar proposals have been put forward for WOC, namely water nucleophilic attack[14] or oxyl radical-oxo coupling[15] These require the generation of a reactive oxo species in the final Kok cycle S_4 state. Artificial catalysts generally use very high-strength oxidizing agents to generate reactive oxo species, either radical oxygen species or highly charged metal electrophilic species. WOC on the other hand is limited to the approximately 1 V oxidizing power of the nearby tyrosyl radical, Y_Z^{OX}.[16] The current mechanisms for WOC which propose the generation of a reactive "hot" oxo species in the S_4 state need to explain how such a species can be generated when the oxidizing capability from the visible light energy available via the $S_3Y_Z^{OX}$ oxidant is around 1V. It is also unclear how triplet O_2 can be produced from the peroxo form with such a mechanism given that the last oxidizing equivalent has been used.

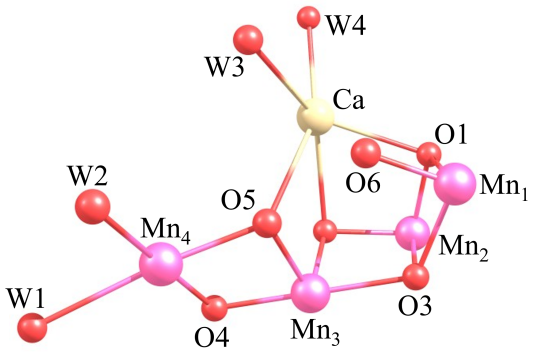

Figure 5.2: WOC catalyst core structure with orientation and numbering scheme used throughout.

$$2H_2O \rightarrow O_2 + 4H^+ + 4e^- \tag{5.1}$$

An alternative mechanistic scenario is the dynamic equilibrium model of S_3 speculated by Renger,[9] consisting of a concerted reduction of Mn coupled to O-O bond formation.[17, 18] Such a mechanism would aesthetically require the WOC cluster design, Figure 5.2, to facilitate the lowering of the O-O bond formation barrier, permitting it to be readily transversed at room temperature without the generation of a reactive oxo form.

For the four-electron oxidation of two water molecules in the aqueous phase,[9] Figure S5.2 it is the first one-electron oxidation of water to form an oxyl radical that represents the major energy barrier with a reduction potential $\geq$ 2 V, well in excess of the 1 V available in $S_3Y_Z^{OX}$. If the WOC can reduce this barrier, then the sequential four-electron oxidation of water is thermodynamically feasible with visible light energy. Here, we demonstrate that the WOC is designed to achieve this task by stabilizing the one-electron oxidation product of water as an $[O2]^{3-}$ ion. Partial O-O bond formation and stabilization of this species are brought about by the unique architecture and magnetism of WOC, which facilitate the electron rearrangement between the O5 and O6 oxo forms engaged in O-O bond formation and the Mn_1 and Mn_4 ions of the WOC. This is combined with the stabilising antiferromagnetic alignment of the $Mn_{1,3,4}$ ions with the unpaired electron of $[O5O6]^{3-}$. This stabilizes nascent O-O bond formation in the S_3 state, permitting low-barrier O-O bond formation, and is supported by the XFEL structural crystallographic data and by the EPR spectra obtained on the 2-flash state of the WOC.

5.3.2 Results and Discussion

5.3.2.1 Electronic Structure Analysis

Our starting point on the pathway to O5-O6 bond formation is an O5 oxo-O6 hydroxo form of the WOC complex, Figure 5.2, formed after the initial formation of the S_3 state. This corresponds to the $S = 3$ form detected by EPR with four Mn (IV) ions.[6] O6 corresponds to the new oxygen atom detected by XFEL upon S_3 state formation.[1, 2] For this oxo-hydroxo model, seven broken symmetry, Ms, states are possible at the optimized geometry. We have shown[6] that two of these, both Ms = 3, $[Mn_4(\downarrow\downarrow\downarrow)Mn_3(\uparrow\uparrow\uparrow)Mn_2(\uparrow\uparrow\uparrow)Mn_1(\uparrow\uparrow\uparrow)]$ and $[Mn_4(\uparrow\uparrow\uparrow)Mn_3(\downarrow\downarrow\downarrow)Mn_2(\uparrow\uparrow\uparrow)Mn_1(\uparrow\uparrow\uparrow)]$, are the lowest in energy and govern the spin density of the complex, resulting in a spin populations of close to 3.0 for Mn_1-Mn_4 combining this with the spin expectation values yields a spin distribution of around 0.5, 0.5, 0.0 and 0.0 for Mn_1-Mn_4. This explains the set of two large (Mn_1 and Mn_2)- and two small (Mn_3 and Mn_4)-magnitude ^{55}Mn hfcs observed using EDNMR spectroscopy.[6, 19] Deprotonation of O6 leads to an O5 oxo-O6 oxo form. At the optimized geometry, two low energy BS states are found, an Ms = 3 form $[Mn_4(\uparrow\uparrow\uparrow)Mn_3(\uparrow\uparrow\uparrow)Mn_2(\uparrow\uparrow\uparrow)Mn_1(\downarrow\downarrow\downarrow)]$ and an Ms = 6 form $[Mn_4(\uparrow\uparrow\uparrow)Mn_3(\uparrow\uparrow\uparrow)Mn_2(\uparrow\uparrow\uparrow)Mn_1(\uparrow\uparrow\uparrow)]$. The energies of these oxo-hydroxo and oxo-oxo states are plotted as a function of O5-O6 distance in Figure 5.3. The oxo-hydroxo form is the lowest energy form for O5-O6 distances of 2.5-2.1 Å.

At 2.1 Å, the Ms = 6 oxo-oxo form is indicated to be energetically most favourable. For the Ms = 3 oxo-oxo form, the crossover with the oxo-hydroxo PES occurs at a higher energy, at an O5-O6 distance of 2.0 Å. The Ms = 6 state remains the lowest energy form up to an O5-O6 distance of 1.65 Å where the Ms = 3 state becomes more favourable as peroxo is formed. At O5-O6 distances less than 2.0 Å, the oxo-hydroxo form becomes unstable, and convergence is not achievable. The PES scan in Figure 5.3 shows that two PES crossovers, facilitated by the unique geometry and magnetism of the WOC complex, provide a low-energy pathway for O5-O6 peroxo bond formation. To monitor the changes in electronic configuration and rationalize the relative energies of the different BS states as we traverse the PES, we monitor the changes in the intrinsic localized bond orbitals involved. These changes are demonstrated for the oxo-oxo Ms = 6 and the oxo-oxo Ms = 3 states in Figures 5.4 and 5.5, respectively.

For the oxo-hydroxo form, no changes are found in the IBOs in the region of 2.5-2.0 Å, and as mentioned above, this model becomes unstable at bond distances less than 2.0 Å. By contrast, significant changes are observed for both oxo-oxo forms. The IBOs which undergo significant changes are located by monitoring the root-mean-square deviation of every IBO from the initial partial charge distribution along the PES.[20, 21] Figures 5.4 and 5.5 identify four main IBOs participating in bond-making and bond-breaking during the reaction. These are the α and β spin

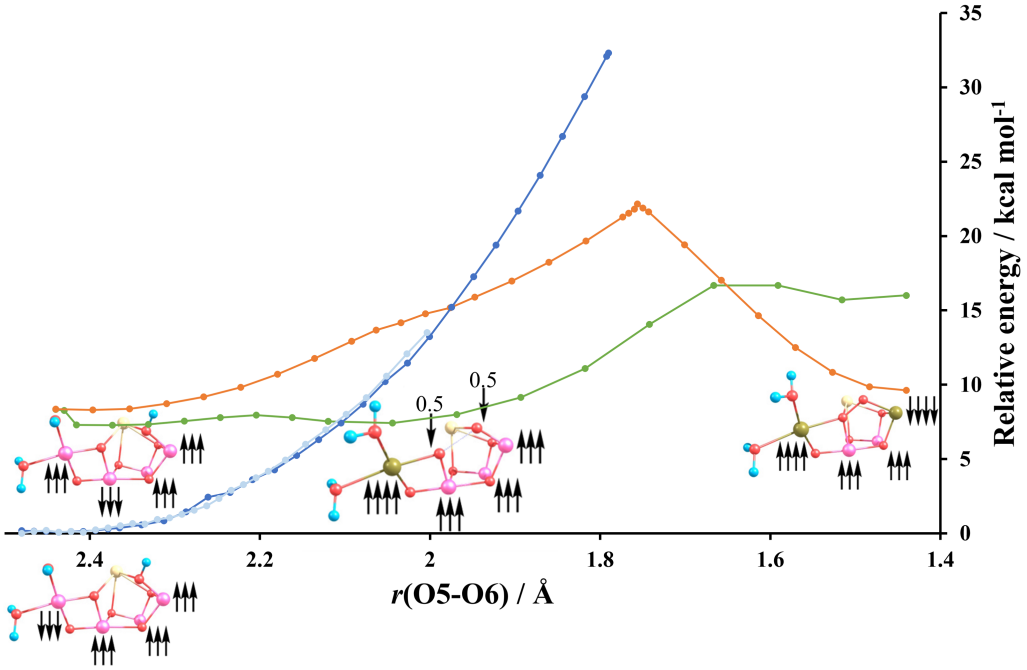

Figure 5.3: S_3 state potential energy scans (PES) for oxo-hydroxo (Mn_3 flipped, dark blue; Mn_4 flipped, light blue), oxo-oxo (Ms = 3, red), and oxo-oxo (Ms = 6, green) forms. The spin alignments for the local energy minima along the PES are illustrated. Each line represents a PES for a specific BS form, with a fixed O5-O6 distance.

orbitals of the Mn_4-O5 σ-bond, the β spin orbital of the Mn_1-O6 σ-bond, and the α spin orbital of one of the π-bonding lone-pair orbitals on O6. As the O5-O6 bond distance is decreased from the nonbonded oxo-oxo form, the α electron density of the Mn_4-O5 σ-bond evolves into a d_z^2 orbital on Mn_4, Figures 5.4 and 5.5 (pink), at an O5-O6 bond distance of around 2.2 Å for Ms = 6 and 2.0 Å for Ms = 3. Concurrently, with this electron density rearrangement, the α density of the π-lone pair on O6 evolves to a σ-bond between the O6 and O5 oxygens, Figures 5.4 and 5.5 (blue). A Mayer bond order analysis,[22] Figure S5.3, also illustrates such a change with a decrease in the Mn_4-O5 bond order from near 1.0 to near 0.5 and an increase in the O5-O6 bond order from 0.0 to near 0.4. In a similar fashion, Mulliken spin population analysis, Figure S5.4, shows a change in the spin population of Mn_4 from near 3.0 to 4.0, signalling a reduction from Mn_4(IV) to Mn_4(III). For the Ms = 3 state, further progression along the PES shows that the β-electron of the Mn_4-O5 σ-bond evolves to become the β-component of the O5-O6 σ-bond, Figure 5.5 (yellow), and the Mn_1-O6 σ-bond β-electron density evolves into a dz^2 orbital on Mn_1, Figure 5.5 (green). For Ms = 6, the β-electron of the Mn_4-O5 σ-bond again evolves to become the β-component of the O5-O6 σ-bond, Figure 5.4 (yellow), while in this case, a Mn_1-O6 π-bond β-electron density evolves into a dπ orbital on Mn_1, Figure 5.4 (green). Mulliken spin populations, Figure S5.4, correspondingly show an increase in spin population from 3 to 4 for Mn_1, illustrating the reduction of

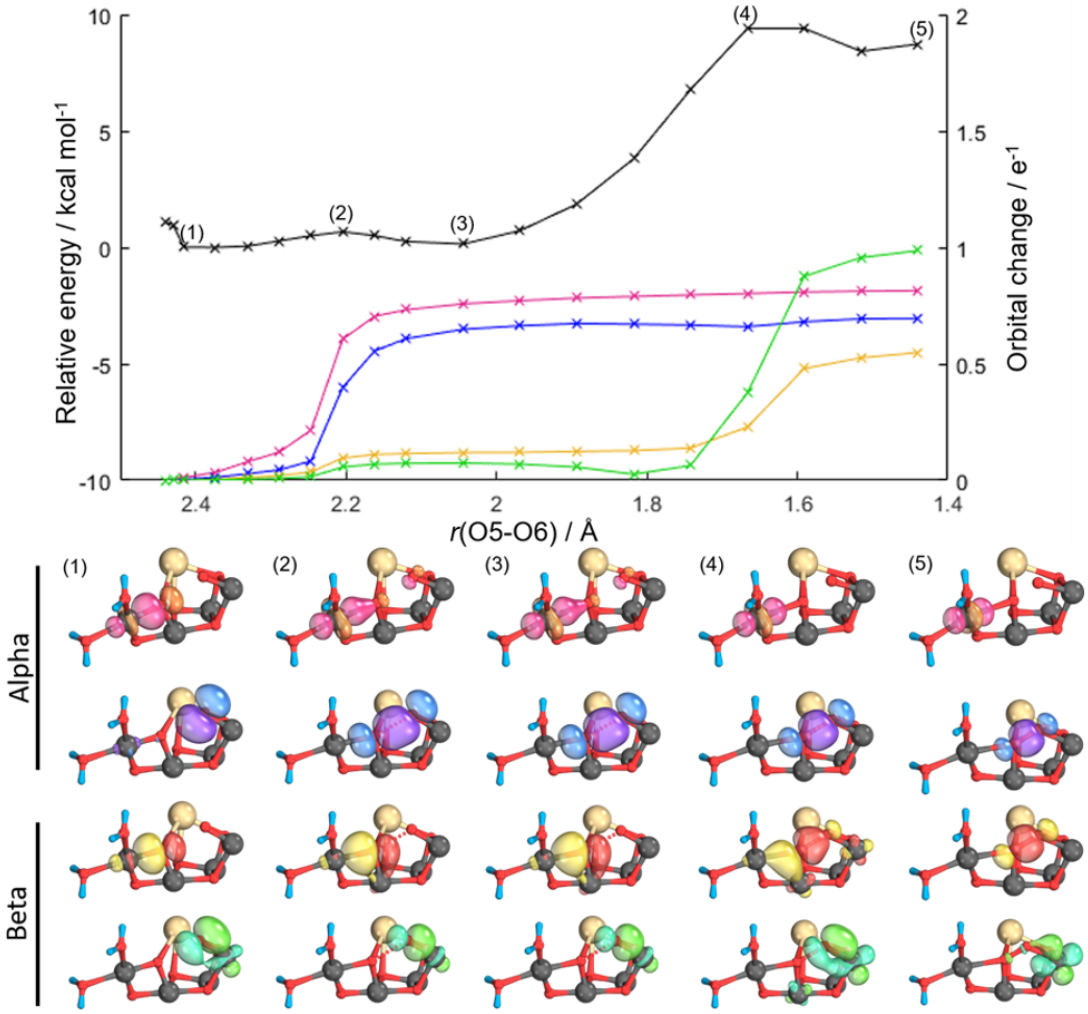

Figure 5.4: Intrinsic bond orbital (IBO) analysis of the Ms = 6 state of the oxo-oxo form. Top, potential energy surface (PES) for O5-O6 bond formation (black) accompanying IBO changes color-coded by the orbitals shown beneath. Representative IBOs are given at the points labelled on the PES above showing α and β spin evolution; see text for details.

Mn_1 to high-spin Mn(III) for Ms = 3, whereas for Ms = 6, the electron transfer of a β-electron to Mn_1 results in the occupation of a dπ orbital, Figure 5.4 (green), resulting in a spin population of 2 and corresponding to a low-spin form of Mn(III). The Mayer bond order values for both Ms states of Figure S5.3 show an increase in the O5-|O6 bond order to near 1.0 as the peroxo is formed.

Our key finding is that for the Ms = 6 oxo-oxo form, an electronic state corresponding to $Mn_4(\uparrow\uparrow\uparrow\uparrow)Mn_3(\uparrow\uparrow\uparrow)Mn_2(\uparrow\uparrow\uparrow)Mn_1(\uparrow\uparrow\uparrow)$[O5O6]($\downarrow$) is found as a shallow local minimum at an O5-O6 distance of 2.0 Å. The IBOs, Figure 5.4, show that electron movement has occurred from O5 to Mn_4, leading to a high-spin Mn_4 (III) and the formation of a nascent two-centre one-electron O5-O6 bond. This species was identified previously by us[7] as a shoulder on the Ms = 3 state (see Figure 5.5). While a shoulder on the Ms = 3 PES, it corresponds to a broad minimum energy

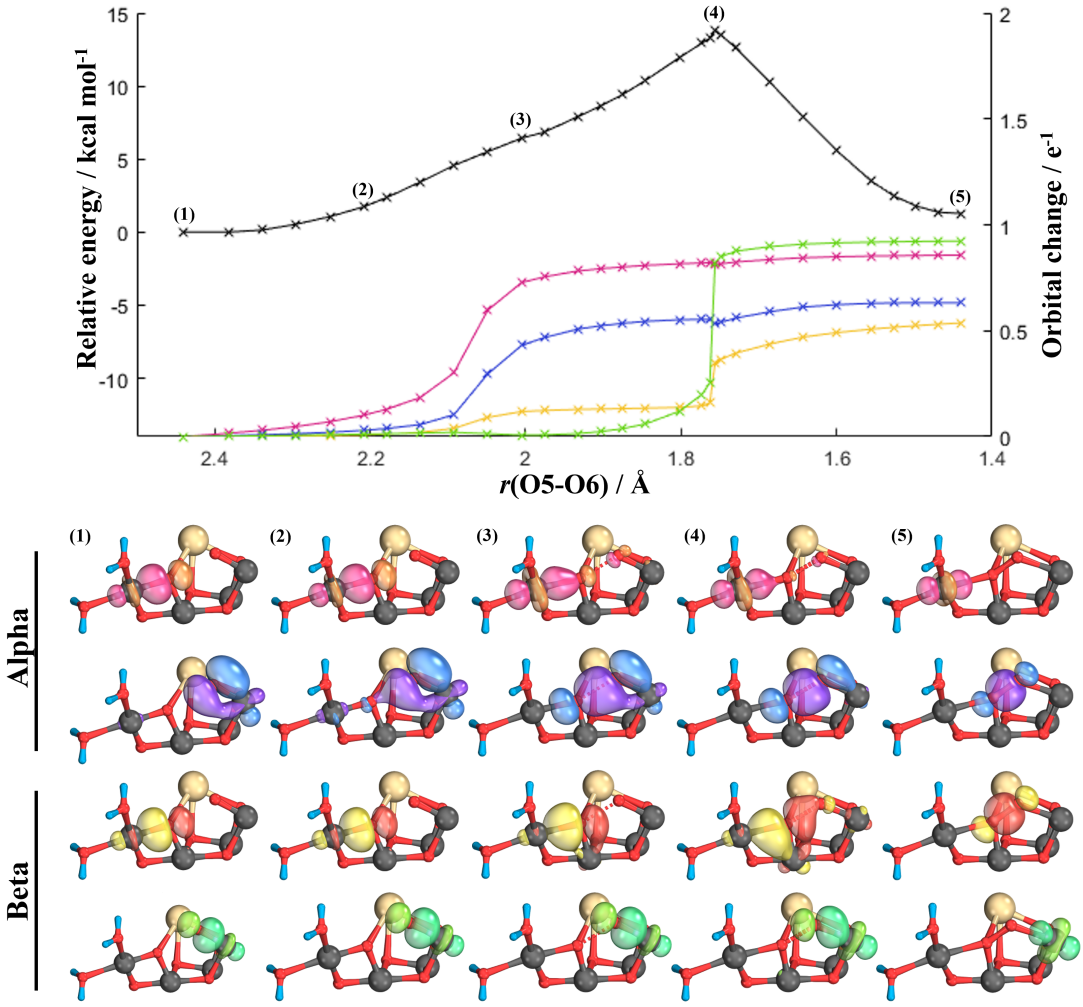

Figure 5.5: Intrinsic bond orbital (IBO) analysis of the Ms = 3 state of the oxo-oxo form. Top, potential energy surface (PES) for O5-O6 bond formation (black) accompanying IBO changes color-coded by the orbitals shown beneath. Representative IBOs are given at the points labelled on the PES above showing α and β spin evolution; see text for details.

structure on the Ms = 6 surface due to the favorable antiferromagnetic coupling with all four Mn ions. We note that this species has been referred by us[7] and others[2, 8] previously as an O5 oxo-O6 oxyl form, but it is best and more appropriately described as $[O5O6]^{3-}$ as a negative spin density is present on both O5 and O6, clearly demonstrated by the spin density plot for this form in Figure 5.6. This Ms = 6 state is stabilized by the strong antiferromagnetic interaction occurring between the β-electron density shared between O5 and O6 and the α-electron spins on the Mn_1, Mn_3, and Mn_4 ions. The strength of this antiferromagnetic coupling is quantitatively demonstrated by the large magnitude $O5O6Mn_1$, $O5O6/Mn_3$, and $O5O6/Mn_4$ J values calculated for this electronic arrangement (see Table S5.1) and also graphically illustrated by the large overlap integral value S calculated for the corresponding locally transformed Mn and O5O6 magnetic orbitals in Figure 5.7.

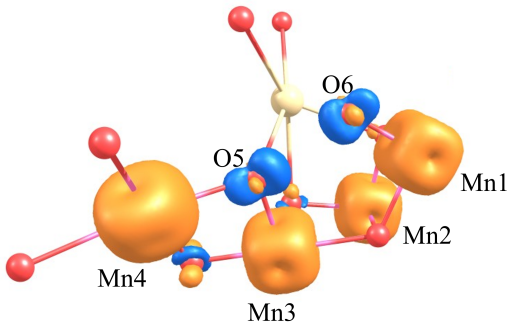

Figure 5.6: Spin density contour plot for the Ms = 6 oxo-oxo model at 2.0 Å on the PES, demonstrating the distribution of negative spin density (blue) on both O5 and O6 positions and signifying the presence of $[O5O6]^{3-}$.

The overlap integral value S is a measure of the strength of the orbital overlap and associated antiferromagnetic coupling between the magnetic orbitals on each of the Mn ions and the O5O6 magnetic orbital. The representation also demonstrates clearly the σ^*_{2p} nature of the magnetic orbital for O5O6 and the nature of its bonding with the Mn ions of the complex. This orbital interacts in a σ-bonding fashion with the Mn_4 ion d-orbitals and has π-bonding interactions with the d-orbitals of Mn_3 and Mn_1. No significant overlap is found for the Mn_2 ion.

Our PES and IBO analyses therefore show that low-barrier O-O bond formation is facilitated in the WOC. The WOC allows for a concerted flow of electrons between the coupling oxo's, O5/O6, and the Mn_1/Mn_4 ions providing low-barrier

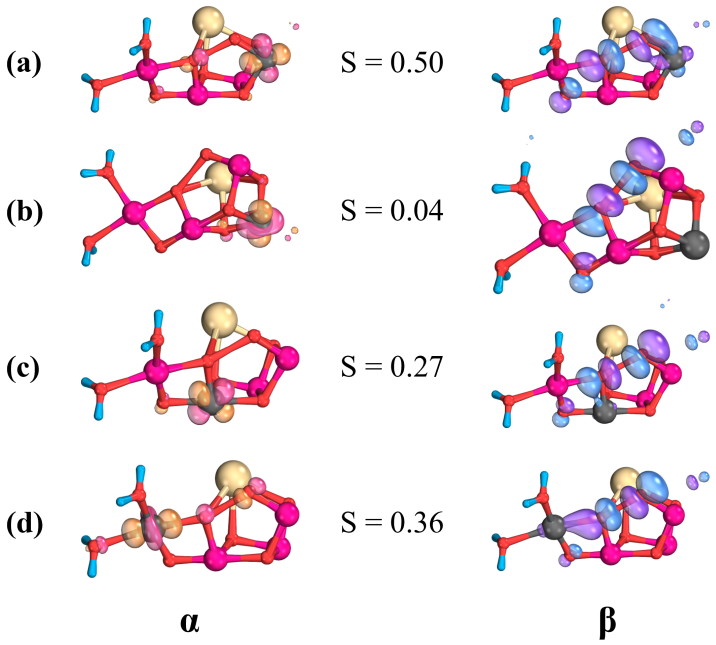

Figure 5.7: Corresponding magnetic orbitals for (a) Mn_1-O5O6, (b) Mn_2-O5O6, (c) Mn_3-O5O6, and (d) Mn_4-O5O6.

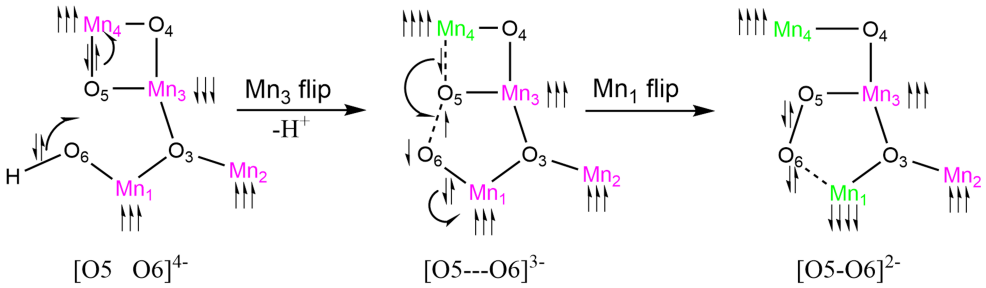

Figure 5.8: Schematic electron flow pattern based on our PES and IBO analyses from Figures 5.4 and 5.5. O5-O6 oxidation status indicated.

PES crossovers. Figure 5.8 demonstrates the key electron movements and spin flips involved. Figure S5.5 uses a simple molecular orbital scheme to illustrate the species involved with the concerted flow of electron from the σ^*_{2p} orbital to Mn_1 and Mn_4 during the O-O bond formation, permitting the formation of the O-O bond without double occupation of the high-energy orbital.

5.3.2.2 Crystallographic and Electron Paramagnetic Resonance Analysis

Studies using X-ray free electron laser (XFEL) atomic resolution structures of the 2-flash state, predominantly S_3 state, generally support the participation of O5 and O6 in O-O bond formation. Suga et al.[23] first reported an O5-O6 bond distance of 1.5 Å, indicating peroxo formation.[17, 24] Later studies proposed an additional oxygen O_x similar to O6 of the structure reported by Suga et al. but with an extended O5-O6/O_x bond length of 2.1 Å.[1, 25, 26] More recently, Suga et al.[2] proposed a best fit O5-O6 bond length of 1.9 Å. All structures of S_3 so far appear to rule out an oxo-hydroxo nonbonded form which requires an O5-O6 bond separation of at least 2.5 Å. Additional structural features are a relatively long Mn_4-O5 bond length of 2.2 Å and a short Mn_1-O6 bond distance of 1.7 Å. Comparison of our calculated minimum energy Ms = 6 structure with the experimental determinations is given in Table 5.1. This demonstrates excellent agreement with the minimum energy point of this state and the experimental XFEL values supporting the presence of $[O5O6]^{3-}$. In addition, recent time-resolved structural changes for the S_3 state formation show significant increases (0.2-0.4 Å) in the Mn_4-W2, Mn_4-Glu333, (Mn-O) bond distances at the 150 µs time point.[26] Both would indicate a reduction of Mn_4 from IV to III, supporting the formation of $[O5O6]^{3-}$.

The interpretation of the $S = 3$ signal EPR from the 2-flash state based on the BS-DFT analysis of the calculated hfcs is highly indicative of an oxo-hydroxo form for the S_3 state.[4, 6, 27] An oxo-hydroxo model is not however compatible

Table 5.1: Comparison of key calculated minimum energy structure bond distances (Å) and experimental XFEL determinations. XFEL bond distances reported are an average from both a and A chains of the deposited crystal structures.

	O5-O6	Mn_4-O5	Mn_3-O5	Mn_1-O6	Mn_4-Mn_3	Mn_3-Mn_2	Mn_2-Mn_1	Mn_1-Mn_3	Mn_4-Mn_1
$[O5O6]^{3-}$	2.0	2.1	1.8	1.7	2.8	2.8	2.8	3.4	5.2
Kern 2018[1]	2.1	2.2	2.0	1.8	2.8	2.9	2.8	3.3	5.1
Kern 2019[2]	1.9	2.2	1.9	1.7	3.0	2.7	2.5	3.4	5.3

with the structure obtained by XFEL. As described above, the $[O5O6]^{3-}$ model does agree with the XFEL structures. This corresponds to a broken symmetry Ms = 6 spin state. This is not a true spin state, S. The true spin state energies can be obtained by the diagonalization of the Heisenberg Dirac van Vleck Hamiltonian using J values obtained by analysing all possible BS states.[28] Table S5.1 shows the calculated J values and energies of the ground spin states using this procedure. From this, an $S = 6$ spin state is calculated to be the ground-state spin. This, therefore, cannot be attributed to the species observed by EPR/EDNMR, which has an $S = 3$ ground-state spin. The PES shows that the two species are related by the protonation state of O6. Intriguingly, an $S = 6$ species was proposed to be formed in the 2-flash S_3 state of spinach samples and was proposed to be the major component (80%) of native samples.[5] The $S = 6$ form was attributed to the so-called closed cubane form of the WOC cluster with a penta-coordinated Mn_4 (IV) ion formed before the second substrate binds. So far, no structural experimental support for such a closed cubane structure of the WOC has been obtained for any S state.[25] It is therefore more likely (see below) that this species corresponds to the $[O5O6]^{3-}$ form alluded to in this manuscript, also with $S = 6$. Experimentally, no $S = 6$ species has so far been reported in cyanobacteria samples, where the high-resolution high-field W-band EPR spectra obtained are attributed to an $S = 3$ form.[19] Simulations of the W-band EPR spectra for the $S = 3$ form are shown in Figure 5.9. Also shown are simulations for an $S = 6$ form using the zero-field splitting parameters reported for the spinach samples.[5] From the simulations, it is clear that the spectral intensity of the $S = 6$ form is much less than that of the $S = 3$ form. This suggests that the $S = 6$ form would be difficult to detect in the W-band EPR experiment. More intriguingly, as shown in Figure 5.9, even with a 70% contribution of the $S = 6$ form, the $S = 3$ form still dominates the spectral envelope, with the $S = 6$ form mainly contributing a distinctive shoulder at around 3500-4000 mT to the overall spectral shape.

It is clear from the spectra presented in Figure 3 of Chrysina et al.[19] that a poorer fit between the experimental and a simulated $S = 3$ spectrum exists in

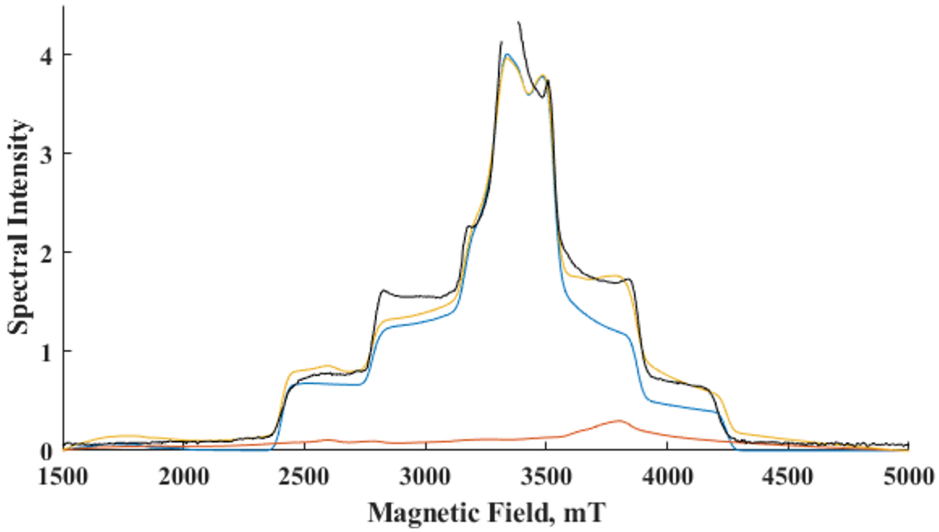

Figure 5.9: Comparison of 94 GHz EPR spectral simulations of $S = 6$ (red), $S = 3$(blue), and a 0.7:0.3 mixture of $S = 6$:S $= 3$ (yellow). The experimental spectrum from Chrysina et al.[19] is shown in black. Simulation parameters used are $S = 6$, $g = 2$, $D = 1.523$ cm^{-}1, $E/D = 0.14$ and $S = 3$, $g = 2$, $D = 0.179$ cm^{-}1, $E/D = 0.28$.

this very region. Figure 5.9 shows that the inclusion of the $S = 6$ form (70%) gives rise to a much improved fit to the experimental spectrum. Additional simulations performed by varying the ratio of the two spin systems are presented in Figures SS5.6 where we can estimate that an $S = 6$ contribution between 60 and 70% is optimal. We therefore suggest that the seeming incompatibility between the XFEL and EPR data for the S3 state lies in the fact that the oxo-hydroxo and $[O2]^{3-}$ forms are in equilibrium. The $[O2]^{3-}$ form detected in the XFEL-determined structure is not readily apparent in the EPR spectrum due to its $S = 6$ nature and the resultant low intensity compared with the $S = 3$ form. Further simulations presented in Figure S5.7 suggest that the $S = 6$ component is also likely a major component of the broadened W-band EPR spectrum caused by methanol and glycerol addition.13 It has been known for some time that the $S = 3$ species does not correspond to all of the S3 spin and that an EPR-"undetectable" component observed only on near-infrared (NIR) irradiation is also present in equilibrium with it.[29, 30] In our analysis, this undetectable component corresponds to the $[O2]^{3-}$ form. This is a different assignment to that previously made for the $S = 6$ form detected in spinach samples where the $S = 6$ form was attributed to a closed cubane form of the WOC cluster with a penta-coordinated Mn_4 (IV) ion, an intermediate formed prior to the binding of the second substrate water.[5] This, however, in striking contrast to the model proposed here, is not supported by the XFEL structural data.[26] In addition, it has been shown that Mn(III) is required for NIR excitation,[31] and the large D value of 1.523 cm^{-1} for the $S = 6$ form strongly suggests the presence of

Mn(III) ion in the complex. It should be noted that it is possible that the peroxo form, Figure 5.3, is also present in a low concentration, and its EPR spectrum is masked by the oxo-hydroxo form. The peroxo complex would have two Mn(III) ions present, likely leading to a large D value similar to the $[O2]^{3-}$ form which would again lead to a low-intensity EPR spectrum compared with the oxo-hydroxo form.

5.3.2.3 X-ray Emission Spectroscopy Analysis

Further experimental support for our S_3 state model comes from the analysis of the X-ray emission spectroscopy (XES) data by Ibrahim et al..[26] The 1F flash first moment XES shift can be confidently assigned to Mn (III) to Mn (IV) oxidation of Mn_4. The first moment shift for the S_3 state is approximately 40% of the 1F shift based on the solution-phase data[26] and the most current time-resolved crystal data (see Figure S5.9). In addition, at least 10% of the oxidation change shift can be attributed to S_1-to-S_2 oxidation based on the S state populations of the 1F state reported by Ibrahim et al.,[26] leaving around 30% Mn oxidation occurring in the S_2-to-S_3 transition. This is what is predicted by our equilibrium model above. The 30% Mn oxidation can be attributed to the formation of the oxo-hydroxo form where Mn_1(III)-to-Mn_1(IV) oxidation occurs. The $[O5O6]^{3-}$ form has, however, an overall Mn oxidation state identical to the S_2 state, that is, one Mn(III) and three Mn(IV), so this will not give rise to a first moment shift.

The computational, structural, and spectroscopic evidence above all points to an S_3 state involving an equilibrium between an O5-O6H oxo-hydroxo and an $[O5O6]^{3-}$ species. The most recent XFEL structures for the S_3[25, 26] state also reveal a very short O6 to OEGlu189 distance of 2.4-2.5 Å, suggesting a low-barrier hydrogen bond between the two atoms. This strongly indicates that the S_3 state equilibrium is established by proton-sharing between these two atoms, as illustrated

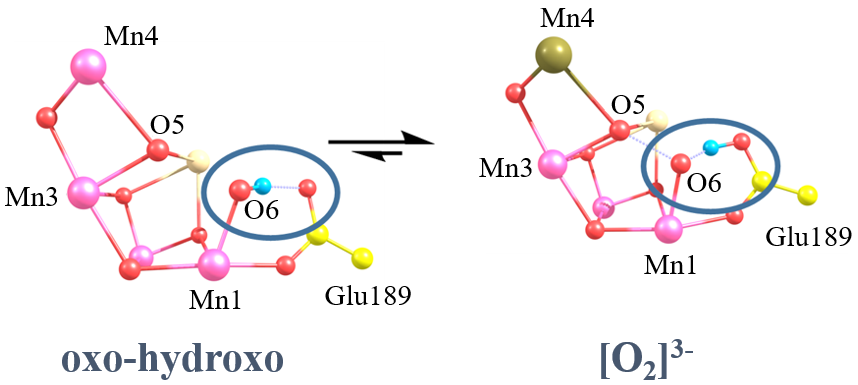

Figure 5.10: S_3 state equilibrium between oxo-hydroxo and $[O2]^{3-}$, highlighting the proposed proton shuffle between O6 and Glu189. Gold color, Mn(III); purple, Mn(IV).

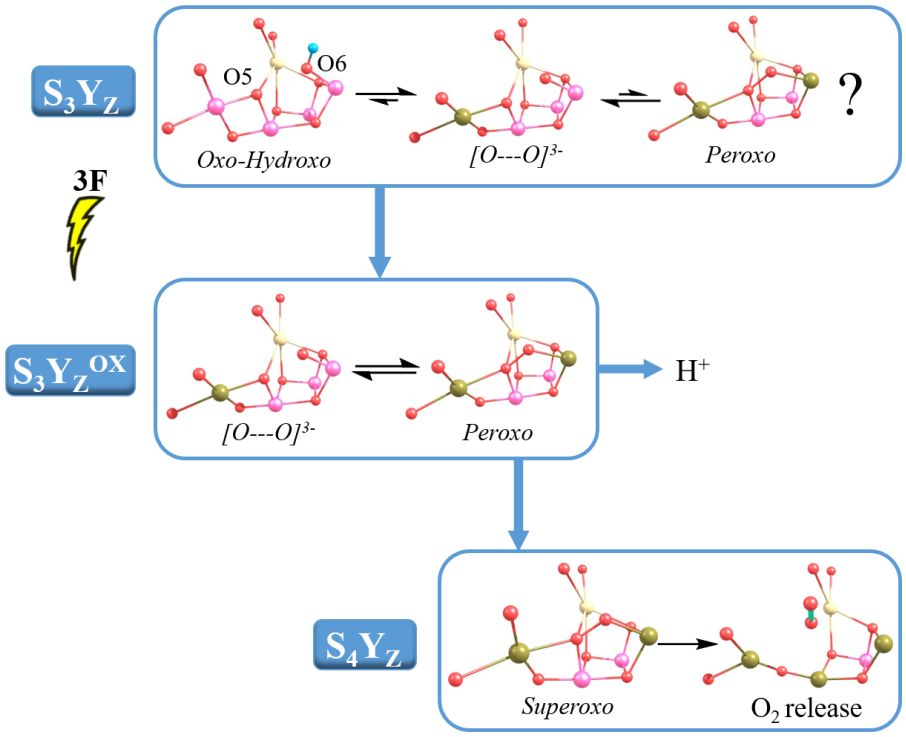

Figure 5.11: Proposed O_2 formation mechanism for the WOC. Gold color, Mn(III); purple, Mn(IV). See text for details.

in Figure 5.10.

Based on our combined computational, spectroscopic, and structural analysis, we demonstrate that O-O bond formation has begun between the O5 and O6 atoms in the S_3 state, with the generation of the $[O5O6]^{3-}$ ion. This is the dominant species present in the S_3 state. Figure 5.3 shows that this provides a low-barrier pathway to the subsequent formation of the peroxo form. As indicated above, this peroxo form could be present in a low concentration in the S_3 state and may be further stabilized after the fourth flash on generation of the $S_3Y_Z^{OX}$ state and further removal of a proton from the WOC, Figure 5.11.

Subsequent oxidation of the WOC by Y_Z^{OX} leads to the oxidation of peroxo, leading to the transient superoxo formation which will rapidly lead to triplet O_2 formation and release from the WOC.[17] The initiation of O-O bond formation in the S_3 or $S_3Y_Z^{OX}$ state is supported by kinetic findings which have shown that there is a kinetic coincidence between the rate of O_2 evolution and Y_Z^{OX} reduction.[32] Time-resolved X-ray emission studies[33] have demonstrated that reduction as opposed to oxidation of the WOC occurs after the third flash, fully supporting O-O bond formation in the S_3 and $S_3Y_Z^{OX}$ states.

5.3.3 Conclusions

Analysis of the electronic structure changes along the reaction path for the O5-O6 bond formation in the S_3 state of the WOC shows that two PES crossovers, facilitated by the geometry and magnetism of the water-oxidizing complex, are used to provide a unique low-energy pathway. The pathway is facilitated via formation and stabilization of the $[O5O6]^{3-}$ ion. This $[O2]^{3-}$ ion is stabilized by antiferromagnetic interaction with the Mn ions of the complex. The combined computational, crystallographic, and spectroscopic data show that an equilibrium exists between an O5 oxo and an O6 hydroxo form, $S = 3$ spin state, and a deprotonated O6 form containing a two-centre one-electron bond in $[O5O6]^{3-}$ which we identify as the form detected by XFEL crystallography. This form gives rise to an $S = 6$ spin state which gives rise to a low-intensity EPR spectrum compared with the accompanying $S = 3$ state, making its detection via EPR difficult and overshadowed by the $S = 3$ form. Simulations assuming a 70% contribution of the $S = 6$ form give rise to a superior fit to the experimental EPR spectrum compared with an $S = 3$ only form. The study reveals the key electronic, magnetic, and structural design features of nature's catalyst, which allows water oxidation to O_2 to be uniquely performed under ambient conditions.

References

[1] J. Kern, R. Chatterjee, I. D. Young, F. D. Fuller, L. Lassalle, M. Ibrahim, S. Gul, T. Fransson, A. S. Brewster, R. Alonso-Mori, et al., *Nature* **2018**, *563*, 421–425.

[2] M. Suga, F. Akita, K. Yamashita, Y. Nakajima, G. Ueno, H. Li, T. Yamane, K. Hirata, Y. Umena, S. Yonekura, et al., *Science* **2019**, *366*, 334–338.

[3] V. Krewald, M. Retegan, N. Cox, J. Messinger, W. Lubitz, S. De Beer, F. Neese, D. A. Pantazis, *Chem. Sci.* **2015**, *6*, 1676–1695.

[4] N. Cox, M. Retegan, F. Neese, D. A. Pantazis, A. Boussac, W. Lubitz, *Science* **2014**, *345*, 804–808.

[5] G. Zahariou, N. Ioannidis, Y. Sanakis, D. A. Pantazis, *Angewandte Chemie International Edition* **2021**, *60*, 3156–3162.

[6] T. A. Corry, P. J. O'Malley, *The Journal of Physical Chemistry B* **2021**, *125*, 10097–10107.

[7] T. A. Corry, P. J. O'Malley, *The journal of physical chemistry letters* **2020**, *11*, 4221–4225.

[8] H. Isobe, M. Shoji, T. Suzuki, J.-R. Shen, K. Yamaguchi, *Journal of chemical theory and computation* **2019**, *15*, 2375–2391.

[9] G. Renger, *Biochimica et Biophysica Acta (BBA) - Bioenergetics* **2012**, *1817*, 1164–1176.

[10] F. Rummel, P. J. O'Malley, *The Journal of Physical Chemistry B* **2022**, *126*, 8214–8221.

[11] D. Shevela, J. F. Kern, G. Govindjee, J. Whitmarsh, J. Messinger, *Biochem. Soc. Trans* **2021**, *6*, 901–913.

[12] J. Soriano-Lopez, W. Schmitt, M. Garcia-Melchor, *Current Opinion in Electrochemistry* **2018**, *7*, 22–30.

[13] D. W. Shaffer, Y. Xie, J. J. Concepcion, *Chemical Society Reviews* **2017**, *46*, 6170–6193.

[14] M. Askerka, G. W. Brudvig, V. S. Batista, *Accounts of chemical research* **2017**, *50*, 41–48.

[15] P. E. Siegbahn, *Biochimica et Biophysica Acta (BBA)-Bioenergetics* **2013**, *1827*, 1003–1019.

[16] H. Dau, M. Haumann, *Biochimica et Biophysica Acta (BBA)-Bioenergetics* **2007**, *1767*, 472–483.

[17] T. A. Corry, P. J. O'malley, *The Journal of Physical Chemistry Letters* **2018**, *9*, 6269–6274.

[18] Y. Pushkar, K. M. Davis, M. C. Palenik, *The Journal of Physical Chemistry Letters* **2018**, *9*, 3525–3531.

[19] M. Chrysina, E. Heyno, Y. Kutin, M. Reus, H. Nilsson, M. M. Nowaczyk, S. DeBeer, F. Neese, J. Messinger, W. Lubitz, et al., *Proceedings of the National Academy of Sciences* **2019**, *116*, 16841–16846.

[20] G. Knizia, J. E. Klein, *Angewandte Chemie International Edition* **2015**, *54*, 5518–5522.

[21] J. E. Klein, G. Knizia, *Angewandte Chemie International Edition* **2018**, *57*, 11913–11917.

[22] A. J. Bridgeman, G. Cavigliasso, L. R. Ireland, J. Rothery, *Journal of the Chemical Society Dalton Transactions* **2001**, 2095–2108.

[23] M. Suga, F. Akita, M. Sugahara, M. Kubo, Y. Nakajima, T. Nakane, K. Yamashita, Y. Umena, M. Nakabayashi, T. Yamane, et al., *Nature* **2017**, *543*, 131–135.

[24] N. J. Beal, T. A. Corry, P. J. O'Malley, *The Journal of Physical Chemistry B* **2018**, *122*, 1394–1407.

[25] R. Hussein, M. Ibrahim, A. Bhowmick, P. S. Simon, R. Chatterjee, L. Lassalle, M. Doyle, I. Bogacz, I.-S. Kim, M. H. Cheah, et al., *Nature communications* **2021**, *12*, 6531.

[26] M. Ibrahim, T. Fransson, R. Chatterjee, M. H. Cheah, R. Hussein, L. Lassalle, K. D. Sutherlin, I. D. Young, F. D. Fuller, S. Gul, et al., *Proceedings of the National Academy of Sciences* **2020**, *117*, 12624–12635.

[27] V. Krewald, M. Retegan, N. Cox, J. Messinger, W. Lubitz, S. DeBeer, F. Neese, D. A. Pantazis, *Chemical Science* **2015**, *6*, 1676–1695.

[28] V. Krewald, M. Retegan, F. Neese, W. Lubitz, D. A. Pantazis, N. Cox, *Inorganic chemistry* **2016**, *55*, 488–501.

[29] A. Boussac, I. Ugur, A. Marion, M. Sugiura, V. R. Kaila, A. W. Rutherford, *Biochimica et Biophysica Acta (BBA)-Bioenergetics* **2018**, *1859*, 342–356.

[30] Y. Sanakis, N. Ioannidis, G. Sioros, V. Petrouleas, *Journal of the American Chemical Society* **2001**, *123*, 10766–10767.

[31] J.-H. Su, K. G. Havelius, F. Mamedov, F. M. Ho, S. Styring, *Biochemistry* **2006**, *45*, 7617–7627.

[32] G. T. Babcock, *Federation of European Biochemical Societies Letters* **1975**.

[33] K. M. Davis, B. T. Sullivan, M. C. Palenik, L. Yan, V. Purohit, G. Robison, I. Kosheleva, R. W. Henning, G. T. Seidler, Y. Pushkar, *Physical Review X* **2018**, *8*, 041014.

5.3.4 Supporting Information

5.3.4.1 Methods

The computational procedure used is similar to those described previously.[1, 2] All calculations were performed using ORCA 4[3] with models initially geometry optimised in the HS oxo-oxo oxidation state of $(Mn^{III})_4$.[2] All calculations used the B3LYP functional[4, 5] with the zeroth-order regular approximation (ZORA) Hamiltonian applied to include scalar relativistic effects.[6–8] ZORA versions of the def2-SVP basis sets were used for C and H atoms. ZORA versions of the def2-TZVP basis set with f functions removed were used for all other atoms.[9] The B3LYP functional was chosen as appropriate for a system of the size studied and because it has a proven track record for energetic and orbital analysis of reactions of this type[10] providing accurate energetic results, particularly for the WOC[11] and many other challenging transition metal based systems.[12] The chain of spheres (RIJCOSX) approximation to exact exchange was applied along with the decontracted general Weigend auxiliary basis sets.[13–17] Dispersion corrections proposed by Grimme with Becke-Johnson damping (D3BJ) were included.[18, 19] The conductor-like polarizable continuum model (CPCM) with a dielectric constant $\epsilon = 8.0$[20, 21] was applied in all calculations. Increased integration grids (Grid6 and IntAcc 6 in ORCA convention) and tight SCF convergence criteria were used with all terminal carbon atoms constrained during optimisation calculations.

To calculate initial BS-DFT wavefunctions for potential energy surface calculations, ZORA versions of the def2-TZVP basis set with f functions removed were used for all atoms.[9] Initial BS guesses were constructed using the 'flipspin' feature of ORCA.[22] Convergence to the correct BS and HS states in all calculations were confirmed by examination of the calculated Mulliken spin populations.

The potential energy surface was calculated using the geometry optimisation method described above, initially reading in the broken symmetry ".gbw" file to correctly model the Ms = 3 state. The O5-O6 bond length was varied from 2.44 to 1.44 Å in several steps with full geometry optimisation at each step to produce the full energy surface in the text. Intrinsic bond orbitals (IBOs) were produced from the optimised PES calculation wavefunctions using IboView with iboexp=2.[23] To obtain the corresponding orbitals illustrating the overlap between the Mn ions and the O5O6 magnetic orbital σ^*_{2p}, we use an atom substitution approach to "switch off" pathways except the interaction between individual Mn ions and the O5O6 orbital. This was achieved by substituting the other ions with either Ga (position 4) or Ge (positions 1, 2 and 3).

All EPR spectral simulations have been performed using the EasySpin 5.2.35 'pepper' function within MATLAB. EPR parameters are given in the text and figure captions.

5.3.4.2 Model systems

All models were generated from the S_3 XFEL crystal structure (PDB: 6DHO)[24] and geometry optimised into the S_3 state. Seven directly coordinated amino acids are included in the models. Six are from the D1 protein chain (Asp-170, Glu189, His-332, Glu-333, Asp-342, Ala-344) and one from the CP43 protein chain (Glu-354). The second sphere His-337 residue was included along with the partial backbone of Glu-329. All terminal carbon atoms were constrained throughout the calculations. The models (Figure S5.1 and SS5.2) contain four directly coordinated water molecules, two bound to Mn_4 (W1 and W2) and two bound to Ca (W3 and W4), along with ten crystallographic water molecules. All bridging oxygen atoms are in the μ-oxo (O2-) form and all coordinated water ligands W1-W4 are in the aquo form.

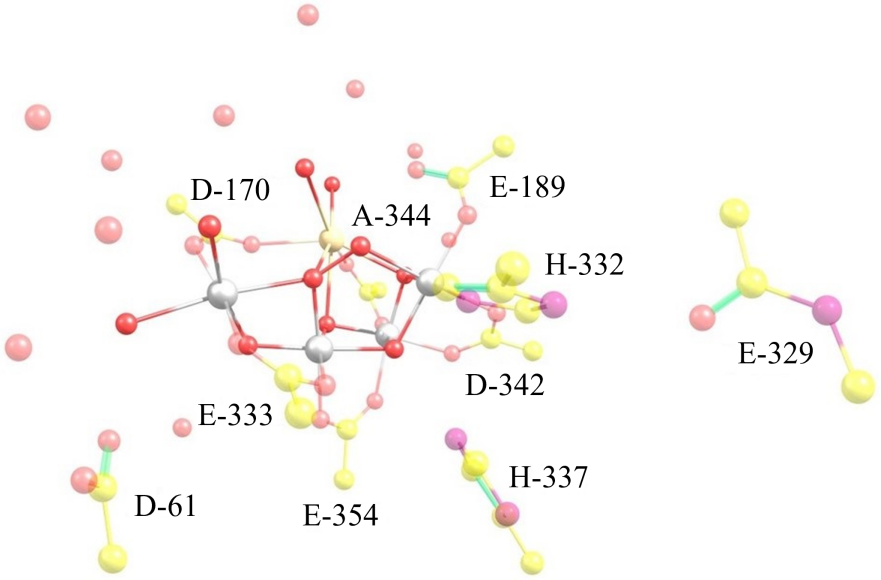

Figure S5.1: Model used as the starting point for all PES calculations. Hydrogens have been excluded for clarity. Colour coding: Mn (silver), oxygen (red), calcium (white), carbon (yellow) and nitrogen (purple).

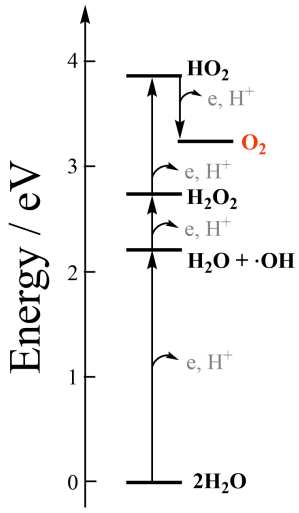

Figure S5.2: Energy level diagram for four sequential electron oxidations of water to O2 in the aqueous phase.

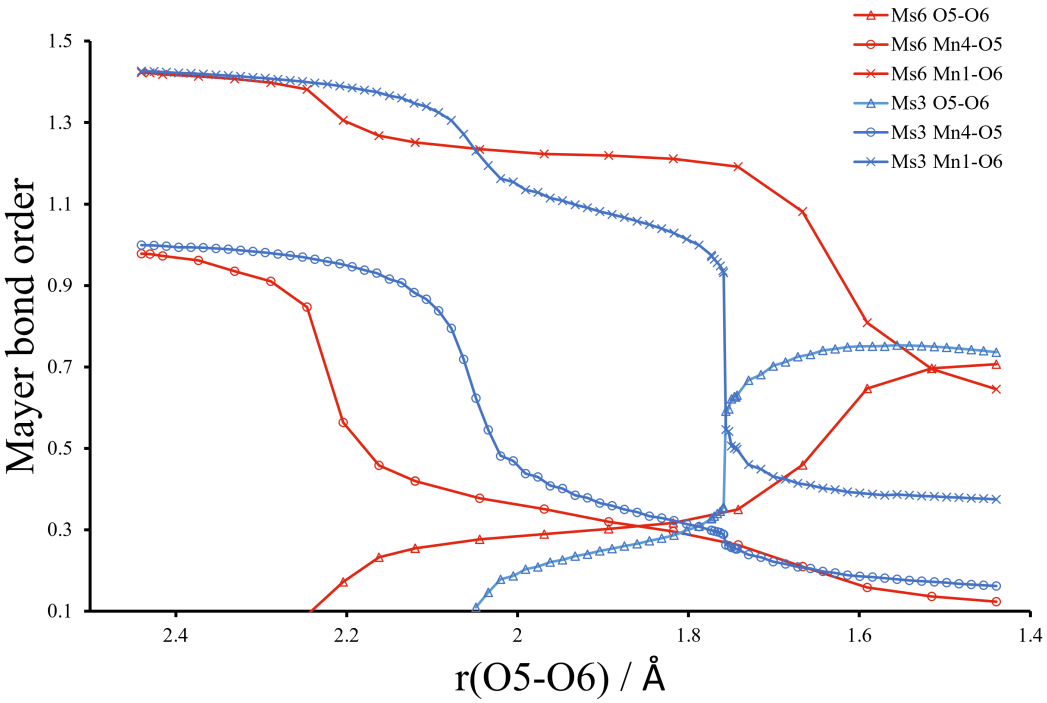

Figure S5.3: Variation of Mayer bond orders for the oxo-oxo Ms = 6 and Ms = 3 BS states along the O5O6 PES.

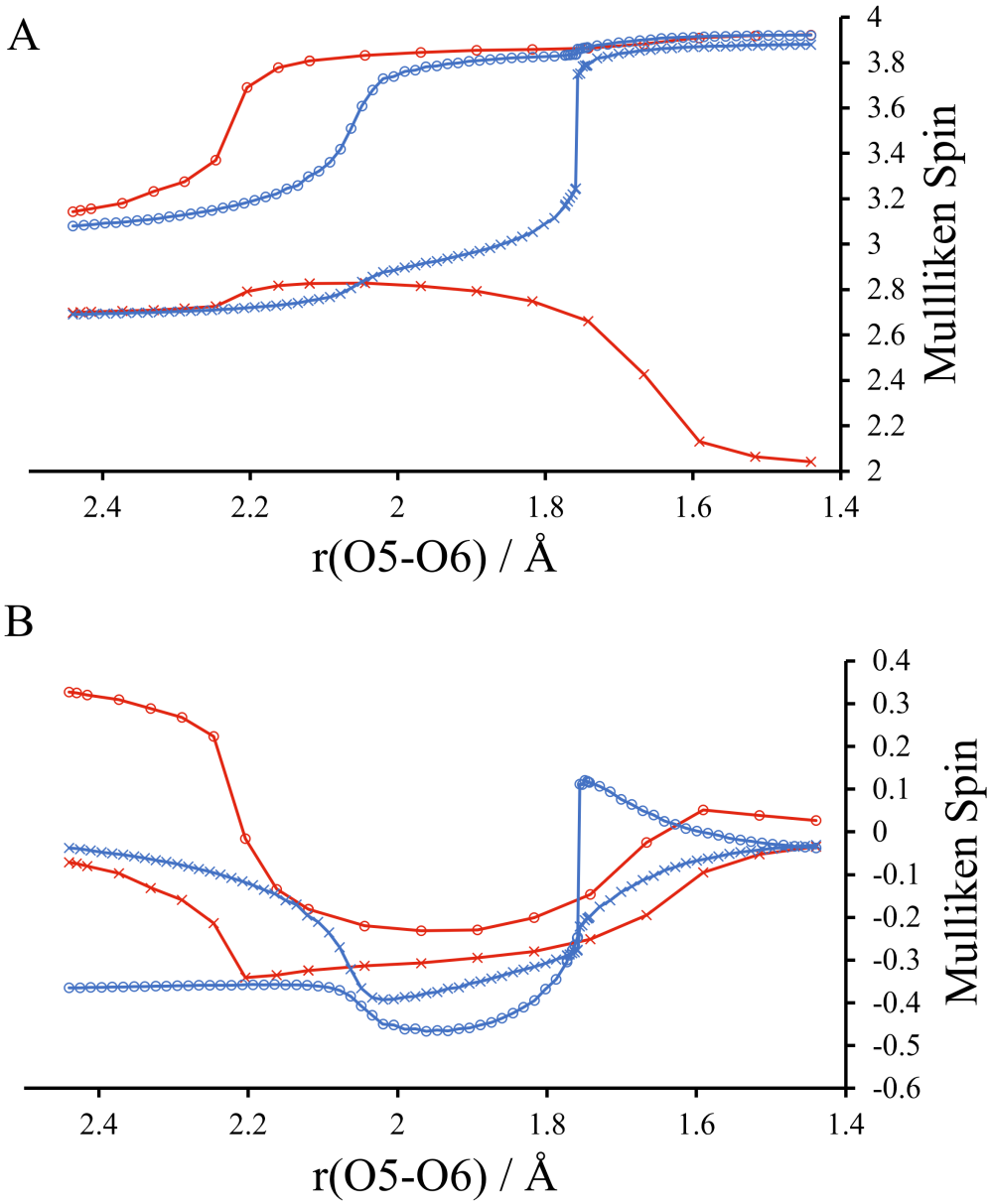

Figure S5.4: Variation of Mulliken spin populations along the O5O6 PES for oxo-oxo Ms = 3 (blue) and Ms = 6 (red). **A**: Mn_1 (x) and Mn_4 (circle). **B**: O5 (x) and O6 (circle).

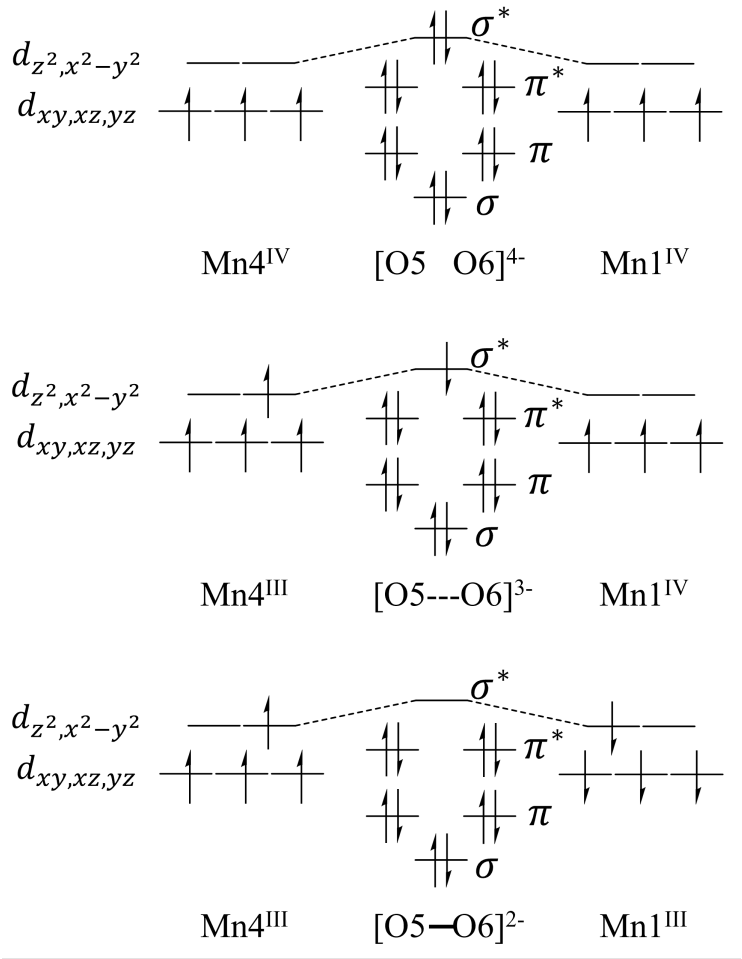

Figure S5.5: Molecular orbital schematic of electronic rearrangements leading to O-O bond formation. For the oxo-hydroxo form, the bond order of zero for $[O5O6]^{4-}$ signifies no covalent bond can exist between O5 and O6. One electron transfer from the σ^*_{2p} orbital to Mn_4 leads to formation of the $[O5O6]^{3-}$ species and a situation with doubly occupied σ_{2p} and one-electron (β) occupied σ^*_{2p} orbitals, resulting in an O5O6 bond order of 0.5. Transfer of the remaining σ^*_{2p} electron to Mn_1 results in the formation of an O5-O6 single bond (peroxo) with a bond order of 1. The key to low-barrier O-O formation in the WOC is the sequential removal of two electrons from the combining O6 and O5 oxos by Mn_1 and Mn_4 respectively thereby resulting in an unoccupied σ^*_{2p} orbital and low barrier O-O bond formation.

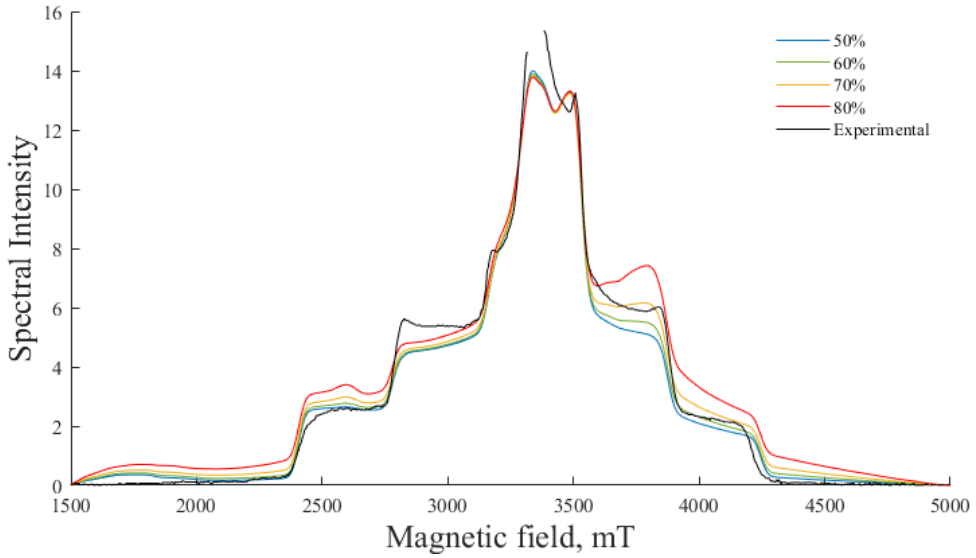

Figure S5.6: Comparison of best simulation fit with experimental W-band EPR spectrum (black) using various percentages of the $S = 6$ signal. Parameters used as given in Figure 5.9 of the main text.

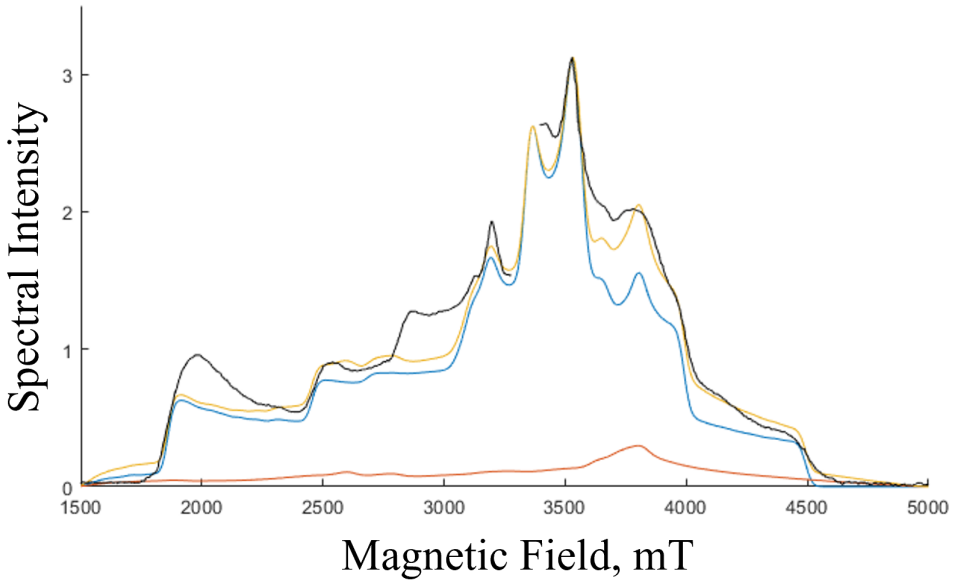

Figure S5.7: Simulated W-band EPR spectrum for broadened S_3 state signal observed after methanol treatment. Red, $S = 6$, $D = 1.523$ cm^{-1} $E/D = 0.14$; blue $S = 3$, $D = 0.281$ cm^{-1}, $E/D = 0.16$; yellow 70% of $S = 6$. Black experimental spectrum. As for the native sample described in main text, the fit to experimental spectrum in the region 3500 - 4500 mT is much improved with the inclusion of an $S = 6$ component.

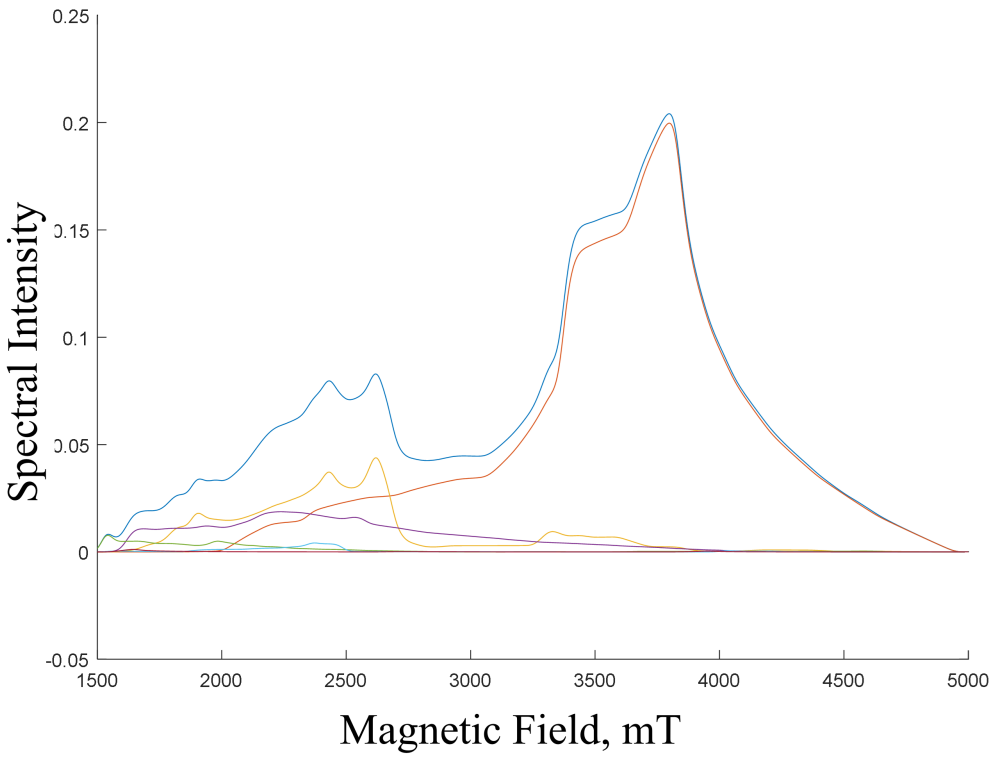

Figure S5.8: $S = 6$, 94 GHz EPR spectrum simulation. Blue envelope corresponds to overall spectrum with the decomposition of this overall envelope into individual transitions shown below, see also Figure S5.8. Simulation parameters, $g = 2$, $D = 1.523$ cm^{-1} and $E/D = 0.14$.

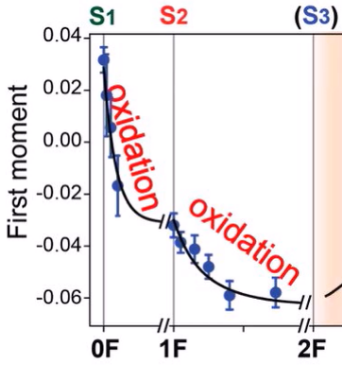

Figure S5.9: Time resolved XES first moment data for the S_1 to S_2 and S_2 to S_3 transitions reproduced from Yano, Y., International Congress on Photosynthesis Research , August 2022, Dunedin New Zealand. The data show an approximately 40% magnitude oxidation change for S_3 formation compared with S_2 formation. This is fully in line with an equilibrium model for the S_3 state comprising oxo-hydroxo (30-40%) and $[O2]^{3-}$ (60-70%) as discussed in main text.

Table S5.1: BS-DFT calculated Mn_i/Mn_j exchange couplings (J_{ij}, cm^{-1}). HDvV calculated total spin (S) ground state (GS) and first excited state (ES) and separation energies (ΔE, cm^{-1})for $[O5O6]^{3-}$.

	$[O5O6]^{3-}$
J_{43}	-18
J_{42}	1
J_{41}	-88
$J_{4-O6/O5}$	-1052
J_{32}	11
J_{31}	-26
$J_{3-O6/O5}$	-433
J_{21}	14
$J_{2-O6/O5}$	0
$J_{1-O6/O5}$	-1301
S_{GS}	6
S_{ES}	5
ΔE	116.7

References

[1] T. A. Corry, P. J. O'Malley, *The Journal of Physical Chemistry Letters* **2019**, *10*, 5226–5230.

[2] T. A. Corry, P. J. O'malley, *The Journal of Physical Chemistry Letters* **2018**, *9*, 6269–6274.

[3] F. Neese, *WIREs Computational Molecular Science* **2018**, *8*, e1327.

[4] C. Lee, W. Yang, R. G. Parr, *Phys. Rev. B* **1988**, *37*, 785–789.

[5] A. D. Becke, *The Journal of Chemical Physics* **1993**, *98*, 1372–1377.

[6] E. v. Lenthe, E. J. Baerends, J. G. Snijders, *The Journal of Chemical Physics* **1993**, *99*, 4597–4610.

[7] E. van Lenthe, E. J. Baerends, J. G. Snijders, *The Journal of Chemical Physics* **1994**, *101*, 9783–9792.

[8] C. van Wüllen, *The Journal of Chemical Physics* **1998**, *109*, 392–399.

[9] F. Weigend, R. Ahlrichs, *Phys. Chem. Chem. Phys.* **2005**, *7*, 3297–3305.

[10] T. A. Corry, P. J. O'Malley, *The Journal of Physical Chemistry B* **2021**, *125*, 10097–10107.

[11] P. E. M. Siegbahn, *Proceedings of the National Academy of Sciences* **2017**, *114*, 4966–4968.

[12] A. Altun, J. Breidung, F. Neese, W. Thiel, *Journal of Chemical Theory and Computation* **2014**, *10*, 3807–3820.

[13] *Chemical Physics Letters* **1995**, *240*, 283–290.

[14] K. Eichkorn, F. Weigend, O. Treutler, R. Ahlrichs, *Theoretical Chemistry Accounts* **1997**, *97*, 119–124.

[15] F. Weigend, *Phys. Chem. Chem. Phys.* **2006**, *8*, 1057–1065.

[16] V. N. Staroverov, G. E. Scuseria, J. Tao, J. P. Perdew, *The Journal of Chemical Physics* **2003**, *119*, 12129–12137.

[17] F. Neese, F. Wennmohs, A. Hansen, U. Becker, *Chemical Physics* **2009**, *356*, 98–109.

[18] S. Grimme, J. Antony, S. Ehrlich, H. Krieg, *The Journal of Chemical Physics* **2010**, *132*.

[19] S. Grimme, S. Ehrlich, L. Goerigk, *Journal of Computational Chemistry* **2011**, *32*, 1456–1465.

[20] N. Cox, M. Retegan, F. Neese, D. A. Pantazis, A. Boussac, W. Lubitz, *Science* **2014**, *345*, 804–808.

[21] D. A. Pantazis, W. Ames, N. Cox, W. Lubitz, F. Neese, *Angewandte Chemie International Edition* **2012**, *51*, 9935–9940.

[22] F. Neese, *WIREs Computational Molecular Science* **2012**, *2*, 73–78.

[23] G. Knizia, J. E. Klein, *Angewandte Chemie International Edition* **2015**, *54*, 5518–5522.

[24] J. Kern, R. Chatterjee, I. D. Young, F. D. Fuller, L. Lassalle, M. Ibrahim, S. Gul, T. Fransson, A. S. Brewster, R. Alonso-Mori, et al., *Nature* **2018**, *563*, 421–425.

Chapter 6

Insights into PSII's $S_3Y_Z^\bullet$ State, Electronic and Magnetic Analysis

Authors: Felix Rummel, Thomas Malcomson, Maxim Barchenko and Patrick O'Malley

Address: School of Chemistry, The University of Manchester, Manchester, M139PL, U.K.

Submission pending

6.1 Preface

Chapter 5 discussed the S_3 state and its possible heterogeneity suggesting an equilibrium of O5 oxo-O6 hydroxo and $[O5O6]^{3-}$ to be present as it best reproduced the experimental observations. In order to form a O-O bond between O5 and O6 from an oxo-hydroxo it is necessary to deprotonate O6. After this the formal O-O bond and consequently molecular oxygen may be formed.

The S_3 state is the final stable S state in the Kok cycle which has so far been isolated and precedes the final S_3 to S_0 transition, as such, understanding its nature helps to shed light onto the mechanism for molecular oxygen production. Recent experimental findings have shed some light onto the sequence of events in the final S_3 to S_0 transition.[1, 2] Initially the fourth flash of light leads to the oxidation of the nearby Tyr161 (Y_Z) residue, forming the $S_3Y_Z^\bullet$ state. Next, deprotonation of PSII is observed, it was proposed that this is due to the O6 proton leaving PSII through the Cl1 channel via Asp61. While this deprotonation appears to occur after the fourth flash it may occur earlier with the proton held nearby until formation of the $S_3Y_Z^\bullet$ state favours it leaving. After this the $Y_Z^{+\bullet}$ was seen to oxidise the OEC to become Y_Z again and the transient S_4 state is reached, which rapidly reforms the S_0 state with the release of molecular oxygen. Formation of the S_0 also requires the uptake of an additional water and its deprotonation.

To better understand the sequence of events and the nature of the $S_3Y_Z^\bullet$ state several models were created, an O5 oxo-O6 hydroxo, an $[O5O6]^{3-}$ and an O5-O6 peroxo. The electronic structures of these as well as the exchange interactions between the spin centres were analysed and changes between the S_3 and $S_3Y_Z^\bullet$ state highlighted. It was found that as the O-O bond forms the interaction between the Y_Z radical and the OEC, in particular with Mn_1, becomes stronger and as such would promote the final oxidation of the OEC and re-reduction of the Y_Z residue.

6.2 Abstract

Using BS-DFT the $S_3Y_Z^\bullet$ state is investigated and compared to the S_3 state. While the O5 oxo-O6 hydroxo shows little difference between states, a previously identified $[O5O6]^{3-}$ is found to exhibit reduced stabilisation of the O5-O6 shared spin. This species is shown to have some coupling with the $Y_Z^\bullet$ centre through Mn_1 and O6. Similarly a peroxo species is found to exhibit significant exchange couplings between the $Y_Z^\bullet$ centre and the Mn cluster through Mn_1. Mechanistic changes in O-O bond formation in the $S_3Y_Z^\bullet$ are highlighted by analysis of IBOs which show deviation for Mn_1 and O6 centred IBOs.

6.3 Manuscript

6.3.1 Introduction

Water oxidation, and subsequent dioxygen formation, is catalysed by the manganese-calcium oxygen-evolving complex (OEC) held within the photosystem II protein framework. [3–6] Taking place over a series of steps such that:

$$2H_2O \xrightarrow{4h\nu} O_2 + 4e^- + 4H^+ \tag{6.1}$$

the mechanism can effectively be broken down into a series of photoactivated oxidation and deprotonation steps with modern efforts, both experimental and theoretical, directed towards the determination of both the order and relative timing of each event[7–15]. An in-depth understanding of this catalytic cycle is intrinsic in driving the development of future technologies aimed at harnessing both the water-splitting potential of the complex, and its capacity to store energy to account for an increasing global energy demand. [16–22]

During water oxidation, the OEC moves through five states (S_0 to S_4) determined by the number of oxidising equivalents stored, signified by the subscript numeral. Of these states, S_0-S_3 can be isolated for study, while S_4 has yet to be isolated and is strongly assumed to be transient. Due to the transient nature of S_4, increased importance is then be placed on the description of S_3 in order to both understand S_3 itself and to determine viable structures at the beginning of S_4.

Early crystal structures of the S_3 state [23, 24] show a short ($\approx$ 1.5 Å) O-O distance between O5 and O6 (figure 6.1) suggesting early onset O-O bond formation in the form of a peroxide or superoxide structure.[24] However, this idea is excluded when interpreted alongside earlier spectroscopic [25, 26], and later SFX structures [27, 28], suggesting an O5-O6 distance of $\approx$ 2.0 Å and therefore non- or weakly-interacting oxygens at the O5 and O6 positions. Recent theoretical work has put forward a comprehensive overview of the potential energy surface as a function of O5-O6 distance throughout the S_3 state.[7–10] An oxo-hydroxo O5-O6 formation

was presented, in line with previous work in the field [26, 29–32], transitioning to an oxo-oxyl intermediate close to the geometry of modern crystal structures.[11] And finally proceeding to a peroxo structure as O5-O6 distance is reduced.

In addition to the initial bonding interaction between O5 and O6, the transition from S_3 to S_4 also comprises of a final oxidation event, [1, 2, 33–35] during which the local Tyr161 (Y_Z) is oxidised to a $Y_Z^\bullet$ state. This oxidation is proposed to have occurred by 50 µs after the flash. This is thought to be followed by a deprotonation event with the proton leaving through the Cl1 channel (200-500 µs). This is followed by OEC oxidation (500-1,200 µs), $Y_Z^\bullet$ reduction (500-730 µs)and molecular oxygen formation (≈ 1,200 µs).[1, 2] The oxidisation event can, in turn, be considered in three discrete phases [36]: first, the oxidation of Y_Z; this is followed by an extended lag phase during which additional oxidation is not reported; finally, the resulting $Y_Z^\bullet$ is reduced. This is followed by the release of molecular oxygen and subsequently another water molecule being inserted and deprotonated along with the reformation of the S_0 state.

Since the initiation of this final oxidation step is thought to mark the formal transition between the S_3 and S_4 states, and the subsequent release of the dioxygen molecule, deducing the effect of Y_Z reduction on the overall S_3 PES is a vital step in understanding the transition from a oxo-hydroxo O5-O6 formation to the pre-O_2 species. In continuation of previously conducted work[7], and accounting for the findings put forward by Pushkar et al.[37] suggesting that the formation of the oxyl may occur during the lag phase, after the oxidation of Y_Z, but prior to its eventual reduction, we present an investigative comparison of the O5-O6 bond formation potential energy surface both before and after the oxidation of Y_Z in an attempt to better understand how the presence of this local $Y_Z^\bullet$ radical species influences the activity of the OEC and the potential role that $Y_Z^\bullet$ formation has on influencing the O-O species formed at each stage of the S_3 state.

6.3.2 Methods

The methods used are similar to those described previously.[7, 8, 38] All calculations were performed in ORCA 4.[39] Models were initially optimised using the

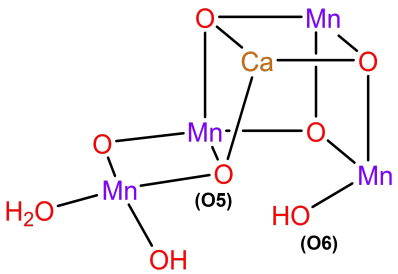

Figure 6.1: Structure of the OEC at the beginning of the S3 state.

B3LYP functional[40, 41] in their HS oxidation states. The zeroth-order regular approximation (ZORA) Hamiltonian was applied to account for scalar relativistic effects[42–44] with the def2-SVP basis sets used for C and H atoms and the def2-TZVP basis set without f functions for all other atoms.[45] For the systems presented here the B3LYP functional was chosen as it has been shown to work well for systems of this size and and for energetics and orbital analysis for the OEC[46] as well as other transition metal systems.[47] The chain of spheres (RIJCOSX) approximation was applied together with the decontracted general Weigend auxiliary basis sets.[48–52] The conductor-like polarizable continuum model (CPCM) with a dielectric constant of $\epsilon = 8.0$ was used throughout to model the protein environment[53, 54], along with the Dispersion corrections proposed by Grimme with Becke-Johnson damping (D3BJ).[55, 56] Tight SCF convergence criteria and increased integration grids (Grid6 and IntAcc 6 in ORCA convention) were used throughout, all terminal carbon atoms were constrained during optimisations.

Initial BS-DFT wavefunctions were calculated using ZORA versions of the def2-TZVP with removed f functions for all atoms, and used for potential energy surface calculations.[45] The initial BS guesses were obtained by use of the 'flipspin' feature of ORCA.[57] And convergence of the correct BS and HS states were confirmed by examination of the calculated Mulliken spin populations for all calculations. Throughout the text these BS states may be referred to as BS1 or BS4 for example, indicating a BS state with Mn_1 or Mn_4 flipped respectively.

The potential energy surface was obtained using the geometry optimisation method as described above. The BS '.gbw' file for the M_s state in question was initially read in, and the O5-O6 bond length was varied between 2.45 to 1.45 Å in 0.05 Å steps, where each point underwent full geometry optimisation to produce the final potential energy surface. To investigate the relative energies of His190 and Y_Z protonated structures a high spin O5-O6 Peroxo or high spin O5 oxo-O6 oxo was optimised. The proton was then moved onto either His190 or Y_Z and single point calculations were performed for various BS states. Intrinsic bond orbitals (IBOs) were produced using IboView with iboexp=2 from the optimised PES wavefunctions.

All models were generated from the S_3 XFEL crystal structure (PDB: 6DHO)[11] and optimised in the $S_3Y_Z^\bullet$ state. Seven directly coordinated amino acids are included in the models. Six are from the D1 protein chain (Asp170, Glu189, His332, Glu333, Asp342, Ala344, Tyr161 (Y_Z), His190) and one from the CP43 protein chain (Glu354). The second sphere His337 residue was included along with the partial backbone of Ser169 (see figure S6.1). Terminal carbon atoms were constrained in all calculations. The directly coordinated water molecules W1-W4 as well as 11 crystallographic water molecules were also included. All oxygen bridges O1-O5 were in their fully deprotonated (O^{2-}), O6 was $^-$OH for the O5 oxo-O6 hydroxo models,

and O^{2-} otherwise. W1, W3 and W4 were fully protonated, W2 was ^-OH for the O5 oxo-O6 hydroxo models, and fully protonated otherwise.

6.3.3 Results and Discussion

6.3.3.1 Modelling the tyrosine radical

In the $S_3Y_Z^\bullet$ state the Y_Z-161 residue is a positive radical, resulting in the presence of an additional unpaired spin-centre, increasing the total number of possible broken-symmetry (BS) states. It was found that in order to produce the correct BS solutions in this state, with $Y_Z^\bullet$ allocated a β spin, intuitively flipping the spin on either the C1 or oxygen atom of the $Y_Z^\bullet$ residue proved to be insufficient, instead requiring both atoms be flipped, or indeed all carbon atoms in the $Y_Z^\bullet$ ring as well as the oxygen (see figure 6.2). Flipping just C1 (see figure 6.2) which carries a majority of the unpaired spin led to problems in the convergence of the wavefunction for many BS states, as such data for comparison with figure 6.2A could not be obtained. Similarly flipping just the $Y_Z^\bullet$ oxygen yielded the incorrect Mulliken spin distribution with the $Y_Z^\bullet$ remaining in the high-spin state. Instead the spin shared between O5 and O6 was found to be flipped. As a result of this any BS state calculated with the incorrect spin flips will not produce the desired spin distribution and as such will compromise both the resulting BS energy and the calculated exchange couplings between spin centres.

In the S_3 state the Y_Z residue was found to be protonated and hydrogen bonded to its hydrogen bonding partner His190, whereas upon generation of the $S_3Y_Z^\bullet$ state the proton from the $Y_Z^\bullet$ residue moved onto the His190 residue, leaving the $Y_Z^\bullet$ oxygen deprotonated. It was found that this movement occurred spontaneously and optimisation with the proton on either $Y_Z^\bullet$ or His190 resulted in the same geometry, with His190 bearing the proton, leaving the $Y_Z^\bullet$ oxygen as a de-protonated phenoxyl. This suggests barrier-less proton transfer or a negligible barrier for proton movement upon oxidation, rather than a separate discrete proton transfer event. Models with O5 and O6 in a peroxo or oxo-oxo arrangement (r[O5O6]=1.4 or 2.4 Å respectively) were created with the proton fixed on Y_Z or His190 to investigate the energy difference for various BS states as well as the HS state. It was found that for the peroxo like arrangement structures with the proton fixed on Y_Z were on average 22 kcal mol^{-1} higher in energy than the His protonated counterpart. In the oxo-oxo arrangement this was increased to 26 kcal mol^{-1}. The $Y_Z^\bullet$ residue remains hydrogen bonded through the phenoxyl oxygen to the OEC through the calcium bound W4; this was not observed to change position or bonding nature significantly when the protonation state of the Y_Z residue changed. Similarly the Y_Z residue can also hydrogen bond through a nearby water molecule indirectly to the OEC by several pathways depending on proton orientation but again the position and orientation of this water molecule was also unaffected by the

protonation state.

6.3.3.2 The Nature of the $S_3Y_Z^\bullet$ State

Previous work in the S_3 state investigated several potential energy surfaces (PES) resulting in the identification of three key species:[7] an O5 oxo-O6 hydroxo; a $[O5O6]^{-3}$ with a single unpaired β spin shared between O5 and O6; and a peroxo species with a formal bond between O5 and O6. Once the Y_Z residue is oxidised and the $S_3Y_Z^\bullet$ state formed there is an additional spin centre present. For the O5 oxo-O6 hydroxo there are now 5 spin centres (Mn_1-Mn_4 and Y_Z) yielding 15 unique BS states (and 1 HS state). Whereas in the S_3 state there are only 7 unique BS states. The relative energies of these are compared in figure 6.3. The most stable BS states are either with Mn_4 or Mn_3 anti-parallel to all other spin centres regardless of the $Y_Z^\bullet$ spin alignment or whether the model is in the S_3 state or $S_3Y_Z^\bullet$ state. Furthermore the alignment of the $Y_Z^\bullet$ radical has no significant effect on the BS energies in the $S_3Y_Z^\bullet$ state. This, in turn, suggests a lack of, or weak coupling between the $Y_Z^\bullet$ radical and the Mn cluster, this aligns with previous work by Retegan et al.[58] in which the $S_2Y_Z^\bullet$ showed no coupling between the $Y_Z^\bullet$ residue and the OEC.

The lack of coupling for the oxo-hydroxo OEC with the nearby $Y_Z^\bullet$ radical observed in figure 6.3 is reflected in the calculated J values shown in table 6.1. Comparing the S_3 and $S_3Y_Z^\bullet$ J values it can be seen that the magnitude is simi-

A

Flipped centres	Total Mulliken Spin		E_{HS}-E_{BS} kcal mol^{-1}
	Y_Z	[O5O6]	
-	1	1.17	0
O	1.01	-0.59	16.7
O,C1	-0.92	1.16	0.1
O,Y_Z ring C	-0.92	1.16	0.1

B

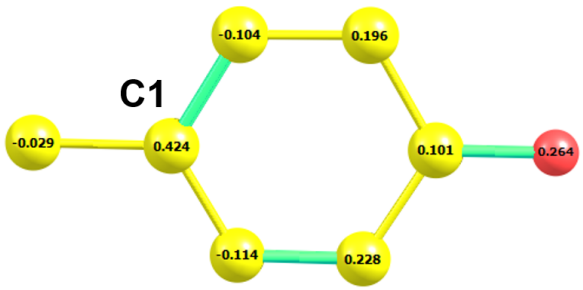

Figure 6.2: Taken from a high spin O5-O6 = 2.1 Å model; A: Total calculated Mulliken spin population for the Y_Z residue for different BS "flipspin" inputs, as well as the relative energies compared to the high-spin system; B: Mulliken spin populations of the $Y_Z^\bullet$ residue. Yellow: carbon and red: oxygen, hydrogens are omitted for clarity.

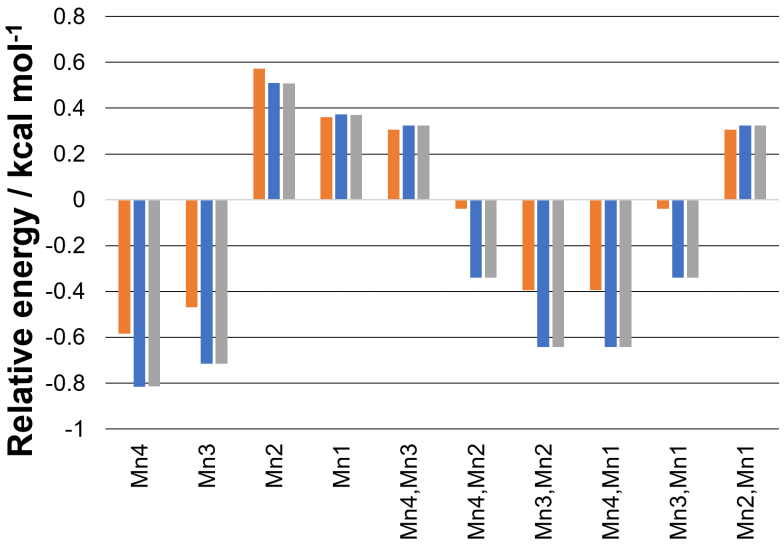

Figure 6.3: Relative energy of the BS states to the HS state for the oxo-hydroxo models, more negative values correspond to more stable BS states. The 'flipped' centres are indicated. Orange: S_3 state, blue: $S_3Y_Z^\bullet$ state with $Y_Z^\bullet$ as α and grey: $S_3Y_Z^\bullet$ state with $Y_Z^\bullet$ as β.

lar for all Mn-Mn couplings. There is also an apparent lack of significant coupling between the Mn centres and the $Y_Z^\bullet$ residue, the coupling here is several orders of magnitude smaller. This agrees with previous findings by Retegan et al.[58] who reported a similar difference in magnitude for the $S_2Y_Z^\bullet$ state.[58] The dominant antiferromagnetic coupling between Mn_3 and Mn_4 agrees well with the BS4 and BS3 states being the most stable.

During O5-O6 bond formation it is necessary to deprotonate O6. At a large O5-O6 separation (>2.2 Å) this yields an oxo-oxo species while optimisation at short O5-O6 distance (<1.6 Å) yields a peroxo structure with O5 and O6 bonded. Optimisation at around 2 Å yields a $[O5O6]^{3-}$ species both in the S_3 and $S_3Y_Z^\bullet$ state. In both states an unpaired β electron is shared between O5 and O6 while other spin centres are in an α alignment, a spin density plot for the $S_3Y_Z^\bullet$ state is shown in figure 6.4 and illustrates both this and the delocalisation of the radical throughout the $Y_Z^\bullet$ residue.

The BS-DFT energies for the $[O5O6]^{3-}$ species are shown in figure 6.5 where for any given BS state the stabilisation is reduced in the $S_3Y_Z^\bullet$ state in contrast to the increased stabilisation observed in the oxo-hydroxo geometry (figure 6.3. Interestingly, the spin alignment of the $Y_Z^\bullet$ as for the O5 oxo-O6 hydroxo has no obvious effect on the energies of most BS states. However, very small differences can be observed for some states, such as the BS1 state. The most stable BS state for both S states is an antiparallel alignment of the [O5O6] shared spin to all other spin centres as expected given the relative magnitudes of the Mn-$O_{5/6}$ J couplings compared to

Table 6.1: BS-DFT calculated Mn-Mn, Mn-Y_Z,Mn-O and O-$Y_Z^\bullet$ exchange couplings, J, values obtained for the O5 oxo-O6 hydroxo, the broad minima corresponding to $[O5O6]^{3-}$ and the O5-O6 peroxo state, in both the S_3 and $S_3Y_Z^\bullet$ state. All values are in cm^{-1}.

	oxo-hydroxo		$[O5O6]^{3-}$		peroxo	
	$S_3Y_Z^\bullet$	S_3	$S_3Y_Z^\bullet$	S_3	$S_3Y_Z^\bullet$	S_3
J_{43}	-35.6	-26.1	-7.7	-17.8	21.4	17.8
J_{42}	0.6	0.4	-0.6	0.6	1.8	1.2
J_{41}	3.7	3.2	-39.6	-87.7	-3.7	-5.8
$J_{4-O5/O6}$	-	-	-536.9	-1051.7	-	-
J_{4Y_Z}	0.0	-	-4.1	-	-10.1	-
J_{32}	8.3	9.4	17.5	11.3	11.1	10.1
J_{31}	-0.1	-1.4	-12.8	-25.7	-4.2	-6.7
$J_{3-O5/O6}$	-	-	-342.1	-432.8	-	-
J_{3Y_Z}	0.0	-	-3.9	-	4.9	-
J_{21}	10.6	12.0	12.6	14.1	-30.8	-33.5
$J_{2-O5/O6}$	-	-	0.5	3-0.2	-	-
J_{2Y_Z}	0.0	-	0.0	-	-11.1	-
$J_{1-O5/O6}$	-	-	-849.9	-1301.1	-	-
J_{1Y_Z}	0.0	-	1.3	-	-27.6	-
$J_{O5/O6-Y_Z}$	-	-	-16.4	-	-	-

the Mn-Mn and Y_Z-$O_{5/6}$ J couplings (table 6.1). Given the relative magnitudes of the [O5O6] couplings, this strongly marked effect may overshadow the more subtle remaining couplings throughout the system.

The calculated J values for the $[O5O6]^{3-}$ species reflect the reduced stability of the $[O5O6]^{3-}$ species in the $S_3Y_Z^\bullet$ state as well as indicating the presence of coupling between the $Y_Z^\bullet$ spin radical and the OEC. Relative to the oxo-hydroxo form the

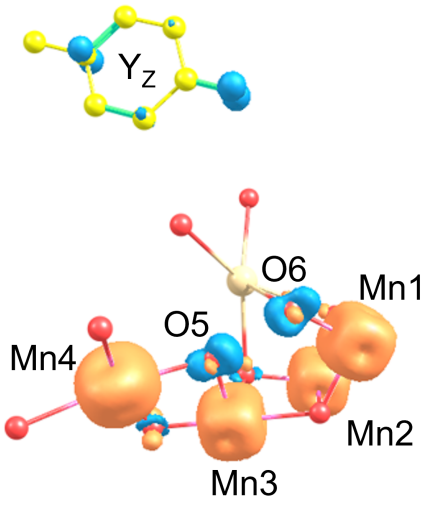

Figure 6.4: Spin density contour plot for the $[O5O6]^{3-}$ species at 2.05 Å O5-O6 separation, negative spin (blue), positive spin (orange), O5 and O6 share spin, confirming the presence of $[O5O6]^{3-}$.

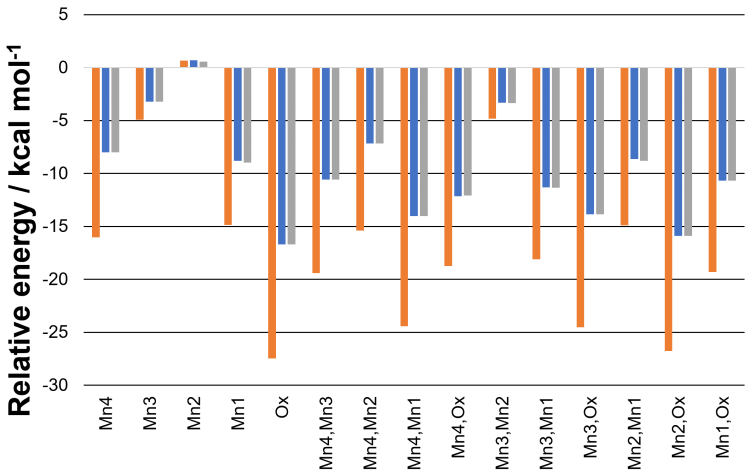

Figure 6.5: Relative energy of the BS states to the HS state for the $[O5O6]^{3-}$ species, more negative values correspond to more stable BS states. The 'flipped' centres are indicated. Orange: S_3 state, blue: $S_3Y_Z^\bullet$ state with $Y_Z^\bullet$ as α and grey: $S_3Y_Z^\bullet$ state with $Y_Z^\bullet$ as β.

$[O5O6]^{3-}$ species is destabilised by 4 kcal mol^{-1} in the $S_3Y_Z^\bullet$ state. From table 6.1 it can be seen that in both states the spin shared between O5 and O6 is stabilised by strong anti-ferromagnetic coupling with the Mn_1, Mn_3 and Mn_4 centres. These couplings are significantly larger than all other couplings and so rationalise why this centre dominates the BS energies. In contrast the coupling between Mn_2 and O5 and O6 is negligible. This is likely due to O5 and O6 being directly bonded to Mn_1, Mn_3 and Mn_4 but not to Mn_2, therefore preventing the strong coupling observed with the other metal centres. This observation is further backed up by the low coupling between Mn_2 and Mn_4 when compared to stronger coupling with Mn_1 and Mn_3. This stabilising coupling with the Mn ions is somewhat diminished in the $S_3Y_Z^\bullet$ state compared to the S_3 state with Mn-[O5O6] couplings decreasing on average by a factor of 1.6, rationalising why the BS-DFT energies in figure 6.5 are reduced in the $S_3Y_Z^\bullet$ state. Interestingly, some anti-ferromagnetic coupling is also observed between $[O5O6]^{3-}$ and the $Y_Z^\bullet$ radical comparable in magnitude to the Mn-Mn couplings, showing the presence of couplings between the OEC and the Y_Z residue. Similarly, although weaker, the Mn ions also show coupling with the $Y_Z^\bullet$ spin. Comparing the S_3 and $S_3Y_Z^\bullet$ state the most significant changes in magnitude are observed for couplings involving Mn_1 and O5/O6.

At short O5-O6 separation the OEC optimised to a peroxo type structure, with a formal O-O bond between O5 and O6. For this species, the BS1 state was found to be the lowest in energy. This peroxo geometry shows a much more significant couplings between the OEC and the $Y_Z^\bullet$ radical. The calculated J values for the peroxo species both in the S_3 and $S_3Y_Z^\bullet$ state are shown in table 6.1 and the BS energies in figure 6.6. While the Mn-Mn couplings are very similar for the S_3 and $S_3Y_Z^\bullet$ state, significant coupling between the Mn centres and the $Y_Z^\bullet$ radical are observed,

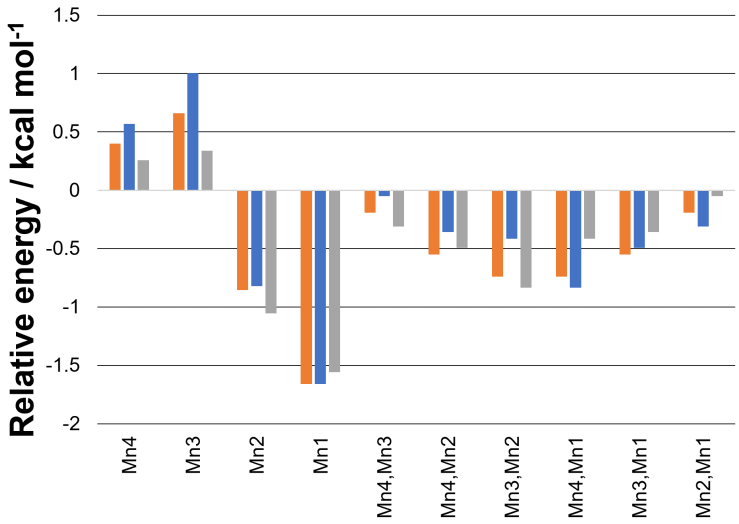

Figure 6.6: Relative energy of the BS states to the HS state for the Peroxo species, more negative values correspond to more stable BS states. The 'flipped' centres are indicated. Orange: S_3 state, blue: $S_3Y_Z^\bullet$ state with $Y_Z^\bullet$ as α and grey: $S_3Y_Z^\bullet$ state with $Y_Z^\bullet$ as β.

the effect of which is reflected in the BS energies, despite the comparatively large separation of the OEC and the $Y_Z^\bullet$ radical. The $Y_Z^\bullet$ radical shows anti-ferromagnetic coupling with Mn_4, Mn_2 and Mn_1 and shows weak ferromagnetic coupling with Mn_3, with the strongest coupling observed with the Mn_1 centre. Mn_3 is shielded from $Y_Z^\bullet$ by Mn_2 and Ca^{2+} rationalising the weaker coupling. The BS energies indicate the most stable BS state to be BS1 with all other centres antiparallel to it. This agrees well with the strong anti-ferromagnetic Mn_1-$Y_Z^\bullet$ coupling and indeed Mn_1-Mn_2.

Investigating the electronic changes by analysis of the Intrinsic Bonding Orbitals (IBOs) in the $S_3Y_Z^\bullet$ state for the partial O-O bond formation of the $[O5O6]^{3-}$ shows no major differences between the S_3 and $S_3Y_Z^\bullet$ state for the high spin Ms = 6.5 oxo-oxo/peroxo surface, see supplementary information figure S6.2 and SS6.3. Here the only apparent difference is the π-bonding lone pair on O6 (magenta) for which the spin orbital's orientation differs; in the S_3 state the spin orbital lies along Mn_1-O6-Mn_3 plane, whereas in the $S_3Y_Z^\bullet$ state it is perpendicular to it.

For the BS1 oxo-oxo/peroxo surface (Ms = 3.5) (figure 6.7), 5 IBOs were observed to change significantly across the PES, as opposed to only four in the S_3 state (see figure S6.4). An α electron from the lone pair on O6 (green) which shows some π-bonding character to Mn_1 forms the α component of the O5-O6 bond around 2 Å. And an α electron from a Mn_4-O5 σ bond (blue) moves to Mn_4 around 2 Å. While corresponding β electron from the Mn_4-O5 σ bond (red) moves to form the β component of the O5-O6 bond around 1.8 Å. These three IBOs and their changes are the same for both the S_3 and the $S_3Y_Z^\bullet$ state. However, the remaining two IBOs differ, in the S_3 state a β electron from a Mn_1-O6 σ bond moved onto Mn_1 around 1.8 Å with an associated orbital change of 1 e^{-1} (see figure S6.4). Whereas here, in the

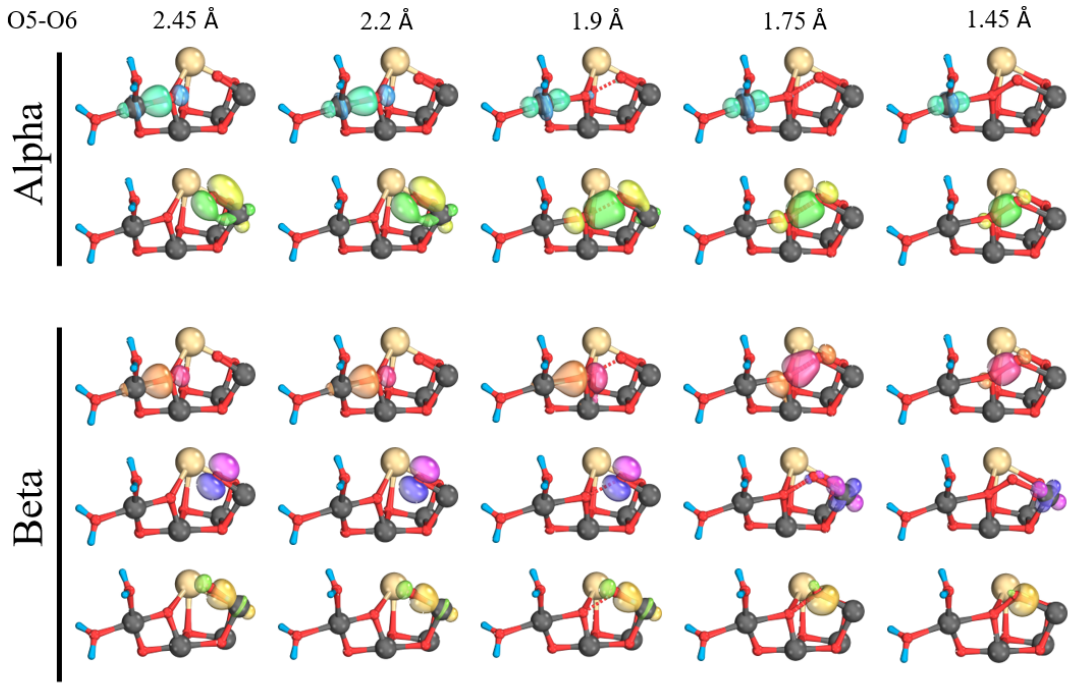

Figure 6.7: Intrinsic bond orbital (IBO) analysis of the Ms= 3.5 state oxo-oxo form. IBOs are given at the indicated O5-O6 separations showing α and β spin evolution.

$S_3Y_Z^\bullet$ state, the β electron from a Mn_1-O6 σ bond (yellow) moves to become a lone pair β on O6 around 1.8 Å with an associated orbital change of 0.5 e^{-1} (see figure S6.3). And finally a lone pair β electron (magenta) which shows no interaction with Mn_1 initially, unlike the corresponding α electron (green), moves to Mn_1 around 1.8 Å with an associated orbital change of 1.5 e^{-1}. These two changes still amount to an overall change of 1 e^{-1} going towards Mn_1 but present different sources for the observed change.

While at first glance a long range spin-spin interaction such as the coupling between the OEC and the $Y_Z^\bullet$ residue seems unlikely, long range spin-spin couplings are well established in literature for both organic and metallic spin centres.[59–62] Within the OEC, the spin-spin couplings have been shown to be superexchange type interactions[38], relying on the oxygen bridges between Mn ions. While superexchange through space is possible, in examples studied by Stanford et. al. [61] it was shown that favourable orbital overlap is required; it has also been shown that long range superexchange can exist in certain systems containing two spin centres linked by covalent bonds.[62] Additionally, solvent molecules may mediate coupling interactions between spin centres, and can aid in electron transfer mechanisms.[63–65] Liu et al.[60] demonstrated the presence of long range coupling between two spin centres, linked by a flexible linker which did not allow for delocalisation, and showed that increasing linker length did not have always have an effect on the magnitude of

the spin-spin coupling. For electron transfer between interacting spin systems it has been found that the relative orientation of the two spin centres can be important for electron transfer and that the strength of the coupling is proportional to the rate of electron transfer as described by Fermi's Golden rule[66–69]. Observation of coupling between the OEC and the $Y_Z^\bullet$ residue may point towards the potential for efficient electron transfer between them. Furthermore, the relative strengths of the couplings between the various spin centres in the OEC with the $Y_Z^\bullet$ suggest the origin of the electron transfer pathway to be through either $[O5O6]^{3-}$, Mn_1, or indeed both, to the $Y_Z^\bullet$ residue. Identifying the nature of the electron transfer process between the OEC and $Y_Z^\bullet$ is crucial as this is a key step in the transition between the S_3 and S_4 state.

6.3.4 Conclusions and Outlook

Both the $[O5O6]^{3-}$ species and the peroxo species presented here showed significant coupling interactions between the $Y_Z^\bullet$ radical and the OEC through the Mn_1 and [O5O6] shared spin. On the other hand the oxo-hydroxo species showed no interaction agreeing well with previous S_2 state work.[58] The species differ by both the O5-O6 separation as well as the O6 protonation state and orbital orientations, as seen for the $[O5O6]^{3-}$ species where the O6 lone pair was found to point towards the $Y_Z^\bullet$ radical in the $S_3Y_Z^\bullet$ state but not in the S_3 state. For the $[O5O6]^{3-}$ species anti-ferromagnetic coupling between the $Y_Z^\bullet$ radical and O5/O6 was observed along with weaker coupling between $Y_Z^\bullet$ and the Mn ions. Weaker couplings between Mn_1 and the remaining Mn ions, and reduced [O5O6]-Mn couplings when compared to the S_3 state, suggest that the $[O5O6]^{3-}$ species is relatively destabilised in the $S_3Y_Z^\bullet$ state compared to the S_3 state.

Similarly, for the peroxo species large couplings were observed between the $Y_Z^\bullet$ radical and the Mn ions, with particularly strong coupling observed with Mn_1. An additional IBO was observed to change significantly in the $S_3Y_Z^\bullet$ state and two IBOs, both involving Mn_1 and O6 showed major differences in their behaviour when compared to the S_3 state, further pointing toward coupling between the $Y_Z^\bullet$ radical and the OEC. This would suggest potential facilitation of electron transfer from OEC to $Y_Z^\bullet$ through the coupled [O5O6], Mn_1 and $Y_Z^\bullet$ spin centres.

Throughout the Kok cycle, Y_Z subsequentially removes electrons from the OEC preparing the system for facile molecular oxygen evolution. As the O5 O6 bond is formed increased coupling between the $Y_Z^\bullet$ radical and the OEC has been shown to emerge. The presence of this coupling between the OEC and $Y_Z^\bullet$ may suggest a mechanism through which removal of the final electron from OEC is promoted. The removal of the final electron would aid to drive the catalytic cycle to completion by promoting the onwards reaction of peroxo. Due to the more stable nature of peroxo it is reasonable to assume that additional driving force would be highly beneficial

to this particular oxidation step.

6.3.5 Conflicts of interest

There are no conflicts to declare.

6.3.6 Acknowledgements

FR acknowledges support from the UK BBSRC Doctoral Training Partnership (DTP) program. This research was supported with a grant from the Leverhulme Trust (RPG-2020-003). The authors would like to acknowledge the assistance given by Research IT and the use of the Computational Shared Facility at The University of Manchester.

References

[1] P. Greife, M. Schönborn, M. Capone, R. Assunção, D. Narzi, L. Guidoni, H. Dau, *Nature* **2023**, *617*, 623–628.

[2] A. Bhowmick, R. Hussein, I. Bogacz, P. S. Simon, M. Ibrahim, R. Chatterjee, M. D. Doyle, M. H. Cheah, T. Fransson, P. Chernev, I.-S. Kim, H. Makita, M. Dasgupta, C. J. Kaminsky, M. Zhang, J. Gätcke, S. Haupt, I. I. Nangca, S. M. Keable, A. O. Aydin, K. Tono, S. Owada, L. B. Gee, F. D. Fuller, A. Batyuk, R. Alonso-Mori, J. M. Holton, D. W. Paley, N. W. Moriarty, F. Mamedov, P. D. Adams, A. S. Brewster, H. Dobbek, N. K. Sauter, U. Bergmann, A. Zouni, J. Messinger, J. Kern, J. Yano, V. K. Yachandra, *Nature* **2023**, *617*, 629–636.

[3] H. Dau, I. Zaharieva, M. Haumann, *Curr. Opin. Chem. Biol.* **2012**, *16*, 3–10.

[4] J. P. McEvoy, G. W. Brudvig, *Chem. Rev.* **2006**, *106*, 4455–4483.

[5] J. Barber, *Q. Rev. Biophys.* **2016**, *49*, e14.

[6] M. Perez-Navarro, F. Neese, W. Lubtiz, D. A. Pantazis, N. Cox, *Curr. Opin. Chem. Biol.* **2016**, *31*, 113–119.

[7] F. Rummel, P. J. O'Malley, *The Journal of Physical Chemistry B* **2022**, *126*, 8214–8221.

[8] T. A. Corry, P. J. O'Malley, *The Journal of Physical Chemistry Letters* **2018**, *9*, 6269–6274.

[9] T. A. Corry, P. J. O'Malley, *The Journal of Physical Chemistry B* **2021**, *125*, 10097–10107.

[10] T. A. Corry, P. J. O'Malley, *The Journal of Physical Chemistry Letters* **2020**, *11*, 4221–4225.

[11] J. Kern, R. Chatterjee, I. D. Young, F. D. Fuller, L. Lassalle, M. Ibrahim, S. Gul, T. Fransson, A. S. Brewster, R. Alonso-Mori, R. Hussein, M. Zhang, L. Douthit, C. de Lichtenberg, M. H. Cheah, D. Shevela, J. Wersig, I. Seuffert, D. Sokaras, E. Pastor, C. Weninger, T. Kroll, R. G. Sierra, P. Aller, A. Butryn, A. M. Orville, M. Liang, A. Batyuk, J. E. Koglin, S. Carbajo, S. Boutet, N. W. Moriarty, J. M. Holton, H. Dobbek, P. D. Adams, U. Bergmann, N. K. Sauter, A. Zouni, J. Messinger, J. Yano, V. K. Yachandra, *Nature* **2018**, *563*, 421–425.

[12] M. Suga, F. Akita, K. Yamashita, Y. Nakajima, G. Ueno, H. Li, T. Yamane, K. Hirata, Y. Umena, S. Yonekura, L.-J. Yu, H. Murakami, T. Nomura, T. Kimura, M. Kubo, S. Baba, T. Kumasaka, K. Tono, M. Yabashi, H. Isobe, K. Yamaguchi, M. Yamamoto, H. Ago, J.-R. Shen, *Science* **2019**, *366*, 334–338.

[13] M. Suga, F. Akita, M. Sugahara, M. Kubo, Y. Nakajima, T. Nakane, K. Yamashita, Y. Umena, M. Nakabayashi, T. Yamane, T. Nakano, M. Suzuki, T. Masuda, S. Inoue, T. Kimura, T. Nomura, S. Yonekura, L.-J. Yu, T. Sakamoto, T. Motomura, J.-H. Chen, Y. Kato, T. Noguchi, K. Tono, Y. Joti, T. Kameshima, T. Hatsui, E. Nango, R. Tanaka, H. Naitow, Y. Matsuura, A. Yamashita, M. Yamamoto, O. Nureki, M. Yabashi, T. Ishikawa, S. Iwata, J.-R. Shen, *Nature* **2017**, *543*, 131–135.

[14] M. Ibrahim, T. Fransson, R. Chatterjee, M. H. Cheah, R. Hussein, L. Lassalle, K. D. Sutherlin, I. D. Young, F. D. Fuller, S. Gul, I.-S. Kim, P. S. Simon, C. de Lichtenberg, P. Chernev, I. Bogacz, C. C. Pham, A. M. Orville, N. Saichek, T. Northen, A. Batyuk, S. Carbajo, R. Alonso-Mori, K. Tono, S. Owada, A. Bhowmick, R. Bolotovsky, D. Mendez, N. W. Moriarty, J. M. Holton, H. Dobbek, A. S. Brewster, P. D. Adams, N. K. Sauter, U. Bergmann, A. Zouni, J. Messinger, J. Kern, V. K. Yachandra, J. Yano, *Proceedings of the National Academy of Sciences* **2020**, *117*, 12624–12635.

[15] E. M. Sproviero, J. A. Gascón, J. P. McEvoy, G. W. Brudvig, V. S. Batista, *Journal of Chemical Theory and Computation* **2006**, *2*, 1119–1134.

[16] S. Chabi, K. M. Papadantonakis, N. S. Lewis, M. S. Freund, *Energy Envirn. Sci.* **2017**, *10*, 1320–1338.

[17] N. Cox, D. A. Pantazis, F. Neese, W. Lubitz, *Interface Focus* **2015**, *5*, 20150009.

[18] T. A. Faunce, W. Lubitz, A. W. Rutherford, D. R. MacFarlane, G. F. Moore, P. Yang, D. G. Nocera, T. A. Moore, D. H. Gregory, F. S., K. B. Yoon, F. A. Armstrong, M. R. Wasielewski, S. Styring, *Energy Envirn. Sci.* **2013**, *6*, 695–698.

[19] M. Gratzel, *Inorg. Chem.* **2005**, *44*, 6841–6851.

[20] J. R. McKone, D. C. Crans, C. Martin, J. Turner, A. R. Duggal, H. R. Gray, *Inorg. Chem.* **2016**, *55*, 9131–9143.

[21] D. G. Nocera, *Acc. Chem. Res.* **2012**, *45*, 767–776.

[22] D. G. Nocera, *Acc. Chem. Res.* **2017**, *50*, 616–619.

[23] J. Kern, R. Chatterjee, I. D. Young, F. D. Fuller, L. Lassalle, M. Ibrahim, S. Gul, T. Fransson, A. S. Brewster, R. Alonso-Mori, R. Hussein, M. Zhang, L. Douthit, C. de Lichtenberg, C. M. H., D. Shevela, J. Wersig, I. Seuffert, D. Sokaras, E. Pastor, C. Weninger, T. Kroll, R. G. Sierra, P. Aller, A. Butryn, A. M. Orville, M. Liang, A. Batyuk, J. E. Koglin, S. Carbajo, S. Boutet, N. W. Moriarty, J. M. Holton, H. Dobbek, P. D. Adams, U. Bergmann, N. K. Sauter, A. Zouni, J. Messinger, J. Yano, V. K. Yachandra, *Nature* **2018**, *563*, 421–425.

[24] M. Suga, F. Akita, K. Yamashita, Y. Nakajima, G. Ueno, H. Li, T. Yamane, K. Hirata, Y. Umena, S. Yonekura, L. Yu, H. Murakami, T. Nomura, T. Kimura, M. Kubo, S. Baba, T. Kumasaka, K. Tono, M. Yabashi, H. Isobe, K. Yamaguchi, M. Yamamoto, H. Ago, J. Shen, *Science* **2014**, *345*, 804–808.

[25] J. Messinger, M. Badger, T. Wydrzynski, *PNAS* **1995**, *92*, 3209–3219.

[26] N. Cox, M. Retegan, F. Neese, D. A. Pantazis, A. Boussac, W. Lubitz, *Science* **2014**, *345*, 804–808.

[27] J. Kern, R. Chatterjee, I. D. Young, F. D. Fuller, L. Lassalle, M. Ibrahim, S. Gul, T. Fransson, A. S. Brewster, R. Alonso-Mori, R. Hussein, M. Zhang, L. Douthit, C. de Lichtenberg, C. M. H., D. Shevela, J. Wersig, I. Seuffert, D. Sokaras, E. Pastor, C. Weninger, T. Kroll, R. G. Sierra, P. Aller, A. Butryn, A. M. Orville, M. Liang, A. Batyuk, J. E. Koglin, S. Carbajo, S. Boutet, N. W. Moriarty, J. M. Holton, H. Dobbek, P. D. Adams, U. Bergmann, N. K. Sauter, A. Zouni, J. Messinger, J. Yano, V. K. Yachandra, *Nature* **2018**, *563*, 421–425.

[28] M. Suga, F. Akita, K. Yamashita, Y. Nakajima, G. Ueno, H. Li, T. Yamane, K. Hirata, Y. Umena, S. Yonekura, L. Yu, H. Murakami, T. Nomura, T. Kimura, M. Kubo, S. Baba, T. Kumasaka, K. Tono, M. Yabashi, H. Isobe, K. Yamaguchi, M. Yamamoto, H. Ago, J. Shen, *Science* **2014**, *345*, 804–808.

[29] V. Krewald, M. Retegan, N. Cox, J. Messinger, W. Lubitz, S. De Beer, F. Neese, D. A. Pantazis, *Chem. Sci.* **2015**, *6*, 1676–1695.

[30] V. Krewald, M. Retegan, F. Neese, W. Lubitz, D. A. Pantazis, N. Cox, *Inorg. Chem.* **2016**, *55*, 488–501.

[31] I. Zaharieva, P. Chernev, G. Berggren, M. Anderlund, S. Styring, H. Dau, M. Haumann, *Biochemistry* **2016**, *55*, 4197–4211.

[32] I. Zaharieva, H. Dau, M. Haumann, *Biochemistry* **2016**, *55*, 6996–7004.

[33] M. Haumann, P. Liebisch, C. Müller, M. Barra, M. Grabolle, H. Dau, *Science* **2005**, *310*, 1019–1021.

[34] M. Haumann, A. Grundmeier, I. Zaharieva, H. Dau, *PNAS* **2008**, *105*, 17384–17389.

[35] D. R. J. Kolling, T. S. Brown, G. Ananyev, G. C. Dismukes, *Biochemistry* **2009**, *48*, 1381–1389.

[36] N. Cox, D. A. Pantazis, W. Lubitz, *Annu. Rev. Biochem.* **2020**, *89*, 795–820.

[37] Y. Pushkar, K. M. Davis, M. C. Palenik, *J. Phys. Chem. Lett.* **2018**, *9*, 3525–3531.

[38] T. A. Corry, F. Rummel, P. J. O'Malley, *The Journal of Physical Chemistry B* **2021**, *125*, 7147–7154.

[39] F. Neese, *WIREs Computational Molecular Science* **2018**, *8*, e1327.

[40] C. Lee, W. Yang, R. G. Parr, *Phys. Rev. B* **1988**, *37*, 785–789.

[41] A. D. Becke, *The Journal of Chemical Physics* **1993**, *98*, 1372–1377.

[42] E. v. Lenthe, E. J. Baerends, J. G. Snijders, *The Journal of Chemical Physics* **1993**, *99*, 4597–4610.

[43] E. van Lenthe, E. J. Baerends, J. G. Snijders, *The Journal of Chemical Physics* **1994**, *101*, 9783–9792.

[44] C. van Wüllen, *The Journal of Chemical Physics* **1998**, *109*, 392–399.

[45] F. Weigend, R. Ahlrichs, *Phys. Chem. Chem. Phys.* **2005**, *7*, 3297–3305.

[46] P. E. M. Siegbahn, *Proceedings of the National Academy of Sciences* **2017**, *114*, 4966–4968.

[47] A. Altun, J. Breidung, F. Neese, W. Thiel, *Journal of Chemical Theory and Computation* **2014**, *10*, 3807–3820.

[48] K. Eichkorn, O. Treutler, H. Öhm, M. Häser, R. Ahlrichs, *Chemical Physics Letters* **1995**, *240*, 283–290.

[49] F. Eichkorn, Karin and Weigend, O. Treutler, R. Ahlrichs, *Theoretical Chemistry Accounts* **1997**, *97*, 119–124.

[50] F. Weigend, *Phys. Chem. Chem. Phys.* **2006**, *8*, 1057–1065.

[51] V. N. Staroverov, G. E. Scuseria, J. Tao, J. P. Perdew, *The Journal of Chemical Physics* **2003**, *119*, 12129–12137.

[52] F. Neese, F. Wennmohs, A. Hansen, U. Becker, *Chemical Physics* **2009**, *356*, 98–109.

[53] N. Cox, M. Retegan, F. Neese, D. A. Pantazis, A. Boussac, W. Lubitz, *Science* **2014**, *345*, 804–808.

[54] D. A. Pantazis, W. Ames, N. Cox, W. Lubitz, F. Neese, *Angewandte Chemie International Edition* **2012**, *51*, 9935–9940.

[55] S. Grimme, J. Antony, S. Ehrlich, H. Krieg, *The Journal of Chemical Physics* **2010**, *132*, 154104.

[56] S. Grimme, S. Ehrlich, L. Goerigk, *Journal of Computational Chemistry* **2011**, *32*, 1456–1465.

[57] F. Neese, *WIREs Computational Molecular Science* **2012**, *2*, 73–78.

[58] M. Retegan, N. Cox, W. Lubitz, F. Neese, D. A. Pantazis, *Phys. Chem. Chem. Phys.* **2014**, *16*, 11901–11910.

[59] K.-S. Bürger, P. Chaudhuri, K. Wieghardt, B. Nuber, *Chemistry – A European Journal* **1995**, *1*, 583–593.

[60] Y. Liu, F. A. Villamena, A. Rockenbauer, Y. Song, J. L. Zweier, *Journal of the American Chemical Society* **2013**, *135*, 2350–2356.

[61] M. W. Stanford, F. R. Knight, K. S. Athukorala Arachchige, P. Sanz Camacho, S. E. Ashbrook, M. Bühl, A. M. Z. Slawin, J. D. Woollins, *Dalton Trans.* **2014**, *43*, 6548–6560.

[62] L. A. Curtiss, C. A. Naleway, J. R. Miller, *Chemical Physics* **1993**, *176*, 387–405.

[63] M. Di Valentin, C. E. Tait, E. Salvadori, L. Orian, A. Polimeno, D. Carbonera, *Biochimica et Biophysica Acta (BBA) - Bioenergetics* **2014**, *1837*, 85–97.

[64] J. Lin, I. A. Balabin, D. N. Beratan, *Science* **2005**, *310*, 1311–1313.

[65] C. Curutchet, A. A. Voityuk, *The Journal of Physical Chemistry C* **2012**, *116*, 22179–22185.

[66] D. Devault, *Quantum Mechanical Tunneling in Biological Systems*, Cambridge University Press, Cambridge, **1984**.

[67] M. D. Newton, N. Sutin, *Annual Review of Physical Chemistry* **1984**, *35*, 437–480.

[68] R. Marcus, N. Sutin, *Biochimica et Biophysica Acta (BBA) - Reviews on Bioenergetics* **1985**, *811*, 265–322.

[69] A. S. Lukas, P. J. Bushard, M. R. Wasielewski, *The Journal of Physical Chemistry A* **2002**, *106*, 2074–2082.

6.3.7 Supporting Information

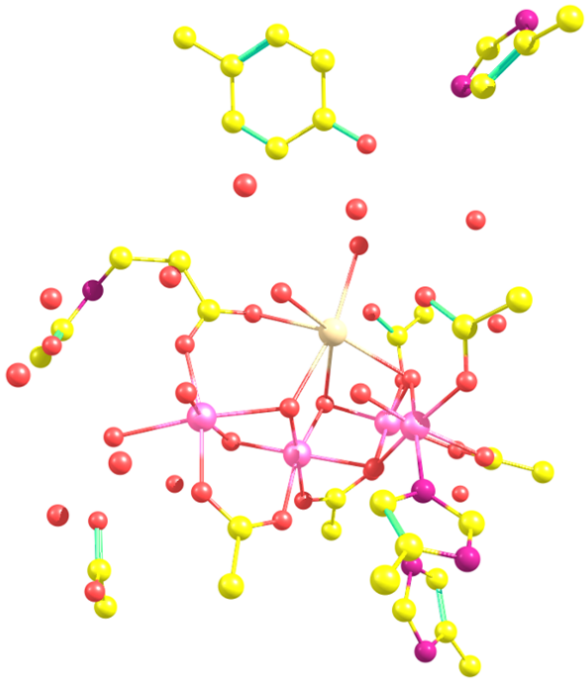

Figure S6.1: Example of model used for all PES calculations. Hydrogens have been excluded for clarity. Colour coding: Mn (purple), oxygen (red), calcium (cream), carbon (yellow) and nitrogen (purple).

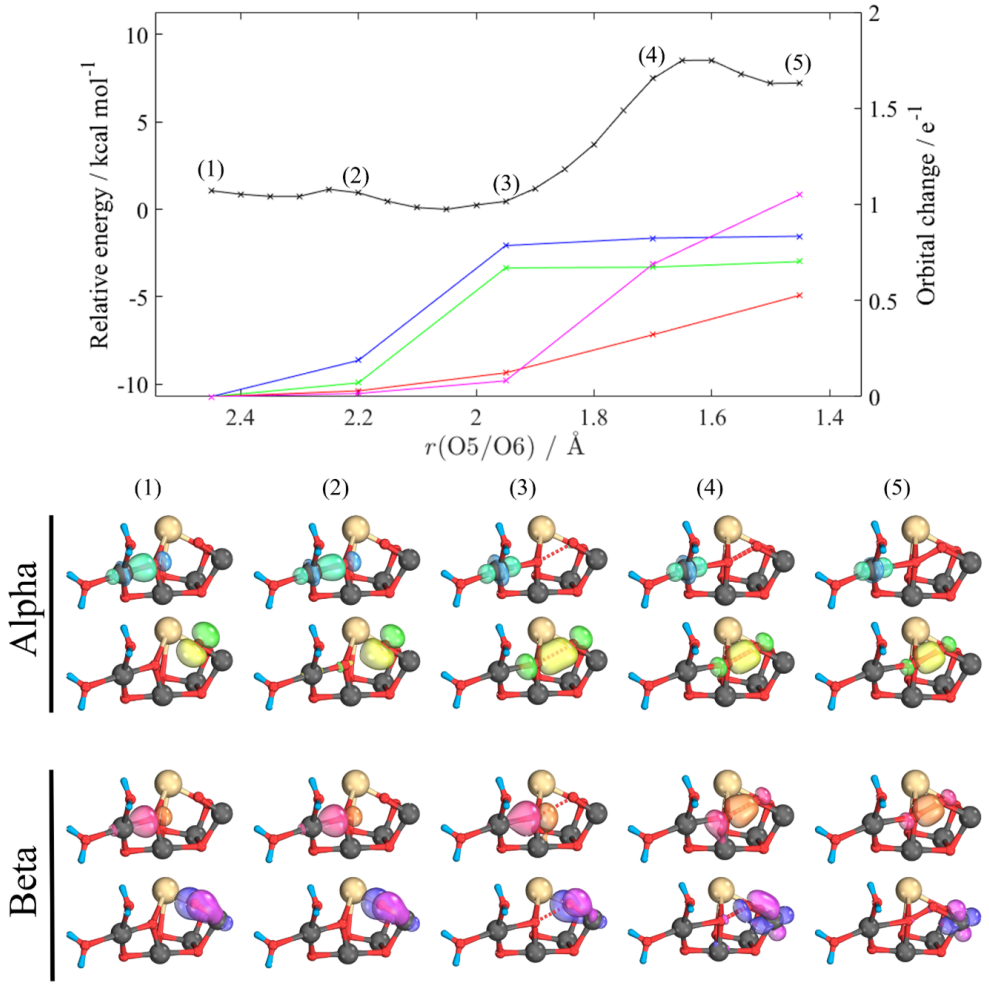

Figure S6.2: Intrinsic bond orbital (IBO) analysis of the Ms= 6.5 state of the oxo-oxo form. Top, potential energy surface (PES) for O5–O6 bond formation (black) with corresponding IBO changes shown beneath, colour coded by orbital. IBOs are given at the labelled points on the PES showing α and β spin evolution.

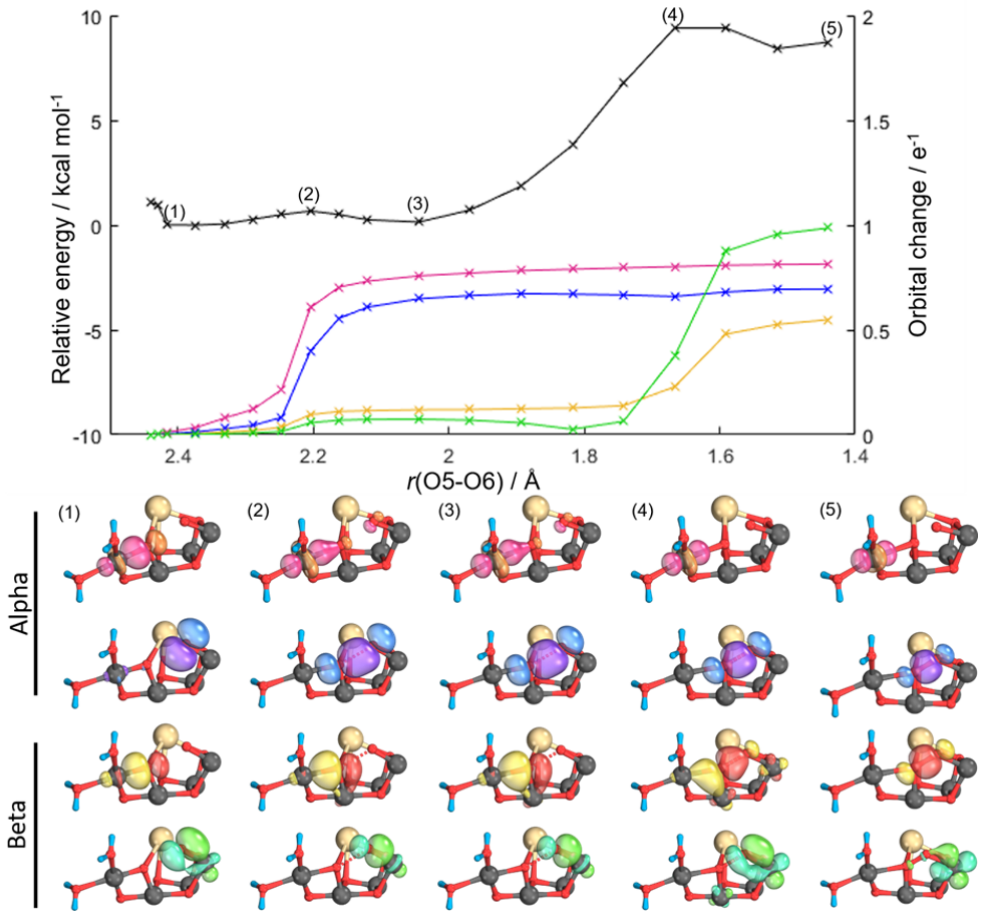

Figure S6.3: Intrinsic bond orbital (IBO) analysis of the Ms= 6 state of the oxo-oxo form in the S3 state. Top, potential energy surface (PES) for O5-O6 bond formation (black) with corresponding IBO changes shown beneath, colour coded by orbital. IBOs are given at the labelled points on the PES showing α and β spin evolution. Reproduced from Rummel et al..[1]

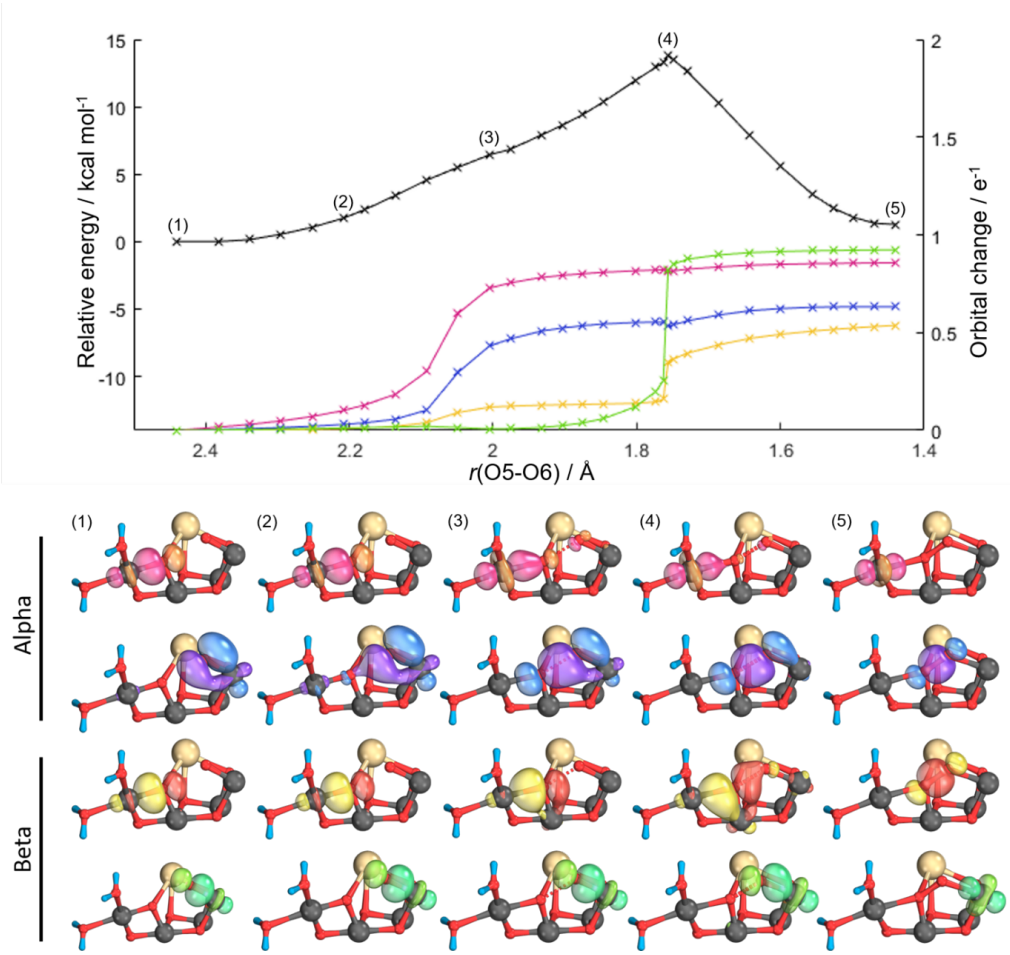

Figure S6.4: Intrinsic bond orbital (IBO) analysis of the Ms= 3 state of the oxo-oxo form in the S3 state. Top, potential energy surface (PES) for O5-O6 bond formation (black) with corresponding IBO changes shown beneath, colour coded by orbital. IBOs are given at the labelled points on the PES showing α and β spin evolution. Reproduced from Rummel et al..[1]

References

[1] F. Rummel, P. J. O'Malley, *The Journal of Physical Chemistry B* **2022**, *126*, 8214–8221.

Chapter 7

The Final Deprotonation of O6 within the S_3 state of Photosystem II

Authors: Thomas Malcomson, Felix Rummel, Maxim Barchenko and Patrick O'Malley

Address: School of Chemistry, The University of Manchester, Manchester, M139PL, U.K.

Submission pending

7.1 Preface

Chapter 5 discussed the nature of the S_3 state, it was proposed that while initially on formation of the S_3 state an O5 oxo-O6 hydroxo structure was present as suggested by EPR data, an equilibrium between the oxo-hydroxo and an O6 deprotonated $[O5O6]^{3-}$ better reproduced and rationalised experimental observations. With 70% $[O5O6]^{3-}$ and 30% oxo-hydroxo giving the best agreement with EPR data. The XFEL data of the S_3 state also suggests a short O5-O6 separation of $\approx$ 2.0 Å, which is best reproduced by $[O5O6]^{3-}$ further supporting this finding while precluding either a peroxo or oxo-hydroxo O5-O6 structure.[1, 2] In order to form an $[O5O6]^{3-}$ or indeed molecular oxygen from O5 and O6 it is necessary to deprotonate O6.

There are several possible pathways for this. The recent PDB:7RF8 S_3 structure[3] would suggest that deprotonation can occur via the nearby Glu189 residue or the Ca bound W3, with W3 being slightly more distant. Experimental evidence of the deprotonation pathway is limited but the proton is thought to leave via the Cl1 channel,[3, 4] potentially via Asp61.[5, 6] A study in the S_2 state showed no minima for the deprotonation pathway to Glu189[7] similarly this study makes a similar finding for the S_3 state giving consistent evidence to its unsuitable nature as a deprotonation pathway.

However it is demonstrated at various O5-O6 separations that abstraction via W3 yields a stable O5 oxo-O6 oxo structure. The stabilising electronic pathways are illustrated and discussed, and PESs for the deprotonations are given.

7.2 Abstract

The deprotonation of O6 within the S3 state marks the final deprotonation event before the formation of oxygen-oxygen bond interactions and eventual production and release of dioxygen. Gaining a thorough understanding of this event, from the proton acceptors involved, to the exfiltration pathways available, is key in determining the nature of the resulting oxygen species, influencing the mechanism through which the first oxygen-oxygen bond forms. Analysis of proton abstraction by the local Glu189 residue provides consistent evidence against this being a viable mechanistic pathway due to the lack of a stable product structure. In contrast, abstraction via W3 shows an increasingly stable oxo-oxo product state between r[O5O6] = 2.1 Å & 1.9 Å. The resulting oxo-oxo state is stabilised through donation of β electron character from O6 to Mn_1 and α electron character from O6 to O5. This donation from the O6 lone pair is shown to be a key factor in stabilising the oxo-oxo state, in addition to showing the initiation of first O5-O6 bond.

7.3 Manuscript

7.3.1 Introduction

Water oxidation in Photosystem II (PSII) is key to the presence of our aerobic atmosphere and as such understanding the catalytic cycle has been of great interest. At the heart of PSII is a $CaMn_4O_{5/6}$ complex, commonly referred to as the oxygen-evolving complex (OEC). Throughout the light driven water oxidation reaction two water molecules are consumed to produce molecular oxygen:

$$2H_2O \xrightarrow{4h\nu} O_2 + 4e^- + 4H^+ \tag{7.1}$$

with this reaction proceeding in a step wise fashion as described by the Kok cycle[8]figure 7.1. Developing an in depth understanding of each event that occurs throughout nature's water oxidation reaction, with particular focus on the sequential deprotonation of each oxygen and the eventual formation of the dioxygen double bond, is key in the development of artificial water splitting complexes, which have direct applications in further addressing the global energy crisis.[9–12]

It is necessary to remove 4 protons throughout the water oxidation reaction. Throughout the S_2 state, and subsequent transition to S_3, the second water molecule is inserted into the OEC and the first of its protons removed. This incoming water is generally thought to insert into the OEC in the "O6" position such that it is bound to Mn_1 (figure 7.2). The general consensus as to the structure of the OEC at the initiation of the S_3 state is an O5 oxo-O6 hydroxo[13–15], as shown in figure 7.2. Recent structural data suggests an O5-O6 distance of ≈ 2.0 Å[1, 16,

17], our group recently proposed that the presence of an equilibrium between this oxo-hydroxo starting structure and an oxo-oxo/$[O5O6]^{3-}$ intermediate structure within the S_3 state is required to rationalise experimental electron paramagnetic resonance (EPR) data with higher accuracy than can be achieved with a pure oxo-hydroxo species.[18, 19]

There are many proposed O–O bond formation mechanisms, predominantly involving bond formation between O5 and O6.[18–26] Additionally, each of these mechanisms agree that, in order to move from an O5 oxo-O6 hydroxo species to molecular oxygen, a further proton must be removed from O6. In the recent PDB:7RF8 S_3 state crystal structure put forward by Hussein et al.[3] two options present themselves based on the availability of proton acceptor species in the local environment: O6 can transfer its proton to the nearby Glu189 residue, situated at a distance of 2.5 Å from O6; or the Ca bound W3, located 3.0 Å from O6 in the resolved crystal structure.

It has been suggested that protons lost from the OEC through the various deprotonation events exit the protein through the Cl1 channel which terminates close to the OEC Mn_4 bound W1 and W2 ligands.[3, 27] Understanding the proton release pathways for the various S state transitions would potentially give insights into the identity, and importance, of the substrate waters throughout the OEC.[28, 29] The proton transfer between W1 and Asp61 has been investigated in more detail by several groups[7, 30–33], and it has been suggested that the nature of the proton pathway between these two facilitates electron transfer from the OEC to the nearby Tyr161 residue in the S_1 to S_2 transition, highlighting the importance

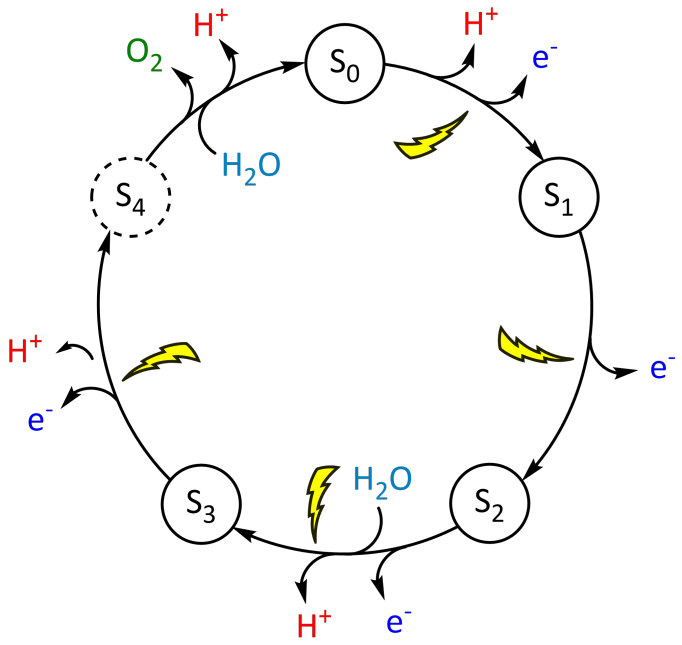

Figure 7.1: Summary of the Kok cycle, summarising the key steps for water oxidation.

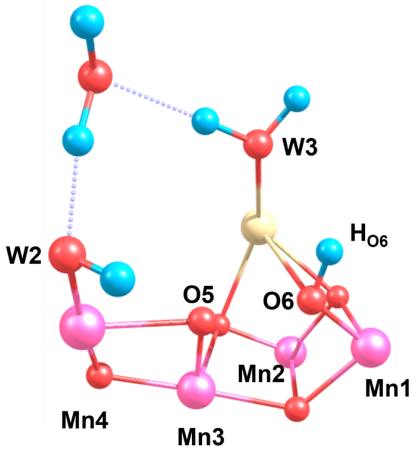

Figure 7.2: Structure of the OEC in the S_3 O5 oxo-O6 hydroxo form, with key residues labelled.

of understanding proton transfer pathways to better rationalise the observed behaviour of the OEC.[31]

While the barrier for W1 to Asp61 proton transfer is generally found to be low so far the O6 to Glu189 barrier has been found to be significant with no stable minima located for a protonated Glu189 in the S_2 state.[7] This study aims to investigate these potential deprotonation pathways in the S_3 state and presents potential energy surfaces for the deprotonation of O6 through abstraction by nearby W3 and Glu189 moieties, and analysis of the relevant structures located on the PES to suggest a potential pathway for O6 deprotonation.

7.3.2 Methods

The methods used are similar to those described previously.[18, 19, 34] All calculations were performed in ORCA 4.2.1.[35] Models were initially optimised using the B3LYP functional[36–39] in their HS oxidation states. The zeroth-order regular approximation (ZORA) Hamiltonian was applied to account for scalar relativistic effects[40–42] with the def2-SVP basis sets used for C and H atoms and the def2-TZVP basis set without f functions for all other atoms.[43]

For the systems presented here the B3LYP functional was chosen as it has a good track record for systems of this size and and for energetics and orbital analysis for the OEC[44] as well as other transition metal systems.[45] The chain of spheres (RIJCOSX) approximation was applied together with the decontracted general Weigend auxiliary basis sets.[46–50] The conductor-like polarizable continuum model (CPCM) [51, 52] with a dielectric constant of $\epsilon = 8.0$ was used throughout to model the protein environment[16, 53], along with the dispersion corrections proposed by Grimme with Becke-Johnson damping (D3BJ).[54–58] Tight SCF convergence criteria and increased integration grids (Grid6 and IntAcc 6 in ORCA

Table 7.1: Mulliken spin distributions of key centres within the OEC, across each broken-symmetry (BS) state presented, at the optimised oxo-hydroxo geometry, with a total system multiplicity of 13 such that $S_{\mathbf{aaaa}}$ = 6 and $S_{\mathbf{baaa/aaba/aaab}}$ = 3.

BS-State	Mn_1	Mn_2	Mn_3	Mn_4	O5	O6
aaaa	3.022	3.008	2.996	3.155	-0.163	0.019
baaa	-3.018	2.990	3.000	3.132	-0.161	-0.029
aaba	3.008	2.989	-2.912	3.066	-0.100	0.020
aaab	3.038	3.006	2.929	-3.059	0.123	0.043

convention) were used throughout, all terminal carbon atoms were constrained during optimisations.

Initial BS-DFT wavefunctions were calculated using ZORA versions of the def2-TZVP with removed f functions for all atoms, and used for potential energy surface calculations.[43] The initial BS guesses were obtained by use of the 'flipspin' feature of ORCA.[59] And convergence of the correct BS and HS states were confirmed by examination of the calculated Mulliken spin populations for all calculations.

All models were generated from the S_3 XFEL crystal structure (PDB: 7RF8)[3] and optimised with an assumed electronic configuration representative of the high-spin (HS) S_3 state with the O5-O6 distance constrained to 2.0 Å to maintain the separation observed in the crystal structure. Twelve directly coordinated amino acids are included in the models: Glu189, His190 , Tyr161 (Y_Z), Asp342, His332, Val185, Glu333, Glu354, Asp170, Ala344, His337, & Asp61. Terminal carbon atoms were modelled as methyl groups (-CH_3) and constrained throughout all calculations.

Additionally, the peptide backbone linking Glu189 and His190 was included to assess the effect on Glu189 orientation, R-groups along the chain were modelled as methyl (-CH_3) groups. The directly coordinated water molecules W1-W4 as well as two bridging and highly resolved crystallographic water molecules were also in-

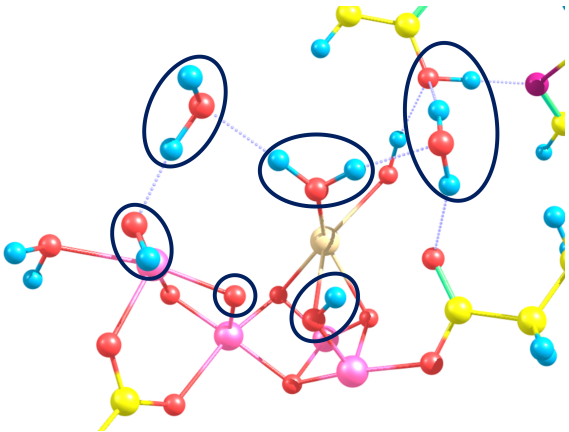

Figure 7.3: Schematic of the oxo-hydroxo structure (additional amino acids removed for clarity), showing the residues left unconstrained (ovals) during the PES optimisations. Carbon = yellow; Oxygen = red; Hydrogen = blue; Manganese = magenta; Calcium = pale brown.

cluded. All oxygen bridges O1-O5 were in their fully deprotonated (O^{2-}) state, O6 was OH^- for the oxo-hydroxo models, and O^{2-} otherwise. W1, W3 and W4 were fully protonated, W2 was OH^- during the optimisation of the oxo-hydroxo starting model. Upon satisfactory optimisation of the HS-13 geometry, further optimisations were conducted with all atoms constrained, with only O5, O6, its corresponding hydrogen, W2, W3, the bridging waters, and the OH group of Yz free to move (figure 7.3). These constraints were deemed accessible through analysis of geometry variation both throughout the MnO complex and the surrounding amino acids, which was observed to be negligible throughout the O5-O6 arrangements studied, in addition to the lack of expected change in geometry throughout the S3 state; in comparison to, as an example, the relative opening of the cubane structure observed in the S2 state, required to facilitate O6 insertion.[3]

Potential energy surfaces were generated utilising the same model chemistry as described above with O5-O6 bond length varied in 0.05 Å steps, where each point underwent optimisation in line with the above constraints to produce the final potential energy surface. Intrinsic bond orbitals (IBOs) were produced using IboView [60, 61] with iboexp=2 from the optimised PES wavefunctions.

Data is presented for four states in total, named in respect to the direction of the unpaired spin on each metal centre, these four states comprise of: a high spin state with a total multiplicity of 13 (S=6), **aaaa**, and three broken symmetry states involving the flipping of the spin on Mn_1 (**baaa**), Mn_3 (**aaba**), and Mn_4 (**aaab**), such that the final spin multiplicity of the complex was 7 (S=3).

For clarity, Mulliken spin distributions, when reported, are presented as the deviation in the magnitude of spin on a given centre along the reaction surface from that of equivalent centre at the oxo-hydroxo geometry in a given electronic state, such that the spin (x) for the O6 centre is expressed as:

$$x^{O6}_{reported} = |x^{O6}|_{scan} - |x^{O6}|_{oxo-hydroxo} \tag{7.2}$$

This has the benefit of presenting a sign-independent interpretation of the spin on a given centre, simplifying the need to account for the inverted spin in the **baaa**,**aaba**, and **aaab** states, such that a positive reported value signifies an increase in overall unpaired spin on a given centre, while a negative value should be interpreted as a reduction in overall unpaired spin (tending to zero) on the centre in question.

7.3.3 Results and Discussion

7.3.3.1 Abstraction by W3

Analysis of the O6-H_{O6} → W3 potential energy surface at an O5-O6 separation of 2.0 Å (figure 7.4), as found in the 7RF8 crystal structure, shows an **aaba** arrangement as the most stable in the oxo-hydroxo state, in line with previous calculations

put forward,[18, 34, 62–64], however all broken-symmetry states are negligibly close in energy at this stage (within 1 kcal mol^{-1}). The difference in energy between the states is shown to steadily increase as the O6-H_{O6} bond is stretched and subsequently breaks, resulting in two clusters: **baaa** and **aaab** which are shown to be disfavoured by $\approx$ 4.5 kcal mol^{-1}; and **aaaa** and **aaba** at lower energies, with **aaaa** being shown to be the most stable at the oxo-oxo geometry. The **aaaa** state boasts a 3.54 kcal mol^{-1} stability over the oxo-hydroxo geometry, providing a promising link with recent independent analysis of the oxo-hydroxo and oxo-oxo states.[18, 34, 62–64] The large drops in energy observed between 1.25 Å and 1.35 Å are attributed to the point at which the proximity of the O6 proton to W3 promotes subsequent and concerted proton transfer from W3 to the local crystallographic water, with a further proton exchange to W2. It is notable that initiation of this transfer occurs earlier for the **aaaa** state than for the others at a O5-O6 separation of 2.0 Å. This transfer marks the dominant shift in the complex from an oxo-hydroxo electronic structure, to one resembling an oxo-oxo arrangement.

Subsequent analysis of the variation in spin on key atomic centres across the reaction coordinate for the **aaaa** state (figure 7.5; top) provides additional insight into the electronic movement within the system. The primary observed change is an increase in the spin on Mn4 (figure 7.5; yellow), which is more pronounced after the W2 protonation, and a decrease in the overall spin on Mn1 (figure 7.5; dark blue). Secondary changes are seen in the spin values of O5 and O6 (figure 7.5; light blue and green, respectively) in which O6 shows an initial gain in spin before a subsequent reduction between 1.25 Å and 1.30 Å, corresponding to a sharp increase in the spin of O5. While the increase in spin found on Mn4 is to be expected, the behaviour of Mn1, O5, & O6 are surprising.

Explanation of the unexpected spin behaviour can be found through consideration of key IBOs in both the oxo-hydroxo and oxo-oxo states (figure 7.6). While initial O6-H_{O6} bond stretch results in minor localisation of the O6 lone pair (LP) onto the oxygen centre, explaining the early increase in spin, transition to an oxo-

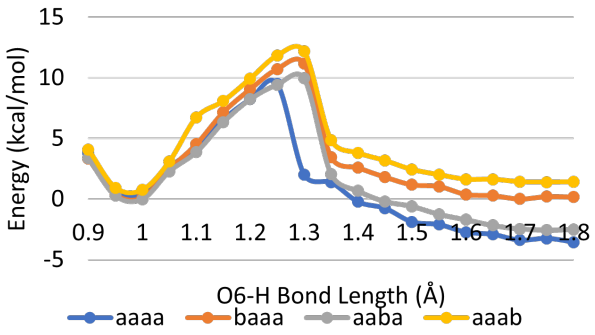

Figure 7.4: Energy profile of scan of increasing O6-H_{O6} distance, towards W3, at a fixed O5-O6 separation of 2.0 Å.

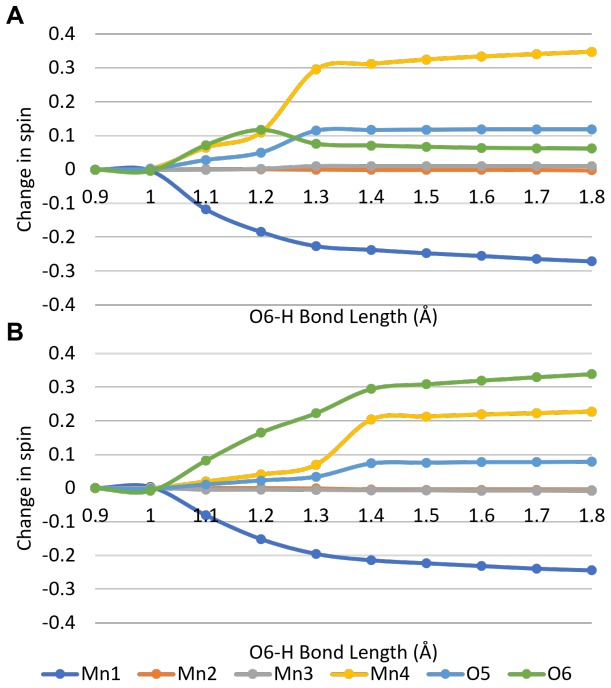

Figure 7.5: Change in absolute spin values of key atomic centres within the system during the oxo-hydroxo to oxo-oxo transition within the **aaaa** state (**A**) and **baaa** state (**B**).

oxo arrangement shows a separation in the O6 LP; movement of the β electron (figure 7.6; top) to the Mn1 centre accounts for the reduction in spin on Mn1 as the incoming β spin pairs with the existing α spin, while concerted movement of the

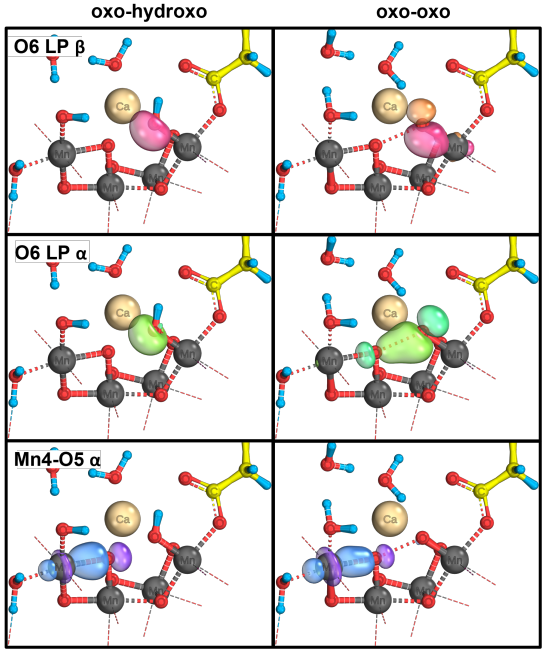

Figure 7.6: IBO representations of the orbitals showing the largest change during the transition between the oxo-hydroxo (left) and oxo-oxo (right) structures in the **aaaa** state, at a fixed O5-O6 distance of 2.0Å, with regards the electronic character of O5, O6, and the Mn centres.

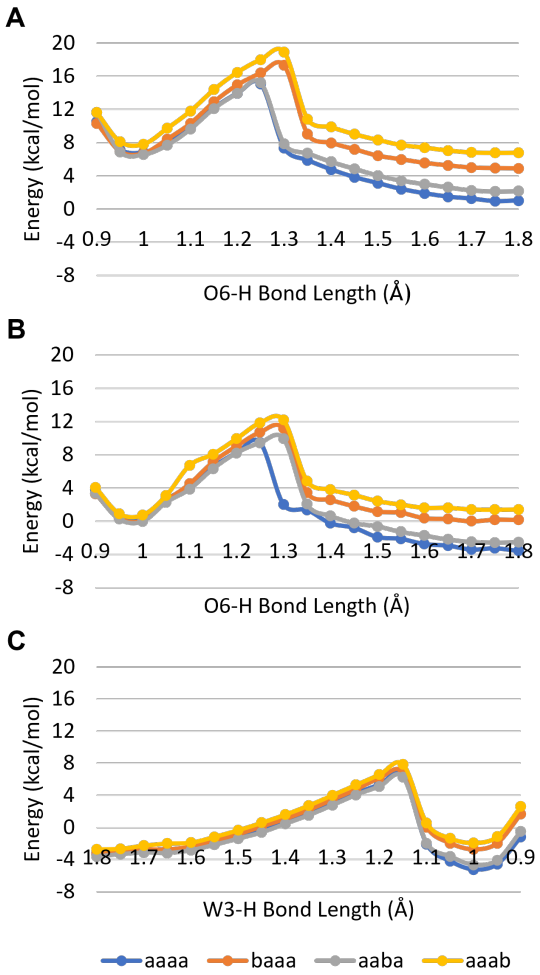

Figure 7.7: Energy profile of **A**: scan of increasing O6-H_{O6} distance, towards W3, at a fixed O5-O6 separation of 1.9 Å; **B**: scan of increasing O6-H_{O6} distance, towards W3, at a fixed O5-O6 separation of 2.0 Å; **C**: scan of decreasing W3-H_{O6} distance, at a fixed O5-O6 separation of 2.1 Å. Each profile is normalised to the HS oxo-hydroxo geometry at r[O5O6] = 2.0 Å.

corresponding α electron (figure 7.6; middle) towards O5 acts to explain the drop in spin on O6 at 1.25 Å, and the resulting increase on the O5 centre, in addition to signifying the initiation of O5-O6 bond formation. The expected increase in spin on the Mn4 centre is rationalised through the movement of an α electron from O5 (figure 7.6; bottom), this movement also accounts for the relatively small overall gain in spin on O5; as α spin is donated from O6, concerted donation of α spin from O5 to Mn4, preventing a large accumulation of spin and, as a result, charge on the O5 centre.

Consideration of changes in the spin distribution, and equivalent IBOs also allow for insight into the difference in energy between the pairs of states shown in figure 7.4. While the **aaba** (figure S7.2; C) state shows a similar spin distribution to that of **aaaa**, **baaa** (figure 7.5; bottom) and **aaab** (figure S7.2; D) present a different distribution. Inversion of the spin on either the Mn1 or Mn4 centres acts to disrupt

the dispersion of residual spin in the oxo-oxo form, post-O6-H_{O6} bond breaking; in the presence of a spin-flipped Mn1 centre, it is an α electron from an O6 LP that now accounts for the decrease in overall spin on Mn1. This, coupled with the unperturbed movement of α spin from O6 to O5 and onward to Mn4, results in a much more significant build up of β spin on the O6 centre, leading to the disfavoured energetics relative to **aaaa**. The spin profile of **aaab** can be explain in an analogous manner, with β spin being pulled from the newly deprotonated O6 to both Mn1 and the spin-flipped Mn4, resulting in an equivalent accumulation of α spin on O6.

7.3.3.2 Variation of O5-O6 Separation

It has been shown previously [18] that complete relaxation of the S3 oxo-hydroxo structure results in a geometric minima with an O5-O6 separation of ≈ 2.4 Å. To investigate the effect of O5-O6 separation on the deprotonation of O6, additional scans were conducted at a separation of 1.9 Å and from 2.1 Å to 2.3 Å. Initial scans were carried out by extending the O6-H_{O6} bond; at 1.9 Å and 2.0 Å these scans resulted in proton abstraction by W3 (figure 7.7; top and middle, respectively), however, at 2.1 Å this approach resulted in an attempted abstraction by Glu189. To address this, an additional scan was conducted by shortening the W3-H_{O6} distance to assess the relevant pathway (figure 7.7; bottom).

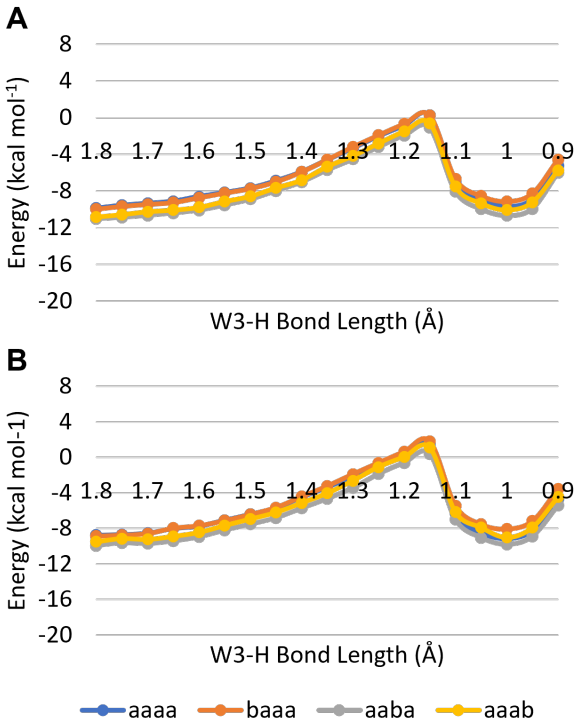

Figure 7.8: **A**: Energy profile of scan of decreasing W3-H_{O6} distance, at a r[O5O6] separation of 2.2 Å; **B**: Energy profile of scan of decreasing W3-H_{O6} distance, at a r[O5O6] separation of 2.3 Å. Each profile is normalised to the HS oxo-hydroxo geometry at r[O5O6] = 2.0 Å.

Comparison of the 1.9 Å and 2.0 Å curves show a near identical profile, with the difference in overall energy explained by the shortening of the O5-O6 distance. The only notable difference in the profiles is the shift of the **aaba** proton rearrangement to coincide with that of the 2.0 Å profile. In contrast, comparison of the 2.0 Å and 2.1 Å surfaces (figure 7.7; middle and bottom, respectively) shows more significant variation. While the relative energy of the oxo-hydroxo starting structure is lower by $\approx$ 4 kcal mol^{-1}, a factor accounted for by the increased O5-O6 distance, the proton rearrangement point also occurs significantly later along the reaction coordinate. Additionally, the resulting oxo-oxo structures, while presenting the same **aaaa**/**aaba** and **baaa**/**aaab** pairings, are significantly less stable compared to the oxo-hydroxo structures ($\approx$ 2 kcal mol^{-1}) than is observed at the r[O5O6] = 2.0 Å geometry.

The explanation for the relative instability of the oxo-oxo structure, particularly in light of the equivalent proton rearrangement barrier ($\approx$ 11 kcal mol^{-1}) can be found in the IBOs (figure S7.19; top) and the spin distribution of the relevant centres (figure S7.4). While these data show similar electron movement as observed at the 2.0 Å separation (figure 7.6) there are notable differences. Donation of the β electron from the O6 LP into the Mn1 centre (figure 7.6 & S7.19; magenta), and an α electron from O5 to Mn4 (figure 7.6; blue, figure S7.19; purple) remains comparable, the increase in O5-O6 distance results in significantly lower transfer of the O6 LP α electron from O6 to O5 (figure 7.6; green, figure S7.19; blue). This lesser degree of electronic donation from O6 to O5 is evident in the relevant spin held on O6 in the oxo-oxo structure; at 2.0 Å this value is 0.081, compared to a value of 0.135 at 2.1 Å. This effect is also observed, to a similar degree, in the O5 and Mn4 centres, showing values of -0.280 & 3.504 at 2.0 Å compared to the reduced -0.260 & 3.459 at 2.1 Å. That the effect of the increased O5-O6 distance is observed on the O6, O5, and Mn4 centres, serves to further suggest that the donation of the α electron from O6 to Mn4 plays a significant role in the eventual reduction of the Mn4 centre as the reaction progresses.

This observation is further evidenced though consideration of the PES at a 2.2 & 2.3 Å O5-O6 separation (figure 7.8). At these separations, the trend of relative destabilisation observed from the 2.0 & and 2.1 Å continues with the oxo-oxo structure now being less stable than their equivalent oxo-hydroxo structure by $\approx$ 1.1 kcal mol^{-1} (2.2 Å) and $\approx$ 1.6 kcal mol^{-1} (2.3 Å), directly linking the O5-O6 distance to the stability of the resulting oxo-oxo structure. Despite their energetic differences, the 2.0 & 2.1 Å spin distributions show similar overall trend regarding the Mn4, O5, & O6 centres; however, increasing r[O5O6] from 2.1 Å to 2.2 Å (figure 7.9) causes a significant change in the the spin distribution, to the point of baring more similarity to the **abaa** & **aaab** distributions at shorter separations (figure 7.5; bottom). The most significant feature is the sole accumulation of spin on the O6

centre, without any corresponding increase in the spin on O5 or Mn4, further showing that the transfer of spin away from O6 and specifically towards Mn4, is a key factor in oxo-oxo stabilisation.

Across the range of r[O5O6] values presented in this work, the observed trend of a steadily increasing stability of the oxo-oxo structure compared to the oxo-hydroxo starting point is most readily explained by behaviour of the α component of the active O6 lone pair. Considering the IBO representation of this orbital at different values of r[O5O6] (figure 7.10) shows minimal change in character at the oxo-hydroxo geometry while, in the oxo-oxo structure, a steadily increasing orbital change is observed from r[O5O6] = 2.1 Å to r[O5O6] = 1.9 Å (figure 7.10; A), forming an overlap with O5 in line with the initiation of a one electron bond (figure 7.10; B). In contrast, no such overlap is observed at r[O5O6] = 2.2 or 2.3 Å; a small degree of orbital distortion is observed in the oxo-oxo structure suggesting the distance is still small enough to allow for interaction between the O5 and O6 centres, but too long to allow for any electron sharing.

A direct comparison of this data should be drawn with similar data put forward by Isobe et al. [65] based on the 5WS6 crystal structure derived by Suga et al..[17] A transition barrier of $\approx$ 24 kcal mol^{-1} is quoted, a significant increase when compared to the barrier presented here. However, the model presented by Isobe et al. assumes the direct transfer of a proton from W3 to W2; to facilitate this transfer, a substantial rearrangement of both the Mn4 and Ca coordination geometries is

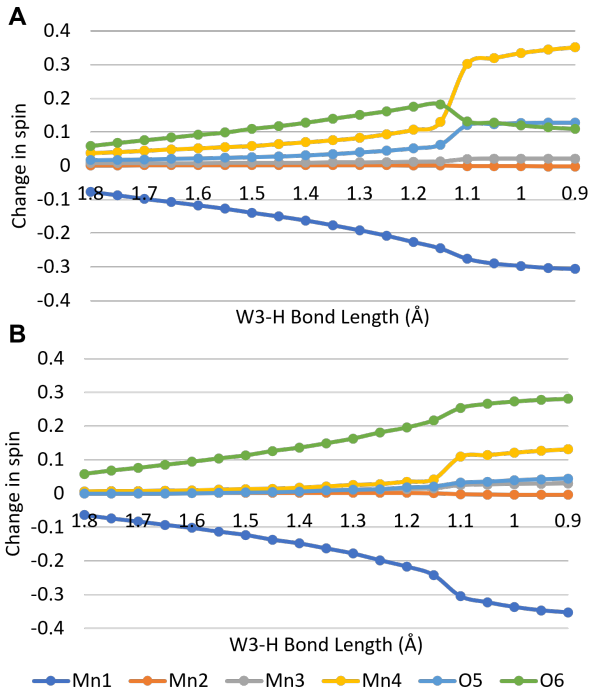

Figure 7.9: Change in absolute spin values of key atomic centres within the system during the oxo-hydroxo to oxo-oxo transition within the **aaaa** state at r[O5O6] = 2.1 Å (**A**) and r[O5O6] = 2.2 Å (**B**).

required, introducing significant strain on the system. In comparison, the presence of a crystallographic water bridging W3 and W2 as found in the 7RF8 structure [3] and by extension, the model presented here, which acts to mitigate the need for that strain and, as a result, lowering the overall barrier for proton rearrangement.

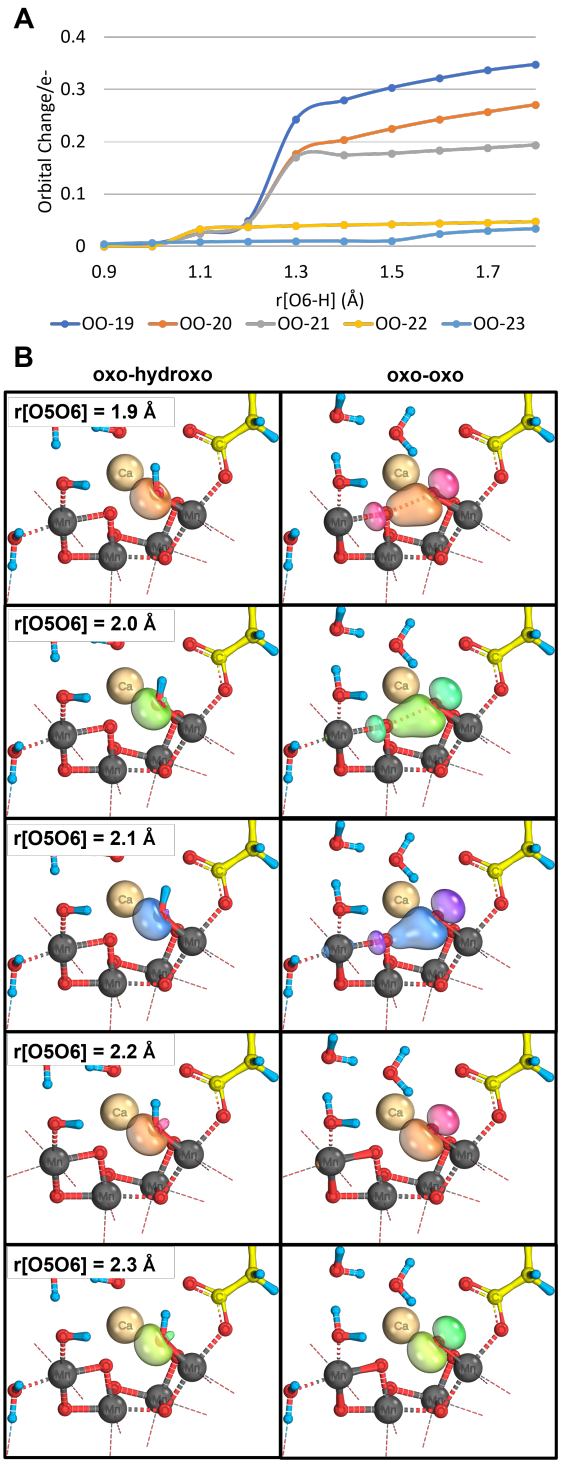

Figure 7.10: **A**: Plot of IBO changes for the α component of the O6 LP during abstraction by W3 at differing values of r[O5O6] in the **aaaa** state; **B**: corresponding IBO representation of the α component of the O6 LP at the oxo-hydroxo (left) and oxo-oxo (right) structures during W3 abstraction.

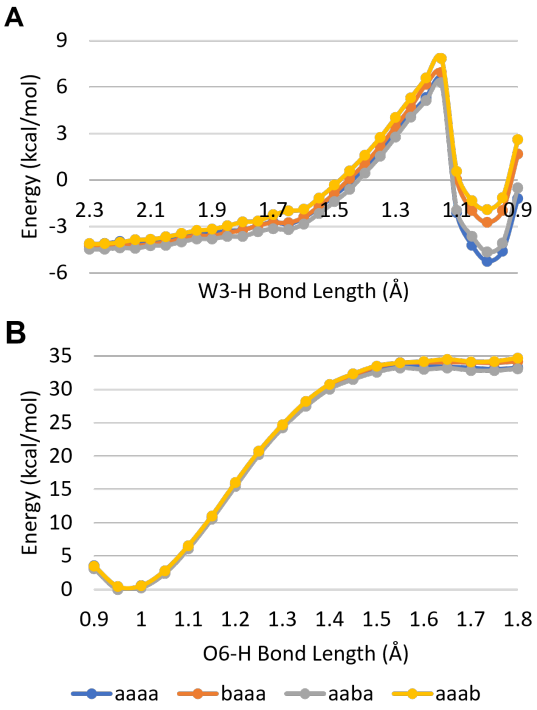

Figure 7.11: Energy profile of **A**: full scan of increasing O6-H_{O6} distance, towards W3, at a fixed O5-O6 separation of 2.0 Å; **B**: scan of increasing O6-H_{O6} distance, towards Glu189, at a fixed O5-O6 separation of 2.1 Å.

Additionally, while the transition presented by Isobe et al. showed a r[O5O6] = 2.41 Å this distance, as shown throughout this work would negate any stabilisation from the formation of the one-electron bond between the O5 and O6 centres. In contrast, at the 2.0 Å separation presented here, this stabilisation is not only possible, but is shown to play a central role in the stabilisation of the deprotonated product.

7.3.3.3 W3 vs. Glu189 Abstraction

Given its close proximity to O6, and prevalence in the literature, in order to access the performance of Glu189 as an alternative proton acceptor, an equivalent analysis was conducted at an O5-O6 separation of 2.1 Å and 2.2 Å. These separations were chosen due to the observation that, while simply extending the O6-H_{O6} bond at 1.9 & 2.0 Å resulted in abstraction by W3, with no interference from Glu189, at 2.1 Å lengthening of the O6-H_{O6} bond resulted in attempted abstraction by Glu189; in contrast, modelling abstraction by W3 required a specific shortening of the W3-H_{O6} distance.

While consideration of the W3 abstraction profile (figure 7.11; A) shows a clear reaction profile, resulting in the expected split in BS states and a marginally more stable oxo-oxo form when compared to the oxo-hydroxo starting point, the profile of the abstraction by Glu189 presents a stark contrast. Initial consideration of the Glu189 abstraction profile (figure 7.11; B) reveals that, not only does stretching the

O6-H_{O6} bond result in an ≈ 33 kcal mol^{-1} destabilisation of the complex, but that there is only negligible local minimum to be found with Glu189 protonated (≈ 0.5 kcal mol^{-1} for the **aaaa** state). Explanation of this significant destabilisation can be rationalised through the IBO and spin data for this particular reaction profile (figure 7.12; top and bottom, respectively); instead of an O6 lone pair proceeding to interact with the surrounding Mn centres, as seen in the W3 abstraction (figures 7.6 & S7.19), the lack of rotation of the O6-H_{O6} bond away from Glu189 and towards the calcium prevents the orientation, and resulting overlap necessary to allow for lone pair interaction as the O6-H_{O6} bond stretches. Instead, figure 7.12 highlights that it is the β electron of the O6-H_{O6} bond that proceeds to interact with Mn1; in contrast, the α electron from the O6-H_{O6} bond remains localised to the O6 centre, with a significant distortion towards the Glu189-H_{O6} centre suggesting the maintenance of a significant hydrogen bond character between O6 and H_{O6} which, coupled with the larger electronegativity to be expected on O6 in comparison to the corresponding oxygen on Glu189, provides insight to the lack of a Glu189-H_{O6} local

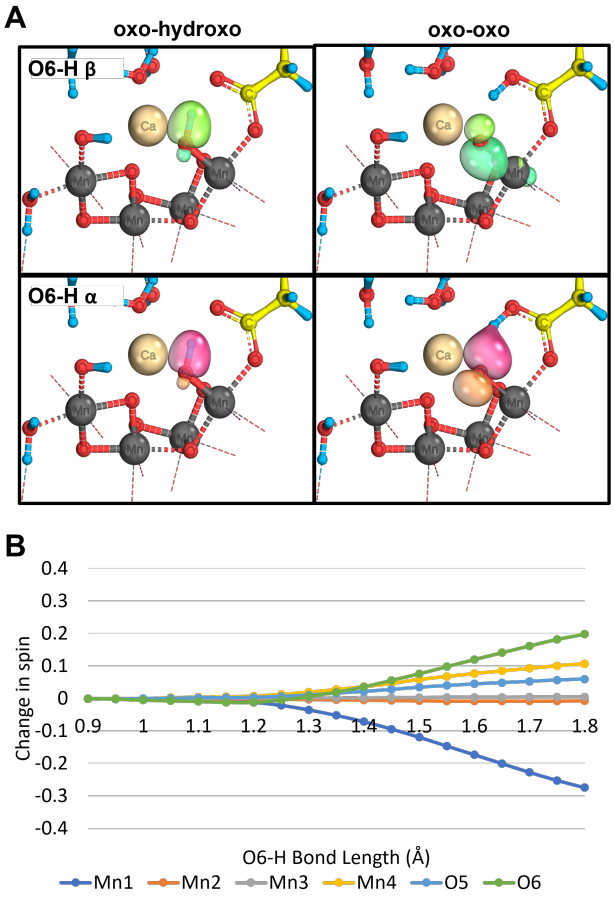

Figure 7.12: Orbital and spin analysis during Glu189 abstraction in the **aaaa** state at a fixed O5-O6 distance of 2.1Å. **A**: IBO representations of the orbitals showing the largest change over the transition between the oxo-hydroxo (left) and oxo-oxo (right) structures. **B**: The corresponding change in spin distribution with regard to the O5, O6, and Mn centres.

minimum, with the pull from O6, held in close proximity to H_{O6} promoting a near barrierless re-abstraction pathway, returning H_{O6} to O6, resulting once again in the vastly more stable oxo-hydroxo structural arrangement.

These data, in which abstraction via Glu189 is highly disfavoured, presents a similar description as that put forward by Mandal et al..[7] In addition to the presentation of both spin and orbital analysis (figure 7.12) to explain the source of the disfavoured energetics, the proposed abstraction via W3 and eventual protonation of W2 results fits into the findings of Mandal et al.[7] in which, of the ligated water molecules throughout the OEC, the protons of W1 are shown to be the most labile, presenting a minimal transfer barrier between W1 and the local Asp61 residue. These findings, when coupled, further suggest that proton egress may occur through the O4 channel, facilitated though inter-ligand proton transfer from W2 to W1.

Despite the clear energetic preference for abstraction via W3, lengthening of the O6-H_{O6} bond alone did not appear to promote this result. However, this can be explained through analysis of the complete range of the corresponding W3 abstraction profile (figure 7.11; A); the rotation of the O6-H_{O6} bond to orientate towards W3 is associated with an $\approx$ 1 kcal mol^{-1} barrier before interaction with W3 occurs at the small shoulder observed at 1.65 Å. While small, this barrier is sufficient to prevent an optimisation from choosing to rotate away from the Glu189 orientation, akin to opting to remain in the same valley despite the steep climb.

In addition to the strong energetic, and electronic arguments against abstraction by Glu189, it is also worth considering the structural arguments against this pathway, each of which has a corresponding point of favour in terms of W3 abstraction. These arguments primarily revolve around the idea that in situation in which Glu189 is protonated, there is no clear and/or obvious pathway through which the deprotonation can occur (omitting O6 as an option) in order to reset Glu189 before reorientation and re-coordination to the calcium centre during the next catalytic cycle with only two possible pathways presenting themselves. The first of these involves subsequent deprotonation of Glu189 through W7, onwards to Y_Z, and proceeding out through the Y_Z network,[3] for which there is no experimental precedent, primarily as it would involve the loss of the Y_Z proton, in contrast to the commonly held proton-switch mechanism in which the same proton moves from Y_Z to His-190 and back again depending on the oxidation state of Y_Z. The second pathway involves passing the proton back into the 5-member water wheel[3] for it to then proceed back out through the O1 channel. Both of these options necessitate a substantial reorientation of the Glu189-H_{O6} bond which presents a significant barrier for the required rotation, in addition to presenting poor interaction with the relevant water molecules that would be required for further proton transfer.

In contrast, abstraction through W3, in addition to the energetic and electronic results, also presents two clear potential routes for eventual expulsion of the proton

into the lumen. The first of these, as modelled here, involves a shuffling of protons toward W2 where inter-ligand proton transfer between W2 & W1 provides access to the coordinating Asp residue and subsequently to the O4 channel. Alternatively, should the protonation state of W1 & W2 result in inability for proton acceptance, the conserved crystallographic water modelled here provides a link to the Cl channel which has been strongly argued as a proton transfer route by Hussein et al..[3]

Each of these structural arguments, relying on well understood features, acts to further bolster the identification of W3 as the preferred proton acceptor when it comes to the final deprotonation of O6.

7.3.4 Conclusions and Outlook

A comprehensive analysis of proton abstraction via the Ca-coordinated W3 shows a steady increase in the relative stability of the deprotonated oxo-oxo state with decreasing r[O5O6] separation, when compared to the oxo-hydroxo starting structure. Interpretation of both spin and IBO data across the potential energy surfaces presented throughout this work highlights that the nature of this emerging stability is driven by the ability of O6 to distribute the resulting spin across the Mn_1 and O5 centres, preventing an overall accumulation of charge on O6. The distribution of α spin from an O6 lone pair across O5 and Mn_4 results in initial formation of a partial O5-O6 bond, while donation of the corresponding β spin to Mn_1 acts to stabilise the second electron before formation of the first bond is competed. Interruption of these spin distribution pathways, as observed in the **baaa** & **aaab** states, results in a significant accumulation of spin on the O6 centre and a corresponding reduction in stabilisation when compared to the oxo-hydroxo equivalent.

Similar analysis of abstraction via Glu189 provides significant evidence against the prevalence of this pathway with no stable oxo-oxo minima observed. Instead, the lack of rotation around the O6-Mn_1 bond results in the active electrons coming instead from the O6-H_{O6} bond; additionally, while donation of the β electron towards Mn_1 still occurs, the formation of a hydrogen bond from the newly protonated Glu189 back to O6 results in reduced movement of α electron required for O5-O6 bond formation.

Overall, this work presents a strong case for both proton abstraction via W3, in addition to the emergence of an oxo-oxo electronic arrangement as a result of the final O6 deprotonation event. Despite the close proximity, and optimal hydrogen-bond orientation, of Glu189 in a wide range of modern crystal structures, we are able to demonstrate, and provide reasoning, for this residue being an inviable proton acceptor within the S3 state, failing to reproduce the relevant electronic arrangement, or a route for proton egress from the OEC.

7.3.5 Conflicts of interest

There are no conflicts to declare.

7.3.6 Acknowledgements

This research was supported with a grant from the Leverhulme Trust (RPG-2020-003). FR acknowledges support from the UK BBSRC Doctoral Training Partnership (DTP) program. The authors would like to acknowledge the assistance given by Research IT and the use of the Computational Shared Facility at The University of Manchester.

References

[1] J. Kern, R. Chatterjee, I. D. Young, F. D. Fuller, L. Lassalle, M. Ibrahim, S. Gul, T. Fransson, A. S. Brewster, R. Alonso-Mori, R. Hussein, M. Zhang, L. Douthit, C. de Lichtenberg, C. M. H., D. Shevela, J. Wersig, I. Seuffert, D. Sokaras, E. Pastor, C. Weninger, T. Kroll, R. G. Sierra, P. Aller, A. Butryn, A. M. Orville, M. Liang, A. Batyuk, J. E. Koglin, S. Carbajo, S. Boutet, N. W. Moriarty, J. M. Holton, H. Dobbek, P. D. Adams, U. Bergmann, N. K. Sauter, A. Zouni, J. Messinger, J. Yano, V. K. Yachandra, *Nature* **2018**, *563*, 421–425.

[2] M. Suga, F. Akita, K. Yamashita, Y. Nakajima, G. Ueno, H. Li, T. Yamane, K. Hirata, Y. Umena, S. Yonekura, et al., *Science* **2019**, *366*, 334–338.

[3] R. Hussein, M. Ibrahim, A. Bhowmick, P. S. Simon, R. Chatterjee, L. Lassalle, M. D. Doyle, I. Bogacz, I. Kim, M. H. Cheah, S. Gul, C. de Lichtenberg, P. Chernev, C. C. Pham, I. D. Young, S. Carbajo, F. D. Fuller, R. Alonso-Mori, A. Batyuk, K. D. Sutherlin, A. S. Brewster, R. Bolotovski, D. Mendez, J. M. Holton, N. W. Moriarty, P. D. Adams, U. Bergmann, N. K. Sauter, H. Dobbek, A. Messinger, J. Zouni, J. Kern, V. K. Yachandra, J. Yano, *Nat. Commun.* **2021**, *12*, 6531.

[4] M. Ibrahim, T. Fransson, R. Chatterjee, M. H. Cheah, R. Hussein, L. Lassalle, K. D. Sutherlin, I. D. Young, F. D. Fuller, S. Gul, et al., *Proceedings of the National Academy of Sciences* **2020**, *117*, 12624–12635.

[5] P. Greife, M. Schönborn, M. Capone, R. Assunção, D. Narzi, L. Guidoni, H. Dau, *Nature* **2023**, *617*, 623–628.

[6] A. Bhowmick, R. Hussein, I. Bogacz, P. S. Simon, M. Ibrahim, R. Chatterjee, M. D. Doyle, M. H. Cheah, T. Fransson, P. Chernev, I.-S. Kim, H. Makita, M. Dasgupta, C. J. Kaminsky, M. Zhang, J. Gätcke, S. Haupt, I. I. Nangca, S. M. Keable, A. O. Aydin, K. Tono, S. Owada, L. B. Gee, F. D. Fuller, A. Batyuk, R. Alonso-Mori, J. M. Holton, D. W. Paley, N. W. Moriarty, F. Mamedov, P. D. Adams, A. S. Brewster, H. Dobbek, N. K. Sauter, U. Bergmann, A. Zouni, J. Messinger, J. Kern, J. Yano, V. K. Yachandra, *Nature* **2023**, *617*, 629–636.

[7] M. Mandal, K. Saito, H. Ishikita, *The Journal of Physical Chemistry Letters* **2020**, *11*, 10262–10268.

[8] B. Kok, B. Forbush, M. McGloin, *Photochemistry and Photobiology* **1970**, *11*, 457–475.

[9] H. Dau, E. Fujita, L. Sun, *ChemSusChem* **2017**, *10*, 4228–4235.

[10] N. Cox, D. A. Pantazis, F. Neese, W. Lubitz, *Interface Focus* **2015**, *5*, 20150009.

[11] T. A. Faunce, W. Lubitz, A. W. Rutherford, D. R. MacFarlane, G. F. Moore, P. Yang, D. G. Nocera, T. A. Moore, D. H. Gregory, F. S., K. B. Yoon, F. A. Armstrong, M. R. Wasielewski, S. Styring, *Energy Envirn. Sci.* **2013**, *6*, 695–698.

[12] M. Gratzel, *Inorg. Chem.* **2005**, *44*, 6841–6851.

[13] V. Krewald, M. Retegan, N. Cox, J. Messinger, W. Lubitz, S. De Beer, F. Neese, D. A. Pantazis, *Chem. Sci.* **2015**, *6*, 1676–1695.

[14] V. Krewald, M. Retegan, F. Neese, W. Lubitz, D. A. Pantazis, N. Cox, *Inorg. Chem.* **2016**, *55*, 488–501.

[15] I. Zaharieva, P. Chernev, G. Berggren, M. Anderlund, S. Styring, H. Dau, M. Haumann, *Biochemistry* **2016**, *55*, 4197–4211.

[16] M. Suga, F. Akita, K. Yamashita, Y. Nakajima, G. Ueno, H. Li, T. Yamane, K. Hirata, Y. Umena, S. Yonekura, L. Yu, H. Murakami, T. Nomura, T. Kimura, M. Kubo, S. Baba, T. Kumasaka, K. Tono, M. Yabashi, H. Isobe, K. Yamaguchi, M. Yamamoto, H. Ago, J. Shen, *Science* **2014**, *345*, 804–808.

[17] M. Suga, F. Akita, M. Sugahara, M. Kubo, Y. Nakajima, T. Nakane, K. Yamashita, Y. Umena, M. Nakabayashi, T. Yamane, N. T., M. Suzuki, T. Masuda, S. Inone, T. Kimura, T. Nomura, S. Yonejura, L. Yu, T. Sakamoto, T. Motomura, J. Chen, Y. Kato, T. Noguchi, K. Tono, Y. Joti, T. Kameshima, T. Hatsui, E. Nango, R. Tanaka, H. Naitow, Y. Matsuura, A. Yamashita, M. Yamamoto, O. Nureki, M. Yabashi, T. Ishikawa, S. Iwata, J. Shen, *Nature* **2017**, *543*, 131–135.

[18] F. Rummel, P. J. O'Malley, *The Journal of Physical Chemistry B* **2022**, *126*, 8214–8221.

[19] T. A. Corry, P. J. O'Malley, *The Journal of Physical Chemistry Letters* **2018**, *9*, 6269–6274.

[20] T. A. Betley, Y. Surendranath, M. V. Childress, G. E. Alliger, R. Fu, C. C. Cummins, D. G. Nocera, *Philosophical Transactions of the Royal Society B: Biological Sciences* **2008**, *363*, 1293–1303.

[21] P. D. A., *Inorganics* **2019**, *7*, 55–85.

[22] T. Saito, S. Yamanaka, K. Kanda, H. Isobe, Y. Takano, Y. Shigeta, Y. Umena, K. Kawakami, J.-R. Shen, N. Kamiya, M. Okumura, M. Shoji, Y. Yoshioka, K. Yamaguchi, *International Journal of Quantum Chemistry* **2012**, *112*, 253–276.

[23] D. J. Vinyard, S. Khan, G. W. Brudvig, *Faraday Discuss.* **2015**, *185*, 37–50.

[24] V. Krewald, F. Neese, D. A. Pantazis, *Journal of Inorganic Biochemistry* **2019**, *199*, 110797.

[25] T. A. Corry, P. J. O'Malley, *The Journal of Physical Chemistry Letters* **2020**, *11*, 4221–4225.

[26] P. E. Siegbahn, *Biochimica et Biophysica Acta (BBA) - Bioenergetics* **2013**, *1827*, 1003–1019.

[27] M. Ibrahim, T. Fransson, R. Chatterjee, M. H. Cheah, R. Hussein, L. Lassalle, K. D. Sutherlin, I. D. Young, F. D. Fuller, S. Gul, I.-S. Kim, P. S. Simon, C. de Lichtenberg, P. Chernev, I. Bogacz, C. C. Pham, A. M. Orville, N. Saichek, T. Northen, A. Batyuk, S. Carbajo, R. Alonso-Mori, K. Tono, S. Owada, A. Bhowmick, R. Bolotovsky, D. Mendez, N. W. Moriarty, J. M. Holton, H. Dobbek, A. S. Brewster, P. D. Adams, N. K. Sauter, U. Bergmann, A. Zouni, J. Messinger, J. Kern, V. K. Yachandra, J. Yano, *Proceedings of the National Academy of Sciences* **2020**, *117*, 12624–12635.

[28] N. Cox, D. A. Pantazis, F. Neese, W. Lubitz, *Accounts of Chemical Research* **2013**, *46*, 1588–1596.

[29] M. Askerka, G. W. Brudvig, V. S. Batista, *Accounts of Chemical Research* **2017**, *50*, 41–48.

[30] H. Kuroda, K. Kawashima, K. Ueda, T. Ikeda, K. Saito, R. Ninomiya, C. Hida, Y. Takahashi, H. Ishikita, *Biochimica et Biophysica Acta (BBA) - Bioenergetics* **2021**, *1862*, 148329.

[31] K. R. Yang, K. V. Lakshmi, G. W. Brudvig, V. S. Batista, *Journal of the American Chemical Society* **2021**, *143*, 8324–8332.

[32] D. Narzi, D. Bovi, L. Guidoni, *Proceedings of the National Academy of Sciences* **2014**, *111*, 8723–8728.

[33] K. Kawashima, T. Takaoka, H. Kimura, K. Saito, H. Ishikita, *Nature Communications* **2018**, *9*, 1247.

[34] T. A. Corry, F. Rummel, P. J. O'Malley, *The Journal of Physical Chemistry B* **2021**, *125*, 7147–7154.

[35] F. Neese, *WIREs Computational Molecular Science* **2018**, *8*, e1327.

[36] B. Miehlich, A. Savin, H. Stoll, H. Preuss, *Chem. Phys. Lett.* **1989**, *157*, 200.

[37] C. Lee, W. Yang, R. G. Parr, *Phys. Rev. B* **1988**, *37*, 785.

[38] A. D. Becke, *J. Chem. Phys.* **1993**, *98*, 1372.

[39] A. D. Becke, *Phys. Rev.* **1988**, *38*, 3098.

[40] E. v. Lenthe, E. J. Baerends, J. G. Snijders, *The Journal of Chemical Physics* **1993**, *99*, 4597–4610.

[41] E. van Lenthe, E. J. Baerends, J. G. Snijders, *The Journal of Chemical Physics* **1994**, *101*, 9783–9792.

[42] C. van Wüllen, *The Journal of Chemical Physics* **1998**, *109*, 392–399.

[43] F. Weigend, R. Ahlrichs, *Phys. Chem. Chem. Phys.* **2005**, *7*, 3297–3305.

[44] P. E. M. Siegbahn, *Proceedings of the National Academy of Sciences* **2017**, *114*, 4966–4968.

[45] A. Altun, J. Breidung, F. Neese, W. Thiel, *Journal of Chemical Theory and Computation* **2014**, *10*, 3807–3820.

[46] K. Eichkorn, O. Treutler, H. Öhm, M. Häser, R. Ahlrichs, *Chemical Physics Letters* **1995**, *240*, 283–290.

[47] F. Eichkorn, Karin and Weigend, O. Treutler, R. Ahlrichs, *Theoretical Chemistry Accounts* **1997**, *97*, 119–124.

[48] F. Weigend, *Phys. Chem. Chem. Phys.* **2006**, *8*, 1057–1065.

[49] V. N. Staroverov, G. E. Scuseria, J. Tao, J. P. Perdew, *The Journal of Chemical Physics* **2003**, *119*, 12129–12137.

[50] F. Neese, F. Wennmohs, A. Hansen, U. Becker, *Chemical Physics* **2009**, *356*, 98–109.

[51] J. Tomasi, B. Mennucci, R. Cammi, *Chem. Rev.* **2005**, *105*, 2999.

[52] F. Lipparini, G. Scalmani, B. Mennucci, E. Cances, M. Caricato, M. J. Frisch, *J. Chem. Phys.* **2010**, *133*, 014106.

[53] D. A. Pantazis, W. Ames, N. Cox, W. Lubitz, F. Neese, *Angewandte Chemie International Edition* **2012**, *51*, 9935–9940.

[54] S. Grimme, S. Ehrlich, L. Goerigk, *J. Comp. Chem.* **2011**, *32*, 1456.

[55] A. D. Becke, E. R. Johnson, *J. Chem. Phys.* **2007**, *127*, 154108.

[56] A. D. Becke, E. R. Johnson, *J. Chem. Phys.* **2005**, *122*, 154104.

[57] A. D. Becke, E. R. Johnson, *J. Chem. Phys.* **2005**, *123*, 154101.

[58] A. D. Becke, E. R. Johnson, *J. Chem. Phys.* **2006**, *124*, 174104.

[59] F. Neese, *WIREs Computational Molecular Science* **2012**, *2*, 73–78.

[60] G. Knizia, *J. Chem. Theory Comput.* **2013**, *9*, 4834–4843.

[61] G. Knizia, J. E. M. N. Klein, *Angew. Chem. Int. Ed.* **2015**, *54*, 5518–5522.

[62] T. A. Corry, P. J. O'Malley, *The Journal of Physical Chemistry Letters* **2018**, *9*, 6269–6274.

[63] T. A. Corry, P. J. O'Malley, *The Journal of Physical Chemistry Letters* **2020**, *11*, 4221–4225.

[64] T. A. Corry, P. J. O'Malley, *The Journal of Physical Chemistry B* **2021**, *125*, 10097–10107.

[65] H. Isobe, M. Shoji, T. Suzuki, J. Shen, K. Yamaguchi, *J. Chem. Theory Comput.* **2019**, *15*, 2375–2391.

7.3.7 Supporting Information

7.3.7.1 Model Geometry

Table S7.1: Geometry of pre-optimised model used throughout the study, optimised at r[O5O6] = 2.0 Å. [a] atoms that are capable of moving during relaxed scans.

Atom Type	Scan Optimised [a]	x	y	z
C		-33.335245000	30.225279000	362.194816000
C		-33.749667000	31.522500000	361.494774000
O		-32.799683000	32.345953000	361.258651000
O		-34.950474000	31.687701000	361.176655000
H		-34.201663000	29.704161000	362.615765000
H		-32.601005000	30.423230000	362.984198000
C		-30.637232000	44.240445000	355.587139000
C		-31.163688000	44.066705000	356.985760000
C		-31.308529000	45.176597000	357.831293000
C		-31.552584000	42.809701000	357.475280000
C		-31.829613000	45.047549000	359.118448000
C		-32.083704000	42.660722000	358.758983000
C		-32.227397000	43.784456000	359.580677000
O	YES	-32.763062000	43.616179000	360.828032000
H		-31.418560000	44.618720000	354.911281000
H		-30.270294000	43.294332000	355.171022000
H		-30.998982000	46.161287000	357.478731000
H		-31.434374000	41.929325000	356.842982000
H		-31.924740000	45.917112000	359.764404000
H		-32.398605000	41.688028000	359.136910000
H	YES	-32.833388000	44.519291000	361.333295000
C		-31.171265000	38.504616000	358.971560000
C		-31.730724000	38.140484000	360.326591000
O		-32.388570000	37.034638000	360.322129000
O		-31.578566000	38.880567000	361.310320000
H		-30.402546000	39.277013000	359.059915000
H		-32.007891000	38.896109000	358.376189000
C		-39.601287000	40.793719000	361.635117000
C		-38.367220000	40.330575000	362.421451000
C		-38.625757000	40.394606000	363.931766000
C		-37.930639000	38.918128000	362.003905000
H		-40.458270000	40.130675000	361.827496000
H		-37.535075000	41.010143000	362.184388000

H	-37.734625000	40.118426000	364.505002000
H	-38.934812000	41.402394000	364.242141000
H	-39.431376000	39.702731000	364.217032000
H	-36.996187000	38.638606000	362.499253000
H	-38.702703000	38.178661000	362.265093000
H	-37.758976000	38.865098000	360.920569000
C	-36.936979000	45.173373000	365.500483000
C	-36.437633000	46.592948000	365.247509000
O	-35.497605000	47.048608000	365.923294000
C	-35.851957000	44.164594000	365.050928000
C	-36.134852000	42.792086000	365.649258000
C	-35.355183000	41.607473000	365.112712000
O	-34.669595000	41.672744000	364.082511000
O	-35.534502000	40.560711000	365.847680000
H	-37.015282000	45.112365000	366.595989000
H	-35.829422000	44.112790000	363.954475000
H	-34.864755000	44.513197000	365.376520000
H	-35.984585000	42.812204000	366.737110000
H	-37.185913000	42.514484000	365.500552000
N	-37.017051000	47.299739000	364.257684000
C	-36.553234000	48.615704000	363.819180000
C	-37.724272000	49.578294000	363.647903000
C	-35.734484000	48.508230000	362.515817000
C	-34.665323000	47.466646000	362.539469000
C	-34.230544000	46.595294000	361.568075000
N	-33.872904000	47.193929000	363.639714000
C	-33.028585000	46.185253000	363.325158000
N	-33.210053000	45.814617000	362.070845000
H	-37.741593000	46.856603000	363.714745000
H	-35.905054000	48.984644000	364.620726000
H	-36.407145000	48.278411000	361.679066000
H	-35.301733000	49.498537000	362.307715000
H	-34.590794000	46.476448000	360.552490000
H	-32.330598000	45.747187000	364.028753000
C	-39.753329000	36.517922000	364.933017000
C	-38.531445000	37.118949000	365.532369000
C	-37.237302000	37.229976000	365.083064000
N	-38.549654000	37.800803000	366.738364000
C	-37.320407000	38.299088000	366.982562000
N	-36.507005000	37.966627000	365.992795000

H	-39.498234000	35.988715000	364.009542000
H	-40.494048000	37.290368000	364.685908000
H	-39.350795000	37.916903000	367.340242000
H	-36.790105000	36.881855000	364.163688000
H	-37.051520000	38.891092000	367.846235000
C	-36.289769000	33.686348000	363.597577000
C	-35.177492000	34.662626000	363.394455000
O	-34.452994000	35.017718000	364.367076000
O	-35.043713000	35.061987000	362.198159000
H	-36.049627000	32.791322000	363.006895000
H	-37.222189000	34.102348000	363.198332000
C	-33.766509000	33.932589000	371.259547000
C	-34.021096000	34.513925000	369.898476000
C	-33.425883000	35.529847000	369.183150000
N	-35.030782000	34.042066000	369.068763000
C	-35.048540000	34.724856000	367.916375000
N	-34.084047000	35.631167000	367.968833000
H	-34.668757000	33.991933000	371.880709000
H	-32.967424000	34.491918000	371.754490000
H	-32.593931000	36.175710000	369.430679000
H	-35.718596000	34.557490000	367.083543000
H	-33.886681000	36.291428000	367.177912000
C	-33.578155000	39.597951000	369.779986000
C	-33.540258000	39.033837000	368.381211000
O	-32.415820000	38.608724000	367.958181000
O	-34.617495000	38.992500000	367.732426000
H	-33.994084000	38.840372000	370.458291000
H	-34.239385000	40.469448000	369.812195000
C	-29.126864000	41.202988000	366.026954000
C	-30.079028000	40.202580000	365.411271000
O	-30.481124000	40.352708000	364.244543000
O	-30.434073000	39.253202000	366.217996000
H	-29.723152000	41.909732000	366.620074000
C	-30.466032000	34.340694000	367.084827000
C	-31.196070000	35.438806000	366.339589000
O	-31.088397000	36.618084000	366.801093000
O	-31.897087000	35.109276000	365.341093000
H	-29.961610000	33.678388000	366.373237000
H	-31.205072000	33.741801000	367.632598000
Ca	-32.712812000	39.610410000	363.216423000

O		-33.011970000	39.628139000	365.552844000
O		-31.689372000	37.666238000	364.328382000
O		-33.646050000	37.220362000	365.819794000
O		-32.340306000	35.518334000	362.678666000
O	YES	-33.926140000	37.344934000	362.945744000
O	YES	-34.963186000	38.769503000	363.891867000
Mn		-34.689936000	38.858607000	365.641035000
Mn		-32.029230000	38.198268000	366.031179000
Mn		-32.956451000	36.361601000	364.156308000
Mn		-33.552627000	36.111439000	361.510727000
O		-33.440638000	34.498157000	360.117136000
O	YES	-34.919588000	36.825458000	360.347958000
O	YES	-35.355660000	42.743929000	361.634574000
O		-32.030036000	41.820600000	362.664193000
O	YES	-34.405559000	40.164067000	361.536971000
H		-33.458858000	32.881623000	371.187266000
H		-29.749940000	34.765187000	367.792294000
H		-32.853788000	29.565365000	361.459626000
H		-30.770729000	37.623226000	358.460384000
H		-29.811501000	44.963065000	355.552558000
H		-39.897963000	41.812632000	361.920146000
H		-39.408104000	40.785716000	360.553882000
H		-28.420696000	40.710890000	366.703989000
H		-28.589140000	41.759479000	365.254100000
H		-32.575357000	39.864945000	370.123073000
H		-36.417875000	33.422802000	364.650733000
H		-40.231736000	35.801815000	365.613721000
H		-37.360857000	50.554433000	363.305362000
H		-38.434964000	49.201108000	362.900514000
H		-38.259698000	49.717026000	364.593806000
C		-38.301573000	44.830040000	364.894562000
H		-38.261154000	44.769533000	363.798329000
H		-38.656485000	43.861314000	365.258779000
H		-39.062894000	45.569133000	365.174313000
H		-33.198241000	33.599145000	360.614161000
H		-34.356101000	34.365162000	359.834355000
H	YES	-35.707418000	36.972255000	360.885559000
H		-31.102293000	41.903869000	362.917047000
H	YES	-34.402511000	39.773794000	360.631845000
H	YES	-35.325726000	39.579404000	363.430754000

H		-32.212063000	42.423467000	361.914294000
H	YES	-34.564709000	43.135214000	361.221226000
H	YES	-35.096998000	42.614250000	362.569511000
H		-34.058037000	47.519142000	364.582823000
H	YES	-34.804683000	41.055198000	361.440918000
H		-35.666133000	33.290158000	369.286752000
O	YES	-34.400547000	39.017354000	359.033449000
H	YES	-35.186778000	39.227774000	358.517360000
H	YES	-34.599140000	38.122571000	359.468316000

7.3.7.2 Changes in Spin Distribution

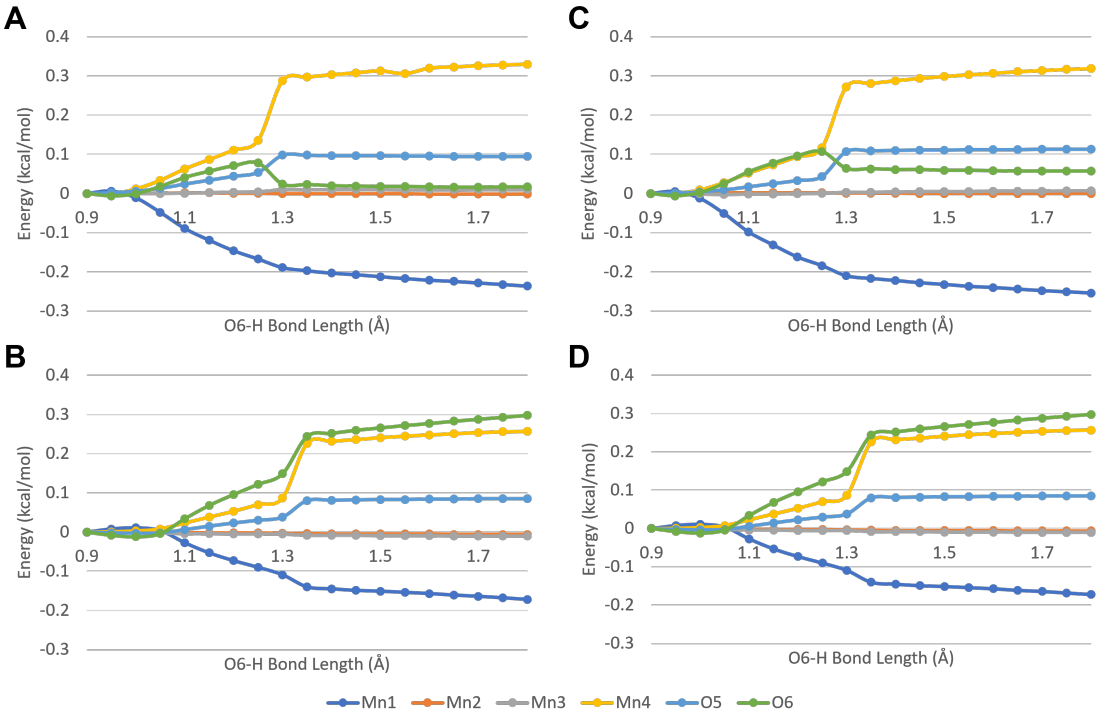

Figure S7.1: Change in absolute spin values of key atomic centres within the system during the oxo-hydroxo to oxo-oxo transition with an O5-O6 separation of 1.9 Å within the **aaaa** (A), **baaa** (B), **aaba** (C), and **aaab** states (D).

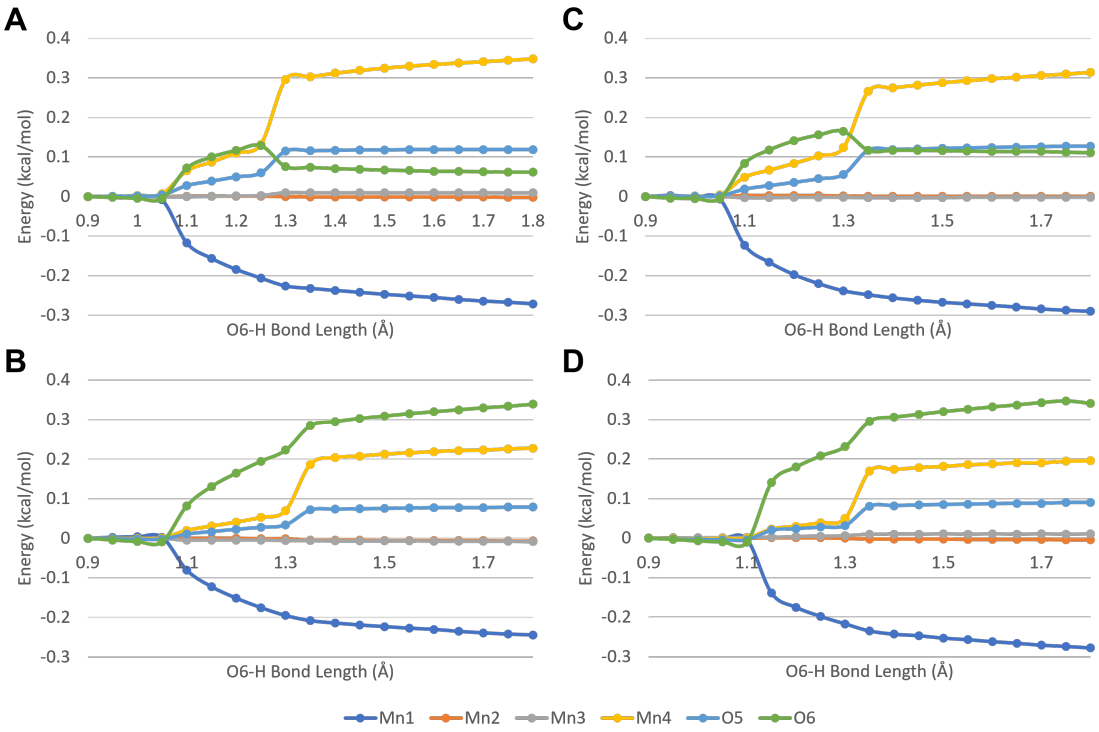

Figure S7.2: Change in absolute spin values of key atomic centres within the system during the oxo-hydroxo to oxo-oxo transition with an O5-O6 separation of 2.0 Å within the **aaaa** (A), **baaa** (B), **aaba** (C), and **aaab** states (D).

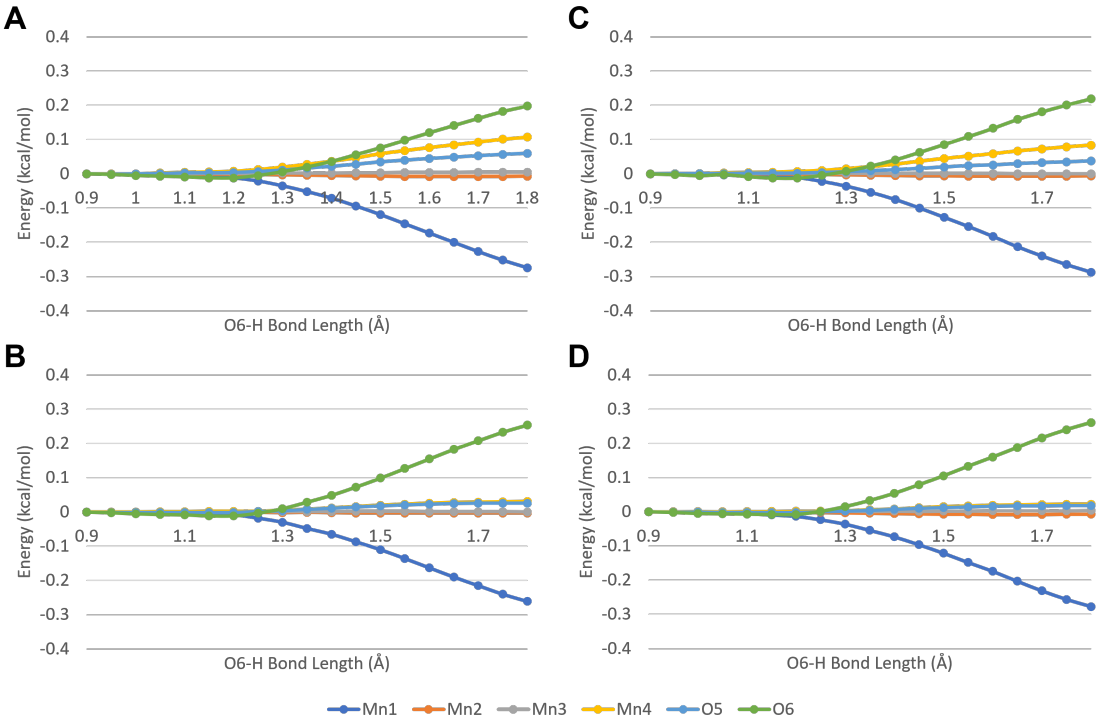

Figure S7.3: Change in absolute spin values of key atomic centres within the system during the oxo-hydroxo to oxo-oxo transition via abstraction by Glu189 with an O5-O6 separation of 2.1 Å within the **aaaa** (A), **baaa** (B), **aaba** (C), and **aaab** states (D).

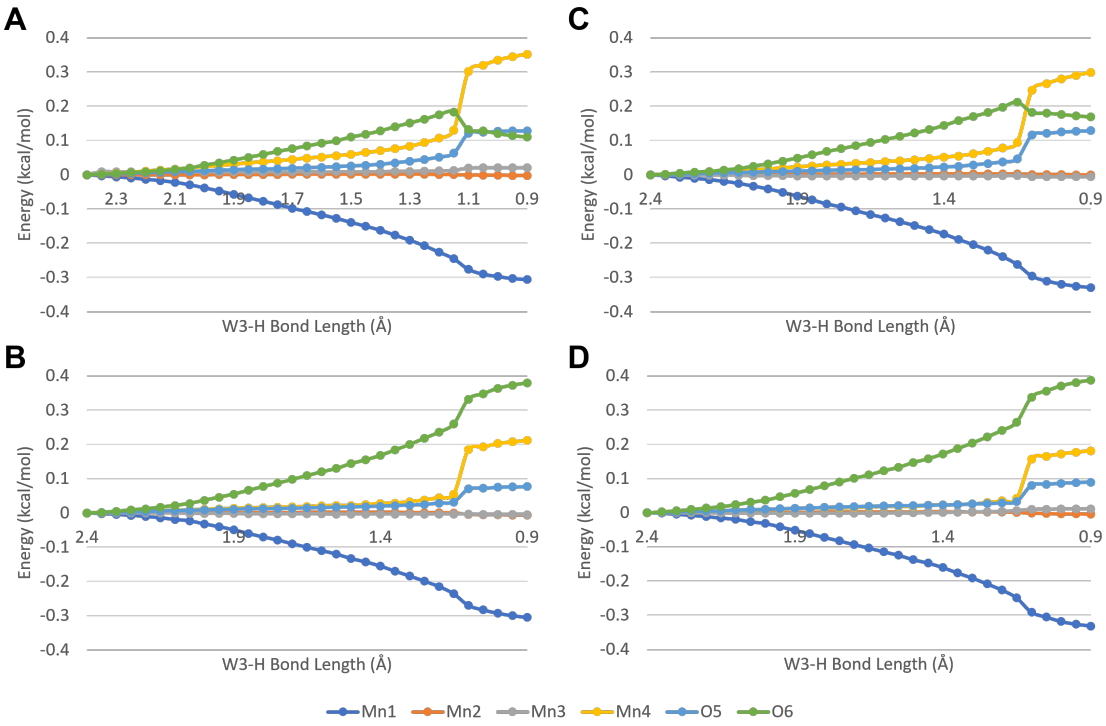

Figure S7.4: Change in absolute spin values of key atomic centres within the system during the oxo-hydroxo to oxo-oxo transition via abstraction by W3 with an O5-O6 separation of 2.1 Å within the **aaaa** (A), **baaa** (B), **aaba** (C), and **aaab** states (D).

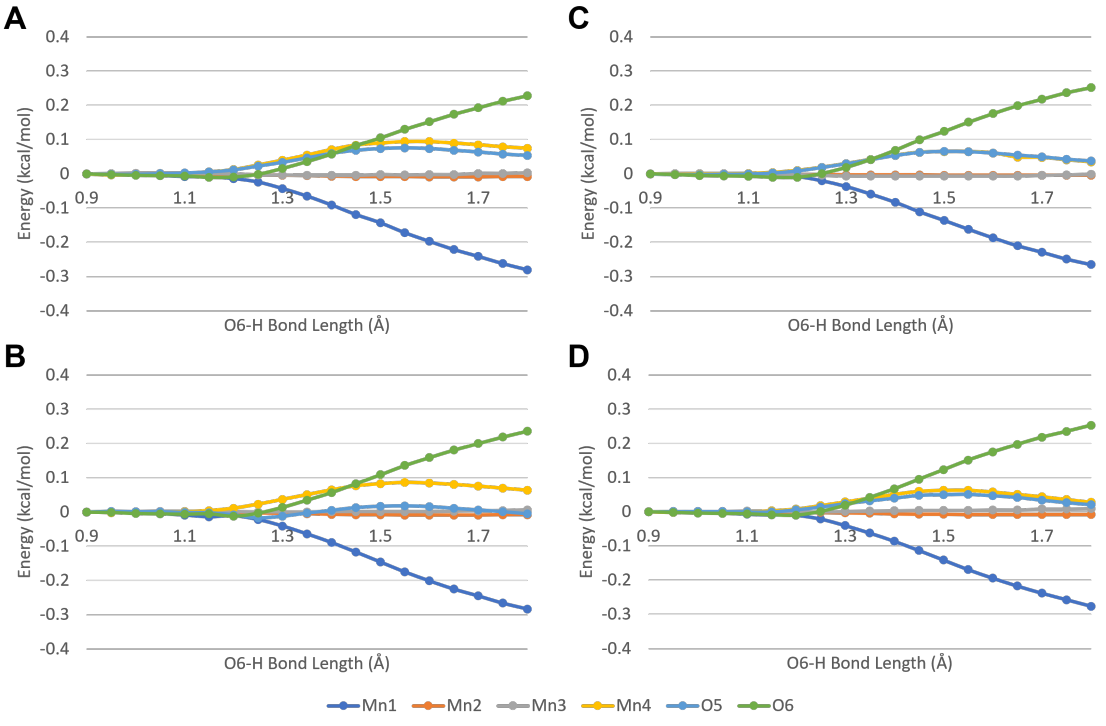

Figure S7.5: Change in absolute spin values of key atomic centres within the system during the oxo-hydroxo to oxo-oxo transition via abstraction by Glu189 with an O5-O6 separation of 2.1 Å within the **aaaa** (A), **baaa** (B), **aaba** (C), and **aaab** states (D).

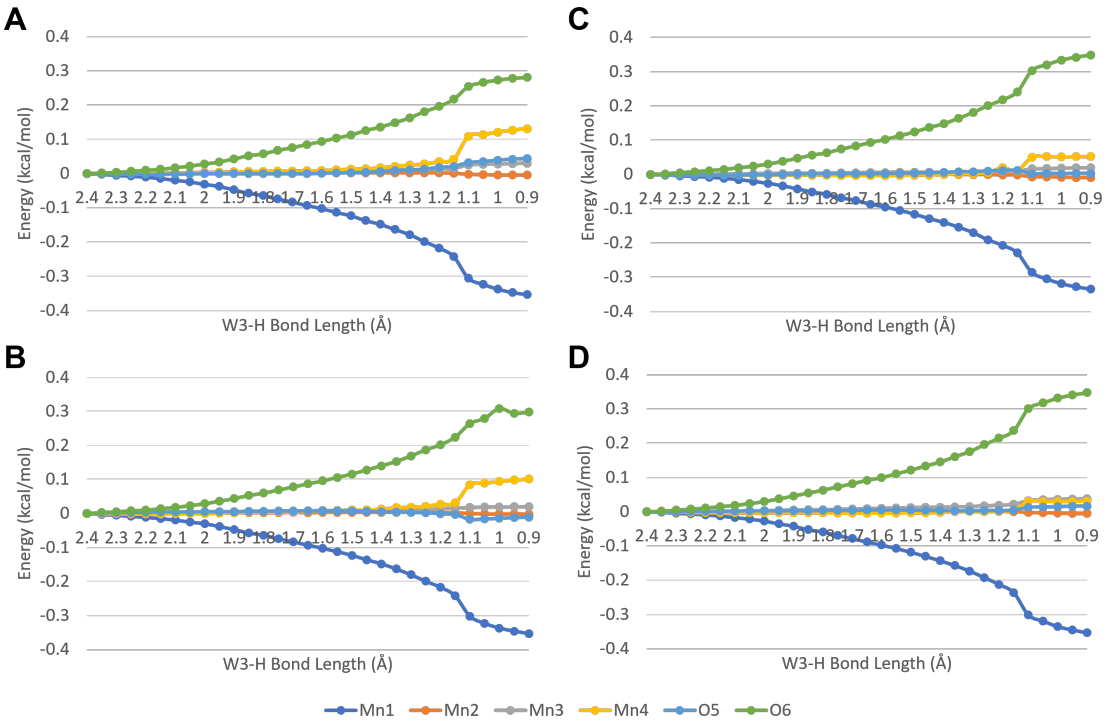

Figure S7.6: Change in absolute spin values of key atomic centres within the system during the oxo-hydroxo to oxo-oxo transition via abstraction by W3 with an O5-O6 separation of 2.1 Å within the **aaaa** (A), **baaa** (B), **aaba** (C), and **aaab** states (D).

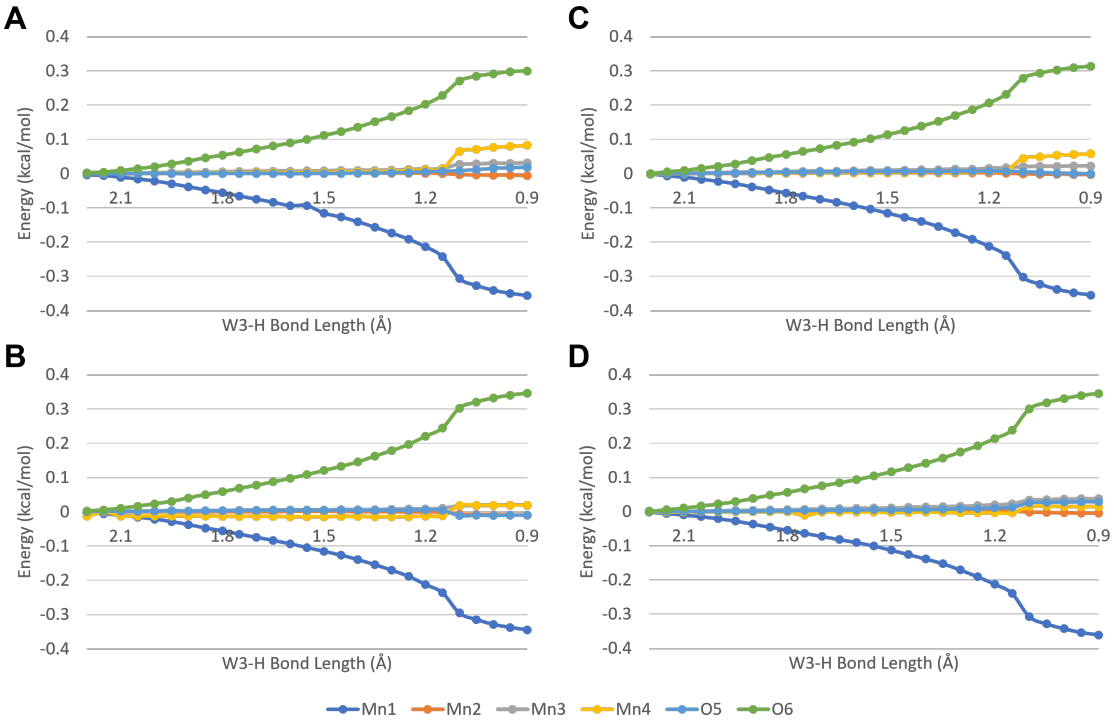

Figure S7.7: Change in absolute spin values of key atomic centres within the system during the oxo-hydroxo to oxo-oxo transition via abstraction by W3 with an O5-O6 separation of 2.3 Å within the **aaaa** (A), **baaa** (B), **aaba** (C), and **aaab** states (D).

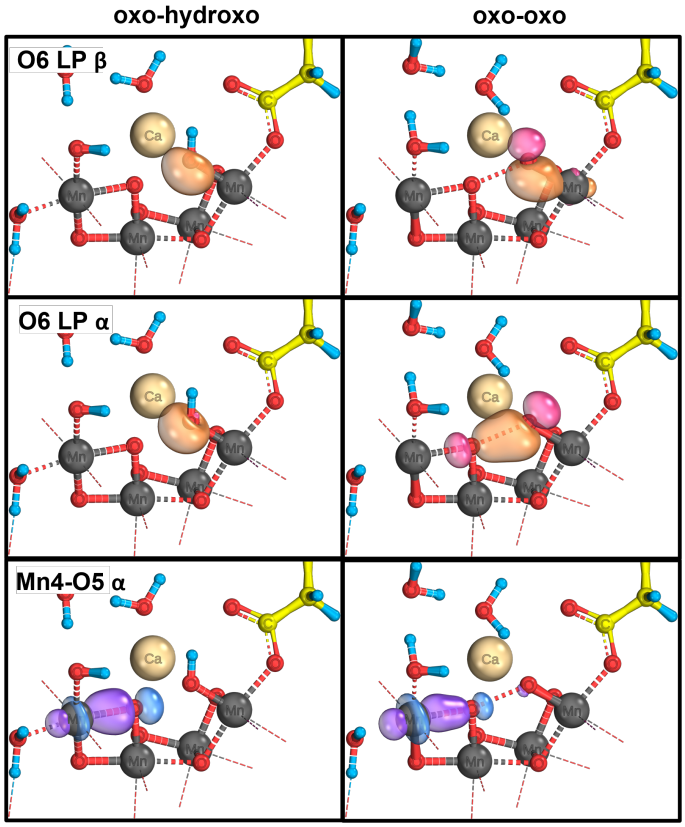

Figure S7.8: IBO representations of the orbitals showing the key transitions between the oxo-hydroxo (left) and oxo-oxo (right) structures during W3 abstraction in the aaaa state, at a fixed O5-O6 distance of 1.9 Å.

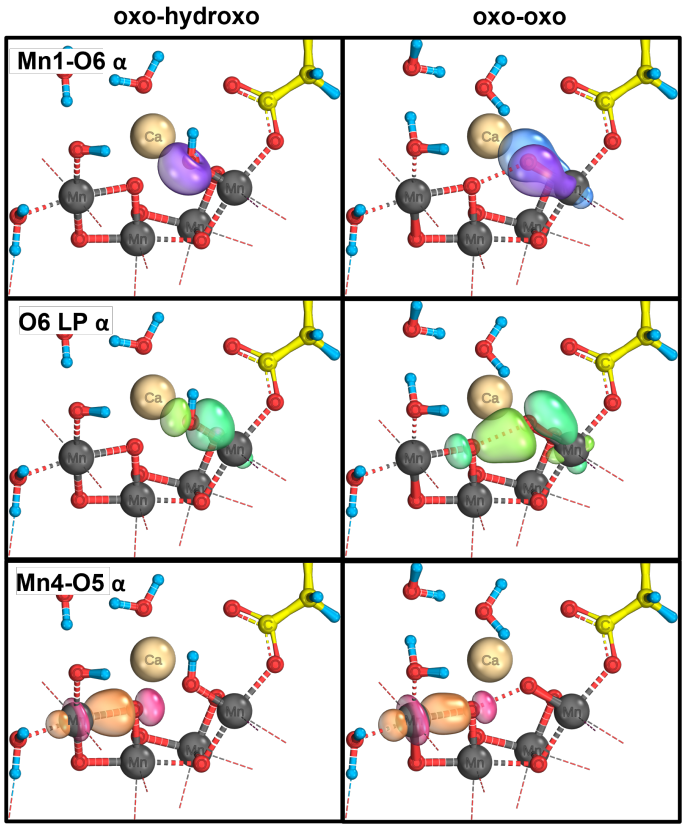

Figure S7.9: IBO representations of the orbitals showing the key transitions between the oxo-hydroxo (left) and oxo-oxo (right) structures during W3 abstraction in the baaa state, at a fixed O5-O6 distance of 1.9 Å.

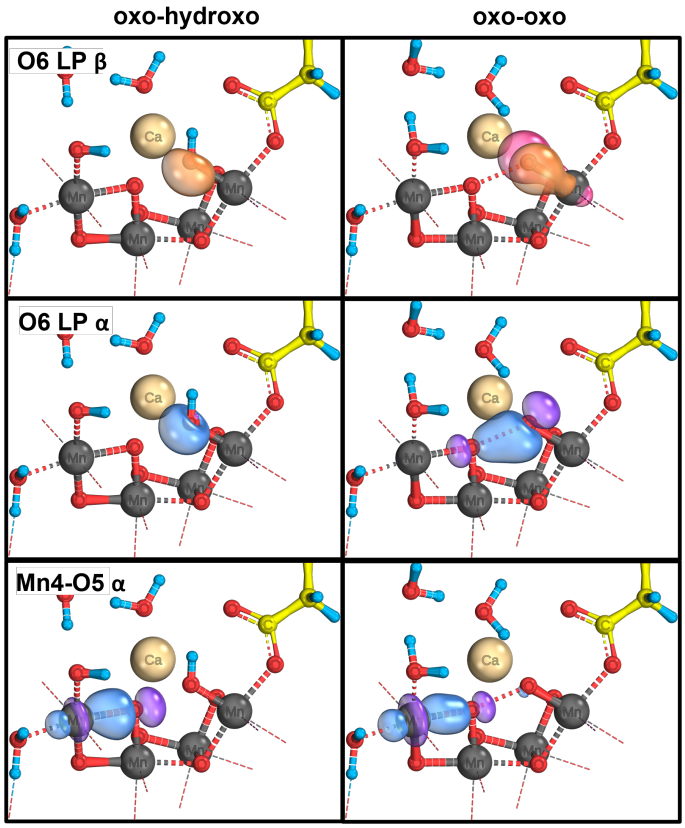

Figure S7.10: IBO representations of the orbitals showing the key transitions between the oxo-hydroxo (left) and oxo-oxo (right) structures during W3 abstraction in the aaba state, at a fixed O5-O6 distance of 1.9 Å.

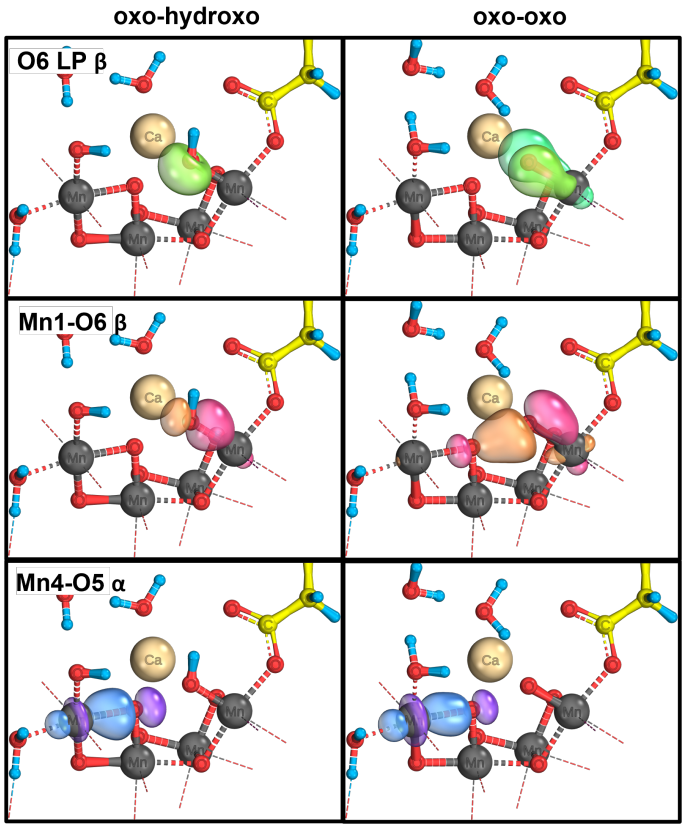

Figure S7.11: IBO representations of the orbitals showing the key transitions between the oxo-hydroxo (left) and oxo-oxo (right) structures during W3 abstraction in the aaab state, at a fixed O5-O6 distance of 1.9 Å.

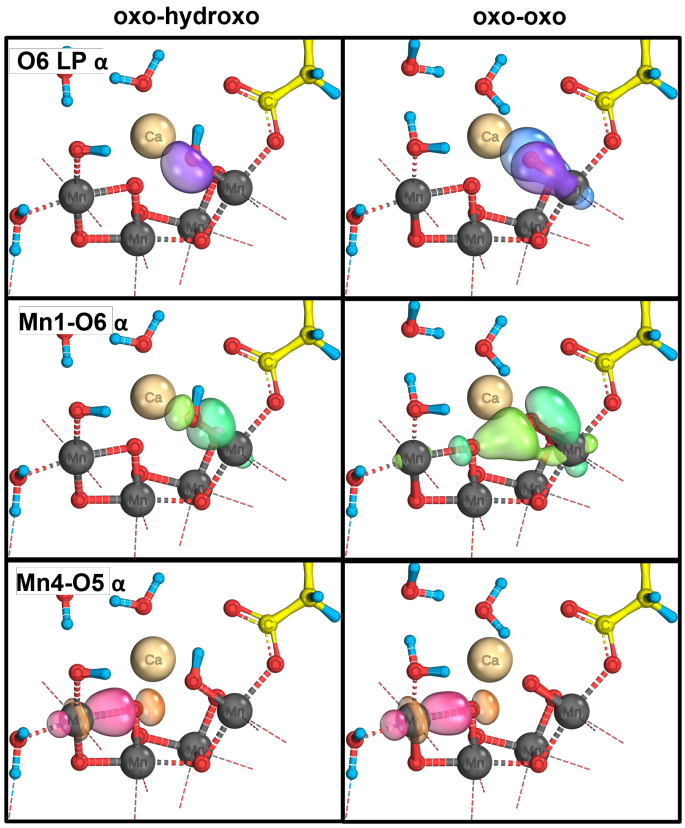

Figure S7.12: IBO representations of the orbitals showing the key transitions between the oxo-hydroxo (left) and oxo-oxo (right) structures during W3 abstraction in the baaa state, at a fixed O5-O6 distance of 2.0 Å.

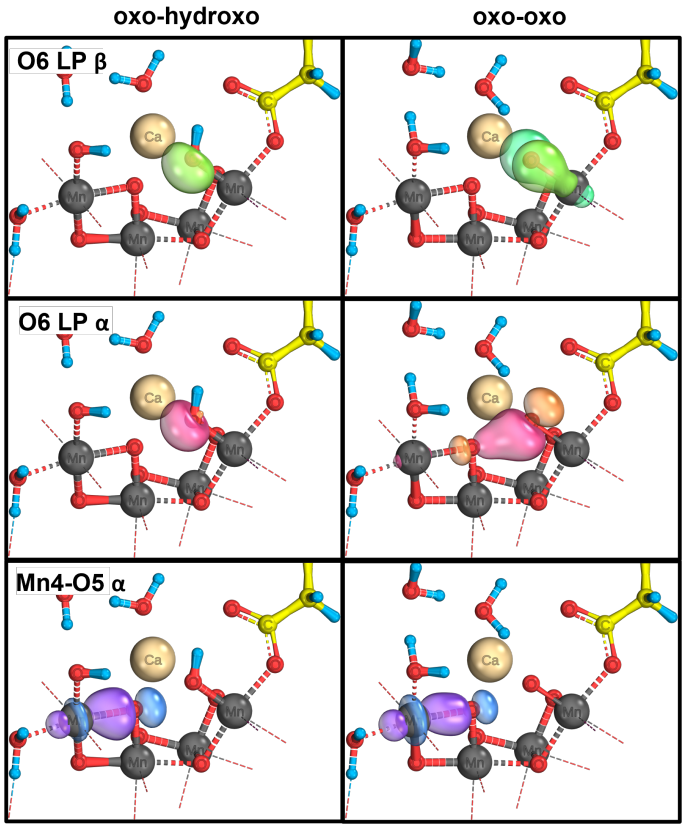

Figure S7.13: IBO representations of the orbitals showing the key transitions between the oxo-hydroxo (left) and oxo-oxo (right) structures during W3 abstraction in the aaba state, at a fixed O5-O6 distance of 2.0 Å.

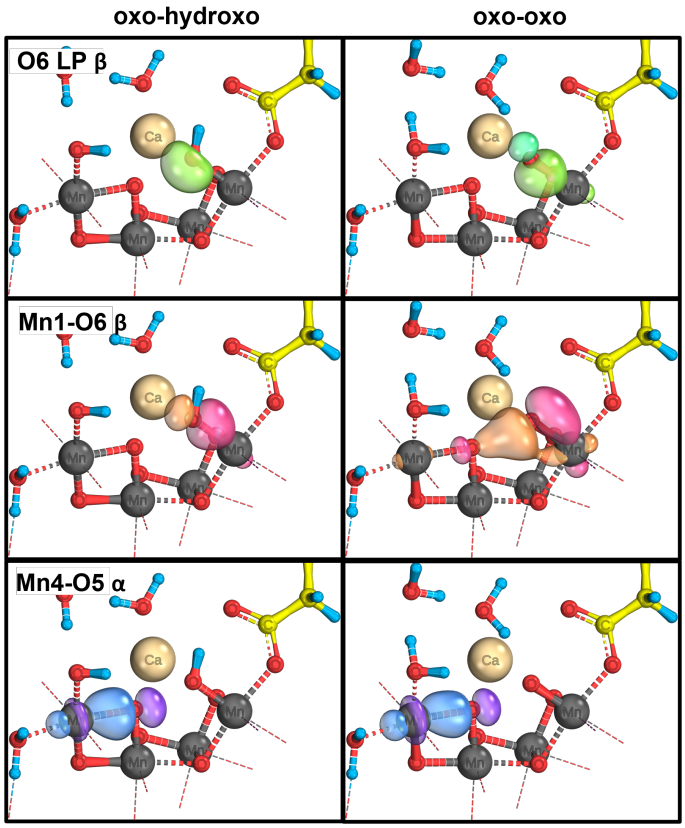

Figure S7.14: IBO representations of the orbitals showing the key transitions between the oxo-hydroxo (left) and oxo-oxo (right) structures during W3 abstraction in the aaab state, at a fixed O5-O6 distance of 2.0 Å.

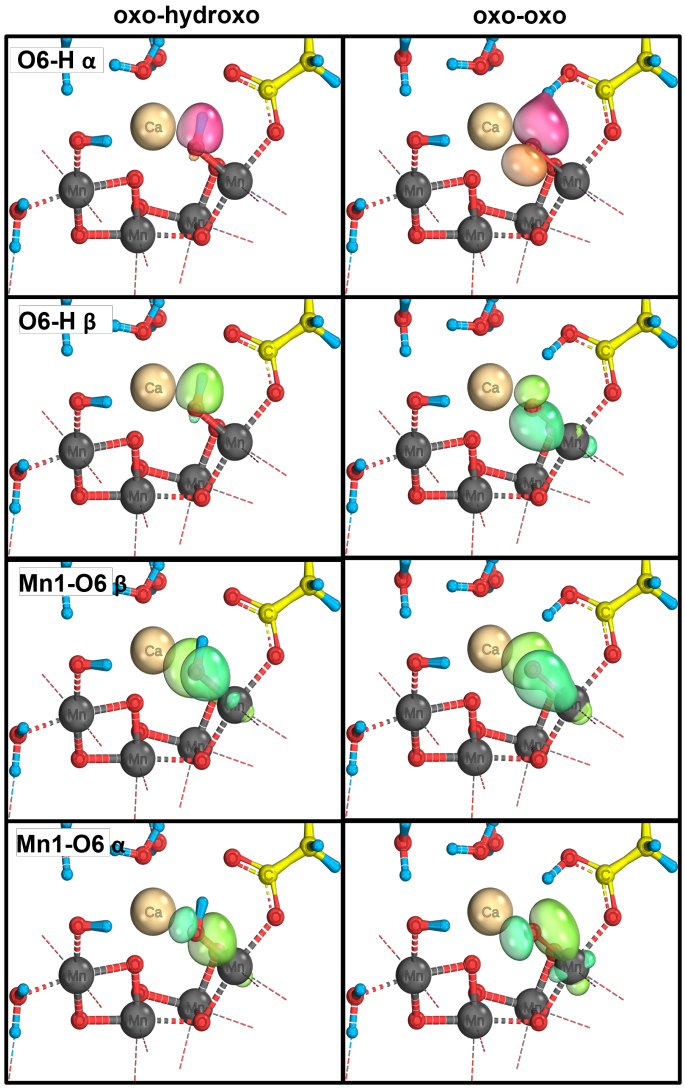

Figure S7.15: IBO representations of the orbitals showing the key transitions between the oxo-hydroxo (left) and oxo-oxo (right) structures during Glu189 abstraction in the aaaa state, at a fixed O5-O6 distance of 2.1 Å.

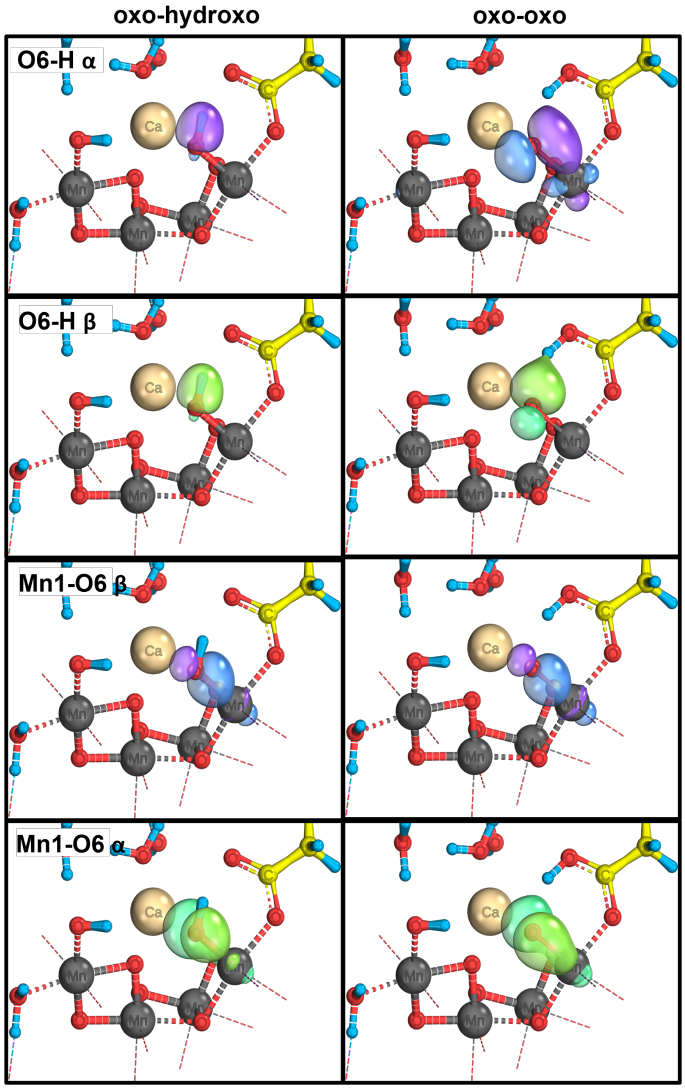

Figure S7.16: IBO representations of the orbitals showing the key transitions between the oxo-hydroxo (left) and oxo-oxo (right) structures during Glu189 abstraction in the baaa state, at a fixed O5-O6 distance of 2.1 Å.

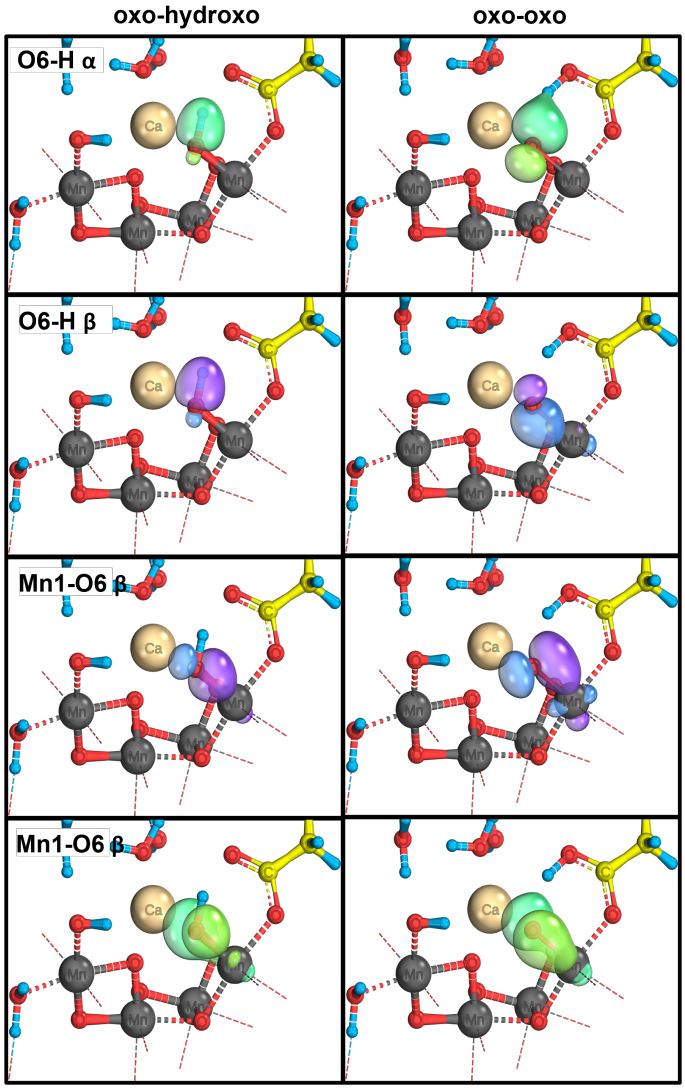

Figure S7.17: IBO representations of the orbitals showing the key transitions between the oxo-hydroxo (left) and oxo-oxo (right) structures during Glu189 abstraction in the aaba state, at a fixed O5-O6 distance of 2.1 Å.

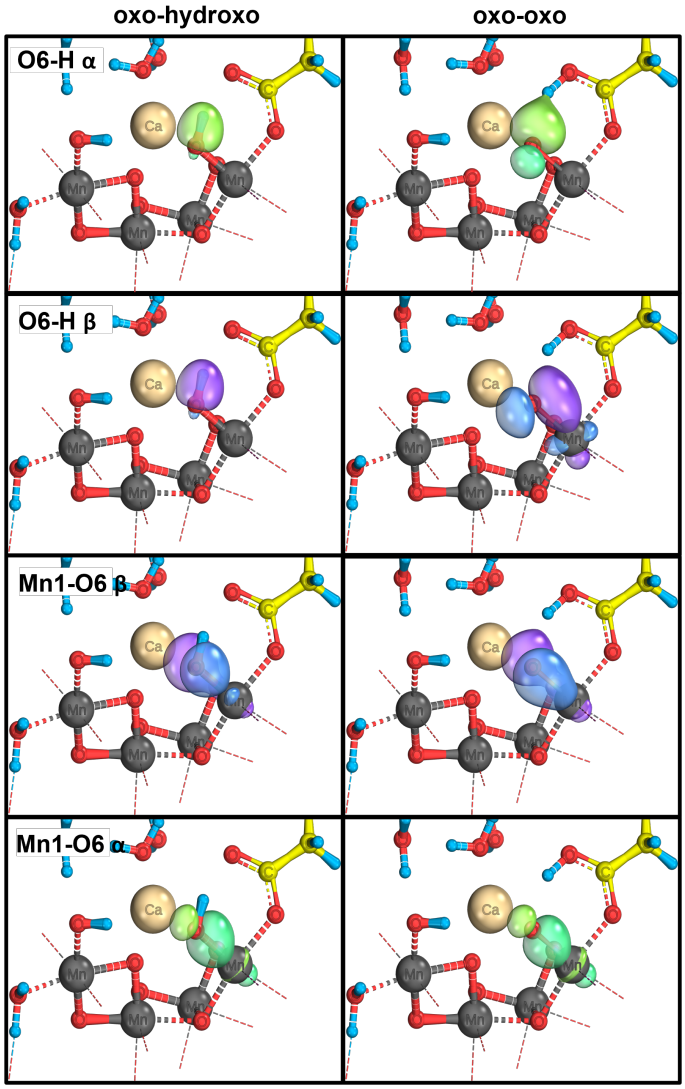

Figure S7.18: IBO representations of the orbitals showing the key transitions between the oxo-hydroxo (left) and oxo-oxo (right) structures during Glu189 abstraction in the aaab state, at a fixed O5-O6 distance of 2.1 Å.

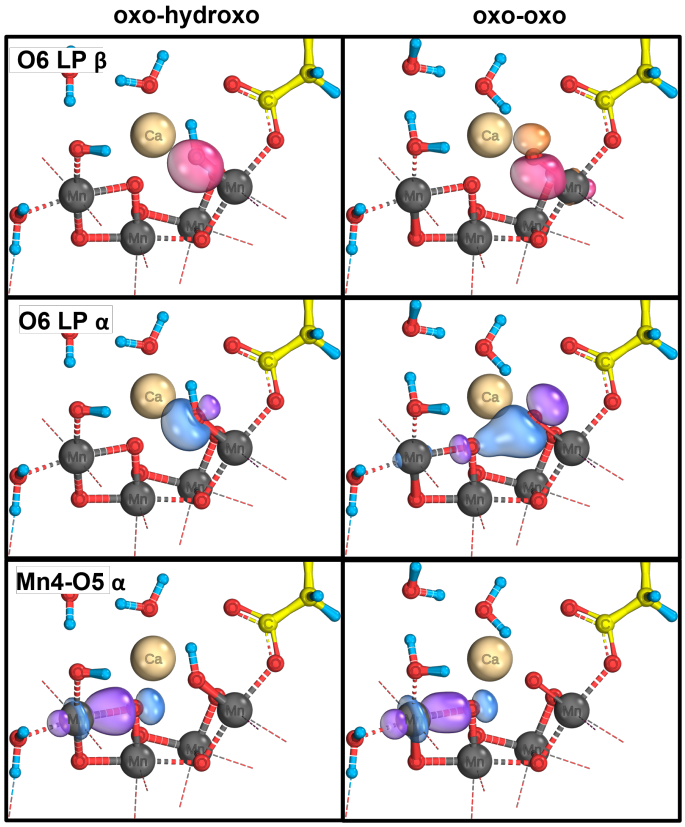

Figure S7.19: IBO representations of the orbitals showing the key transitions between the oxo-hydroxo (left) and oxo-oxo (right) structures during W3 abstraction in the aaaa state, at a fixed O5-O6 distance of 2.1 Å.

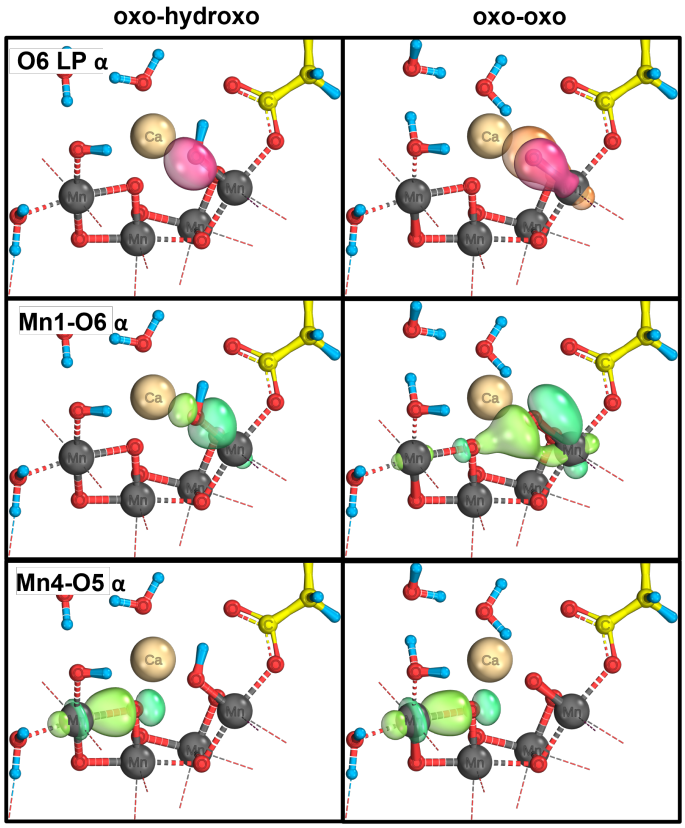

Figure S7.20: IBO representations of the orbitals showing the key transitions between the oxo-hydroxo (left) and oxo-oxo (right) structures during W3 abstraction in the baaa state, at a fixed O5-O6 distance of 2.1 Å.

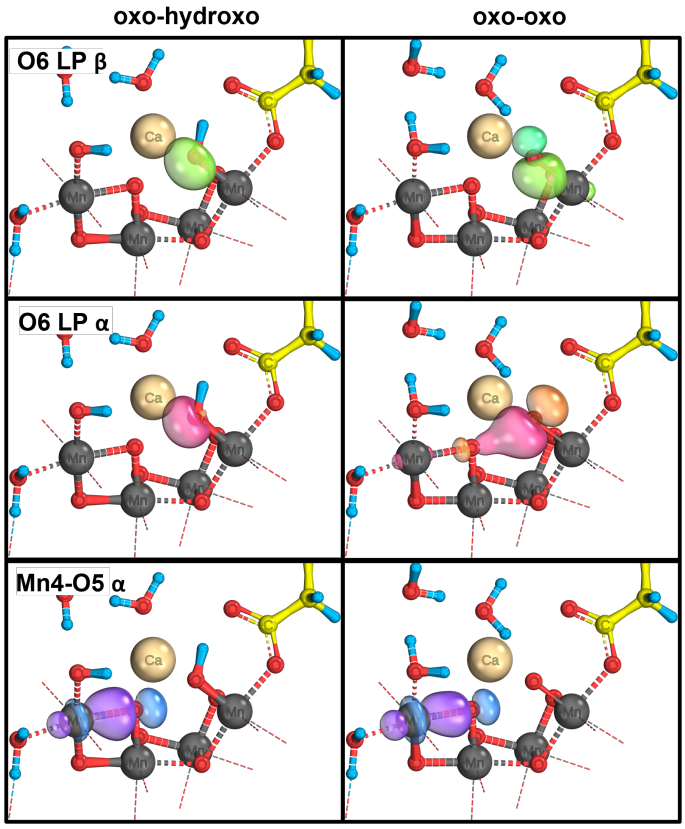

Figure S7.21: IBO representations of the orbitals showing the key transitions between the oxo-hydroxo (left) and oxo-oxo (right) structures during W3 abstraction in the aaba state, at a fixed O5-O6 distance of 2.1 Å.

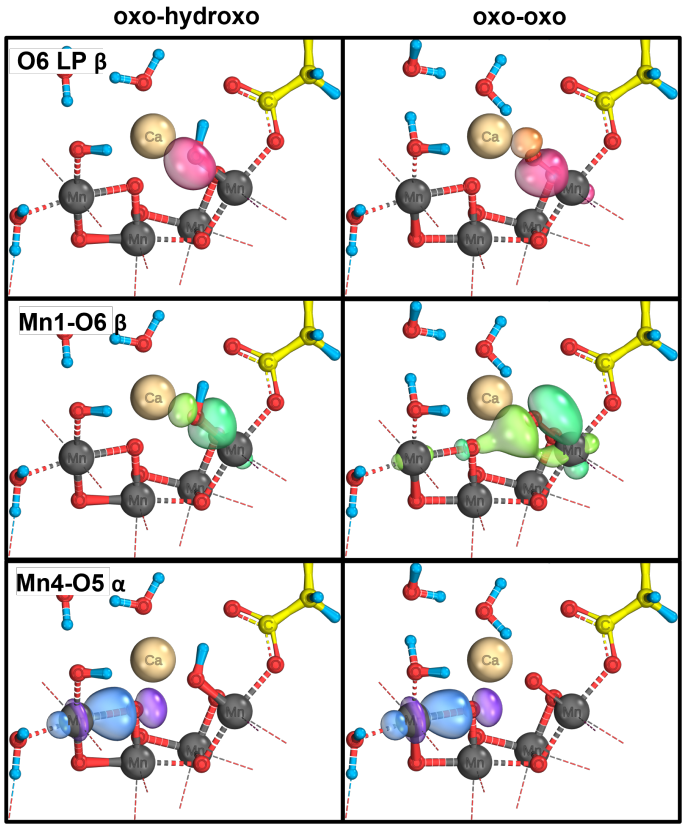

Figure S7.22: IBO representations of the orbitals showing the key transitions between the oxo-hydroxo (left) and oxo-oxo (right) structures during W3 abstraction in the aaab state, at a fixed O5-O6 distance of 2.1 Å.

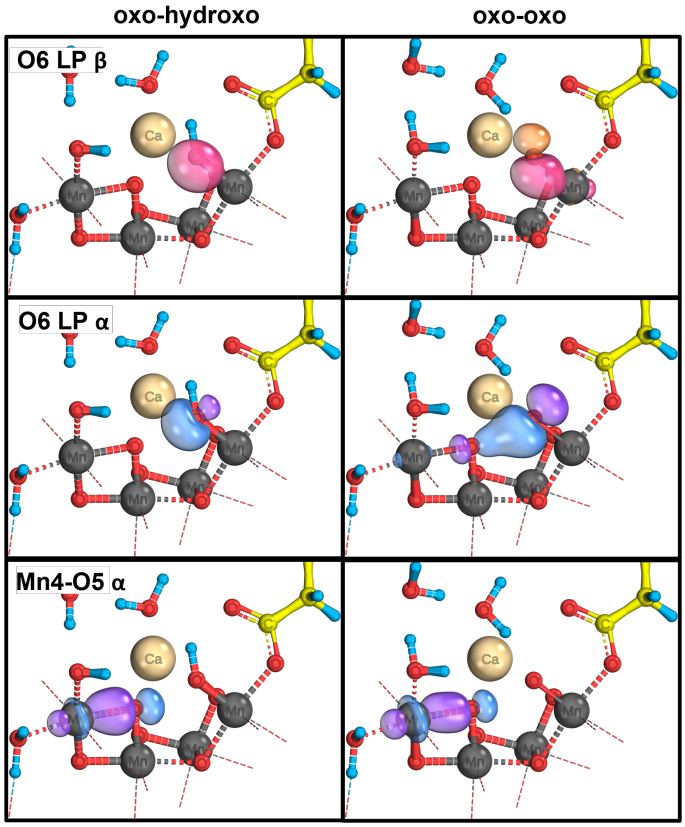

Figure S7.23: IBO representations of the orbitals showing the key transitions between the oxo-hydroxo (left) and oxo-oxo (right) structures during W3 abstraction in the aaaa state, at a fixed O5-O6 distance of 2.3 Å.

Chapter 8

Conclusion and Outlook

The studies presented in this thesis have focused mostly around the S_3 state of the OEC. Being the final stable intermediate which has so far been isolated and penultimate S-state in the Kok cycle understanding it is key to understanding how PSII can facilitate efficient water oxidation. Throughout the last years many new experimental insights have been made into not just the isolated S_3 state, through crystal structures, but it has also been possible to capture snapshots during S-state transitions, shedding some light onto the sequence of events throughout the Kok cycle.[1–5] On the other hand it has also been pointed out that even though experimental techniques are becoming ever more powerful there are still shortcomings with the crystal structures with potentially de-hydrated structures[6] or structures with inconsistent oxidation states, often being over-reduced, compared to pure S states.[7, 8] These experimental insights have aided in theoretical research providing better starting points for models of the OEC and helping in the determination of the sequence of events throughout the Kok cycle. Computational models remain important to the research as illustrated in the work presented in this thesis and the field as a whole, allowing for complex electronic structures to be analysed and visualised as well as permitting a better understanding of the design of the OEC which permits it to efficiently catalyse water oxidation. The key findings of the presented work in this thesis as well as future areas of development will be summarised in this chapter.

Chapter 4 discussed the nature of the bonding and magnetic exchange pathways in the OEC as well as small Mn-Mn dimers, these were uniquely presented by corresponding orbitals (COs) and intrinsic bonding orbitals (IBOs). The role of the Ca^{2+} ion within the OEC was also discussed.

Initially covering the more simple Mn^{IV}-Mn^{IV} dimers linked by oxygen bridges it was found that exchange primarily occurred as superexchange mediated by the oxygen bridges. It was shown that the exchange was between the oxo p-type orbitals and the Mn magnetic orbitals d_{xy}, d_{xz} and d_{yz}, agreeing with previous studies[9–11]. The oxo ligand lead to a stabilising anti-ferromagnetic interaction

in the Mn dimers. By analysis of the COs the π type interactions were the main contributors to the superexchange. With σ interactions being significantly weaker. When a Ca^{2+} ion was placed in the proximity of one of the oxygen bridges in the dimer it was found that the exchange interaction through that particular oxygen was weakened, whereas exchange interactions through the other oxo ligand was unaffected. This overall lead to a decrease in the anti-ferromagnetic stabilisation, the cause of this was attributed to the decrease in symmetry as well as the Ca^{2+} ionic interaction with the proximal oxo bridge, weakening the π type overlap.

These findings were then directly compared to the OEC, where when taking a pair of adjacent Mn-Mn ions the structure was similar to that of the dimer model, since in the OEC each Mn-Mn adjacent pair is linked by two oxo bridging ligands. Great similarity in the exchange mechanism was observed for all oxo bridges except for O3. Oxo bridges other than O3 each are μ_2 type bridges being bonded to two other moieties, whereas O3 is a μ_3 type bridge being bonded to three other moieties (Mn_1, Mn_2 and Mn_3). It was observed then that oxo bridges in proximity to the Ca^{2+} ligand in the OEC showed weaker interactions with the Mn ions thus lowering the strength of the exchange. O3 was found to not mediate exchange as no π pathways between it and Mn centres was observed. This was reflected in the exchange value or the $Mn_{2/3}$ bridge being ferromagnetic rather than anti-ferromagnetic as in the related Mn-Mn dimer model.

By analysis of the IBOs the differing behaviour of O3 was further rationalised. For the O3 centre three σ bonds were found, one to each Mn centre, as well as a lone pair. No π type bonding was observed, explaining the lack of observed superexchange coupling through O3. On the other hand the μ_2 oxo ligands each showed two σ bonds, a lone pair and π type bonds with the Mn centres they bridged. It was also noted that oxo bridges adjacent to the Ca^{2+} showed weaker π type overlap.

For Mn^{III}-Mn^{IV} dimers an extra magnetic orbital is present, the Mn^{III} d_{z^2}, leading to an additional overlap of the d_{z^2} with a d_{xy} orbital on Mn^{IV}. This interaction was associated with a large S value indicating it would be the dominant interaction, this was supported by a larger calculated exchange coupling. Otherwise the same interactions were seen and observed effects and trends were the same, such as the effect of the Ca^{2+} ligand causing a decrease in orbital overlap and as such a decrease in the exchange couplings.

As it has been reported that protonation states of oxo bridges can affect the exchange coupling between the bridged ligands[12, 13], a comparison for protonated and deprotonated oxo bridges for the Mn^{IV}-Mn^{IV} dimer was also presented. This was of particular interest as our group has previously demonstrated it is possible to rationalise the S_2 state EPR signals without the need to invoke a closed cubane, by

protonation of the O4 bridge in the OEC. This protonation was shown to change the exchange between the bridged Mn_3 and Mn_4 from anti- to ferromagnetic leading to a different ground state spin. It was clearly demonstrated by the IBOs that π type interactions through the protonated bridge were eliminated in the model dimer system and that the COs based on the protonated bridge showed largely reduced overlap, again observing the exchange interaction to become ferromagnetic as a result.

Finally the nature of the Ca^{2+} bond in the OEC was investigated. It had been shown that the proximity of Ca^{2+} to oxo bridges lead to a decreased overlap of COs and as such a decrease in superexchange. This effect was smaller than the effect of protonation. It was graphically demonstrated that Ca^{2+} displays purely ionic interaction, as it shows no bonding IBOs, as further supported by Mayer bond order analysis. As such its effect was concluded to be non-directional, allowing for a more flexible geometry in its vicinity. Since throughout the Kok cycle two water molecules are consumed and a new oxygen can be seen to bind to the OEC[14] the non-directional ionic nature of Ca^{2+} was deemed to be essential to the OEC's functioning.

Chapter 5 combined BS-DFT calculations and EPR simulation to propose a pathway for O-O bond formation in the S_3 state. The pathway was facilitated by formation of an $[O5O6]^{3-}$ ion which when compared structurally agreed very well with the S_3 crystal structures.[15, 16] Given that the PSII is limited to the $\approx$ 1 V oxidising power of the Y_Z residue and the brevity of the S_4 state suggested that pre-forming the O-O bond prior to the final oxidation would be favourable, as previously proposed by Renger.[17–19] This mechanism requires lowering the barrier to O-O bond formation, and would retain the last oxidising equivalent (flash) for the final push towards molecular oxygen.

The PESs for O-O bond formation between O5 and O6 were presented, a unique low energy pathway to O5-O6 peroxo was found. Starting with an oxo-hydroxo form, the Mn_3 and Mn_4 flipped BS states were found to be most favourable (and almost equivalent in their profile), as the O5-O6 distance was decreased the oxo-hydroxo became increasingly unstable and higher in energy. As such it was deprotonated and the PES for an O5 oxo-O6 oxo to peroxo investigated. Both a high-spin surface (Ms = 6) and a Mn_1 flipped surface (Ms = 3) were presented and found to provide the energetically most favourable path. With the Mn_1 flipped form being the most favourable at the peroxo geometry and the high-spin form most favourable $\approx$ 2 Å. A broad shallow minima was identified here corresponding to an $[O5O6]^{3-}$ species, in which a single unpaired β electron shared between O5 and O6 was strongly stabilised by anti-ferromagnetic interactions with Mn_1, Mn_3 and Mn_4. All Mn centres were in an α alignment. While previously an $O_2{}^{3-}$ form had

been identified[16, 20, 21] it was assigned as an O5 oxo-O6 oxyl, the here identified $[O5O6]^{3-}$ however was demonstrated to have its spin shared between both O5 and O6.

IBO's for O-O bond formation which were seen to change significantly were presented and analysed. For both oxo-oxo surfaces it was found that overall an electron from the α Mn_4-O5 σ bond moved onto Mn_4 in the peroxo form. The corresponding β electron formed one half of the O5-O6 bond. An α electron from an O6 lone pair moved to form the α component of the O5-O6 bond and a β electron from the Mn_1-O6 σ bond moved onto Mn_1. These changes were observed both in the IBOs as well as the calculated Mulliken spin populations. Overall the presented IBOs and PESs facilitated low-barrier O-O formation by allowing for concerted electron flow between the O5, O6, Mn_1 and Mn_4 ions.

Next the computational models were compared to experimental data, XFEL structures suggest an O5-O6 separation of $\approx$ 2.0 Å as such agreeing excellently with the identified $[O5O6]^{3-}$ species.[15, 16] This would also preclude the presence of an oxo-hydroxo or a peroxo form since in these the O5-O6 would be $\approx$ 2.4 or 1.4 Å respectively. The XFEL is somewhat in contrast to the EPR data, the EPR signal in the S_3 state suggests an $S = 3$ species to be present and based on the analysis of the hfcs was assigned to be due to an oxo-hydroxo form.[22–24] The calculated ground state spin for the $[O5O6]^{3-}$ species was found to be $S = 6$ appearing incompatible with this finding. However an $S = 6$ species had been put forwards as a major component in spinach samples[25], and assigned to a penta-coordinated Mn_4 closed cubane. This does not agree with the XFEL data as no closed cubane has so far been identified for any S state.[26] As such simulations were carried out using a mixture of $S = 3$ and $S = 6$ oxo-hydroxo and $[O5O6]^{3-}$ respectively with various ratios. The pure $S = 6$ form was found to only yield a very weak spectra showing only a shoulder between 3.5-4 T. Using EPR data from Chrysina[27] it was shown that using a 70 % $[O5O6]^{3-}$ to 30 % oxo-hydroxo mixture gave superior agreement to experiment compared to a pure oxo-hydroxo simulation.

Overall it was proposed that in the S_3 state an equilibrium between oxo-hydroxo and $[O5O6]^{3-}$ exists, with potentially also an equilibrium to a peroxo form in small quantities. Upon the final flash the $[O5O6]^{3-}$ species would then be pushed towards peroxo, eventually forming molecular oxygen via a superoxo species.

Chapter 7 investigated the final deprotonation event before O-O bond formation. Gaining understanding of this event would aid in the identification of the final oxygen species. Within the study an O6 to Glu189 pathway was analysed and found to be dis-favourable, whereas an alternative O6 to Ca^{2+} bound W3 pathway was found to give a stable deprotonated product.

Glu189 lies close to O6 and as such offers itself up as a potential proton

abstractor at first sight. The PES for proton abstraction via this pathway was obtained, at O5-O6 distances of < 2.1 Å simply extending the O6-H bond length led to abstraction to W3 rather than Glu189, however at ≥ 2.1 Å it was possible to obtain a PES for proton abstraction to Glu189. However for all tested BS states as well as the HS state no minima with the proton on Glu189 was found and instead a large barrier >30 kcal mol^{-1} was obtained before the PES levelled out. This agrees with a similar study carried out by Mandal et al. in the S_2 state.[28] The presented study however rationalised why this abstraction pathway was disfavoured by analysing the IBOs. It was shown that the spin evolving on O6 as a result of its deprotonation was not able to stabilise due to the short O6-Glu189 separation essentially fixing the O6 orbital orientation. For the W3 pathway the O6 spin was seen to interact with O5 stabilising the system and strengthening the O5-O6 interaction, whereas in the Glu189 pathway this is not observed thus explaining the energetic penalty. Preliminary findings also showed that rotating the Glu189 proton to point away from O6 was energetically highly unfavourable presenting a large barrier, further showing that this deprotonation pathway to be less facile.

The study found the W3 pathway to be far more favourable in contrast, PESs were obtained for various O5-O6 distances between 1.9 and 2.3 Å and it was found that while each PES gave a minima for the O6 deprotonated state, shorter O5-O6 separation was energetically more favourable compared to the start point. In each case the HS and BS states were comparative in energy for the O6 protonated species. As the O6-H distance is increased the proton moves across to W3, once the W3-H_{O6} bond is formed there is a large drop in energy and a concerted proton exchange from a W3 proton to W2 via another nearby water molecule. Notably, the BS and HS states are now split with the HS state not only dropping in energy sooner but also being the most stable deprotonated state, with the Mn_3 flipped state just higher in energy and then the $Mn_{1/4}$ flipped BS states being significantly higher in energy. The HS oxo-oxo state is favoured by ≈ 4 kcal mol^{-1} compared to the oxo-hydroxo agreeing well with recent studies of these two states.[18, 22, 29–31]

The study further rationalised the observed trends by analysis of the IBOs. As the proton is abstracted from O6 a lone pair on O6 is seen to stabilise in the evolving $[O5O6]^{3-}$ species. The α lone pair electron is stabilised by σ type interaction with O5 forming a partial bond, concurrently an alpha electron from the Mn_4-O5 σ bond becomes more localised onto Mn_4. The equivalent O6 β lone pair electron is stabilised by donation towards Mn_1. As the O5-O6 distance is decreased the stabilisation gained from sharing the spin between O5 and O6 is increased by the same mechanism as discussed in chapter 5 thus also explaining why the HS state is the most favourable. At 2.3 Å no stabilising interaction of this spin was observed and as such the finding that the oxo-oxo BS states are all very similar in energy is rationalised, further highlighting the importance of the spin

being stabilised between O5 and O6 as the O-O bond is formed.

A similar study by Isobe et al[32] found the W3 pathway to be unfavourable, but as the O5-O6 distance was larger in that model ≈ 2.4 Å and a key bridging water between W3 and W2 was missing it is expected to give a greater barrier, since the evolving O6 spin can't be stabilised and the W3 to W2 transfer is less favourable due to larger distortion around Mn_4 being necessary.

Finally in chapter 6 the $S_3Y_Z^\bullet$ was investigated having studied both the S_3 state and the final deprotonation event. Three stable structures, an O5 oxo-O6 hydroxo, an $[O5O6]^{3-}$ and a O5-O6 peroxo were identified. For each a full BS analysis was performed and the exchange couplings between the spin centres calculated. As the O-O bond formed an increasingly strong OEC-Y_Z long range interaction was observed. As a link between exchange coupling magnitude and electron transfer rate exists this would encourage the final oxidation event of the OEC.[33–36] This observation further reaffirms the role of the OEC to facilitate efficient oxygen production by stabilising intermediates and lowering reaction barriers. Here the OEC stabilised reaction intermediates and encourages reduction of the Y_Z once the O-O bond is formed, driving the reaction forward, consequently explaining the lack of observed peroxo.

The oxo-hydroxo intermediate was found to be highly similar in both the S_3 and the $S_3Y_Z^\bullet$ state, with similar exchange couplings and with Mn_4 BS state most stable. No significant interaction between the OEC and the Y_Z radical was found, this is similar to previous findings made by Retegan et al. in the $S_2Y_Z^\bullet$ state also finding no significant interaction between the OEC and $Y_Z^\bullet$.[37]

The $[O5O6]^{3-}$ displayed some differences between the states in terms of the exchange couplings, but still maintaining the same most stable BS state, with the shared O5-O6 spin being antiparallel to all others spin centres. The spin alignment of the Y_Z radical was not found to make a significant difference to the BS energies. Strong anti-ferromagnetic couplings between the shared O5-O6 spin and the directly bonded $Mn_{1,3,4}$ ions stabilised this intermediate, although these were significantly smaller in the $S_3Y_Z^\bullet$ compared to the S_3 state, indicating that upon Y_Z oxidation this state may become relatively destabilised. Spin plots for this state confirmed that the spin between O5 and O6 was still shared, as well as the delocalised nature of the Y_Z radical. Weak interaction between the OEC and the Y_Z radical was detected.

Finally the peroxo state was found to display strong anti-ferromagnetic interactions between Mn_1, Mn_4 and the Y_Z radical, with these interactions being of the same magnitude as the Mn-Mn interactions. This was reflected in the BS energies which showed significant differences between BS states with Y_Z as α or β. That being said the BS state with Mn_1 antiparallel to all other spin centres remained the

most stable.

Lastly the IBOs for O-O bond formation were tracked and the IBOs displaying significant changes were analysed. It was found that while α spin orbitals behaved the same in both S states, there were differences in the β spin orbitals. In the $S_3Y_Z^\bullet$ state a β Mn_1-O6 σ bond becomes a lone pair β on O6 with an orbital change of 0.5 e^{-1} and concurrently a lone pair β O6 spin orbital moves to Mn_1 with an orbital change of 1.5 e^{-1}. Resulting in an overall change of 1 e^{-1} going towards Mn_1. In the S_3 state however a β Mn_1-O6 σ orbital moves onto Mn_1 with an orbital change of 1 e^{-1} in favour of Mn_1. The same overall results is obtained by two differing pathways. Changes between the S_3 and $S_3Y_Z^\bullet$ state are observed around Mn_1 further indicating an emerging coupling has an effect on the electronic characteristics of the OEC.

Figure 8.1 shows a summary of the findings presented in this thesis. Initially in the S_3 state an oxo-hydroxo species is formed, which establishes an equilibrium with an $[O5O6]^{3-}$ species, requiring Mn_4 to become Mn^{III}. The proton from O6 is transferred via W3 and held either at W2 or continues to the Asp61, as experimental evidence points towards the final proton leaving from Asp61 in the final S_3 to S_0 transition.[4, 5] Upon oxidation of the Y_Z residue and loss of the aforementioned proton the $S_3Y_Z^\bullet$ state is formed. The $[O5O6]^{3-}$ species may then form or be in equilibrium with a peroxo species, with both Mn_1 and Mn_4 now being Mn^{III} and a formal O–O bond having formed. The peroxo species may then be readily oxidised by the $Y_Z^\bullet$ radical due to favourable interactions between the OEC and $Y_Z^\bullet$. The origin of the electron is not clear, and warrants further study as multiple origins and pathways are reasonable. Reduction of the $Y_Z^\bullet$ radical forms the formal but transient S_4 state, forming a superoxo species would rapidly form molecular oxygen with a final reduction of Mn_3 to Mn^{III}. As soon as oxygen is formed and dissociates the hole left in the OEC would likely be rapidly filled by a nearby water, potentially W3, this would require a final deprotonation event as observed. The water network may then adjust more slowly to refill the site from which the new O5 originated, reforming the S_0 state.[4]

As computational power continues to increase more and more complex models will become feasible for study, allowing for more accurate modelling as well faster calculation times. This would allow for additional residues to be modelled, and for example more complete water networks and channels around the OEC to be included. One of the bottlenecks encountered throughout the work performed and presented in this thesis was the time it takes to obtain a full PES, especially in the $S_3Y_Z^\bullet$ for example, there can be potentially 6 spin centres present creating 31 BS states in addition to the HS state. It quickly becomes very time intensive to obtain

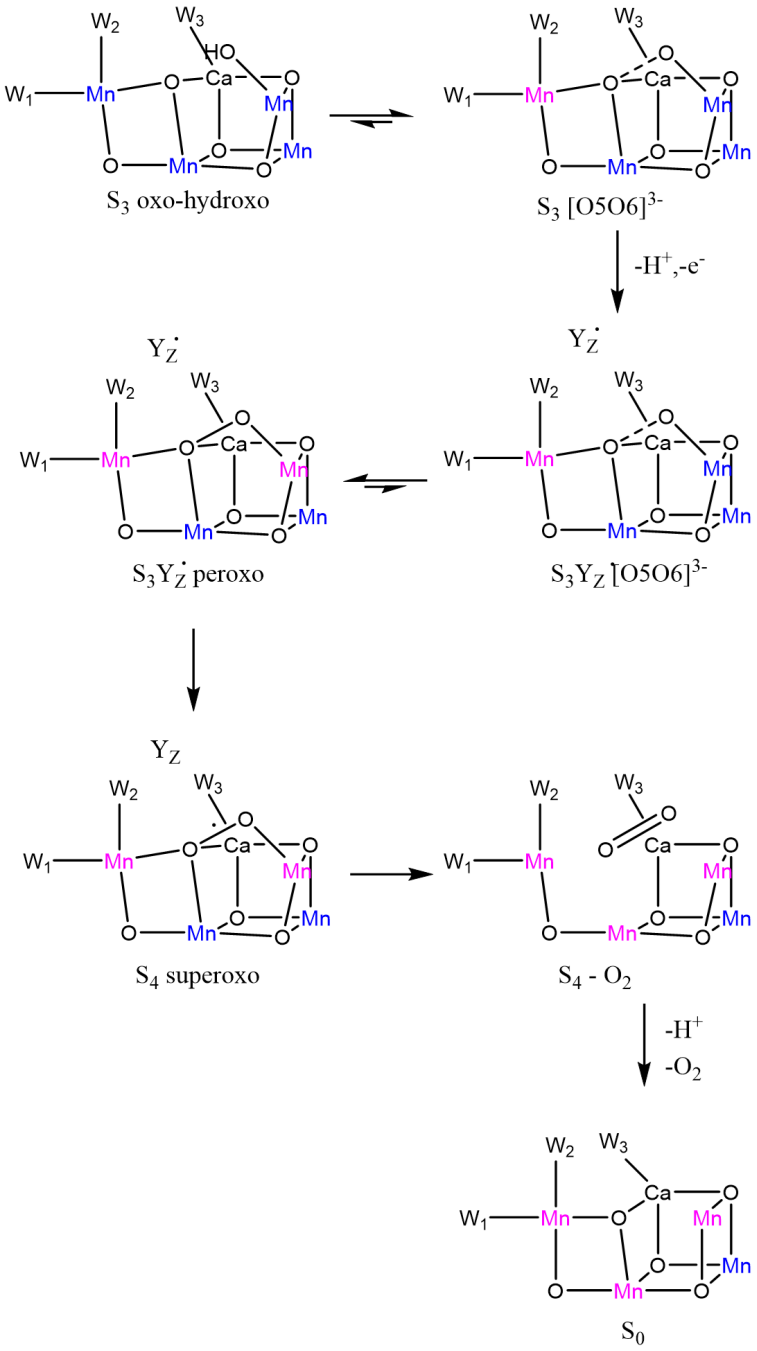

Figure 8.1: Summary of the findings in this thesis on the S_3 to S_4 transition. Blue: Mn^{IV}, Magenta: Mn^{III}.

a full set of PESs even for just one reaction coordinate of one form. Furthermore it has been shown that the choice of method, in particular the amount of modelled Hartree-Fock exchange can impact the relative stability of the various species and as such care needs to be taken[32], warranting further study. Rather than using DFT cluster models it would also be of interest to perform QM/MM calculations, which are becoming more commonplace in the study of PSII,[38–40] allowing for a better simulation of the protein as a whole, though the current computational theory struggles to accurately model the QM/MM interface. With incorrect bond

character between the two.[41, 42] QM/MM methods would also benefit from being more user friendly.

Another area which has and will likely continue to improve in future is the experimental side of research, with ever more accurate structural data becoming available regularly and more data XFEL data on the sequence of events between the formal S states.[1–5] These will better inform the decisions taking in creating computational models and studies, perhaps eventually addressing some questions fully. Of course computational models remain important, as still the resolution of structures obtained experimentally are too low to resolve some questions such as protonation states and reports of faults and inaccuracies even in recent structures mean they should not be solely relied upon.[6–8, 43] Furthermore to fully explore conformational freedom and flexibility as well as for the study of experimentally inaccessible transition states computational techniques remain the method of choice.

This thesis explored primarily around the S_3 and $S_3Y_Z^{\bullet}$ state, due to their importance in molecular oxygen formation being the final S-state which can be experimentally isolated, and as such understanding their nature could provide valuable insights in to the mechanism of oxygen formation. Current work in the group and preliminary work not presented in this thesis was and is aimed to extend this further, looking at the superoxo species, the final reduction of the Y_Z radical prior to molecular oxygen formation as well as the PES for molecular oxygen formation.

While this thesis worked with models in which O5 and O6 formed the oxygen bond and as such O_2, other suggestions have been put forward.[44–46] Studies into water insertion could provide valuable insights not just into which oxygens form the O-O bond but also into the roles of the water channels and how the cycle resets to the S_0 state. Indeed any part of the Kok cycle can still be studied and understood better, and while understanding water oxidation is of interest ultimately the goal should be to apply the gained knowledge to allow for the development of artificial efficient photosynthesis and green hydrogen production, perhaps tackling some of the current energy and climate crisis.[47–49]

References

[1] M. Suga, F. Akita, K. Yamashita, Y. Nakajima, G. Ueno, H. Li, T. Yamane, K. Hirata, Y. Umena, S. Yonekura, L.-J. Yu, H. Murakami, T. Nomura, T. Kimura, M. Kubo, S. Baba, T. Kumasaka, K. Tono, M. Yabashi, H. Isobe, K. Yamaguchi, M. Yamamoto, H. Ago, J.-R. Shen, *Science* **2019**, *366*, 334–338.

[2] M. Ibrahim, T. Fransson, R. Chatterjee, M. H. Cheah, R. Hussein, L. Lassalle, K. D. Sutherlin, I. D. Young, F. D. Fuller, S. Gul, I.-S. Kim, P. S. Simon, C. de Lichtenberg, P. Chernev, I. Bogacz, C. C. Pham, A. M. Orville, N. Saichek, T. Northen, A. Batyuk, S. Carbajo, R. Alonso-Mori, K. Tono, S. Owada, A.

Bhowmick, R. Bolotovsky, D. Mendez, N. W. Moriarty, J. M. Holton, H. Dobbek, A. S. Brewster, P. D. Adams, N. K. Sauter, U. Bergmann, A. Zouni, J. Messinger, J. Kern, V. K. Yachandra, J. Yano, *Proceedings of the National Academy of Sciences* **2020**, *117*, 12624–12635.

[3] R. Hussein, M. Ibrahim, A. Bhowmick, P. S. Simon, R. Chatterjee, L. Lassalle, M. Doyle, I. Bogacz, I.-S. Kim, M. H. Cheah, S. Gul, C. de Lichtenberg, P. Chernev, C. C. Pham, I. D. Young, S. Carbajo, F. D. Fuller, R. Alonso-Mori, A. Batyuk, K. D. Sutherlin, A. S. Brewster, R. Bolotovsky, D. Mendez, J. M. Holton, N. W. Moriarty, P. D. Adams, U. Bergmann, N. K. Sauter, H. Dobbek, J. Messinger, A. Zouni, J. Kern, V. K. Yachandra, J. Yano, *Nature Communications* **2021**, *12*, 6531.

[4] A. Bhowmick, R. Hussein, I. Bogacz, P. S. Simon, M. Ibrahim, R. Chatterjee, M. D. Doyle, M. H. Cheah, T. Fransson, P. Chernev, I.-S. Kim, H. Makita, M. Dasgupta, C. J. Kaminsky, M. Zhang, J. Gätcke, S. Haupt, I. I. Nangca, S. M. Keable, A. O. Aydin, K. Tono, S. Owada, L. B. Gee, F. D. Fuller, A. Batyuk, R. Alonso-Mori, J. M. Holton, D. W. Paley, N. W. Moriarty, F. Mamedov, P. D. Adams, A. S. Brewster, H. Dobbek, N. K. Sauter, U. Bergmann, A. Zouni, J. Messinger, J. Kern, J. Yano, V. K. Yachandra, *Nature* **2023**, *617*, 629–636.

[5] P. Greife, M. Schönborn, M. Capone, R. Assunção, D. Narzi, L. Guidoni, H. Dau, *Nature* **2023**, *617*, 623–628.

[6] A. Sirohiwal, D. A. Pantazis, *Journal of the American Chemical Society* **2022**, *144*, PMID: 36413491, 22035–22050.

[7] M. Drosou, G. Comas-Vilà, F. Neese, P. Salvador, D. A. Pantazis, *Journal of the American Chemical Society* **2023**, *145*, 10604–10621.

[8] M. Amin, *Photosynthesis Research* **2023**, *156*, 89–100.

[9] C. D. Delfs, R. Stranger, *Inorganic Chemistry* **2001**, *40*, 3061–3076.

[10] D. A. Pantazis, V. Krewald, M. Orio, F. Neese, *Dalton Trans.* **2010**, *39*, 4959–4967.

[11] C. J. Stein, D. A. Pantazis, V. Krewald, *The Journal of Physical Chemistry Letters* **2019**, *10*, 6762–6770.

[12] T. A. Corry, P. J. O'Malley, *Journal of the American Chemical Society* **2020**, *142*, PMID: 32431144, 10240–10243.

[13] T. A. Corry, P. J. O'Malley, *The Journal of Physical Chemistry Letters* **2019**, *10*, PMID: 31429574, 5226–5230.

[14] M. Suga, F. Akita, M. Sugahara, M. Kubo, Y. Nakajima, T. Nakane, K. Yamashita, Y. Umena, M. Nakabayashi, T. Yamane, T. Nakano, M. Suzuki, T. Masuda, S. Inoue, T. Kimura, T. Nomura, S. Yonekura, L.-J. Yu, T. Sakamoto, T. Motomura, J.-H. Chen, Y. Kato, T. Noguchi, K. Tono, Y. Joti, T. Kameshima, T. Hatsui, E. Nango, R. Tanaka, H. Naitow, Y. Matsuura, A. Yamashita, M. Yamamoto, O. Nureki, M. Yabashi, T. Ishikawa, S. Iwata, J.-R. Shen, *Nature* **2017**, *543*, 131–135.

[15] J. Kern, R. Chatterjee, I. D. Young, F. D. Fuller, L. Lassalle, M. Ibrahim, S. Gul, T. Fransson, A. S. Brewster, R. Alonso-Mori, et al., *Nature* **2018**, *563*, 421–425.

[16] M. Suga, F. Akita, K. Yamashita, Y. Nakajima, G. Ueno, H. Li, T. Yamane, K. Hirata, Y. Umena, S. Yonekura, et al., *Science* **2019**, *366*, 334–338.

[17] G. Renger, *Biochimica et Biophysica Acta (BBA) - Bioenergetics* **2012**, *1817*, 1164–1176.

[18] T. A. Corry, P. J. O'malley, *The Journal of Physical Chemistry Letters* **2018**, *9*, 6269–6274.

[19] Y. Pushkar, K. M. Davis, M. C. Palenik, *The Journal of Physical Chemistry Letters* **2018**, *9*, 3525–3531.

[20] T. A. Corry, P. J. O'Malley, *The journal of physical chemistry letters* **2020**, *11*, 4221–4225.

[21] H. Isobe, M. Shoji, T. Suzuki, J.-R. Shen, K. Yamaguchi, *Journal of chemical theory and computation* **2019**, *15*, 2375–2391.

[22] T. A. Corry, P. J. O'Malley, *The Journal of Physical Chemistry B* **2021**, *125*, 10097–10107.

[23] V. Krewald, M. Retegan, N. Cox, J. Messinger, W. Lubitz, S. DeBeer, F. Neese, D. A. Pantazis, *Chemical Science* **2015**, *6*, 1676–1695.

[24] N. Cox, M. Retegan, F. Neese, D. A. Pantazis, A. Boussac, W. Lubitz, *Science* **2014**, *345*, 804–808.

[25] G. Zahariou, N. Ioannidis, Y. Sanakis, D. A. Pantazis, *Angewandte Chemie International Edition* **2021**, *60*, 3156–3162.

[26] R. Hussein, M. Ibrahim, A. Bhowmick, P. S. Simon, R. Chatterjee, L. Lassalle, M. Doyle, I. Bogacz, I.-S. Kim, M. H. Cheah, et al., *Nature communications* **2021**, *12*, 6531.

[27] M. Chrysina, E. Heyno, Y. Kutin, M. Reus, H. Nilsson, M. M. Nowaczyk, S. DeBeer, F. Neese, J. Messinger, W. Lubitz, et al., *Proceedings of the National Academy of Sciences* **2019**, *116*, 16841–16846.

[28] M. Mandal, K. Saito, H. Ishikita, *The Journal of Physical Chemistry Letters* **2020**, *11*, 10262–10268.

[29] T. A. Corry, P. J. O'Malley, *The Journal of Physical Chemistry Letters* **2020**, *11*, PMID: 32374174, 4221–4225.

[30] T. A. Corry, F. Rummel, P. J. O'Malley, *The Journal of Physical Chemistry B* **2021**, *125*, 7147–7154.

[31] F. Rummel, P. J. O'Malley, *The Journal of Physical Chemistry B* **2022**, *126*, 8214–8221.

[32] H. Isobe, M. Shoji, T. Suzuki, J.-R. Shen, K. Yamaguchi, *Journal of Chemical Theory and Computation* **2019**, *15*, 2375–2391.

[33] D. Devault, *Quantum Mechanical Tunneling in Biological Systems*, Cambridge University Press, Cambridge, **1984**.

[34] M. D. Newton, N. Sutin, *Annual Review of Physical Chemistry* **1984**, *35*, 437–480.

[35] R. Marcus, N. Sutin, *Biochimica et Biophysica Acta (BBA) - Reviews on Bioenergetics* **1985**, *811*, 265–322.

[36] A. S. Lukas, P. J. Bushard, M. R. Wasielewski, *The Journal of Physical Chemistry A* **2002**, *106*, 2074–2082.

[37] M. Retegan, N. Cox, W. Lubitz, F. Neese, D. A. Pantazis, *Physical chemistry chemical physics : PCCP* **2014**, *16 24*, 11901–10.

[38] M. Askerka, G. W. Brudvig, V. S. Batista, *Accounts of chemical research* **2017**, *50*, 41–48.

[39] M. Capone, L. Guidoni, D. Narzi, *Chemical Physics Letters* **2020**, *742*, 137111.

[40] X. Song, B. Wang, *Journal of Chemical Theory and Computation* **2023**, *19*, 2684–2696.

[41] R. A. Friesner, *Drug Discovery Today: Technologies* **2004**, *1*, 253–260.

[42] G. A. Bramley, O. T. Beynon, P. V. Stishenko, A. J. Logsdail, *Phys. Chem. Chem. Phys.* **2023**, *25*, 6562–6585.

[43] A. Galstyan, A. Robertazzi, E. W. Knapp, *Journal of the American Chemical Society* **2012**, *134*, 7442–7449.

[44] B. Zhang, L. Sun, *Dalton Trans.* **2018**, *47*, 14381–14387.

[45] N. Cox, J. Messinger, *Biochimica et Biophysica Acta (BBA) - Bioenergetics* **2013**, *1827*, Metals in Bioenergetics and Biomimetics Systems, 1020–1030.

[46] K. Yamaguchi, K. Miyagawa, M. Shoji, H. Isobe, T. Kawakami, *Chemical Physics Letters* **2022**, *806*, 140042.

[47] C. Wang, M. P. O'Hagan, B. Willner, I. Willner, *Chemistry – A European Journal* **2022**, *28*, e202103595.

[48] P. Hunter, *EMBO reports* **2022**, *23*, e56149.

[49] T. Faunce, S. Styring, M. R. Wasielewski, G. W. Brudvig, A. W. Rutherford, J. Messinger, A. F. Lee, C. L. Hill, H. deGroot, M. Fontecave, D. R. MacFarlane, B. Hankamer, D. G. Nocera, D. M. Tiede, H. Dau, W. Hillier, L. Wang, R. Amal, *Energy Environ. Sci.* **2013**, *6*, 1074–1076.